

Modelling the Oxidation of Tungsten and Tungsten Alloys for Fusion Reactor First Walls

Ryan David Kerr, MChem, MScR, MRSC

School of Engineering

Lancaster University

A thesis submitted for the degree of

Doctor of Philosophy

October, 2025

Modelling the Oxidation of Tungsten and Tungsten Alloys for Fusion Reactor First Walls

Ryan David Kerr, MChem, MScR, MRSC.

School of Engineering, Lancaster University

A thesis submitted for the degree of *Doctor of Philosophy*. October, 2025.

Abstract

To address the growing demand for low-carbon energy, the United Kingdom has committed to building the world's first nuclear power plant by 2040, the Spherical Tokamak for Energy Production (STEP). One of the challenges faced by the STEP project concerns the oxidation of the reactor's tungsten-based first wall, which may occur during a loss of coolant accident or remote maintenance handling. The oxidation of tungsten begins at 673 K. This ultimately leads to the formation of tungsten trioxide, a volatile phase which may be a vector for the distribution of radioactive isotopes into the surroundings. This poses a safety hazard for site staff and first responders, and therefore, the suppression of oxide formation stands as one of the key motivations in first wall research, including the development of Self-passivating Metal Alloys with Reduced Thermo-oxidation materials, or 'SMART' materials.

This thesis explores the transport of oxygen through the observed tungsten oxide phases, including the sub-stoichiometric Magnéli phases, using density functional theory. Therefore, the relationships between the physical and electronic structures of the stoichiometric and sub-stoichiometric oxide phases are presented. In the second part of this thesis, the roles of Cr and Y in the SMART alloy W-11.4Cr-

0.6Y are elucidated using density functional theory and classical mechanics. The results show that yttrium acts as an oxygen scavenger at the grain boundaries of the alloy, whilst chromium diffuses via a vacancy exchange mechanism which is sensitive to the presence of oxygen. Crucially, it is demonstrated that, in the absence of yttrium, impurity oxygen reduces the availability of vacancies in the tungstenchromium grains, inhibiting the self-passivating action of the alloy by preventing the migration of chromium to the surface.

Acknowledgements

First and foremost, I would like to thank Samuel Murphy at Lancaster University - not only for taking me on for this studentship in the first place, but for providing me with all the help and support that I needed to make it through (and beyond). I could not have asked for a better supervisor and mentor, and the many, many lessons that I have learned during my time at Lancaster will undoubtedly stay with me for the rest of my life.

I would also like to thank Mark Gilbert and Duc Nguyen-Manh from the UK Atomic Energy Authority, who were my most regular collaborators during the project. Their insights and experiences helped to shape the project through many monthly meetings, and I look forward to many more years of collaboration as a member of their team.

This work would not have been possible without the HPC services provided by the Lancaster University HEC, the ARCHER2 UK National Supercomputing Service (http://www.archer2.ac.uk) via the UK's HEC Materials Chemistry Consortium (EP/R029431), and the Physical Sciences Data-science Service hosted by the University of Southampton and STFC (EP/S020357/1). It was also supported by the ESPRC-funded Centre for Doctoral Training in GREEN (Growing skills for Reliable Economic Energy from Nuclear) (EP/S022295/1).

Last and certainly not least, I would like to thank my mum and dad for their consistent support during my time at Lancaster, and for the many years at university leading up to it as well!

Declaration

I declare that the work presented in this thesis is, to the best of my knowledge and belief, original and my own work. The material has not been submitted, either in whole or in part, for a degree at this, or any other university. This thesis does not exceed the maximum permitted word length of 80,000 words including appendices and footnotes, but excluding the bibliography. A rough estimate of the word count is: 45644.

Ryan David Kerr

Publications

The following publications were created from the results presented in this thesis:

R. D. Kerr, M. R. Gilbert, and S. T. Murphy. "Relating the Formation Energies for Oxygen Vacancy Defects to the Structural Properties of Tungsten Oxides". In: Computational Materials Science 252 (2025), p. 113781

R. D. Kerr et al. "Stability of Oxide Phases in W-Cr-Y SMART Alloys". In: Nuclear Materials and Energy 45 (2025), p. 101987

Contents

1	Intr	oductio	on	1
2	Bac	kgroun	\mathbf{d}	6
	2.1	Develo	pment of Fusion Technology	6
		2.1.1	Principles of Nuclear Fusion	6
		2.1.2	Magnetic Confinement Fusion	10
		2.1.3	Spherical Tokamaks	15
	2.2	Fusion	Reactor First Walls	17
		2.2.1	Layout of a Tokamak Reactor	17
		2.2.2	Neutron Environment at the First Wall	20
		2.2.3	First Wall Materials	23
		2.2.4	Tungsten Under Neutron Irradiation	26

2.3	Diffus	ion in Solids	30
	2.3.1	Definition of Crystal Structures	30
	2.3.2	Intrinsic and Extrinsic Point Defects	32
	2.3.3	Defect Formation Enthalpy	37
	2.3.4	Point Defect Concentration	38
	2.3.5	Diffusion Mechanisms	40
	2.3.6	Transition State Theory	42
2.4	Oxida	tion of Tungsten	44
	2.4.1	Theory of Oxidation in Solids	44
	2.4.2	The Tungsten-Oxygen System	47
	2.4.3	Mechanism of Tungsten Oxidation	50
	2.4.4	Loss of Coolant Accidents	52
2.5	Self-P	assivating Tungsten Alloys	54
	2.5.1	Early Development of tungsten-based SMART Alloys	54
	2.5.2	Yttrium as the Active Element	57
	2.5.3	Synthesis of Tungsten-Based SMART Alloys	59
	2.5.4	Spinodal Decomposition	61

		2.5.5	Oxidation of Tungsten-Based SMART Alloys	62
	2.6	Resear	rch Aims	68
3	$\operatorname{Th}\epsilon$	eory		69
	3.1	Procee	dures in Atomistic Simulations	71
		3.1.1	Energy Minimisation	71
		3.1.2	Molecular Dynamics	74
		3.1.3	Temperature Accelerated Dynamics	76
			3.1.3.1 The TAD Algorithm	78
		3.1.4	Periodic Boundary Conditions	80
		3.1.5	Nudged Elastic Band Method	81
		3.1.6	Special Quasirandom Structure (SQS) Approach	83
		3.1.7	Calculation of ΔG_{mix} in Binary Alloys	84
	3.2	Quant	um Mechanics	85
		3.2.1	Principles of Quantum Mechanics	85
		3.2.2	Density Functional Theory	88
		3.2.3	Exchange-Correlation Potentials	92
			3.2.3.1 Local Density Approximation	92

			3.2.3.2	Generalised Gradient Approximation
			3.2.3.3	Hybrid Functionals
		3.2.4	Plane-W	Vave DFT
			3.2.4.1	k-point Sampling
		3.2.5	Pseudop	potentials
		3.2.6	The DF	$\Gamma + U$ Formalism
	3.3	Intera	tomic Pot	sentials
			3.3.0.1	Coulombic Potential
			3.3.0.2	Short Range Potential
		3.3.1	Embedd	ed Atom Potentials
4	Mo	del Va	lidation	106
	4.1	Plane-	-wave Cut	s-off Energy
	4.2	Summ	ary of Pa	rameters
	4.3	Tungs	$ an \dots$	
		4.3.1	Physical	Structure and Chemical Potential
		4.3.2	Electron	ic Structure
		4.3.3	Lattice 1	Dynamics

		4.3.4	Elastic Properties	115
	4.4	Chron	nium	117
		4.4.1	Physical Structure and Chemical Potential	117
		4.4.2	Electronic Structure	119
		4.4.3	Lattice Dynamics	121
		4.4.4	Elastic Properties	122
	4.5	Yttriu	um	124
		4.5.1	Physical Structure and Chemical Potential	124
		4.5.2	Electronic Structure	125
		4.5.3	Lattice Dynamics	127
		4.5.4	Elastic Properties	128
	4.6	Oxyge	en	129
5	Oxy	$_{ m gen}~{ m V}$	acancy Formation in the Tungsten Oxides	133
	5.1	Metho	odology	135
	5.2	Result	s and Discussion	137
		5.2.1	Stability at 0 K	137
		5.2.2	Crystal Structure	139

		5.2.3 Electronic Structure	13
		5.2.4 Oxygen Vacancy Formation Energies	l6
		5.2.5 Oxygen Vacancy Migration Barriers	53
	5.3	Summary	56
6	Stal	lity of Oxide Phases in W-Cr-Y SMART Alloys 15	8
	6.1	Methodology	5 0
	6.2	Lattice Parameters and Atomisation Energies of Bulk Phases 16	60
	6.3	Defect Formation Energies in bcc-W	3
	6.4	Formation Enthalpy of Oxide Phases in W-Cr-Y SMART alloys 16	i8
	6.5	Binding Capacity of Y	3 9
	6.6	Summary	7 0
7	Seg	egation of Chromium in W-Cr Alloys 17	'1
	7.1	Methodology	⁷ 2
	7.2	Thermodynamics of W-Cr Segregation	⁷ 4
	7.3	Grain Boundary Segregation in W-Cr-Y	30
		7.3.1 Solubility of Cr and Y at W Grain Boundaries	30

		7.3.2 Effect of Cr Concentration on Grain Boundary Segregation .	. 184
	7.4	Summary	. 187
8	Mig	gration of Chromium in W-Cr Alloys	188
	8.1	Methodology	. 190
	8.2	Effect of Cr concentration	. 191
	8.3	Effect of vacancy concentration	. 198
	8.4	Comparison with Density Functional Theory	. 200
	8.5	Summary	. 203
9	Effe	ect of Oxygen on Vacancy-Mediated Diffusion	204
	9.1	Methodology	. 205
	9.2	Migration of O around W Vacancy	. 206
	9.3	Migration of Cr in the Presence of O	. 210
	9.4	Summary	. 213
10	Con	aclusions and Outlook	214
$R\epsilon$	efere	nces	220

List of Tables

2.1	The Wyckoff positions of the monoclinic $P2_1/c$ space group	. 32
3.1	Valence orbitals included in the pseudopotentials employed throughout this thesis	. 99
4.1	Computational parameters used for DFT and MD calculations, unless specified otherwise	. 108
4.2	Optimised lattice parameter (a) of bcc-W calculated using PBE and PBEsol GGA functionals and the EAM potential for the Fe-Cr-W system by Bonny et al., compared to existing theoretical and experimental work	. 111
4.3	The single crystal elastic constants and averaged bulk modulus (B_0) , Young's modulus (E_0) and shear modulus (G_0) of bcc W polycrystal calculated using the PBE exchange-correlation functional. All values in GPa	. 115

4.4	Minimum energy per unit cell (E_0) , optimized lattice parameter (a) , and energy difference (ΔE_0) between AFM and NM configurations of bcc Cr, calculated using PBE and PBEsol GGA functionals	117
4.5	The single crystal elastic constants and averaged bulk modulus (B_0) , Young's modulus (E_0) and shear modulus (G_0) of AFM bcc-Cr polycrystal calculated using the PBE exchange-correlation functional. All values in GPa	122
4.6	Optimised lattice parameter (a) and axial ratio (c/a) of hcp-Y calculated using PBE and PBEsol GGA functionals, compared to theoretical and experimental data	124
4.7	The single crystal elastic constants and averaged bulk modulus (B_0) , Young's modulus (E_0) , and shear modulus (G_0) of polycrystalline hcp-Y calculated using the PBE exchange-correlation functional. All values in GPa	128
4.8	Bond lengths (L) , binding energies (E_{bind}) , and HOMO-LUMO gaps (ΔE_{gap}) predicted using the PBE and PBEsol GGA exchange-correlation functionals and the B3LYP and PBE0 hybrid functionals in this work, compared to previous theoretical and experimental data.	131
5.1	The values of U for each species investigated in this chapter, calculated according to the method detail by Cococionni <i>et al.</i> and discussed in Section 3.2.6 [216]	125

5.2	Lattice parameters and band gaps (E_g) , where applicable, for WO ₃ ,	
	WO_2 , $W_{18}O_{49}$, and $W_{25}O_{73}$. Asterisks (*) denote parameters, cell	
	volumes, and band gaps calculated in this work. Experimental values	
	are indicated with a U parameter of '-', while DFT studies without	
	a U correction are listed as $U=0$. Band gaps not evaluated are	
	marked with a '-'	140
5.3	Optimised bond lengths in WO_3 and WO_2 . The number of the oxygen	
	atom in the W-O bond is given in Figure 5.4	141
5.4	Defect formation energies for oxygen vacancy defects in WO_2 and	
	WO_3 . For WO_3 , all defect energies are quoted at the valence band	
	maximum. In the O-rich case, the oxygen chemical potential is taken	
	as half the energy of the O_2 molecule; in the O-poor case, it is	
	determined from the oxide and the metal. Chatten et al. [291] and	
	Lambert-Mauriat et al. [292] report values only under O-rich conditions	s.148
5.5	Oxygen vacancy migration barriers through tungsten trioxide in the	
	+0, $+1$, and $+2$ charge states between two unique oxygen vacancy	
	sites, i.e., A to B. Values for the reverse migration (B to A) are	
	included in brackets	155
5.6	Oxygen vacancy migration barriers through tungsten dioxide. As	
	there are only two unique oxygen vacancy sites, the migration barrier	
	between two identical, adjacent vacancy sites has also been included.	155
6.1	Summary of lattice parameters and energy of atomisation of the	
0.1	oxide phases considered in this chapter, using the PBE and PBEsol	
	exchange-correlation functionals. Experimental data obtained from	
	[233, 300]	161

6.2	Formation enthalpies of point defects in bcc-W, calculated using
	the PBE and PBEsol exchange-correlation functionals. The EAM
	potential by Bonny et al. has also been used to calculate the
	formation enthalpy of Cr defects and the tungsten vacancy [218] 162
6.3	Formation enthalpy of oxide phases observed during the oxidation
	of W-Cr-Y smart alloys, from both constituent metallic phases
	and molecular oxygen, and from point defects in bulk bcc-W. The
	formation enthalpy per oxygen atom present in the oxide and the
	experimental formation enthalpy (where available) have also been given. 166
7.1	Grain boundary energies, γ_{GB} , of three low-symmetry grain bound-
	aries in pure W. The grain boundary cross-section is given by $b \times c$,
	and the total energy difference is $\Delta E = E_{grain} - E_{bulk}$. Reference
	values from [308, 309]
8.1	Cumulative elapsed time over the course of the simulation at each Cr
	concentration

List of Figures

1.1	Project changes in electricity generation (in TWh) in the United	
	Kingdom until 2050 [14]. 'CCUS' refers to carbon capture and storage	
	technologies	3
1.2	The main challenges in fusion engineering up to 2030 according to the	
	Fusion Industry Association's 2023 report, based on responses from	
	38 fusion engineering institutions and companies [15]	4
2.1	The increase of the maximum obtained fusion triple product by year,	
	compared with the progress in transistor performance, until 2000 [18].	Ö
2.2	Lyman Spritzer and the Model A Stellarator, the precursor to the	
	Model C, circa 1952	11
2.3	Progress on the International Thermonuclear Experimental Reactor	
	near Cadarache, France, in September 2023 (ITER Organisation). $aaaaaaaaaaaaaaaaaaaaaaaaaaaaaaaaaaaa$	14
2.4	Cross-section of the conceptual design of the Spherical Tokamak for	
	Energy Production and its components [62]	16
2.5	Cross-section of the ITER cryostat. Credits to the ITER Organisation.	18

2.6	Neutron energy spectra at the outboard equatorial first wall of DEMO (predicted) versus a fuel assembly in a pressurised water [fission] reactor. The region of thermal neutrons (1 - 10 MeV) is shown with	
	a blue arrow [82]	21
2.7	Neutron flux and displacements per atom over a full power year for a theoretical DEMO-like first wall made of iron [82]	22
2.8	The various plasma facing materials used in JET, colourised for ease of identification [90]	24
2.9	Transmutation products of W at the first wall under ITER-like operating conditions [101]	27
2.10	A unit cell, showing its crystal axes (x, y, z) , lattice parameters (a, b, c) , and inclinations (α, β, γ) . Multiple unit cells form a crystal lattice. Credit to Christopher Auyeung, CK-12 Foundation, under CC BY-NC 3.0	30
2.11	An example of point defects in a binary solid of species M (blue) and N (red). (Left) A Frenkel pair of species V_M and M_i . (Right) A Schottky pair of species V_M and V_N	33
2.12	An example of (left) an antisite defect and (right) a substitutional in a generic alloy MN . In the substitutional defect, the substituting species, X , is shown in green	35
2.13	The nearest neighbours of the (left) octahedral interstitial site and (right) tetrahedral interstitial site in a body-centred cubic lattice. Credit to Philippe Lours, École des mines d'Albi-Carmaux, under CC BY-NC-SA	36

2.14	A simplified representation of an oxide scale, showing the direction of	
	ion and electron transport according to the Wagner theory of oxidation.	46
2.15	The phase diagram of the tungsten-oxygen system extended down to 0 °C, in terms of temperature and the oxygen content (in both wt%	
	and at%) [133]	48
2.16	The thermochromism seen in WO_3 over a range of temperatures [143].	50
2.17	Activity of tungsten after irradiation. Obtained by Gilbert <i>et al.</i> using the following data sources (from top to bottom): conceptual power plant neutron spectra at the first wall, blanket and shield, and from JET DD experimental neutron spectrum [152]	53
2.18	Temperature of a conventional tokamak tungsten first wall over 100 days following a loss of coolant accident for four different conceptual tokamak power plant designs. [156]	55
2.19	Oxidation of (left) pure tungsten after 10 hours and (right) tungsten- chromium SMART alloy after 2 days, at 1273 K [159]	56
2.20	Mass change during the oxidation of (1) pure W, (2) HIP W-Cr-Y SMART alloy, (3, 4) FAST W-Cr-Y SMART alloys [166]	60
2.21	Grain structures of W-Cr-Y synthesised under (left) 'FAST 1' and (right) 'FAST 6' conditions [166]	61
2.22	Phase diagram of the tungsten-chromium system from experimental data. The region of spinodal decomposition is shown in the lower portion of the phase diagram (the $\alpha_1 + \alpha_2$ region), whereas the (α Cr, W) denotes the homogeneous solid solution at high temperature [177].	63

2.23	Cross-section of W-Cr and W-11.4Cr-0.6Y alloys after 10 minutes of oxidation in 80% Ar, 20% O_2 atmosphere at 1273 K [166]	64
2.24	Microstructure cross-sections of W-11.4Cr-xY at various Y concentrations. The small, dark spots are identified as a Y-containing phase [183]	65
2.25	Mass change of W-11.4Cr-xY at various concentrations of Y [183]	66
2.26	Mass change of W-11.4Cr-0.6Y at various concentrations of O [183].	66
2.27	X-ray diffraction patterns of W-11.4Cr- x Y at various concentrations of Y [183]	67
3.1	The length- and timescales of different simulation techniques. Credit to David Holec, under CC BY-SA 4.0	70
3.2	Simplified example of a potential energy surface and a representation of the energy minimisation process [193]	72
3.3	Example of the extrapolation of the transition time (t) from T_{high} back to T_{low} in a generic TAD procedure. Two possible transitions are shown with different transition times at T_{low} , with the fastest transition at the target temperature shown in red	79
3.4	A simplified, two-dimensional representation of periodic boundary conditions. The dashed circles encompass the atoms interacting with the highlighted atoms (black), whereas the dashed lines represent the	00
	periodic boundary. [199]	80

3.5	Representation of the nudged elastic band on a potential energy surface and the elucidation of the minimum energy path (MEP) from an initial band	32
3.6	The external potential and the wavefunction of the all-electron solution (AE) and under the psuedopotential approach (PS) [212] 9	8
3.7	Examples of the Born-Mayer, Lennard-Jones and Buckingham potentials for arbitrary values of V_{ij}^{sr} and $r.$ r_0 denotes the equilibrium distance between two particles in the Lennard-Jones potential. The mathematical forms of the potentials are given in Equations 3.52, 3.53, 3.54)3
4.1	Convergence testing on the plane-wave cut-off energy, E_{cut} 10	19
4.2	Band structure and electronic density of states of bcc-W obtained using the (top) PBE and (bottom) PBEsol exchange-correlation functionals, relative to the Fermi level	.3
4.3	Phonon dispersion of bcc-W obtained using the PBE exchange- correlation functional	4
4.4	Band structure and electronic density of states of bcc-Cr obtained using the (top) PBE and (bottom) PBEsol exchange-correlation functionals, relative to the Fermi level. For the electronic density of states, the up-spin component is shown black, and the down-spin component is shown in grey	20
4.5	Phonon dispersion of antiferromagnetic bcc-Cr obtained using the PBE exchange-correlation functional	21

4.6	Band structure and electronic density of states of hcp-Y obtained using the (top) PBE and (bottom) PBEsol exchange-correlation functionals, relative to the Fermi level	26
4.7	Phonon dispersion of hcp-Y obtained using the PBE exchange-correlation functional	27
4.8	The molecular orbitals of the O ₂ dimer in the triplet state and their energies as calculated in this work using the (a) PBE, (b) PBEsol, (c) PBE0 and (d) B3LYP exchange-correlation functionals. The up-spin states are shown in black, whilst the down-spin states are shown in grey	30
5.1	Unit cells of (a) WO_3 , (b) WO_2 , (c) $W_{18}O_{49}$ ($WO_{2.72}$) and (d) $W_{25}O_{73}$ ($WO_{2.92}$). Grey atoms denote tungsten. Red atoms denote oxygen. Unique Oxygen sites in WO_2 and WO_3 are denoted by the numbers 1-2 and 1-3, respectively	34
5.2	The convex hull showing the enthalpies of formation for a wide range of W_xO_y systems as a function of the atomic percentage of oxygen. The red line denotes the convex hull itself, consisting of the thermodynamically stable tungsten oxide phases	38
5.3	The section of the W_xO_y convex hull (shown above) from 60 to 80 at% O, showing the stable tungsten oxide phases	38

5.4	The numerical labels assigned to oxygen atoms in (a) WO_3 and (b) WO_2 for discussion of $W-O_x$ bond lengths. Grey atoms represent tungsten and red atoms represent oxygen. The labels 1-2 for WO_2 and 1-3 for WO_3 also correspond to the unique oxygen sites highlighted in Figure 5.1	. 142
5.5	Projected and total density of states of the tungsten oxide phases investigated in this study. The Fermi level was set to zero. The black line represents the total density of states and the red and grey lines represent the projected density of states for the O $2p$ and W $5d$ orbitals respectively. The grey vertical line denotes $E-E_f=0$. 144
5.6	Distribution of magnetic moments in $W_{18}O_{49}$, ranging from 0.000 μ_B (white) to +0.494 μ_B (red). The larger atoms denote tungsten, whilst the smaller atoms denote oxygen	145
5.7	Total electronic density of states for monoclinic WO_3 , calculated with a U parameter of (a) 0 eV and (b) 5.13 eV. The total electronic density of states, as calculated using the HSE06 hybrid functional, is shown in (c). The plots have been centered on the valence band maximum for ease of comparison.	147
5.8	Oxygen vacancy formation energy in tungsten trioxide as a function of the Fermi level in the (a) O-rich and (b) O-poor limits. The solid line denotes the $+0$ charge state, the dashed line denotes the $+1$ charge state, and the dotted line denotes the $+2$ charge state. The valence band maximum lies at 0 eV, whilst the conduction band maximum begins at 2.53 eV. The blue line the V_{O2} and the red line the V_{O3} defect	:.150

5.9	Oxygen vacancy formation energies in the Magnéli phases (a) $W_{18}O_{49}$	
	and (b) $W_{25}O_{73}$. The black atoms represent tungsten, whilst	
	the oxygen atoms are coloured according to their oxygen vacancy	
	formation enthalpy. The formation enthalpies are calculated in the	
	O-rich limit	152
5.10	Bond lengths in $W_{18}O_{49}$ and $W_{25}O_{73}$. The view of $W_{25}O_{73}$ has been	
	truncated along the y -axis for clarity	154
6.1	Unit cells of (a) Cr_2WO_6 , (b) $CrWO_4$, (c) Y_2O_3 and (d) $YCrO_3$. Grey	
	atoms denote tungsten. Red atoms denote oxygen. Green atoms	
	denote chromium. Yellow atoms denote yttrium	159
6.2	Some of the defects studied in this chapter: (a) O_{TIS} , (b) Cr_{OIS} and	
	(c) Y_W	164
7.1	Configurations of W-Cr predicted by the special quasirandom struc-	
	ture approach for (a) 12.5% , (b) 25% , (c) 37.5% and (d) 50% Cr.	
	The grey atoms denote W, and the green atoms denote Cr. These	
	are identical to the configurations above 50 at % Cr	172
7.2	The enthalpy of mixing for the W-Cr system across the Cr concen-	
	tration range, calculated using density functional theory (black) and	
	molecular statics (red) using the Fe-Cr-W potential by Bonny $\it et~\it al.~$.	175
7.3	The configurations with the (a) lowest and (b) highest ΔH_{mix} at 50	
	at% Cr. Note that (b) also matches the SQS structure at 50 at% Cr	
	shown in Figure 7.1	175

7.4	The lattice parameter of the W-Cr system across the Cr concentration
	range, calculated using density functional theory (black) and molec-
	ular statics using the Fe-Cr-W potential by Bonny $\it et~\it al,$ compared to
	the expected value as per Vegard's Law (blue)
7.5	The Gibbs energy of mixing, ΔG_{mix} for the W-Cr system in
	configurations obtained via the SQS approach, calculated for a range
	of temperatures from 0 to 2000 K
7.6	Predicted spinodal phase diagram of the W-Cr system based on
	density functional theory calculations on the structures obtained via
	the SQS approach. Simulations in which the magnetic moments were
	allowed to relax are show in red (NM-AFM), whilst those in which
	the magnetic moments were fixed at 0 μB are shown in blue (NM).
	The experimental values of the order-disorder transition temperature
	are shown in black [177]
7.7	The Cr vacancy formation enthalpy in W-Cr as a function of Cr
	concentration
7.8	The (a) $\langle 210 \rangle [100]$, (b) $\langle 310 \rangle [100]$, and (c) $\langle 112 \rangle [110]$ grain boundaries
	in pure W
7.9	The enthalpy of solution of Cr as a function of distance from
	the $\langle 210 \rangle [100]$ grain boundary in W, as calculated using the PBE
	functional and the EAM potential by Bonny et al The enthalpy of
	formation of the Cr_W defect in the bulk is given as a dashed line for
	each data set

7.10	The enthalpy of solution of Y as a function of distance from the $\langle 210 \rangle [100]$ grain boundary in W. The enthalpy of formation of the	
	Cr_W defect in the bulk is given as a dashed line	82
7.11	The substitution sites a through e in the $\langle 210 \rangle [100]$ grain boundary 1	83
7.12	Segregation of Cr to the $\langle 210 \rangle [100]$ grain boundary in W-Cr, with grain concentrations of 10 at% and 30 at% Cr. The number of Cr atoms as a function of distance from the grain boundary $(d=0)$ is shown beneath the view of the simulation cell along the [010] axis. The initial and final configurations of the simulation cell are shown in (a) and (b), respectively	85
8.1	Simplified illustration of the sequence of atom-vacancy exchanges required for the atom of interest (green) to migrate through a lattice (black) <i>via</i> a vacancy-hopping mechanism	89
8.2	Average displacements, $d(t)$, of Cr (green) and W (grey) atoms in 128- atom W-Cr supercells at different Cr concentrations, (a) 5 at%, (b) 10 at%, (c) 20 at%, and (d) 35 at%. The total average displacement is shown in black	91
8.3	Radius of gyration of Cr clusters in W-Cr as a function of time, coloured according to the number of Cr atoms in the cluster, for (left) 5 at% and (right) 35 at% Cr concentrations	93
8.4	Radial distribution functions at $t=0$ and $t=t_{seg}$ for the (left) 5 at% Cr and (right) 35 at% Cr systems. The RDF at $t=0$ is shown in black, and at $t=t_{seg}$ in red	94

8.5	Images of (a, b, c) 5 at% and (d, e, f) 35 at% Cr concentration W-Cr, viewed along the $\langle 111 \rangle$ axis. Snapshots taken at (a, d) $t=0$, (b, e) $t=t_{seg}$, and (c, f) $t=t_{end}$. Grey atoms represent W. Green atoms represent Cr. Green lines show the trajectory of the Cr atoms up to and including the snapshot. Note that the trajectories have been unwrapped, <i>i.e.</i> , atoms that have moved outside the periodic boundaries of the simulation cell are shown in their actual positions.	. 195
8.6	Migration barriers for all transitions observed in the simulation of (left) 5 at% and (right) 35 at% Cr systems. Green points represent barriers for the migration of Cr; grey points represent barriers for the migration of W.	. 197
8.7	Radius of gyration of Cr clusters in W-Cr at 5 at% Cr concentration, for (a) 431-atom and (b) 1457-atom simulation cell sizes, coloured according to the number of Cr atoms in the cluster	. 198
8.8	Atoms where $d(t) \ge 0.1$ at t_{seg} in W-Cr at 5 at% Cr for (a) 431-atom and (b) 1457-atom simulation cell sizes. Grey atoms represent W. Green atoms represent Cr	. 198

8.9	The migration barrier of a Cr atom exchanging positions with a	
	vacancy, where the Brillouin zone has been sampled using (left)	
	the Γ -point only, with 5 intermediate images, and (right) a $3\times3\times3$	
	mesh, with 9 intermediate images. The black dashed line represents	
	a cubic spline fitted to the data for illustrative purposes. The	
	red line represents the maximum height of the barrier to the	
	intermediate state, whilst the blue line represents the relative energy	
	of the intermediate state itself. Below, the 1st, 4th, 8th and 11th	
	configurations in the latter simulation are shown in (a) through (d)	
	respectively, with the red square denoting the vacant site, the green	
	atoms denoting Cr, and the grey denoting W	. 201
8.10	Comparison of migration barriers obtained <i>via DFT</i> (red) and TAD	
	(blue) for 5 at% Cr concentration. Only the migration barriers	
	obtained using nine images, as described in Section 8.1, are shown.	
	ID is the number assigned to the randomly selected transition	. 202
9.1	All O_{TIS} starting positions used throughout this chapter. The O_{TIS}	
0.1	sites were placed relative to (a) the vacancy site and (b) the first	
	nearest neighbour. Each O_{TIS} is connected to each of its three nearest	
	neighbours by a black line	. 205
9.2	The difference in total energy of the system as a function of the	
0.2	distance between the vacancy and the O_{TIS} defect in bcc-W, relative	
	to the total energy of a bcc-W system where both V_W and O_{TIS} are	
	isolated from one another	206
	Isolanca Irolli Olic allonici	. 400
9.3	NEB profiles of \mathcal{O}_{TIS} migration at various distances from a \mathcal{V}_W site	
	in bcc-W: (a) on-site, ~ 1.5 Å; (b) first nearest neighbour, ~ 2.0 Å;	
	(c) first nearest neighbour, ~ 2.5 to 3.0 Å	. 207

9.4	Migration pathways of O_{TIS} defects, corresponding to the barriers in	
	Figure 9.3a, b and c. The white atom denotes the position of the	
	vacancy, the red-grey atoms denote other O_{TIS} positions around the	
	site, and the path between the start and end sites is shown in blue. As	
	such, the red atoms denote the start and end positions of the single	
	O_{TIS} defect	208
9.5	The difference in total energy of the system as a function of the	
	distance between the vacancy and the O_{TIS} defect in 5 at% W-Cr,	
	relative to the total energy of a bcc-W system where both \mathbf{V}_W and	
	O_{TIS} are isolated from one another	209
9.6	NEB profile of the vacancy-mediated migration of Cr in the presence	
	of O_{TIS} . The heights of the forward and reverse migrations are shown	
	in red and black respectively	210
9.7	NEB profile of the vacancy-mediated migration of Cr in the presence	
	of O_{TIS} when the defect does not lie along the $\langle 100 \rangle$ axis relative to	
	the V_W defect and the migrating Cr ion	211
9.8	Migration pathways of Cr in the presence of O_{TIS} when the O_{TIS} -Cr-	
	V_W angle is (a, b) 108.9 °, (c, d) 53.9°. The initial configurations are	
	(a) and (c), whilst the final configurations are (b) and (d)	212

Chapter 1

Introduction

More than a million years have passed since hominids discovered chemical combustion [3]. Since then, our ancestors have used fire for warmth, cooking, and protection. To an alien observer, our species' newfound interest in generating heat from fuels other than plant matter must come as a surprise - a whiplash-inducing turn away from a multi-million-year-old tradition of burning biomass. Recent evidence suggests that coal has only been used for around 3,600 years [4], a stepping stone that would later pave the way for the Industrial Revolution of the 18th- and 19th centuries. The work of Savery, Newcomen, and Watt throughout the 18th century brought about the advent of steam power, a fantastic new use for the combustion of coal, which, coupled with the work of electrical pioneers in the early 19th century, sparked perhaps the most incredible socio-technological leap in human history. The impact of entwining steam and electricity on society cannot be understated; the abundance of electrical power enabled the creation of complex machines capable of harvesting food and minerals en masse, brought light and heat to homes, and allowed the synthesis of new materials. Literacy rates rose, and mortality rates fell, and as more nations industrialised, the global population soared [5, 6].

This population surge has underlined one crucial fact: each year, we need more and more energy to sustain us. By 2100, the United Nations estimates that the global population will reach approximately 10.4 billion [7], though the uncertainty in these estimates is substantial. Estimates based on current energy consumption trends [8] and the speculative needs of the world's future population suggest that a production increase of 124% from 2018 levels would be required to sustain us [9]. Throughout the 20th century, scientists constantly sought to generate electricity from steam in the most efficient way possible. The development of nuclear power through the fission of uranium marked the next most significant stepping stone since the first use of fossil fuels for generating electricity. Mass-for-mass, one kilogram of uranium provides around 162,500 times more energy than one kilogram of coal [10], whilst producing orders of magnitude fewer pollutants than fossil fuels [11]. However, nuclear disasters such as Three Mile Island, USA, in 1979, Chernobyl, USSR, in 1986, and Fukushima, Japan, in 2011 have left long-lasting impacts on the public perception of nuclear fission as a source of energy [12]. The challenge of managing radioactive waste from commercial reactors remains a top priority of multidisciplinary research [13].

Over the next twenty years, the energy mix of the United Kingdom is expected to become much more diverse as the use of fossil fuels for energy production declines, as shown in Figure 1.1 [14]. In Europe and North America, the development of new fission power plants has largely stalled since the 1980s, whilst renewable energy sources such as wind and solar have steadily increased over the last twenty years. However, these energy sources are closely dependent on weather and climate, which are becoming increasingly volatile. A reliable and consistent baseline is required to support our national energy grids, provided by the cleanest and most efficient source possible. To address this, the development of nuclear fusion has been the objective of more than seventy years of research aimed at harnessing the mechanism by which the Sun and stars operate. The commercialisation of nuclear fusion represents just

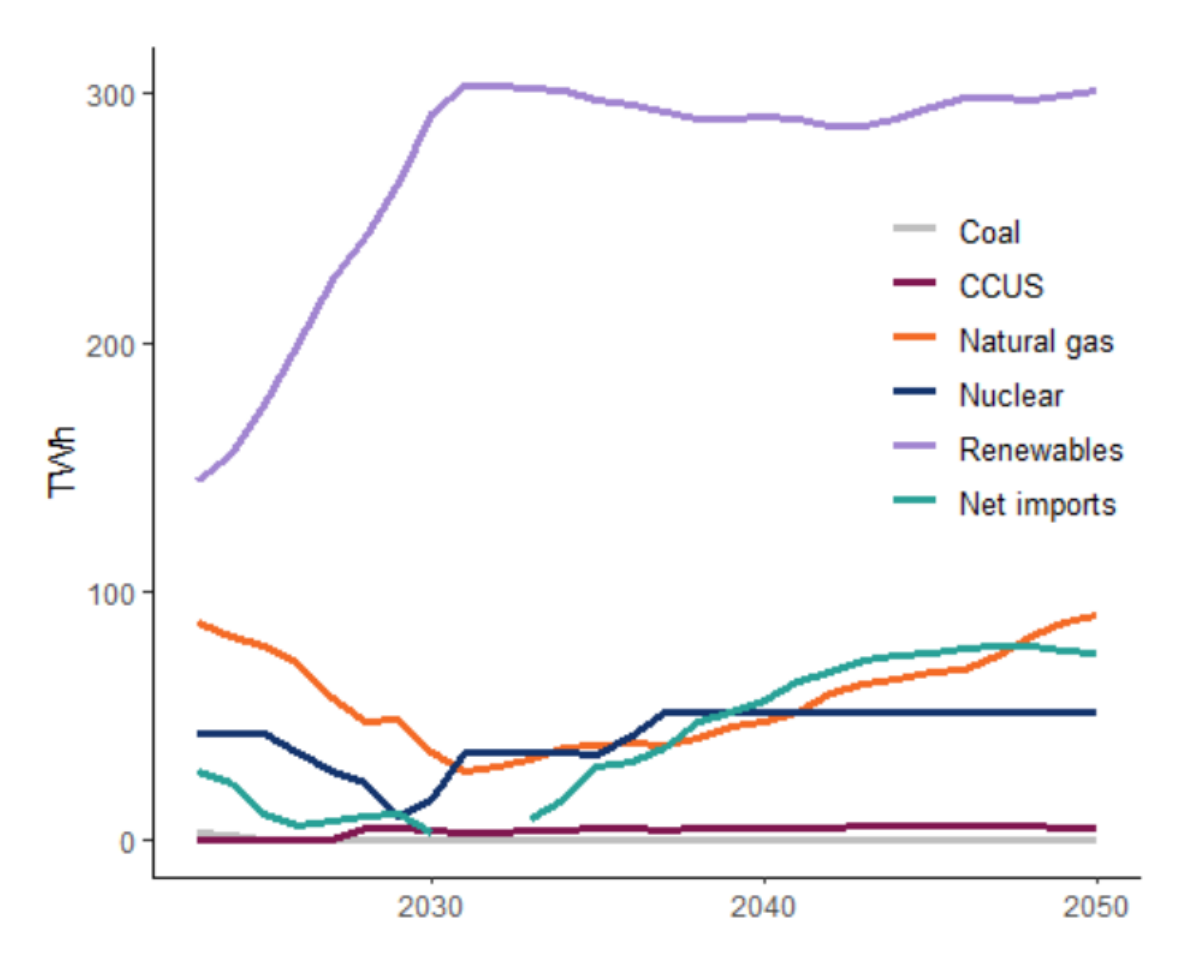


Figure 1.1: Project changes in electricity generation (in TWh) in the United Kingdom until 2050 [14]. 'CCUS' refers to carbon capture and storage technologies.

one part of the ongoing technological revolution, playing its role among advances in medicine, computing and engineering. There is growing confidence in the public and private sectors over nuclear fusion's scientific and economic viability, hallmarked by a surge in private investments since 2017. For instance, most private fusion companies predict that economically viable fusion power will be attained between 2030 and 2040 [15].

As the fusion industry grows, the need to overcome the significant challenges in fusion science, which have plagued researchers for decades, becomes necessary. Figure 1.2 shows some of the findings from the 2023 report of the Fusion Industry Association [15], a US-based non-profit organisation composed of private fusion

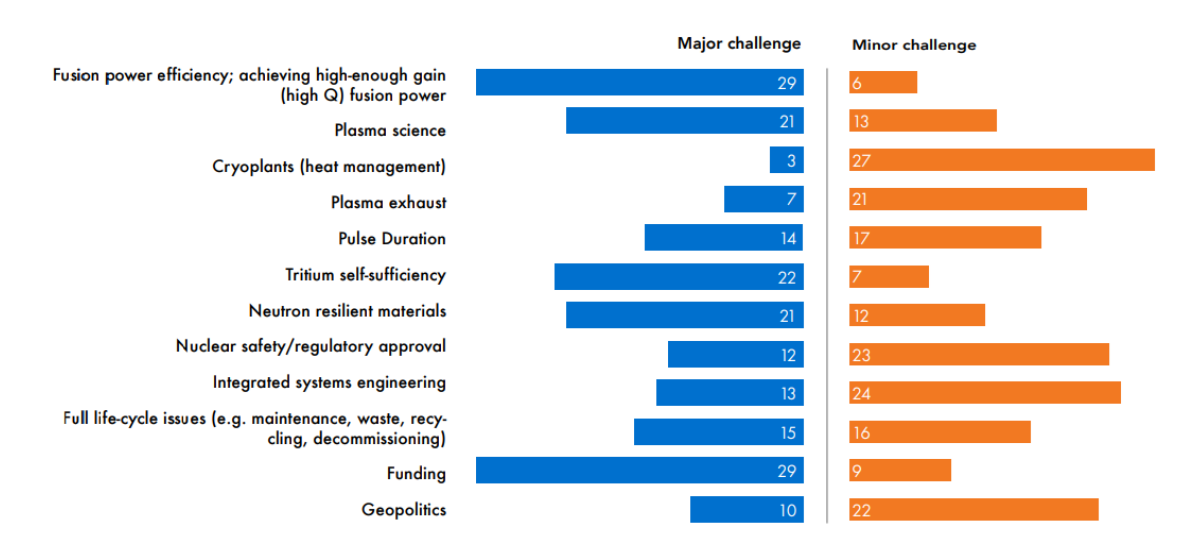


Figure 1.2: The main challenges in fusion engineering up to 2030 according to the Fusion Industry Association's 2023 report, based on responses from 38 fusion engineering institutions and companies [15].

companies, revealing several areas that pose major challenges to the development of commercial fusion. Among these areas is the development of neutron-resistant materials - ones that are capable of resisting the intense neutron flux present in the heart of a nuclear fusion reactor. As will be discussed in Chapter 2, these materials are crucial for the longevity of any fusion reactor. Part of the reason why neutron-resistant materials are such an urgent topic in the field of nuclear fusion is that the materials under consideration are low on the materials technology readiness scale [16] - *i.e.*, we do not know enough about the behaviour of these materials in a real nuclear fusion reactor environment to justify their use confidently. Of course, this is a double-edged sword: how can we hope to learn more about these materials without building a fusion reactor in which to test them?

While this is the objective of many fusion programmes worldwide, the tremendous financial, material and political expense of building a fusion reactor is a limiting factor. When it comes to anything in nuclear science, the days of "put it together and see what happens" are long gone; the monumental reprocessing efforts that take place at sites such as Sellafield in the United Kingdom, where decades of legacy

waste pose their own research dilemmata, show us the importance of foreplanning where radioactive materials are concerned. The construction of new fusion reactors is slower today than it once was, with much more consideration put into the design and lifecycle of the reactor than in previous decades. This is just one of the many reasons why experimental data may seem sparse beyond laboratory-scale experiments, which might often demand expensive, built-for-purpose research installations. However, this does not consider the rapid advances in computer science witnessed in recent decades, or even in recent years. Simulation is more frequently filling in the gaps left by the absence of experiments on shorter timescales and smaller budgets and at an ever-increasing speed. Moreover, simulation often reaches where experiments cannot.

As such, this thesis aims to exploit those advances in computer science to probe deeper into the behaviour of neutron-resistant first wall candidate materials, namely tungsten and tungsten-based 'SMART' (Self-passivating Metal Alloys with Reduced Thermo-oxidation). In the following chapter, our current understanding of tungsten and tungsten-based SMART alloys will be reviewed, highlighting the knowns and unknowns that surround them, as well as the rationale behind their use as a plasma-facing component. Then, the oxidation behaviour of these materials will be examined using computational techniques such as density functional theory (DFT) and molecular dynamics (MD), aiming to shed light upon the mechanism of oxidation at the atomic level. In doing so, this thesis aims to provide a reliable foundation for future theoretical work in the area of tungsten and tungsten-based SMART alloys.

Chapter 2

Background

2.1 Development of Fusion Technology

2.1.1 Principles of Nuclear Fusion

During nuclear fusion, elements with a low atomic mass ('low-Z') are combined to form heavier elements with a slightly lower total mass than the sum of the fused atoms. This difference in mass, known as the mass defect, is released during the process as energy. For example, in the fusion of deuterium (D, ²H) and tritium (T, ³H),

$$^{2}H + ^{3}H \longrightarrow {}^{4}He + n \tag{2.1}$$

the mass defect is equivalent (via Einstein's mass-energy relationship, $E = mc^2$), to 17.6 MeV. This fusion energy is the combined kinetic energy of the fusion products, from which a reaction's neutronicity can be calculated. The neutronicity,

 η , measures how much fusion energy is contained within the neutrons produced by the reaction (if any). It is defined as,

$$\eta = \frac{E_n}{E_{fus}},$$
(2.2)

where E_{fus} is the total fusion energy proportional to the mass defect and E_n is the kinetic energy of all neutrons produced by the reaction. To achieve nuclear fusion, the Coulombic (electrostatic) repulsion of protons and heavier nuclei must be overcome such that the reactants may be brought close enough for the strong nuclear force to bind them. This may be achieved when the nuclei are heated to very high 'thermonuclear' temperatures, on the order of $\sim 10 \text{ keV}$ ($\sim 100 \text{ million }^{\circ}\text{C}$) for the D-T fusion reaction shown in Equation 2.1.

The energy released by a nuclear fusion reaction is order of magnitudes greater than that released by a chemical reaction; the binding energy of nuclear particles, released when a nuclear reaction takes place, is much greater than the energy contained in molecular bonds. For example, the ionisation energy of hydrogen is approximately 13.6 eV - a factor of 10^6 smaller than the energy released by D-T fusion. Likewise, the energy density of fusion reactions is only surpassed by the direct conversion of mass to energy (*i.e.*, matter-antimatter annihilation). This fact is often overlooked, as individual nuclear fission reactions, which occur among elements of much higher atomic mass, release more energy in total. For example, in the binary mode of 235 U fission (*i.e.*, where two larger fission fragments are generated),

$$^{235}U + n \longrightarrow ^{144}Ba + ^{90}Kr + 2n,$$
 (2.3)

the binding energy released is approximately 200 MeV. However, the energy released per atomic mass is much greater in fusion reactions than it is in fission reactions:

3.52 MeV per Z in D-T fusion versus ~ 0.85 MeV per Z in 235 U fission.

Although the energy density of nuclear fusion reactants is much greater than that of current energy sources, the technological demands for creating, confining, and utilising thermonuclear plasma are incredibly high. However, since the 1950s, there have been many improvements in reactor designs, which have helped to improve two key parameters ubiquitous across all reactor designs and which may be used to compare them:

The first of these is the energy gain factor (Q). This is defined as,

$$Q \equiv \frac{P_{fus}}{P_{heat}} \tag{2.4}$$

where P_{fus} is the fusion power produced and P_{heat} is the power required to maintain the plasma in a steady state. After raising the reactants to thermonuclear temperatures of ~100 million °C, the resulting plasma begins to lose energy via Bremsstrahlung radiation at a rate of P_{Br} . There are other sources of power loss, depending on the reactor design and the reactants used, such as losses through synchrotron radiation (if a magnetic field confines the plasma) and interactions with impurities in the plasma. Reaching the break-even point, where Q = 1, marks an essential milestone in the design and operation of any fusion reactor. Even at the break-even point, a reactor will still cool down without auxiliary heating; however, at higher values of Q, the self-heating of the reactor removes the need for external heat sources. This is known as ignition. In 2022, the National Ignition Facility in the USA reported that they had obtained a 'burning plasma', marking the first time where a Q factor of >1 had been obtained [17].

The other parameter of great interest is known as the fusion triple product, nTt_e , where n is the plasma density, T is the plasma temperature, and t_e is the confinement

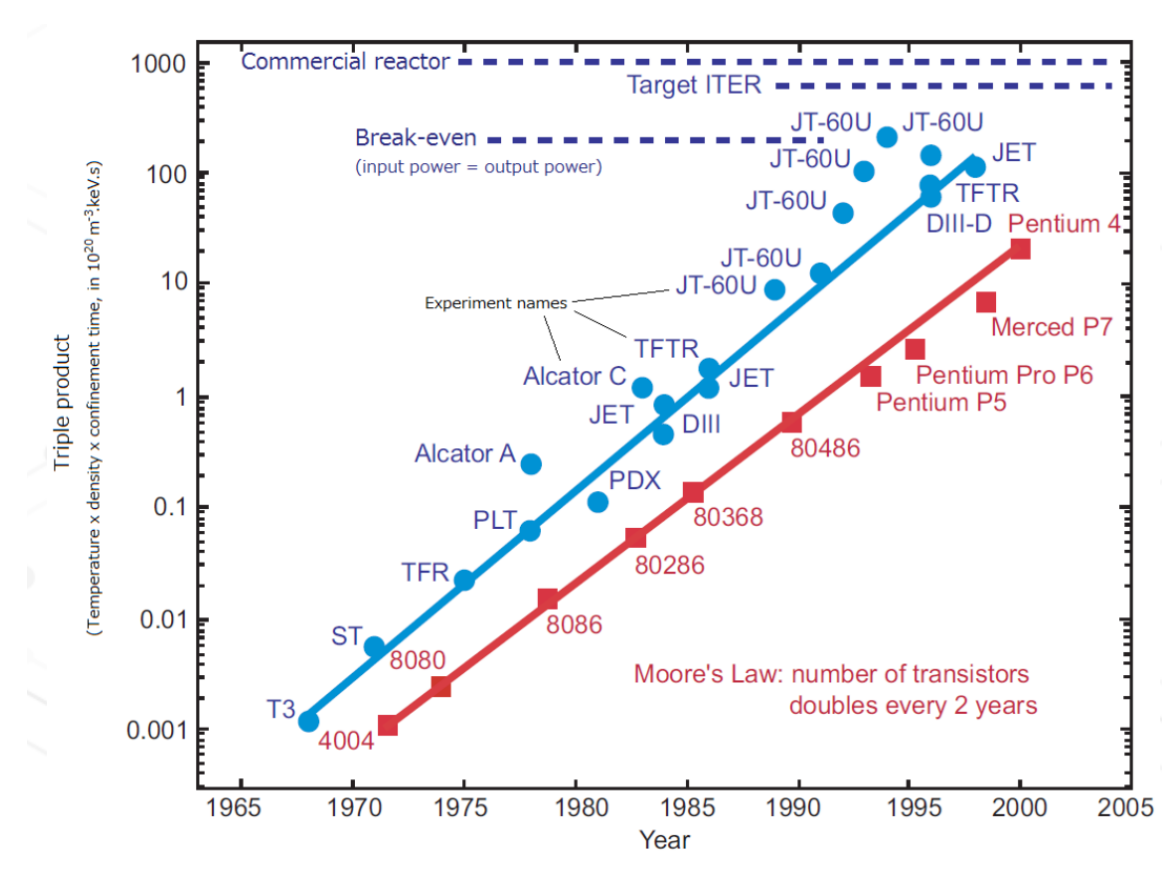


Figure 2.1: The increase of the maximum obtained fusion triple product by year, compared with the progress in transistor performance, until 2000 [18].

time. In most fusion reactors, the plasma density is inversely proportional to temperature by the relation,

$$n \propto \frac{p^2 \langle \sigma_v \rangle}{T^2},$$
 (2.5)

where p is the pressure in the plasma, and $\langle \sigma_v \rangle$ is the average product of the fusion cross section and the relative velocity. Thus, the plasma density (and therefore the triple product) is greatest when T^2 is at a maximum. Fusion reactors can, therefore, be designed to maximise the triple product whilst maintaining $Q \geq 1$, allowing for more compact and efficient reactors. As shown in Figure 2.1, the maximum triple product achieved by fusion reactors has doubled roughly every 1.8 years [18],

coming ever closer to the triple product required for a commercially viable reactor. This trend is comparable with the progress in other fields, such as the number of transistors in integrated computer circuits, a trend which is often referred to as Moore's Law.

2.1.2 Magnetic Confinement Fusion

As inferred by the expression nTt_e , one way to increase the fusion triple product is by confining the plasma for extended periods. In magnetic confinement fusion (MCF), powerful magnetic fields are used to confine the plasma in a fixed volume for a relatively long period (on the order of 10^{-1} seconds), during which thermonuclear fusion may be achieved [19]. Several MCF reactor designs have been experimented upon since the 1950s. One of the earliest such concepts is the use of a Z-pinch, in which the plasma, circulating in an external magnetic field, experiences a contraction due to the Lorentz force pulling the charged particles towards one another [20]. Although the physics behind the concept existed since the early 20th century, the first Z-pinch experiments for the potential application of nuclear fusion did not take place until the 1950s, with British, American and Soviet teams working in parallel [21, 22, 23, 24]. However, instabilities in the plasma, leading to insufficiently low confinement times, resulted in the focus of fusion research shifting to other concepts by the 1960s [25, 26, 27].

The next major step in MCF came with the development of the stellarator, proposed in May 1951, in which a magnetic field is applied by external currents flowing in solenoidal coils that encircle the plasma [28]. The tube containing this plasma, which the superconducting coils are wrapped around, is bent to produce a torus. However, a simple torus does not confine a particle circulating in the plasma indefinitely, as inhomogeneities in the magnetic field result in particles drifting towards the tube walls [29, 30, 31]. A rotational transform (or poloidal twist) is



Figure 2.2: Lyman Spritzer and the Model A Stellarator, the precursor to the Model C, circa 1952.

introduced to the torus to overcome this. In the Heliac Stellarator, this twist comes from the torsion of the magnetic axis, which in turn requires careful and precise control over the geometry of the solenoidal coils to maintain the plasma in a steady state [32, 33].

Initial work on practical stellarators began not long after Lyman Spritzer (pictured in Figure 2.2) proposed the concept, and funding for the first figure-of-eight stellarators started on July 1st 1951, marking the beginning of Project Matterhorn [34]. However, as predicted by Spritzer, there was a substantial loss of particles from the plasma, which he attributed to Bohm diffusion arising from density gradients and electrical field gradients across the magnetic field [35]. The culmination of early stellarator research was the Model C stellarator, whose construction was completed in 1961. Although previous experiments had indicated that Model C would not be capable of large-scale fusion, the device's heating and magnetic systems were improved upon over the following years and eventually reached ion temperatures of

400 eV, and the device was used primarily for studies on ion transport [36]. However, in 1968, Soviet scientists published the results of experiments performed on their T-3 tokamak reactor, demonstrating ion temperatures of 1000 eV and confinement times at least ten times greater than any other design at the time [37]. Despite initial scepticism over the results, British experts were invited to conduct experiments on the T-3 device. Subsequently, they published a paper in Nature confirming the results that the Russian team had announced [38]. The verification of the Soviets' results sparked what is known as the 'Tokamak Stampede', an international rush to construct and improve upon the Soviet tokamak design [39].

The term 'tokamak' is derived from the Russian acronym for either Toroidal Chamber with Magnetic Coils or Toroidal Chamber with Axial Magnetic Field [40]. Like the stellarator, the tokamak design introduces the rotational transform necessary to counteract the drift of particles in the plasma by creating a poloidal magnetic field using a toroidal electrical current. The result is good plasma confinement relative to the stellarator design [41]. However, although Lyman Spritzer identified this method in one of his initial reports to the Matterhorn Project, he discarded the notion of using a secondary magnetic field on the basis that the current generated in the poloidal circuit will lead to oscillations in the plasma, making a steady-state plasma somewhat more challenging to maintain [42]. Due to this, tokamaks can only operate in pulses, whereas stellarators can theoretically operate in steady-state conditions, albeit at the cost of much greater engineering complexity [41].

In the late 1970s, tokamak experiments in the US and the USSR yielded tremendous improvements over the Model C stellarator and T-3 tokamak designs. In 1978, the Princeton Plasma Physics Laboratory (PPPL) constructed and tested the Princeton Large Torus (PLT) device, demonstrating ionic temperatures of 8000 eV ($\sim 6 \times 10^7$ °C) [43]. These promising results paved the way for the second generation of tokamak experiments: the American tritium-burning Tokamak Fusion

Test Reactor (TFTR); the Joint-European Torus (JET), housed at the Culham Center for Fusion Energy in Oxfordshire, UK; the Japanese JT-60, known as the 'Break-even Plasma Test Facility'; and the USSR's superconducting tokamak, the T-15. These devices began operations in 1982, 1983, 1985 and 1988, respectively [44, 45, 37].

The first of these, the American TFTR, was designed to achieve break-even (Q = 1) using deuterium and tritium plasmas and to study the interactions of particles within the plasma. In 1988, it was reported that the reactor had reached ionic temperatures of up to 30 keV. However, the energy gain factor, Q, was only about 0.2, far below what was needed to achieve break-even. Furthermore, it was predicted that α - α interactions would become significant at higher values of Q and that new instability would arise due to this repulsive interaction [46]. Although the TFTR achieved world record energy outputs in 1994, producing 10.7 MW (gross), it was deactivated in 1997 in favour of the National Spherical Tokamak Experiment (NSTX) [47].

The Joint European Torus, constructed at the Culham Center for Fusion Energy (CCFE) in the UK, was a pan-European experiment whose operations continued until 2024. Initially, the purpose of JET was to study the behaviour of plasma as it approached reactor-like conditions and the interactions of the plasma with itself and with the reactor walls [48]. At the time of construction, the JET was only the second reactor designed to operate on deuterium and tritium, and in 1991, it became the first reactor to achieve D-T fusion [49]. By 1997, the JET had set the record for the closest approach to break-even, at Q = 0.67, and had set many records for the highest fusion triple product [50]. However, the inability to break even made the need for a much larger, much more expensive design apparent, leading to the international effort behind ITER (pictured in Figure 2.3) [51].

The concept of a joint international project on nuclear fusion predated many of



Figure 2.3: Progress on the International Thermonuclear Experimental Reactor near Cadarache, France, in September 2023 (ITER Organisation).

the results obtained from these second-generation reactors. As early as 1973 there were plans for such a project in the form of the INternational TOkamak Reactor (INTOR), which stemmed from talks between Richard Nixon and Leonid Brezhnev [52]. However, it was not until after the Geneva Summit of 1985 between Ronald Reagan and Mikhail Gorbachev that a formal agreement was signed between the US, USSR, the European Atomic Energy Community and Japan, forming the political basis of the International Thermonuclear Experimental Reactor (ITER) [53]. ITER is designed to achieve 500 MW of fusion power with a fusion energy gain of $Q \approx 10$ and a confinement time of ~ 1000 s. In addition to these technical objectives, ITER is also slated to be a test bed for a wide range of reactor components and systems, including but not limited to tritium breeding modules and reactor first-wall materials [54]. In 2016, it was announced that ITER would achieve its first plasma in 2025 [55]; however, numerous setbacks have pushed completion of the device and, subsequently,

initial experiments into the late 2030s [56].

Although construction work on ITER has yet to be completed, a proposal for a joint European successor reactor has already been made, one that would bridge the gap between ITER and a first-of-a-kind tokamak fusion power plant. Intended to build on the results of experiments conducted on ITER, the DEMOnstration Power Plant (abbr. DEMO) is a design study to deliver fusion power by the middle of the 21st century, however, a detailed design concept for the reactor is not expected until the late 2020s. A future design for the DEMO reactor must be capable of at least 2000 MW of fusion power, with a Q value of \sim 25, which is much greater than the parameters expected of ITER. In addition, DEMO must also generate its own tritium for self-sufficiency and be a reproducible unit with a design closer to that of a commercial power plant than an experimental reactor [57, 58]. However, since the inception of DEMO, there have already been revisions to the project timeline that have delayed operations, and there are concerns that the project may not proceed beyond a prototype reactor due to lack of investment [59, 60, 61].

2.1.3 Spherical Tokamaks

Spherical tokamaks (ST) are a branch of the conventional tokamak design in which the size of the torus' central hole has been reduced as much as possible. They are characterised by their lower aspect ratio, the ratio of the reactor's diameter to the cross-sectional diameter of the volume in which the plasma is confined. It was noted by the team of Carreras and Hender at Oak Ridge National Laboratory, USA, that tokamak reactors are inherently more stable at lower aspect ratios, primarily due to the suppression of instabilities that had been observed in Z-pinch devices, and which are still prevalent in both stellarators and tokamaks. The other major advantage of low aspect ratio designs is an economic one: spherical tokamaks allow the toroidal magnets to be placed much closer to the plasma, reducing both the cost of the

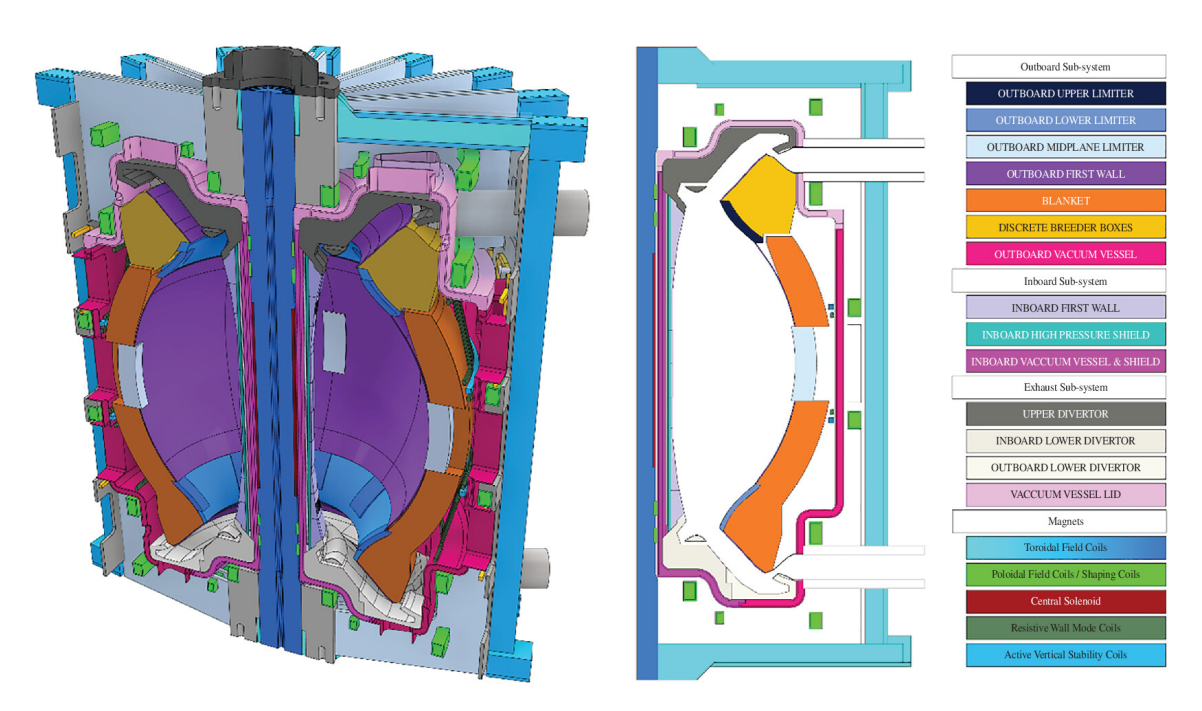


Figure 2.4: Cross-section of the conceptual design of the Spherical Tokamak for Energy Production and its components [62].

magnets and the cost to power them. However, this comes with the disadvantage that much more robust shielding must be given to the magnets to prevent radiation damage due to the extremely high flux of neutrons, occupying additional space in a configuration where there is already very little to spare [63].

The first functional ST was the Small Tight Aspect Ratio Tokamak (START), operated between 1990-1998 at the CCFE, UK. The reactor was most notable for obtaining much higher β values than existing tokamaks. In plasma physics, the value β represents the ratio between the plasma and the magnetic pressure, where higher values of β imply that a lesser magnetic force is required to confine the plasma. Therefore, greater values of β are desirable in tokamak reactors [64]. START reached β record values of between 0.32 and 0.40 during its operational life, owing to higher plasma pressures and lower magnetic pressures, among other design choices [65].

In 1998, the START reactor was taken offline and transported to the ENEA laboratory in Italy, while the UK team moved on to the Mega Ampere Spherical

Tokamak (MAST) project, commissioned by the United Kingdom Atomic Energy Authority (UKAEA). MAST operated between 1999 and 2013, whereafter it underwent refurbishment. The MAST Upgrade (MAST-U) experiment began operation again in 2020, with the results of the first experimental campaign being published in 2024 [66]. Importantly, MAST-U is the first device to trial the so-called 'Super-X' divertor [66, 67]. This component is crucial to tokamak reactors, extracting heat and impurities from the plasma during operation, thereby increasing performance and lifetime. The MAST Upgrade project aims to help answer fundamental questions relevant to the design and operation of future tokamak reactors, particularly those of the spherical variety [68, 69].

The next generation of UK-based spherical tokamak reactors is the Spherical Tokamak for Energy Production (STEP), a conceptual design for which is shown in Figure 2.4. The project aims to produce a first-of-a-kind prototype fusion power plant by 2040, utilising the results from START and MAST Upgrade [70]. In October 2022, the West Burton power stations site in Nottinghamshire, UK, was selected as the site for STEP. On 1st November 2024, the leadership of the STEP programme transitioned from the UKAEA to the newly established subsidiary United Kingdom Industrial Fusion Solutions (UKIFS) Ltd.

2.2 Fusion Reactor First Walls

2.2.1 Layout of a Tokamak Reactor

Both conventional (such as the one pictured in Figure 2.5) and spherical tokamak reactors (pictured in Figure 2.4) are designed around the same principles and requirements. To achieve the conditions required for nuclear fusion, the plasma must be confined such that it does not interact with other matter - *i.e.*, in a vacuum

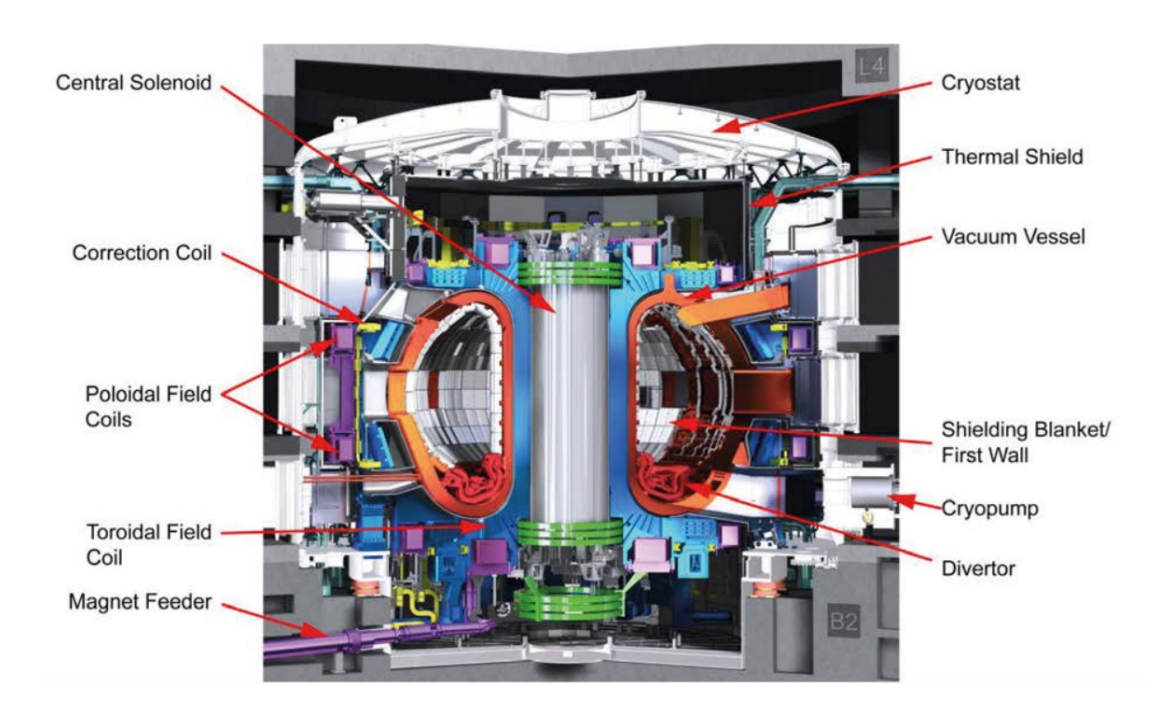


Figure 2.5: Cross-section of the ITER cryostat. Credits to the ITER Organisation.

chamber and not in contact with the walls of the vessel. This confinement is made possible by the use of superconducting magnets. In older tokamak reactor designs such as JET, these magnets were made of copper. However, more contemporary designs utilise low-temperature superconductors such as NbTi or Nb₃Sn [71, 72]. These materials exhibit superconductivity below 9.3 K and 18 K, respectively, and upper critical field strengths of 11.5 and 29.2 T, respectively [73, 74, 75]. The low temperatures required to maintain superconductivity in these materials pose yet another engineering challenge. However, future reactor designs may utilise a class of materials known as rare earth barium copper oxides (REBCO), which are a type of high-temperature superconductor. For example, yttrium-barium-copper oxide (YBCO) exhibits a critical temperature of 93 K and a critical field strength of over 100 T [76].

Another factor that must be considered in designing a tokamak reactor, and a general consideration for the life cycle of such a device, is the source of tritium used in D-T reactions. Tritium has a half-life of only 12.32 years, and, as a result, the availability of tritium is extremely scarce [77]. Although it is naturally present in seawater, its concentration is only 10^{-18} parts tritium to hydrogen. Most tritium on Earth arises due to the operation of heavy water fission reactors such as CANDU in countries such as Canada, South Korea, Argentina, China, India and Romania [78], at a rate of 210-260 g/GWe/fpy (grams per GW of electricity per year of full power operation on one reactor) [79, 80]. Current estimates suggest that the tritium produced in these reactors, in conjunction with current stockpiles, is sufficient to power ITER. Still, there is uncertainty over the amount of commercially available tritium remaining for other reactor programs. Therefore, it is generally accepted that tritium will need to be generated in situ by the transmutation of ⁶Li according to the reaction,

$$^{6}\text{Li} + n \longrightarrow {}^{3}\text{H} + {}^{4}\text{He}.$$
 (2.6)

The neutrons required for this transmutation to occur can be created *via* D-T fusion. Therefore, a self-sustaining fusion reaction can be achieved if the number of tritium atoms generated by the neutron flux is greater than the number of atoms expended to sustain the D-T reaction. This ratio is quantified as the tritium breeding ratio (TBR), which must be greater than 1 to maintain a fusion reaction.

In contemporary reactor designs, the tritium breeding blanket containing a Li-rich material lies immediately behind the first wall, the region responsible for shielding the rest of the reactor, particularly the poloidal and toroidal field coils, from the high neutron flux of the D-T plasma. The first wall is also a part of the system responsible for generating electrical power, as active cooling is typically passed through the armour. Without the first wall's shielding, neutron bombardment causes catastrophic microstructural damage to the superconducting magnets, rendering the reactor unable to confine the plasma. Furthermore, the first wall's armour slows the

incident neutrons into the thermal regime, enabling the $^6\text{Li}(n,\alpha)$ T reaction in the tritium breeding blanket (Equation 2.6) [81].

Another important plasma-facing component of note is the divertor, which is responsible for maintaining a clean plasma in the reactor vessel. During operation, impurities accumulate in the plasma in the form of helium ash (as a direct byproduct of the D-T reaction) and metal ions from the first wall, which are sputtered by neutron impacts. These heavy atoms, which are not completely ionised, unlike deuterium or tritium in the plasma, radiate in the ultraviolet and X-ray regions of the electromagnetic spectrum due to the excitation of their remaining electrons. This leads to plasma cooling and a reduction in its fusion yield, and, as such, it must be purged from the reactor vessel. The divertor acts as a target for the particle flux, directed towards them by the elongation of the magnetic field induced by the poloidal field magnets. The divertor is subject to some of the most extreme environments in the tokamak reactor, especially in the case of a 'disruption' - a highly energetic event whereby the plasma collapses near-instantaneously, depositing its energy into the divertor. The heat load can be several orders of magnitude greater during such events than during regular operation. Due to this, the divertor must be made of a material which can withstand high heat loads without melting. The primary candidate material for this is tungsten, whose melting point is 3695 K, however, other materials have been previously considered for this purpose.

2.2.2 Neutron Environment at the First Wall

Understanding the effects of the extreme environments experienced by fusion reactor first walls is one of the critical outstanding issues surrounding next-step devices such as ITER, DEMO and STEP. Special attention is paid to understanding the effects of neutrons, which cause significant damage to materials through atomic displacements and non-elastic nuclear reactions (*i.e.* transmutation). A subset of the latter are

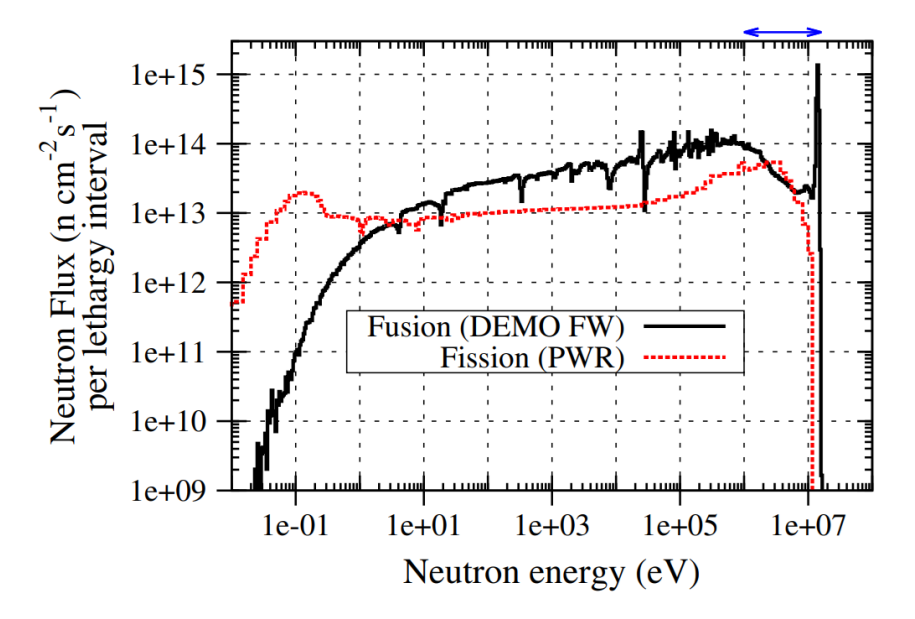


Figure 2.6: Neutron energy spectra at the outboard equatorial first wall of DEMO (predicted) versus a fuel assembly in a pressurised water [fission] reactor. The region of thermal neutrons (1 - 10 MeV) is shown with a blue arrow [82].

nuclear reactions, which produce gas particles, e.g. He, which can accumulate inside plasma-facing materials over time and lead to further mechanical breakdown of the first wall. Transmutation is especially problematic in the context of nuclear fusion (compared to similar environments experienced by materials in nuclear fission) due to the greater flux of fast neutrons [82]. As shown in Figure 2.6, predictions made using the Monte Carlo neutron transport code MCNP [83] show that the fast neutron flux in a fuel assembly of the average pressurised water reactor decreases to zero in the 1 to 10 MeV range, whilst the predicted peak neutron energy on the outboard equatorial first wall in a DEMO-like tokamak reactor is around 14 MeV.

When discussing the effects of neutron irradiation on a material, quantifying the displacements per atom (dpa) is a useful and widely used metric. As the name suggests, this is the number of atoms displaced from their original positions due to collisions with either a fast neutron or another atom which has been displaced previously. Figure 2.7 demonstrates the damage that might be caused by neutron

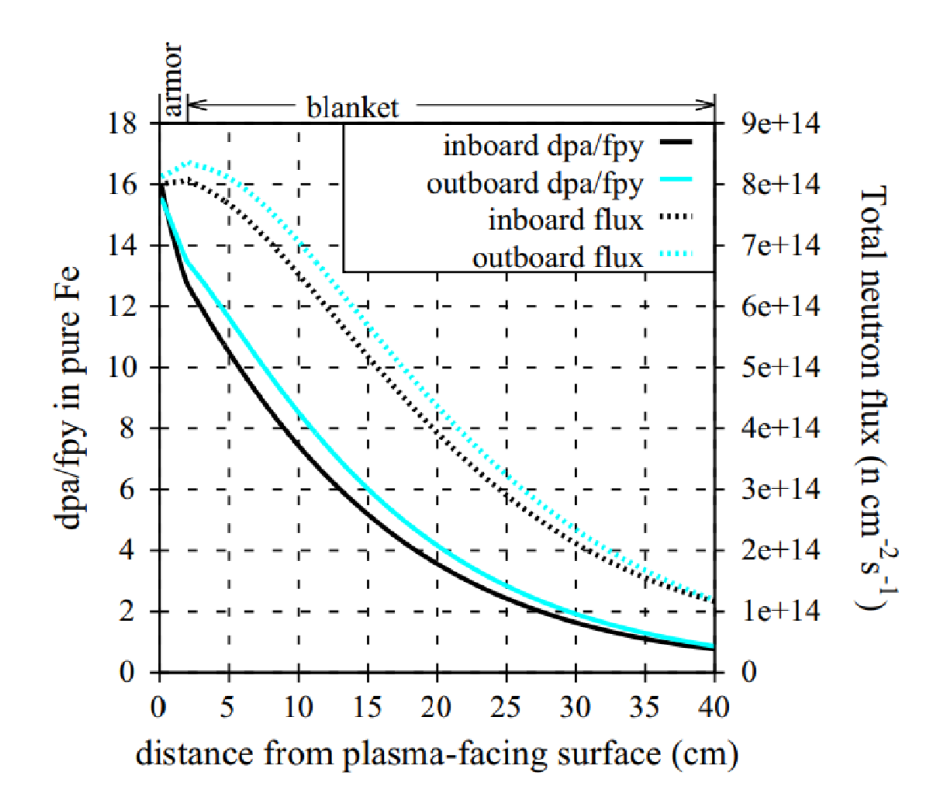


Figure 2.7: Neutron flux and displacements per atom over a full power year for a theoretical DEMO-like first wall made of iron [82].

irradiation, in this case against iron, a common structural material that is likely to present in the form of stainless steel in the wall of a tokamak reactor. At the surface of the first wall, the high neutron flux - on the order of 8×10^{14} n cm⁻²s⁻¹ - causes up to 16 atomic displacements on each Fe atom over a year of full power operation, on average. Such high amounts of radiation-induced displacements leads to the accumulation of defects in the crystal structure of the first wall material, and the subsequent weakening of the first wall. Defects in crystal structures are discussed in Section 2.3.5.

As mentioned previously, protecting sensitive reactor components is crucial to the reactor's lifespan. Selecting the appropriate first wall material is critical to the safety and viability of both the reactor and the overall reactor program. Throughout the practical history of nuclear fusion, several materials have been tried, tested, and theorised as potential first wall materials.

2.2.3 First Wall Materials

In the 1980s and 1990s, several tokamak reactors utilised graphite tiles for the first wall, including JET, NSTX and JT-60U [84]. At face value, carbon is an ideal material for use in a fusion reactor: it is a low-weight material with a low neutron capture cross-section, good thermal conductivity and low vapour pressure, making it resilient to neutron irradiation at elevated temperatures at the first wall [85]. However, graphite is readily eroded by hydrogen isotope bombardment during reactor operation due to sputtering [86] and is highly permeable to tritium. Moreover, tritium that becomes trapped within graphite is notoriously difficult to remove; a study on tritium retention in graphite, carbon films and tungsten (which will be discussed later) showed that there was no reduction in the amount of entrapped tritium in graphite after six months of storage. In contrast, the tritium content of carbon films and tungsten was reduced by significant amounts over much shorter periods [87]. As mentioned previously, the retention of tritium is a significant factor in the choice of material for the first wall, as the embrittlement it causes can lead to catastrophic mechanical failure. An investigation of the graphite tiles in the JT-60U reactor in the early 1990s highlighted the deficiencies in the mechanical performance of graphite tiles, wherein plasma disruptions had destroyed several tiles [88]. Furthermore, the level of hydrogen isotope retention in carbon-based materials was found to be related to the level of radiation damage in the material, with deuterium solubility in graphite rising by a factor of 20 to 50 following saturation at a radiation damage level of 0.3 dpa [89].

Subsequently, in the early- to mid-1990s, fusion reactor programmes underwent a switch to alternative first wall materials, forgoing graphite and carbon films. In addition to the significant problems mentioned above, pollution of the D-T plasma

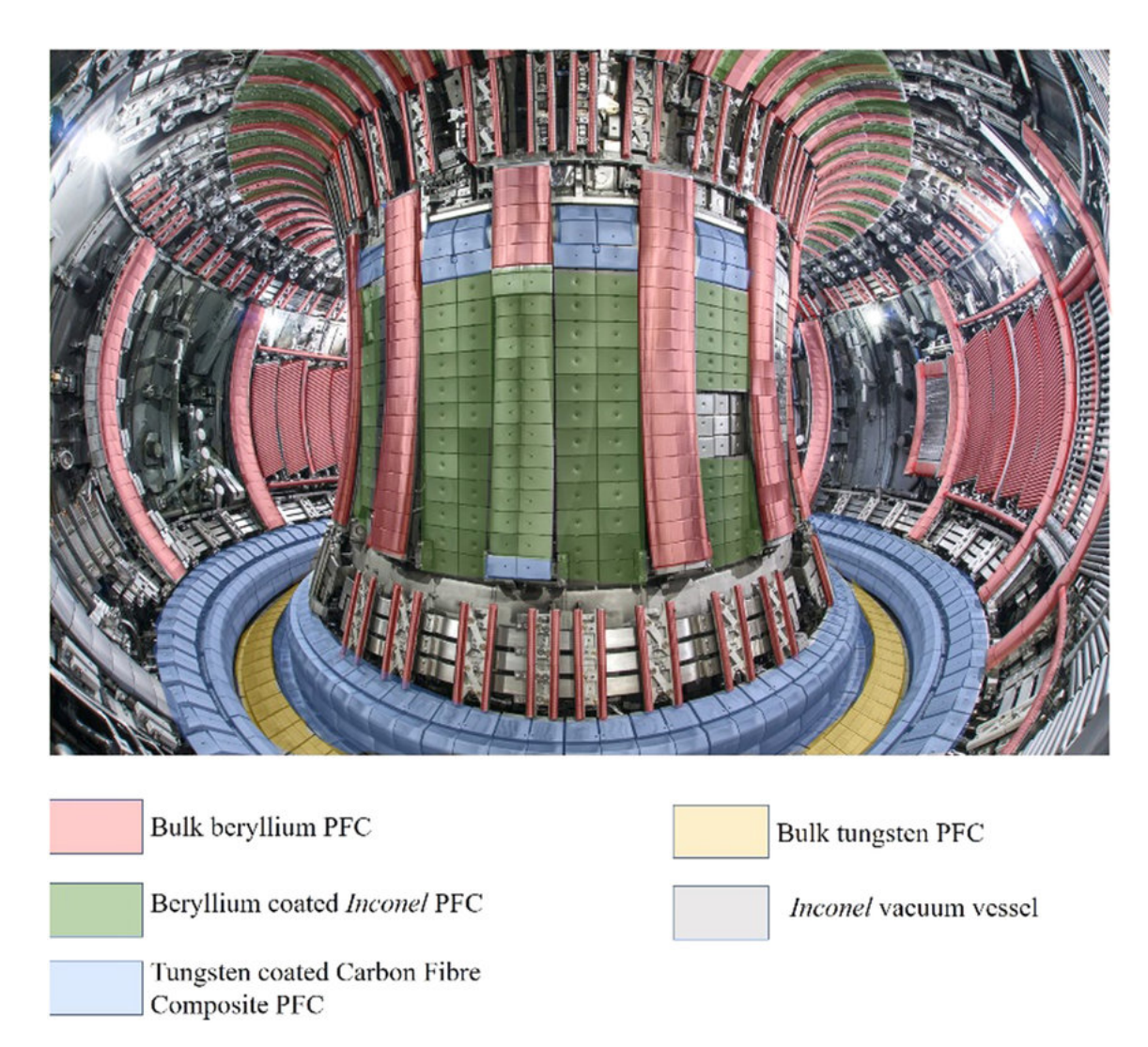


Figure 2.8: The various plasma facing materials used in JET, colourised for ease of identification [90].

due to sputtered C atoms became a limiting factor for operating devices with carbon-based first walls. One of the most notable choices from this period was the selection of beryllium as a first wall material, which significantly improved the plasma performance of devices such as JET [91]. Unlike graphite, beryllium has a low affinity for tritium retention and further helps to maintain a clean plasma by retaining gaseous oxygen, which would otherwise cause disruptions [92]. However, beryllium is a highly toxic material, and long-term exposure to beryllium dust can cause Chronic Beryllium Disease (CBD) if inhaled [93]. Although site safety controls have successfully mitigated the effects of beryllium on their respective

workforces, beryllium poses a significant liability issue. However, despite beryllium's good performance as a first wall material, its major limitation lies in its melting point, which is only 1560 K [94]. Although this is sufficient for normal reactor conditions, transient heat loads during off-normal conditions cause localised heating and melting, especially on beryllium divertor tiles [95].

Another material which saw its first use in the 1990s was pure lithium. As mentioned previously, one of the major factors in the context of plasma stability is not the presence of charged particles in the plasma - which can be directed to the divertor via their interaction with the magnetic field - but instead the presence of neutral particles which are not confined by the field. One mechanism by which neutral particles accumulate within the plasma is recycling: as particles escape the plasma and reach the first wall, they become a cold, uncharged gas. Due to the temperature gradient between the hot plasma and the neutral gas, the uncharged particles are mixed (or 'recycled') into the plasma. Therefore, plasma stability can be increased by preventing the recycling of particles back into the plasma [96]. Lithium achieves this due to its high reactivity with most chemical elements, which allows it to form stable Li-based compounds at the surface of the first wall. For example, a report from the TFTR (USA) in 1996 showed that a 20 mg coating of lithium on the first wall of the reactor enabled a two-fold improvement in plasma confinement due to the formation of Li-based compounds [97]. Of course, an additional benefit to using lithium at the first wall lies in its tritium breeding properties, discussed in Section 2.2.1. In a similar vein, more recent experiments have investigated the feasibility of liquid lithium coatings to circumvent the issue of radiation damage in solid plasmafacing surfaces. In the early 2000s, experiments of liquid lithium as a first wall material began with the CDX-U device at PPPL, demonstrating a reduction in the recycling rate and an eight-fold improvement in the plasma's confinement time [98]. However, despite the potential benefits of using lithium (either solid or liquid) as a first wall material, lithium is nevertheless highly chemically reactive, which

complicates its use in a practical fusion reactor.

As of 2024, the most ubiquitous first wall material for current and future tokamak reactor designs - and the subject of this thesis - is tungsten. Tungsten has a melting point of 3695 K, the highest melting point of all known chemical elements, making it resilient to off-normal heat loads at the plasma-facing surface. It has good thermal conductivity and a high density, the latter of which makes it suitable as a neutron shield [99]. It has a high cohesive energy (the energy required to separate a solid into individual atoms), making it much more resilient to erosion compared to other first wall materials. For instance, under ITER-like conditions, beryllium is expected to erode at a rate of around 3 mm /fpy, whereas tungsten erodes at a rate of around 0.1 mm /fpy [100]. Compared to other first wall materials, tungsten has a much lower tritium retention; as was mentioned previously, graphite exhibits almost no loss in retained tritium after six months of storage. On the other hand, the tritium retained by tungsten falls by half in just 18 days. In 2009/2010, JET installed an ITER-like beryllium first wall with a tungsten divertor. Whereas this was initially intended to be an experiment to guide the choice of the first wall material for ITER, a review of the toxicity of beryllium and its suitability for use in fusion led to the ITER Organisation changing the first wall design to a full-tungsten first wall in 2023.

2.2.4 Tungsten Under Neutron Irradiation

Tungsten occurs in the form of five natural isotopes: 180 W (0.12 - 0.13 %), 182 W (26.30 - 26.50 %), 183 W (14.30 - 14.31 %), 184 W (30.64 - 30.70 %), and 186 W (28.43 - 28.60 %) [100, 102]. In a fusion reactor, tungsten is transmuted into rhenium, osmium and tantalum via the following nuclear reactions:

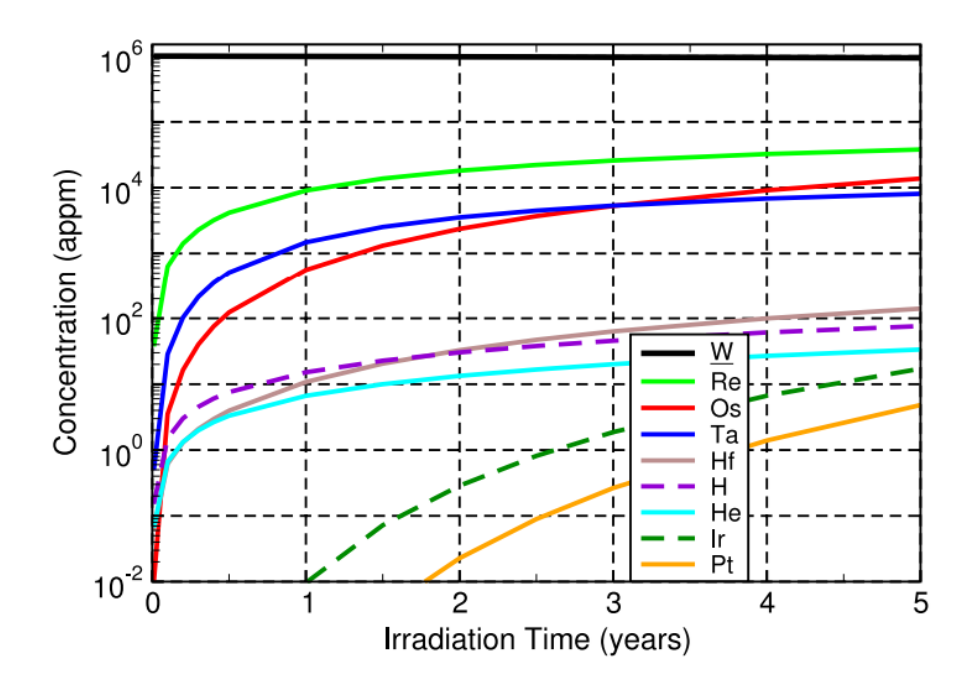


Figure 2.9: Transmutation products of W at the first wall under ITER-like operating conditions [101].

$${}^{186}W(n,\gamma){}^{187}W \to (\beta-){}^{187}Re \left\{ (n,\gamma){}^{188m}Re \to (\gamma){}^{188}Re \to (\beta){}^{188}Os \right\}$$

$$(2.7)$$

$$^{184}W(n,\gamma)^{185}W \to (\beta-)^{185}Re(n,\gamma)^{186}Re \to (\beta-)^{186}Os$$
 (2.8)

Figure 2.9 shows the expected concentration of the transmutation products of tungsten after five years under ITER-like operating conditions (*i.e.*, the expected lifetime of tungsten armour in a power plant). In this case, 'ITER-like operating conditions' refers to approximately $3,300 \times 400$ s pulses per year, with a neutron flux of 2.38×10^{14} n cm⁻²s⁻¹ during these pulses [101]. The result is a significant transmutation of tungsten into the aforementioned elements in concentrations of 3.8 at% Re, 1.4 at% Os, and 0.81 at% Ta. The *in situ* transmutation of tungsten effectively turns pure tungsten into an alloy of tungsten and its transmutation

elements. As expected, this influences its material properties in different ways, and how the properties of tungsten changes during irradiation must be clearly understood.

As a regular alloying element, rhenium is the only element known to improve the ductility and mechanical hardness of tungsten at room temperature [103, 104]. However, its suitability as an alloying element in a first wall environment is more dubious. In one study, tungsten was alloyed with rhenium in a ratio of 74:26% by weight (which henceforth will be notated W-26Re). Under irradiation at a flux of 1×10^{27} n m⁻² with 0.1 MeV neutrons, Nemoto et al. revealed the presence of multiple intermetallic (W/Re) precipitates in the tungsten lattice [105]. These precipitates cause the embrittlement of tungsten, which can lead ultimately lead to mechanical failure, but are only present at relatively high (i.e., around 26 wt%) concentrations of Re. On the other hand, rhenium has been shown to have a beneficial effect on the radiation-induced swelling of tungsten [106]. Work by Williams et al. showed that the lattice parameter of W-5Re increased by around 0.4 pm under irradiation at a neutron flux of 5.4×10^{25} n m⁻² and a temperature of around 900 K. On the other hand, W-25Re expanded by only 0.1 pm under identical conditions [107]. Nevertheless, the isotopes of rhenium present in the first wall of a fusion reactor differ from those which occur naturally, and, as shown in Equations 2.7 and 2.8, decay to the stable and metastable isotopes of osmium. As a result, rhenium is expected to be depleted over the first wall's lifetime, offset by the further production of rhenium from neutron interactions with tungsten. This equilibrium makes it possible to maintain these positive mechanical benefits by maintaining a low concentration of rhenium in the first wall [108]. On the other hand, recent studies indicate the formation of both rhenium and osmium can be suppressed viathe depletion of ^{186}W [109].

Several minor transmutation products may also accumulate in tungsten, including heavy metals such as iridium, hafnium and platinum [101]. Of the non-metallic

products, hydrogen and helium are noteworthy. Hydrogen is primarily produced by reactions involving the capture of a neutron followed by the emission of a proton, (n,p), whereas helium is produced by reactions that produce an α particle (n,α) . For instance,

$$n + {}^{186}\text{W} \rightarrow {}^{186}\text{Ta} + p$$
 (2.9)

$$n + {}^{186}\text{W} \rightarrow {}^{183}\text{Hf} + \alpha$$
 (2.10)

are both possible sources of protons and α (⁴He) respectively [110, 111]. Theoretical results from Gilbert *et al.* indicate that these gases accumulate in concentrations of 80 atomic parts per million (appm) and 30 appm respectively, after five years of ITER-like operation conditions [101]. These gases typically accumulate and concentrate in metals, forming bubbles or so-called 'blisters', which in turn cause mechanical degradation of the metal on a macroscopic scale [112, 113]. On an atomic level, these blisters range from 1 to 100 μ m in diameter, and, in the case of hydrogen, can exhibit internal pressures in the GPa range, placing enormous strain upon the surrounding tungsten structure [114].

Therefore, the formation of transmutation products poses a significant and complex problem when considering the long-term performance of tungsten as a first wall material. The role of transmutation products is not considered in this work. However, it is important to keep in mind the problem they pose; future work will invariably require a more detailed description of the materials of interest under reactor-like conditions, whereas this work focuses on the oxidation of non-irradiated tungsten and tungsten alloys.

2.3 Diffusion in Solids

In order to facilitate a discussion of the oxidation of tungsten and tungsten alloys during a loss of coolant accident, this section will provide an introduction to point defects, diffusion and corrosion in crystalline solids.

2.3.1 Definition of Crystal Structures

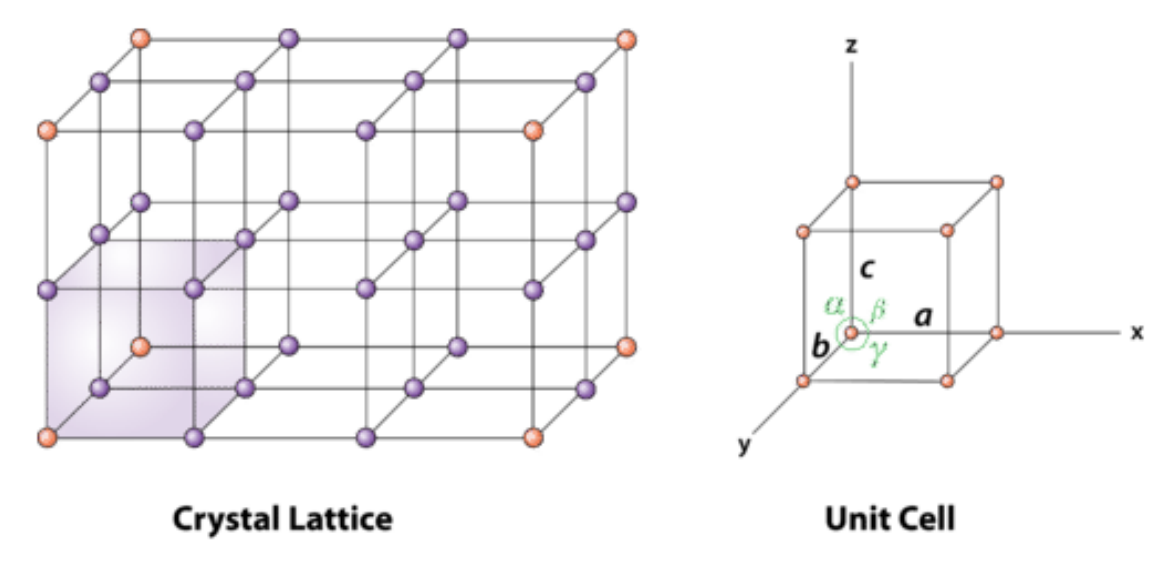


Figure 2.10: A unit cell, showing its crystal axes (x, y, z), lattice parameters (a, b, c), and inclinations (α, β, γ) . Multiple unit cells form a crystal lattice. Credit to Christopher Auyeung, CK-12 Foundation, under CC BY-NC 3.0.

Solid materials are primarily divided into two categories based on the ordering of their constituent ions: crystalline solids, in which the constituent ions are ordered, and amorphous solids, in which they are disordered. A crystalline solid can be described in terms of its crystal axes, lengths along those axes, and relative inclination. This is known as the law of rational intercepts, proposed by René Haüy in 1784 [115]. This description allows the definition of a unit cell - the smallest, repeatable configuration of ions which represents the crystal structure as a whole, as shown in Figure 2.10. Seven unique crystal symmetry systems form the basis

of all crystal structures: cubic, hexagonal, tetragonal, orthorhombic, monoclinic, rhombohedral and triclinic. In 1848, Auguste Bravais recognised that there were fourteen unique ways of arranging lattice points within these seven systems, hence termed the Bravais lattices [116].

A further descriptor that can be applied to any of these fourteen Bravais lattices is the crystal's space group. This is a purely mathematical description of the lattice's symmetry, which has its roots in group theory, being the combination of the thirty-two crystallographic point groups with the fourteen Bravais lattices. A given space group contains the translational symmetry of the unit cell (arising from the Bravais lattice), the point group symmetry operations of rotation, reflection and improper rotation, and the glide plane and screw axis transformations. The latter are special compound operations - *i.e.* a combination of rotations, reflections and translations. Therefore, by considering all possible symmetry operations in the Bravais lattices, any given crystal system can be described using one of the 230 space groups [117, 118, 119].

Space groups are referred to by their Hermann-Mauguin notation [120, 121]. The general structure of this notation is to combine an upper case letter denoting the Bravais lattice with an alphanumerical identifier for the point group. The Bravais lattices are denoted with the letters: P (primitive), I (body-centered), F (face-centered), A (a-centered), B (b-centered), C (c-centered), and R (rhombohedral). The point group identifier is more complex, but in general denotes the symmetry operations along each crystal axis:

- m reflection plane in the given axis,
- n rotation of $\frac{360}{n}$ ° around the given axis,
- \bar{n} improper rotation of $\frac{360}{n}$ ° followed by reflection in the given axis,
- n_x screw axis with rotation $\frac{360}{n}$ ° and translation $\frac{a}{n}$ along the given axis,

 \bullet a ... e - denoting glide translations of various forms.

For instance, if a crystal in the monoclinic lattice with a two-fold screw axis on the a-axis and a glide plane perpendicular to the a-axis with translation along the b-axis is defined as being in the space group $P2_1/c$. It may also be referred to by its space group number, an international standard short-hand for the Hermann-Mauguin notation. In this case, the $P2_1/c$ space group is number 14; therefore, it may be referred to in full as $P2_1/c$ (14).

The Wyckoff system, developed by American crystallographer Ralph Wyckoff, is a related system for defining crystal structures in terms of their symmetry. In this system, the positions of ions in a crystal are described as so-called 'Wyckoff positions', which correspond to a unique set of points within the crystal according to its space group. Each position is labelled with a letter, which describes a symmetry operation that links each equivalent position in the crystal, and a multiplicity, which defines how many equivalent positions there are for that symmetry operation. For instance, the $P2_1/c$ space group can be defined by the Wyckoff positions (and corresponding fractional coordinates) shown in Table 2.1.

Table 2.1: The Wyckoff positions of the monoclinic $P2_1/c$ space group.

Wyckoff Position	Fractional Coordinates
2a	(0, 0, 0) (0, 0.5, 0.5)
2b	(0.5, 0, 0) (0.5, 0.5, 0.5)
2c	(0, 0, 0.5) (0, 0.5, 0)
2d	(0.5, 0, 0.5) (0.5, 0.5, 0)
2e	(x,y,z) (-x, y + 0.5, -z + 0.5) (-x,-y,-z) (x,-y + 0.5, z + 0.5)

2.3.2 Intrinsic and Extrinsic Point Defects

The description above applies to 'perfect' crystal structures. However, crystal structures are never perfect. Defects may arise *via* several mechanisms, including

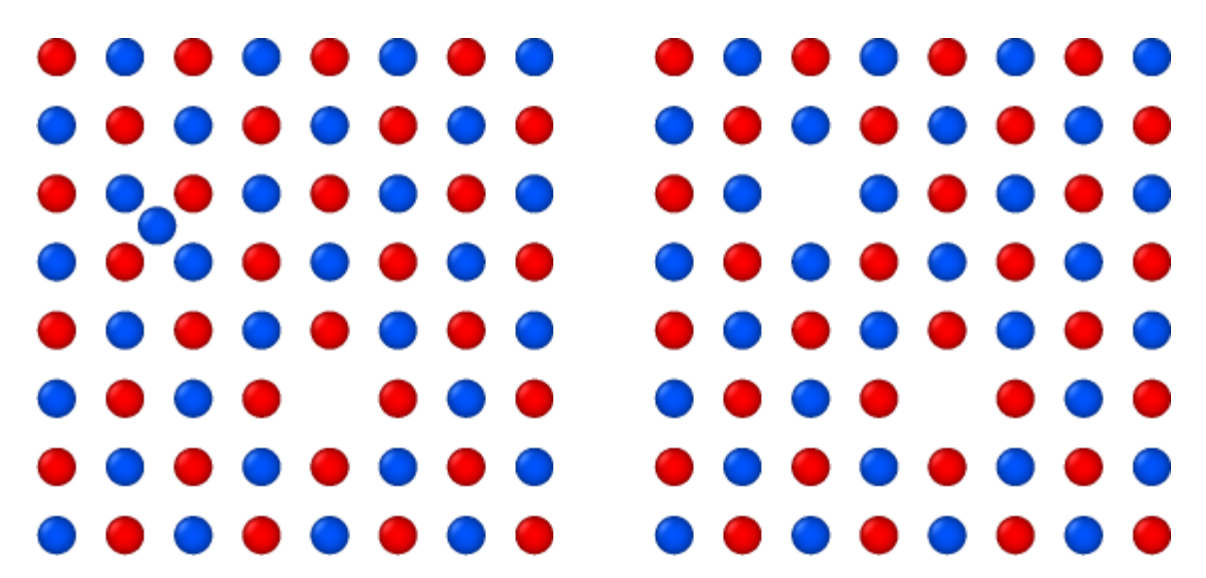


Figure 2.11: An example of point defects in a binary solid of species M (blue) and N (red). (Left) A Frenkel pair of species V_M and M_i . (Right) A Schottky pair of species V_M and V_N .

radiation damage from neutron bombardment, irregularities which arise from crystal growth, or simply from thermally-activated movement of the crystal's ions. In general, defects are divided into two categories: point defects, concerning localised irregularities over just a few lattice sites, and extended defects, such as slip dislocations (where a substantial fraction of the crystal structure is translated), grain boundaries and surfaces. Within the category of point defects, there are intrinsic and extrinsic defects, which concern the absence or presence of foreign atoms, respectively.

Point defects are referred to using Kröger-Vink notation, which follows the scheme M_S^C [122]. In this scheme, M is the defect species, which can be one of the following: atoms (e.g., W, Cr, etc.), vacancies (non-italicised V, as italicised V represents vanadium), interstitials (i), electrons (e), or holes (h). S is the site at which the defect species is present. For example, W_{Cr} denotes a tungsten atom on a lattice site in Cr, or O_i denotes an oxygen atom at an interstitial site. Finally, C denotes the charge of the defect species. This notation is used throughout this work.

One of the most common intrinsic point defects is the vacancy. As the name suggests, this is simply an unoccupied lattice site, which an atom may have previously occupied. Single vacancies are generally stable at room temperature; however, as discussed in Section 2.3.5, they may swap positions with a neighbouring ion at elevated temperatures. The absence of an ion on a lattice site introduces deformation in the neighbouring lattice sites; the defect is said to have a strain field, which has a limited range in which it perturbs the perfect crystal structure. During the formation of a vacancy, the manner by which the displaced ion moves gives rise to one of two kinds of disorder in the crystal structure: (1) Frenkel disorder, in which the displaced ion becomes trapped in an interstitial site (discussed below), and (2) Schottky disorder, in which the displaced ion forms a new bulk layer at the surface of the solid. A generic representation of these defect pairs is shown in Figure 2.11. For a generic binary alloy of species M^{2+} and N^{2-} , the formation of a Frenkel pair and Schottky pair, respectively, can be described by the equations:

$$M_M \longrightarrow V_M + M_i^{2+}$$
 (2.11)

$$M_M + N_N \longrightarrow V_M + V_N + MN$$
 (2.12)

The next types of point defects are those in which the total number of ions in the structure remains the same, which may be either intrinsic or extrinsic. Figure 2.12 shows the antisite and substitutional defects. The antisite defect is one in which two ions, M_M and N_N , swap sites:

$$M_M + N_N \longrightarrow M_N + N_M \tag{2.13}$$

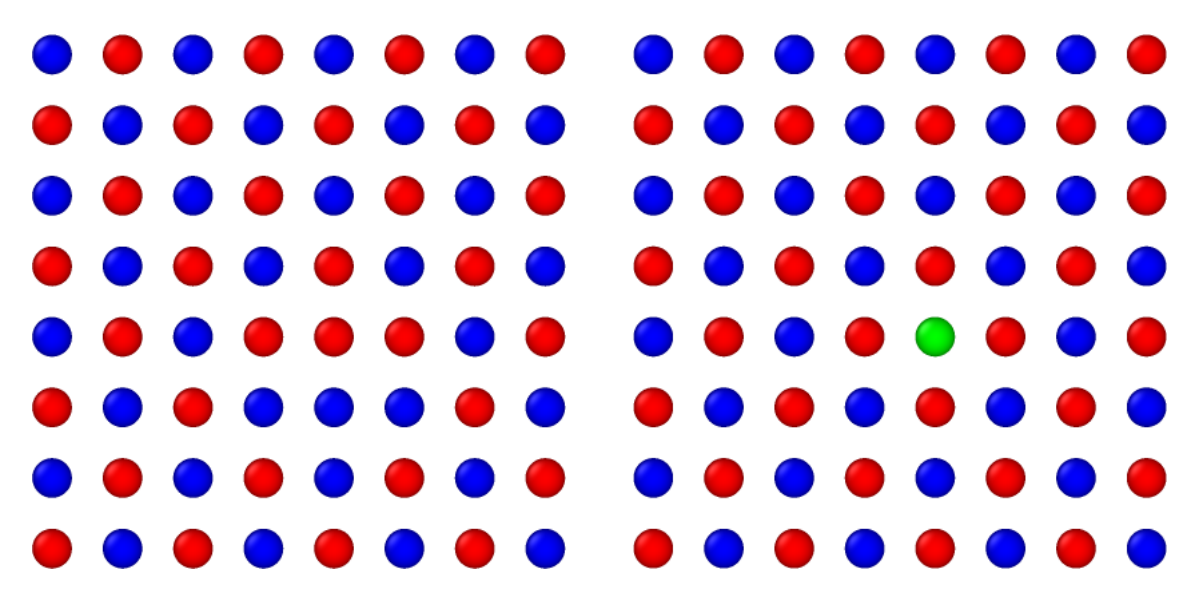


Figure 2.12: An example of (left) an antisite defect and (right) a substitutional in a generic alloy MN. In the substitutional defect, the substituting species, X, is shown in green.

As may be expected, placing a positively-charged ion in an environment preferentially occupied by a negatively-charged ion is energetically unfavourable, and so the energy required to form an cation-anion antisite defect is usually large. On the other hand, an extrinsic substitution - i.e., a foreign species, X, occupying a lattice site is not necessarily formed with a large energetic penalty. For instance, if the extrinsic species exhibits a similar ionic charge and/or similar ionic radius compared to the species native to the host crystal structure - such as in the example shown in Figure 2.12 - the energy required to make a substitution may be close to zero. Likewise, the strain field associated with the extrinsic species may also be negligible.

The final type of point defect - which can again be intrinsic or extrinsic - is the interstitial defect, M_i , shown in Figure 2.13. The term interstitial is derived from the Latin term *intersistere*, which directly translates as 'to stand in between'. As the phrase suggests, it is a defect where the defect species stands between lattice sites, where space is at a premium. Due to their large strain fields, interstitial defects typically exhibit more severe energy penalties for their formation, which arise from very short-ranged interactions with the surrounding crystal lattice. Since their exact

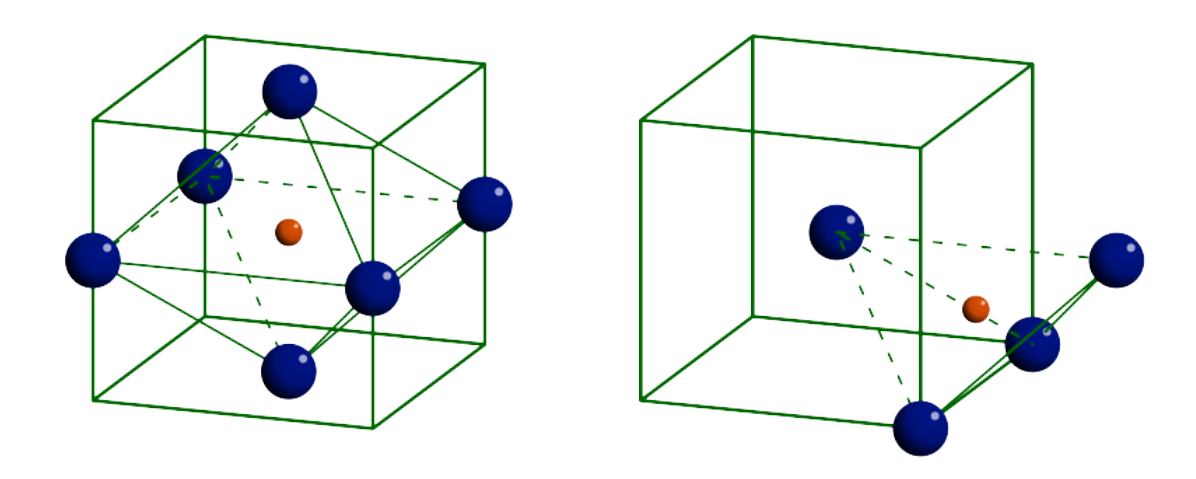


Figure 2.13: The nearest neighbours of the (left) octahedral interstitial site and (right) tetrahedral interstitial site in a body-centred cubic lattice. Credit to Philippe Lours, École des mines d'Albi-Carmaux, under CC BY-NC-SA.

positions are linked to the crystal lattice itself, the general description of the position of an interstitial defect depends upon the symmetry of the crystal.

In this thesis, interstitial defects are primarily considered in the context of a body-centred cubic (bcc) structure in a simple cubic Bravais lattice. The bcc lattice has two distinct interstitial sites: the octahedral interstitial site (OIS) and the tetrahedral interstitial site (TIS).

There are six octahedral sites per bcc unit cell located at the centre of each face and the midpoint of each edge of the unit cell boundary. The positions of these sites relative to the centre of the unit cell, in terms of the lattice parameters a, b and c, are:

$$\mathbf{r}_{i} = \begin{cases} (\pm \frac{1}{2}a, & \pm \frac{1}{2}b, & c) \\ (a, & b, & \pm \frac{1}{2}c) \end{cases}$$
 (2.14)

Likewise, twelve tetrahedral sites per bcc unit cell are located halfway between the

octahedral sites and equidistant between the four nearest-neighbour ions. Their relative positions are given by the general form:

$$\mathbf{r}_i = (\pm \frac{1}{2}a, \pm \frac{1}{4}b, c)$$
 (2.15)

2.3.3 Defect Formation Enthalpy

The defect formation enthalpy, ΔH_f , has been calculated for defects systems throughout this thesis. The defects formed include vacancies, substitutionals and interstitial point defects as described in Section 2.3.2. In general, the defect formation enthalpy is given by,

$$\Delta H_f = (E_x - E_0) + \sum_i n_i \mu_i + q (E_{VBM} + E_F) + k_{corr}$$
 (2.16)

where E_x and E_0 are the total energies of the defect-containing supercell and the perfect supercell, respectively; n_i and μ_i are the fractional quantity and chemical potential of defect i, respectively; q is the charge of the supercell; E_{VBM} and E_F are the energies of the valence band maximum and the Fermi energy, respectively; and k_{corr} is the finite size error correction term.

The supercell approach has been used to calculate the properties of all defect-containing structures, as discussed in Section 3.1.4. However, due to the computational constraints imposed by density functional theory, simulations are often necessary on slightly smaller supercells. As such, in charged systems, there may be Coulombic interactions between a charged defect and its periodic image, which artificially raises the energy of the supercell. This is known as a finite size error and is corrected by the term k_{corr} in Equation 2.16. In this thesis, the form of

 k_{corr} is described by the Kumagai charge correction factor [123],

$$k_{corr} = \frac{q^2}{2V\epsilon_0} \sum_{G \neq 0} \frac{4\pi}{\left|\mathbf{G}^2\right| \epsilon(\mathbf{G})}$$
 (2.17)

where V is the volume of the supercell, ϵ_0 is the permittivity of free space, \mathbf{G} are the reciprocal lattice vectors of the supercell, and $\epsilon(\mathbf{G})$ is the dielectric constant of the material evaluated at \mathbf{G} . The dielectric constant can be obtained using density functional perturbation theory, DFPT.

The chemical potential of the electron must also be taken into account for charged systems, and is incorporated in the term $q(E_{VBM} + E_F)$. The energy of the valence band maximum and the Fermi energy can be obtained from the total density of states of the material. In some cases, it is useful to vary the Fermi energy from 0 to E_{CBM} (the energy of the conduction band minimum), *i.e.*, to vary the Fermi energy across the band gap. This can be used to assess the most likely charge state of the defect as the Fermi energy is varied.

For a neutral system, Equation 2.16 reduces to,

$$\Delta H_f = (E_x - E_0) + \sum_i n_i \mu_i. \tag{2.18}$$

2.3.4 Point Defect Concentration

The concentration of point defects in a solid is a function of temperature; as temperature increases, the number of ions with sufficient energy to migrate away from their lattice sites increases. At the same time, the internal energy of the system, U, and the configurational entropy of the system, S_{conf} , also increase. The latter

represents the number of ways to arrange the ions in the system, which inherently increases as they migrate away from their lowest-energy positions. At constant pressure and temperature, the change in the Gibbs free energy of the system is:

$$\Delta G = \Delta U - T\Delta S \tag{2.19}$$

In the general case of forming any defect, x, the change in the internal energy, ΔU , is equal to the formation energy of the defect, E_f^x , such that:

$$\Delta U = n_x E_f^x \tag{2.20}$$

The increase in the configurational entropy of the crystal can be obtained using the Boltzmann relation:

$$\Delta S_{conf} = k_B \ln \omega \tag{2.21}$$

where k_B is the Boltzmann constant (8.62 eV K⁻¹) and ω is the number of ways of arranging n_x defects of type x. The latter value can be obtained using the equation:

$$\omega = \frac{N!}{n_x!(N - n_x)!} \tag{2.22}$$

where N is the total number of ions which can form defect x in the system. Substitution of ω into Equation 2.21 yields:

$$\Delta S = k_B \left[\ln(N!) - \ln \left[(N - n_x)! \right] - \ln \left[(n_x)! \right] \right]$$
 (2.23)

which may be simplified using Stirling's approximation, $\ln(N!) \approx N \ln(N) - N$, to:

$$\Delta S = k_B \left[N \ln \frac{N}{N - n_x} + n_x \ln \frac{N - n_x}{n_x} \right]$$
 (2.24)

This can be substituted back into Equation 2.19 to obtain the explicit form for the change in Gibbs free energy:

$$\Delta G = n_x E_f^x - k_B T \left[N \ln \frac{N}{N - n_x} + n_x \ln \frac{N - n_x}{n_x} \right]$$
 (2.25)

Since the Gibbs free energy is at a minimum when the system is in thermodynamic equilibrium, we can take the derivative of Equation 2.25 with respect to n_x to obtain:

$$\frac{\partial G}{n_x} = E_f^x - k_B T \ln \frac{N - n_x}{n_x} = 0 {(2.26)}$$

Lastly, if the number of defects of type x is small compared to the total number of ions in the system - i.e., the system is in the 'thermodynamic limit' - the concentration of defect x is expressed as:

$$\frac{n_x}{N} = \exp\left(\frac{-E_f^x}{k_B T}\right) \tag{2.27}$$

2.3.5 Diffusion Mechanisms

The diffusion of atoms in a solid can be generalised as the movement of atoms due to a driving force or combination of driving forces. One of the most common examples of a driving force for diffusion is the chemical gradient - *i.e.*, atoms move from regions

of high concentration to regions of low concentration. Diffusion in one dimension is given by the mathematical descriptor posited by Alfred Fick - the eponymously named Fick's law of diffusion [124]:

$$J = -D\frac{\partial C}{\partial x} \tag{2.28}$$

where J is the flux of atoms through a plane of a unit of area per a unit of time, D is the diffusivity constant, and C is the concentration of the diffusing atoms, whose first derivative is the concentration gradient. In solids, this concentration gradient arises from the presence of point defects; as was established in Equation 2.27, for a finite (non-zero) temperature, there is concomitantly non-zero concentration of point defects in the crystal structure. Therefore, at elevated temperatures, the diffusion of ions through a solid structure is enabled by the presence of defects.

Unlike liquids and gases, ions in solids migrate via so-called 'hops', discrete steps from one position to another. The energy required to perform this hop is sensitive to the chemical environment which the diffusing species starts in, ends in, and travels through. At the same time, the frequency of these hops is related to several factors, including the migration energy, the jump distance, and the jump frequency which is dependent upon the number of unique pathways which a hop may be attempted along [125].

Three main mechanisms exist by which ions can perform these hops, facilitated by the presence of different point defects. The first is the vacancy hop, in which an ion on a lattice site exchanges positions with a vacancy. The vacancy and the diffusant may belong to different sublattices, *i.e.*, the vacancy may have been formed from a cationic species, and the diffusant may be anionic. For instance, given sites A and B for a unary solid of species M:

$$M_A + V_B \longrightarrow V_A + M_B$$
 (2.29)

In the case of interstitial diffusion, two closely related mechanisms exist. The first is the interstitial hop, which is analogous to the vacancy hop, whereby the interstitial hops to a nearby interstitial site. The second is known as the interstitial cy mechanism, which typically occurs if the migration energy of an interstitial hop is large. In this mechanism, the interstitial species displaces a species on a lattice site, which itself becomes an interstitial. For example, in the binary system MN with the generic interstitial i and interstitial sites a and b:

$$i_a + M_M \longrightarrow i_M + M_b \tag{2.30}$$

2.3.6 Transition State Theory

As mentioned previously, the energy required for an ion to perform a hop is sensitive to the chemical environments in which the ion starts, ends, and passes through. The latter is especially important in solids, as the process invariably requires the ion to pass through a space between two or more ions, where proximity to those ions places the diffusant in an energetically unfavourable state - *i.e.*, the transition state. Since the energy required to reach the transition state is typically larger than the thermal energy available to the system (k_BT) , the ions in a crystalline system vibrate around their equilibrium positions until they are thermally activated.

Transition state theory (TST) forms the basis for defining the activation energy of a given diffusion mechanism. Suppose that the system of interest begins in state A, a unique position on the potential energy surface which defines the relationship between the system's geometry and its total energy. At equilibrium, the system

vibrates around the local minima on the potential energy surface until it is thermally activated, transitioning to a new local minima, which is state B. Therefore, the activation energy is the energy required to make this transition. This assumes that the transition from state A to state B is not correlated - i.e., there is no spontaneous transition to another state once the system has reached state B; it immediately reaches thermal equilibrium.

In transition state theory, the rate constant of the transition $A \to B$ is taken to be the flux through the dividing surface. However, this can be simplified by an extension of the theory known as harmonic transition state theory (hTST). In hTST, the vibrational modes of the system near the transition state are described in terms of a harmonic oscillator. The rate constant is given the form,

$$k = \nu_0 \exp\left(\frac{\Delta G^{\dagger}}{k_B T}\right) \tag{2.31}$$

where ΔG^{\dagger} is the change in Gibbs free energy required to reach the transition state, †, and which expands to,

$$\Delta G^{\dagger} = \Delta H^{\dagger} - T \Delta S^{\dagger}. \tag{2.32}$$

The pre-exponential term ν_0 is the Vineyard co-factor, which accounts for the inaccuracies arising from the treatment of the potential energy surface as having quadratic curvature around the local minima. The Vineyard co-factor expands to,

$$\nu_0 = \nu^* \exp\left(\frac{\Delta S^\dagger}{k_B}\right) \tag{2.33}$$

where ν^* is the reference attempt frequency. When substituted into 2.32, this gives:

$$k = \nu_0 \exp\left(\frac{\Delta E^{\dagger}}{k_B T}\right). \tag{2.34}$$

Therefore, the rate of diffusion can be obtained from the activation energy of the barrier which the system must overcome, ΔE^{\dagger} .

2.4 Oxidation of Tungsten

2.4.1 Theory of Oxidation in Solids

The subject of this work concerns the oxidation of tungsten and its alloys, which is not just its chemical oxidation (i.e., the increase in tungsten's oxidation state) but also the formation of oxide phases. Going forward, the term 'phase' refers to a distinct, homogeneous portion of a material characterised by its elemental composition and space group. Phases are separated in physical space by boundaries or interfaces and in the temperature and pressure domains by phase transitions. Many metals and alloys oxidise at elevated temperatures in the presence of oxygen, and understanding the formation of their oxide phases - the conditions and mechanisms by which they form and their physical properties - plays a vital part in the development of specialised materials.

Early theories of the formation of oxide phases by the likes of Tammann, Pilling and Bedworth found that the thickness of the metal oxide scale (layer) at the surface of many metals was proportional to the square root of the time taken for the scale to form, *i.e.*,

$$L(t) \propto t^{\frac{1}{2}} \tag{2.35}$$

where L(t) is the thickness of the oxide scale. This parabolic law makes multiple assumptions regarding the concentration of oxygen throughout the oxide scale and at the oxide-gas and oxide-metal interfaces. It also assumes that the oxide scale grows due to the diffusion of uncharged particles.

Later, Carl Wagner proposed a theory based on the assumption that the oxide scale grows due to the diffusion of charged particles [126]. Wagner's theory of oxidation was partially based on the work of Nernst and Debye on ionic diffusion of electrolytes in liquids. The theory makes the following key assumptions [127]:

- the rate-limiting step is the diffusion of ions or electrons across the oxide scale,
- the oxide scale is stoichiometric, or close to stoichiometric,
- thermodynamic equilibrium has been established through the oxide, as well as at the interfaces.
- the oxide scale is well-adhered to the bulk metal.

The assumption that a thermodynamic equilibrium at the oxide-gas and oxidemetal interfaces leads to the establishment of an activity gradient for both the metal species, M, and oxygen, O, across the oxide scale. This enables the transport of metal cations towards the surface (as proposed earlier by Pfeil) and oxygen anions towards the metal (similar to the theory developed by Tammann, Pilling and Bedworth). The transport of ionic species across the oxide scale also establishes an electric field, enabling the transport of electrons towards the surface (though no transfer of charge takes place, as the exchange of ions and electrons is simultaneous). Therefore, there is not only a chemical gradient acting as a driving force for diffusion but also an electric gradient.

Three kinetic regimes are likely to be encountered during the oxidation of any

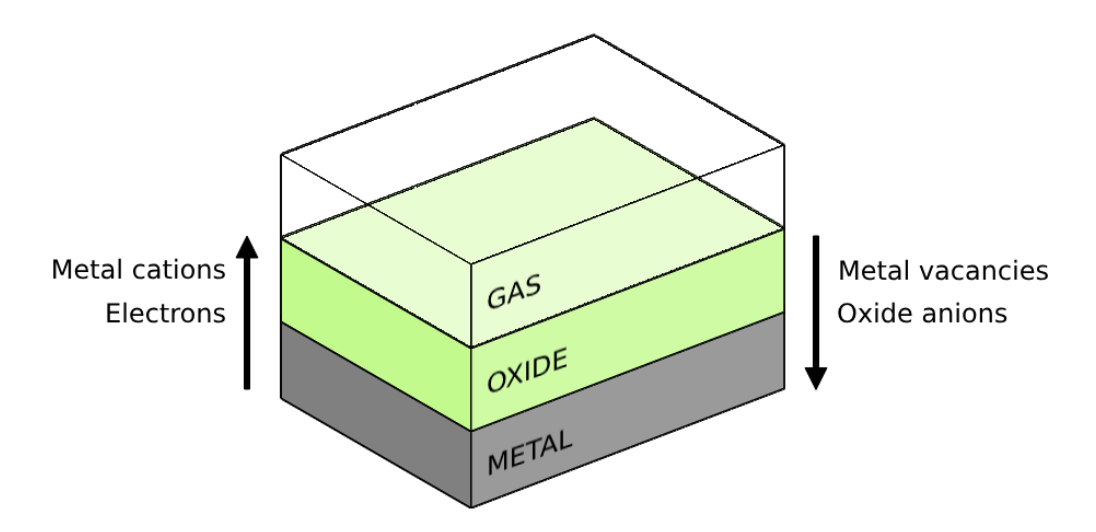


Figure 2.14: A simplified representation of an oxide scale, showing the direction of ion and electron transport according to the Wagner theory of oxidation.

metal. The first is the linear oxidation regime, where the oxide scale thickens as a linear function of time:

$$L(t) = k \cdot t. \tag{2.36}$$

This typically takes place when the rate-limiting step is a process occurring at a phase boundary, such as the adsorption of oxygen to the metal surface. Therefore, linear oxidation is expected in the very initial stages of oxidation, when the oxide scale is sufficiently thin, and the activity of the metal is close to the bulk value.

As oxidation proceeds, the thickness of the oxide scale grows, and the activity of the metal across the scale reduces accordingly. At this stage, the rate-limiting process becomes the transport of ions through the oxide scale as described by the Wagner theory of oxidation, discussed above and shown in Figure 2.14. The rate of growth follows a parabolic rate law,

$$L(t)^2 = k_p \cdot t \tag{2.37}$$

where the parabolic rate constant k_p is,

$$k_p = k_0 \cdot (p_{O_2})^{\frac{1}{n}} \exp\left(-\frac{\Delta E^{\dagger}}{k_B T}\right)$$
 (2.38)

where k_B is the Boltzmann constant, 8.617×10^{-5} eV K⁻¹ at⁻¹.

The third regime is logarithmic oxidation, where a very low oxidation rate soon follows an initial period of rapid oxidation. This generally occurs at lower temperatures (up to 700 K) and for very thin ($\leq 0.1 \ \mu \text{m}$) layers. In this case, the oxide scale grows according to,

$$x = k_{log} \log (t + t_0) + A \tag{2.39}$$

where k_{log} is the logarithmic rate constant and t_0 and A are constants.

2.4.2 The Tungsten-Oxygen System

The oxidation of tungsten has been widely studied and continues to be of interest to many fields of research beyond that of plasma-facing materials. Beyond the context of this thesis, the oxidation of tungsten is relevant in the field of semiconductors for solar panels, photocatalysis, sensors and photochromic devices [128, 129, 130, 131, 132]. Nevertheless, the oxidation mechanism is poorly understood and is subject to debate in the literature, as discussed in Section 2.4.3.

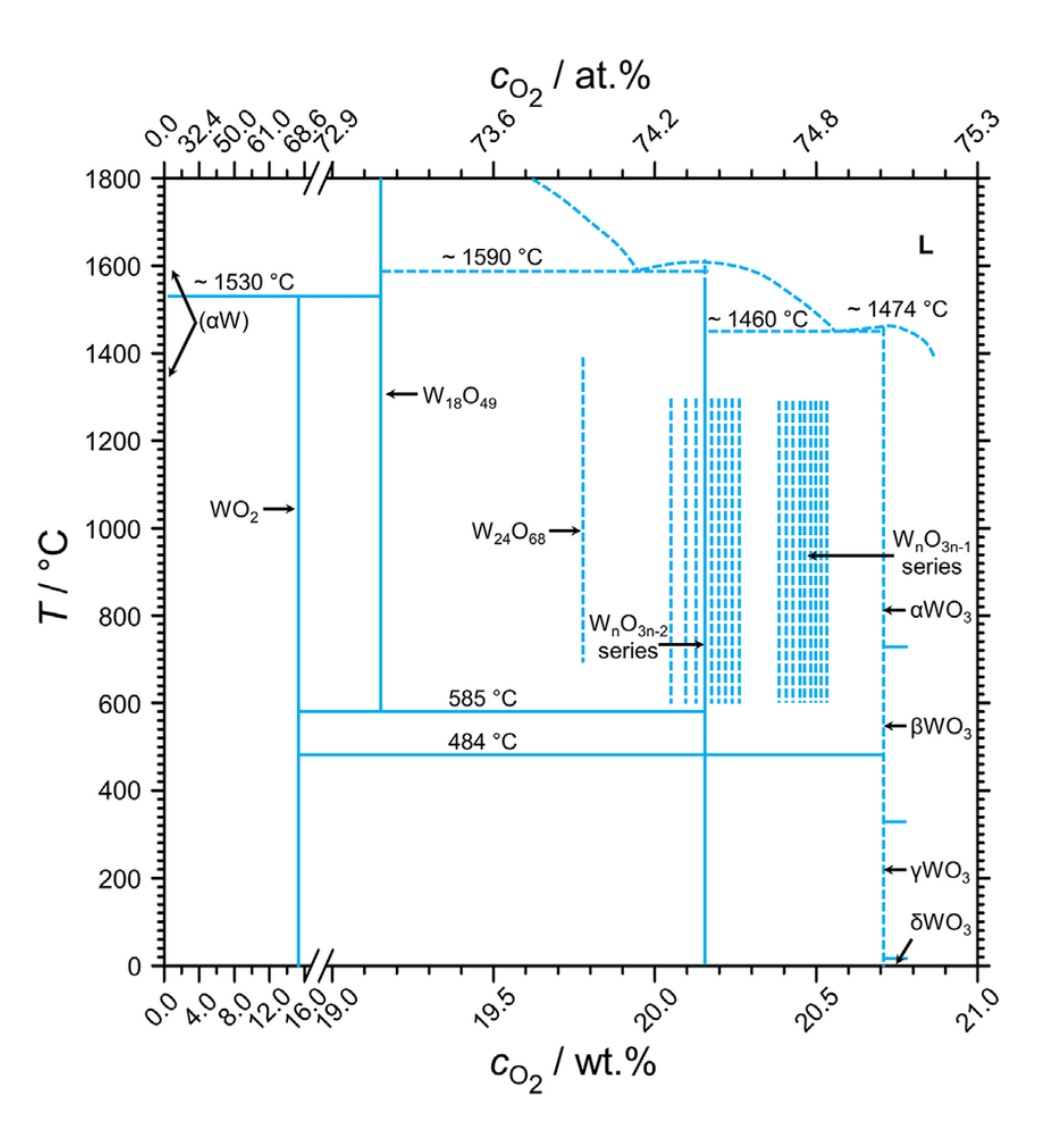


Figure 2.15: The phase diagram of the tungsten-oxygen system extended down to 0 °C, in terms of temperature and the oxygen content (in both wt% and at%) [133].

The lack of consensus on the oxidation mechanism largely stems from the complexity of the problem. During the oxidation of tungsten, several tungsten oxide phases form and have been verified experimentally. The experimental phase diagram for the tungsten-oxygen system is shown in Figure 2.15 [133]. Each of the major, stable phases of the tungsten-oxygen system will be described below.

The first oxide phase that forms during tungsten's oxidation is tungsten dioxide, WO_2 , which forms at all temperatures up to around 1800 K [134]. Prior to this, tungsten exists in its body-centered cubic form, so-called αW . The most stable

form of tungsten dioxide crystallises in the monoclinic $P2_1/c$ (no. 14) space group. One W⁴⁺ ion occupies the 4e Wyckoff position, whilst two inequivalent oxygen ions occupy 4e Wyckoff positions.

At around 73% oxygen content, from temperatures upwards of 858 K, the first of the stable Magnéli phases (named after Swedish chemist Arne Magnéli) is observed. This phase has the stoichiometry $W_{18}O_{49}$, sometimes referred to as $WO_{2.72}$ [135]. It exhibits a tungsten bronze-like structure, crystalising in the space group P2/m (no. 10) with a β angle of 115.20°according to Salje *et al.* This phase consists of 16 oxygen ions at 2n Wyckoff positions, nine at 2m Wyckoff positions, and one oxygen ion at the 1f Wyckoff position. In a 10:8 mixture of W⁵⁺ and W⁶⁺ oxidation states, the tungsten ions occupy the 2n Wyckoff positions.

The next major Magnéli phase occurs at around 74% oxygen content. At this concentration, there are multiple so-called 'line phases' in the experimental phase diagram - distinct, sub-stoichiometric phases occurring at discrete oxygen contents between various temperatures. The $W_{25}O_{73}$, or $WO_{2.92}$ phase is the most stable of these line phases [136]. It is blue and exhibits a 'shear' structure in the monoclinic P2/c space group with a β angle of 98.3°. The shear structure can be described as consisting of corner-sharing WO_6 octahedra arranged in columnar blocks. At the boundary between two blocks, the structure is 'sheared' in one direction, causing one block to be half a unit cell higher than the other. The $WO_{2.92}$ phase consists of 37 unique oxygen sites, one at the 2f Wyckoff positions and the remaining at the 4g Wyckoff positions. The tungsten ions occupy 13 unique sites, one at the 2f Wyckoff position and the remainder at the 4g Wyckoff positions, in a 1:12 mixture of W^{5+} and W^{6+} oxidation states.

Last, tungsten trioxide, WO₃, forms at 75% oxygen content, up to its melting point of around 1747 K [137]. It exhibits several polymorphs up to its melting point, all of which have been verified experimentally:



Figure 2.16: The thermochromism seen in WO_3 over a range of temperatures [143].

- ϵ -WO₃, monoclinic Pc (no. 7), < 223 K [138],
- δ -WO₃, triclinic P\bar{1} (no. 2), 223 288 K [139],
- γ-WO₃, monoclinic P21/c (no. 14), 288 603 K [140],
- β-WO₃, orthorhombic Pbcn (no. 60), 603 1013 K [141],
- α -WO₃, tetragonal P4/mmm (no. 123), > 1013 K [142].

Within each of these phases, a wide range of stoichiometries is observed, which can be described by the general formula WO_{3-n}. In its room temperature phase, γ -WO₃ crystallises in the space group P21/c. This phase includes three unique oxygen sites at the 4e Wyckoff positions, each bonded to two equivalent W⁶⁺ ions at 4e Wyckoff positions. Furthermore, the α , β and γ phases exhibit thermochromism, the dependence of colour on temperature. The colour of the γ phase ranges from yellow-green to orange, as shown in Figure 2.16 [143, 144].

2.4.3 Mechanism of Tungsten Oxidation

As mentioned previously, there is considerable debate in the literature over the exact mechanism of oxidation in tungsten. Although it is widely accepted that

oxidation occurs in three stages, disagreement arises over exactly which tungstenoxygen phases occur at each stage, and each has a distinct mechanism.

The first stage of oxidation concerns the pure, unoxidised metal surface in contact with an oxidising gas. At temperatures up to around 673 K, oxygen adsorps to the surface at the interstitial positions, preferentially occupying sites with threefold coordination to neighbouring tungsten atoms [145]. This forms an oxide scale no greater than around 0.1 μ m in thickness [146], which grows according to a logarithmic rate law (Equation 2.39). Experimentalists report that the initial oxide scale is dark blue, which various researchers attribute to different oxide phases. Webb et al. posited that it may be the sub-stoichiometric phase $WO_{2.75}$ based on an analysis of the rate of oxidation which incorporates the tungsten-oxygen ratio [147]. A later study by Keller et al., with supporting observations by Magnéli, refutes that the oxide is a sub-stoichiometric phase and that it is instead W₁₈O₄₉ [148]. On the other hand, a much earlier analysis by Hickman and Gulbransen in 1947 suggested that the initial oxide scale is more simply WO₂ [149]. Nevertheless, during this stage, the further oxidation of bulk tungsten is inhibited until the entire surface has been covered, after which point the growth of the oxide scale changes from the logarithmic regime to the parabolic.

During the second stage of oxidation, the dark blue layer continues to grow. Above 873 K, the yellow-green WO₃ layer also begins to form. At first, the growth of the oxide scale follows a parabolic rate law (Equation 2.37), as it is governed by diffusion; in particular, the growth rate is determined by the diffusivity of oxygen ions through WO₃. Oxidation experiments from Sikka *et al.* and Cifuentes *et al.* demonstrated this to be the case, with the former showing that the thickness of the WO₃ scale remained constant between 50 and 100 hours of oxidation, whilst the inner sub-stoichiometric oxide layer continued to grow [149, 150]. As the inner scale reaches its maximum thickness, cracking of the oxide scale due to stresses arising from the formation of WO₃ leads to a transition from the parabolic to the linear

oxidation regime [151]. At this point, the sub-stoichiometric oxide layer is no longer protective against oxidation, as oxygen can easily ingress through the cracks. In addition, the assumptions made by the Wagner theory of oxidation (principally, that the oxide scale must be well-adhered to the surface) break down.

The final stage of oxidation occurs at temperatures above 1023 K, where WO₃ begins to sublime. At higher temperatures (> 1573 K), the rate of sublimation is equal to, or exceeds, the rate of oxidation, meaning that no oxide scale forms at the surface. This does not mean that the formation of WO₃ is suppressed, but instead that any WO₃ that does form is immediately volatilised. Both Grossweiner et al. and Belton et al. suggest that the presence of water vapour increases the volatility of WO₃ [127, 146] and, by extension, the rate of oxidation of bulk tungsten. Grossweiner et al. suggests that the reaction forms the gaseous species:

$$WO_{3(s)} + H_2O_{(g)} \longrightarrow WO_3 \cdot H_2O_{(g)},$$
 (2.40)

whereas Belton et al. suggests the following reaction:

$$W_{(s)} + 4H_2O_{(g)} \longrightarrow WO_3 \cdot H_2O_{(g)} + 3H_{2(g)}.$$
 (2.41)

2.4.4 Loss of Coolant Accidents

The formation of volatile $(WO_3)_x$ clusters is the key safety concern and source of consternation over using tungsten as plasma-facing material. As discussed in Section 2.2.4, tungsten exposed to the vacuum vessel is expected to exhibit activity levels of greater than 10^{16} Bq/kg for up to a year [152]. The volatilisation of any amount of this irradiated tungsten provides a vector for transferring radioactive material

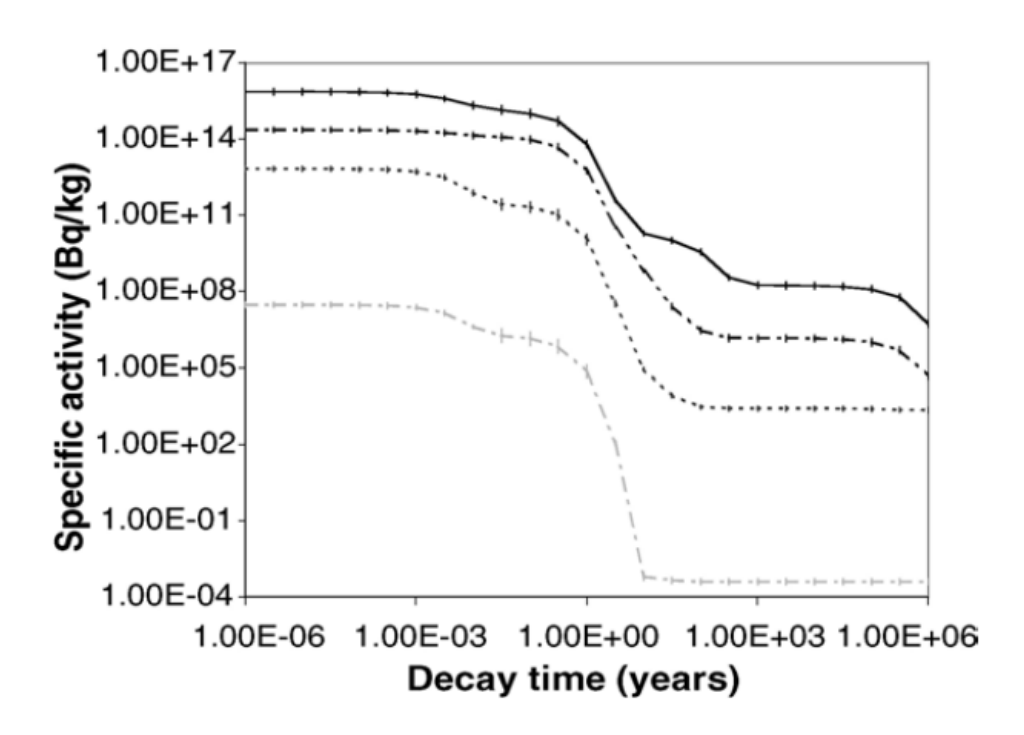


Figure 2.17: Activity of tungsten after irradiation. Obtained by Gilbert *et al.* using the following data sources (from top to bottom): conceptual power plant neutron spectra at the first wall, blanket and shield, and from JET DD experimental neutron spectrum [152].

outside the reactor vessel or, worse, into biological systems. Furthermore, if the reactions proposed in Equations 2.40 and 2.41 are realistic, gaseous WO₃ may also be tritiated, *i.e.*, as WO₃·HTO or WO₃·T₂O.

In nominal operating conditions, the tungsten first wall is in contact with a vacuum at a constant, relatively low temperature. For instance, JET operated at an ambient temperature of 593 K and a base vacuum pressure of 5×10^{-8} bar [153]. By comparison, the vacuum pressure at the surface of the Moon is estimated to be around 1×10^{-12} to 1×10^{-15} bar [154]. These conditions are insufficient for the oxidation of tungsten on any appreciable timescale, especially considering the sputtering of tungsten atoms from the surface due to neutron bombardment. However, in a loss of vacuum accident (LOVA), air may enter the reactor vessel; likewise, in a loss of coolant accident (LOCA), the temperature of the first wall may

exceed the threshold required for oxidation.

No single point of failure may lead to a loss of coolant accident. For instance, it may occur due to electrical failure of the coolant pumps or due to the rupturing of coolant channels if the first wall is integrated with the tritium breeding blanket [155]. Figure 2.18 shows the first wall temperature over 100 days after a loss of coolant accident in four conceptual designs for the DEMO power plant [156]. In most cases, the temperature of the first wall rises sharply to over 1300 K, and certainly well above the 1000 K threshold for the sublimation of WO₃. Estimations made in the context of DEMO also suggest that between 50-150 kg of tungsten may be lost due to sublimation per hour in these conditions, which, as shown, may persist for weeks at a time.

The leakage of radioactive material is designed to be minimal at worst, corresponding to dose rates of around $2\sim20$ mSv (the annual limit for radiation workers in the UK). Nevertheless, any improvements that can be made to reduce this risk must be undertaken. Likewise, the loss of such large volumes of tungsten via sublimation is an unacceptable consequence of a loss of coolant accident and one which may very likely spell the end of a power plant (or, at best, a long period of recommissioning).

2.5 Self-Passivating Tungsten Alloys

2.5.1 Early Development of tungsten-based SMART Alloys

One method of suppressing the oxidation of tungsten is by using a Self-passivating Metal Alloy with Reduced Thermo-oxidation, or 'SMART' alloy, which is protected from further oxidation by the oxide scale which forms on its surface. The most

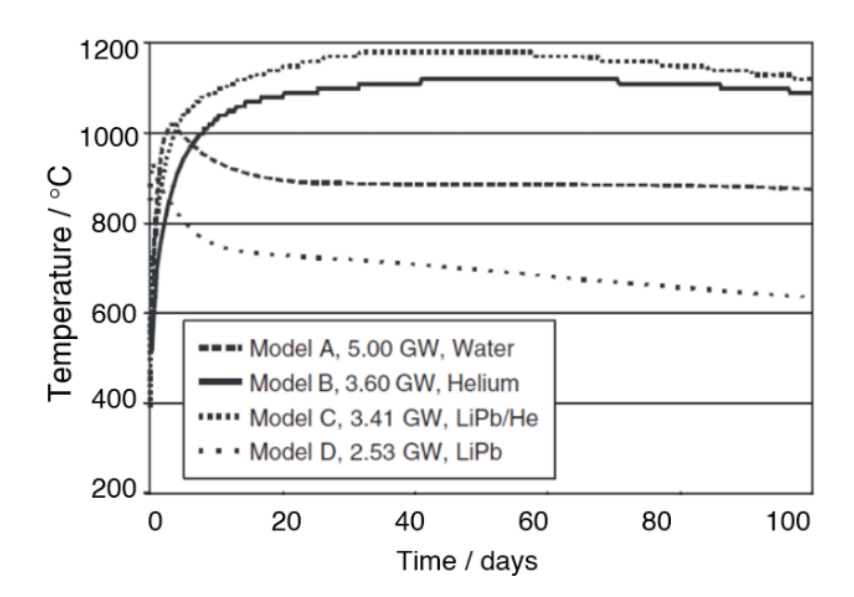


Figure 2.18: Temperature of a conventional tokamak tungsten first wall over 100 days following a loss of coolant accident for four different conceptual tokamak power plant designs. [156].

widespread examples of a self-passivating materials are stainless steel, which forms a layer of chromium oxide on its surface, and aluminium, which forms a layer of aluminium oxide. When these layers are scraped away, the oxide scale rapidly regenerates to provide its passivating effect continuously.

Since around 2007, there has been ongoing research into self-passivating tungsten alloys with this phenomenon in mind. The initial work by Koch and Bolt at this time investigated the effects of elemental composition on the oxidation of W, W-Si and W-Cr-Si thin films [157]. Their key results showed that the binary W-Si alloys formed a passivating layer of SiO₂ at the surface. Whilst oxidation of the tungsten was not fully suppressed, the oxidation rate decreased as a function of silicon concentration. Likewise, for the ternary W-Cr-Si alloy, they observed multiple oxide passivating oxide layers, which led to delamination ('flaking') of the oxide scale. In the latter, a reduction of the oxidation rate by a factor of 10⁴ was observed.

Further work then incorporated zirconium and yttrium as the ternary alloying

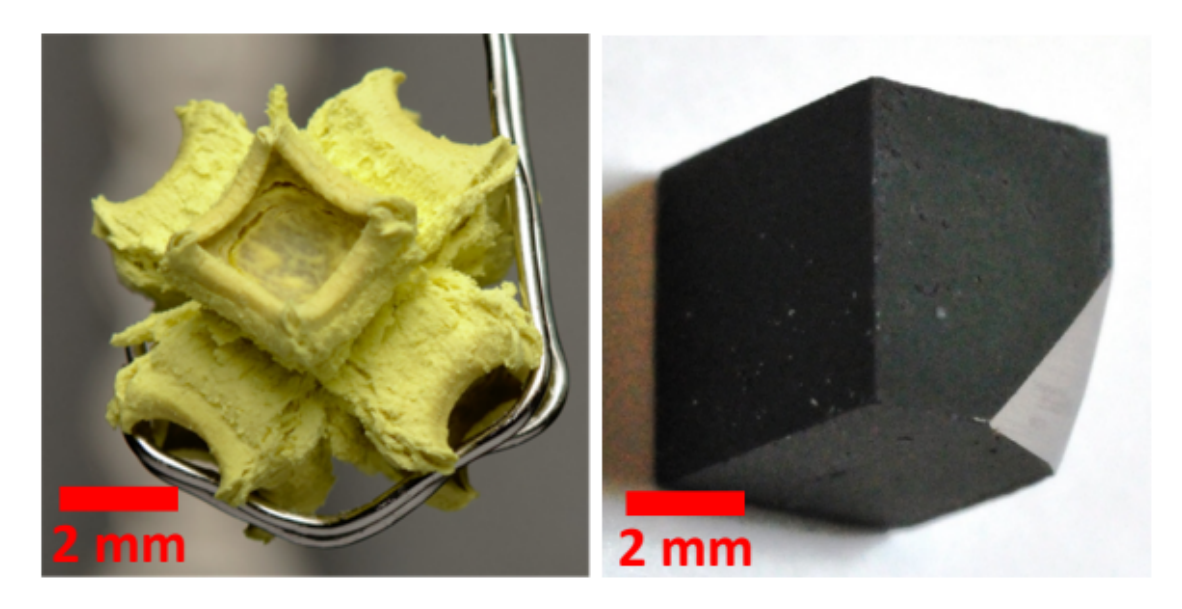


Figure 2.19: Oxidation of (left) pure tungsten after 10 hours and (right) tungstenchromium SMART alloy after 2 days, at 1273 K [159].

element to a similar effect and highlighted an essential property of these alloys in the context of a plasma-facing component [158]. During nominal operating conditions, the lighter alloying elements are preferentially sputtered from the surface of the alloy, leaving behind a layer of pure tungsten. Therefore, the desirable neutron shield property of the first wall is maintained. Under oxidative conditions, alloying elements were proposed to diffuse towards the surface to provide the self-passivating effect on demand.

Despite the excellent oxidation resistance offered by W-Si systems, tungsten silicides have poor workability due to their low elasticity. Further work by Foch et al. in 2011 brought attention to the W-Cr-Ti ternary alloy, with greater passivating potential and ductility than W-Cr-Si [160]. In the latter, a passivating layer of chromium oxide, Cr₂O₃, sometimes referred to as chromia, protects the rest of the alloy from oxidation. This can be seen in Figure 2.19 as a thin black oxide scale on the surface of the alloy. Around 2016, W-Cr-Y alloys became the primary focus of ongoing research in this area of study. At this time, parallel research showed that yttrium had an extremely positive effect on the stability and passivating behaviour

of stainless steels [161, 162, 163, 164, 165]. In particular, it was recognised that the choice of the third alloying element - the so-called 'active' element - was crucial to the long-term performance of W-Cr SMART alloys [166]. After much research with different alloying elements, yttrium became the active element of choice.

2.5.2 Yttrium as the Active Element

The beneficial properties of yttrium inclusion ('doping') in alloys have been understood for several decades, though its mechanism is poorly understood. For example, Przybylski et al. demonstrated that in a cobalt alloy with 45 wt% chromium (Co-45Cr), a yttrium dose of 2×10^{16} at cm⁻² was sufficient to reduce the rate of oxidation by a factor of 100 [161]. They also observed that the growth of the oxide scale changed from being limited by the outward diffusion of chromium to being limited by the inward diffusion of oxygen. This is the result of yttrium segregation to the alloy's grain boundaries, though, at the time, the mechanism by which this altered the growth of the chromium oxide layer was unknown. Furthermore, their energy dispersive X-ray analysis (EDX) indicated the presence of the ternary perovskite phase YCrO₃ at the grain boundaries. However, there was no evidence to suggest that this phase was directly responsible for inhibiting chromium diffusion to the surface. A similar observation was made in pure chromium by Stroosnijder etal. in 1996, with one difference being that they proposed the presence of YCrO₄ at the grain boundaries, rather than YCrO₃ [162]. As before, the exact mechanism by which yttrium affected the oxide scale growth was unknown; they proposed that this may be due to a simple blocking effect preventing chromium from diffusing along grain boundaries. It was also highlighted that the accumulation of vacancies at the oxide-metal interface was suppressed, leading to better adherence of the oxide scale to the bulk metal. In another study by Yang et al., it has been suggested that the strong binding energy between yttrium and a vacancy at the grain boundary,

which the passivating element would otherwise use to diffuse to the surface, causes grain boundary migration to be hindered [167]. However, Zhang *et al.* suggests that yttrium improves the segregation of the passivating element to the surface and provides nucleation points for the formation of the oxide scale [168].

Yttrium also has a distinct effect on grain growth and toughness in alloys. For instance, Wang et al. report a reduction in grain size from 2.02 μ m to 0.97 μ m in PH13-8Mo stainless steel and an improvement in the tensile strength of the alloy [169]. In part, they attributed these properties to the precipitate strengthening, i.e., the strengthening of the alloy via the formation of yttrium-containing nanoparticles. However, this is not always the case. Guimarães et al. found that small amounts of yttrium in the nickel alloy 718 increased the grain size, whereas higher quantities of yttrium embrittled the alloy, owing to the formation of Ni₁₇Y₂ and Y₂O₃.

Another property that yttrium exhibits as an active element is its propensity towards binding impurities. Importantly, Pajor et al. investigated the effect of yttrium doping in Zr₅₀Cu₄₀Al₁₀ by adding the stoichiometric and doublestoichiometric amounts of yttrium required to scavenge oxygen impurities from the alloy [170]. This alloy is part of a class of advanced materials known as bulk metallic glasses, which have highly desirable mechanical properties [171]. However, the presence of oxygen as an impurity inhibits the ability of the alloy to form a glass, owing to the high affinity between zirconium and oxygen. In their study, this detrimental effect was reduced by adding yttrium, which 'scavenges' oxygen from the alloy to form Y_2O_3 . However, they note that the stoichiometric amount of yttrium was insufficient to sequest all oxygen in the system thoroughly. In a similar vein, yttrium exhibits a strong affinity towards iron, which is especially useful for radiation-resistant materials. Brodick et al. found that the Y₂O₃-Fe interface in oxide dispersion strengthened (ODS) iron acted as a trap for interstitial defects and vacancies, which are commonplace in radiation-damaged crystal structures [172]. This enabled their recombination with minimal overall change to the microstructure

of the metal itself.

There is no clear consensus on how yttrium improves the oxidation resistance of various alloys, especially when comparing different alloys or oxidation conditions [168]. As mentioned previously, no catch-all statement accurately defines the behaviour of yttrium as the active element. It is not a given that the inclusion of yttrium will increase or decrease the oxidation resistance, grain size, tensile strength and impurity-scavenging properties of a given alloy.

2.5.3 Synthesis of Tungsten-Based SMART Alloys

Bulk W-Cr-Y alloys are synthesised using a combination of mechanical alloying and sintering [166]. In earlier studies on the alloy, elemental powders - *i.e.*, pure metallic tungsten, chromium and yttrium - were combined in a planetary ball mill under an inert atmosphere. Powder X-ray diffraction analysis showed that, after 60 hours, tungsten and chromium had fully mixed to form a homogeneous solid solution.

The second stage of bulk alloy synthesis can be achieved via one of two techniques. The first, utilised in earlier studies (c. 2011 - 2017), is hot isostatic pressing (HIP), wherein the alloyed powder is compressed at high temperatures to consolidate the powder and stimulate grain combination. The temperatures employed in these studies ranged from 1493 to 1623 K. The technique successfully creates dense, compact alloys which exhibit enhanced oxidation performance due to the formation of tungsten-yttrium nanoparticles at the surface of the alloy [173]. Nevertheless, flake-like grains of pure W were observed after HIP by López-Ruiz et al. [174], indicating that this method is not entirely sufficient, likely due to the spinodal decomposition which the tungsten-chromium system undergoes at low temperatures. This phenomenon will be discussed below in Section 2.5.4. Furthermore, the necessity of thermal treatment of the resulting alloy was highlighted by Calvo et

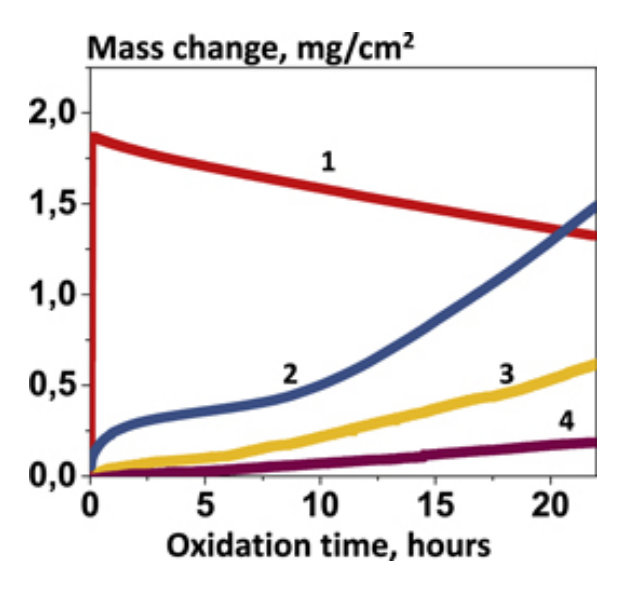


Figure 2.20: Mass change during the oxidation of (1) pure W, (2) HIP W-Cr-Y SMART alloy, (3, 4) FAST W-Cr-Y SMART alloys [166].

al.; without thermal treatment, alloys created via HIP exhibited catastrophic failure when undergoing thermal shock testing [173].

Although the HIP process and thermal treatment take just a few hours each under laboratory conditions, a faster sintering technique is desirable for upscaling W-Cr-Y alloy production. The inhomogeneities found during HIP must also be addressed to ensure the stable mechanical performance of the alloy. The second technique, Field-Assisted Sintering Technology (FAST), aims to address both. FAST is similar to HIP in that pressure is used to compact the powdered alloy; however, the heat required to sinter the alloy is transferred by a low voltage, high (direct) current pulse [175]. Litnovsky et al. utilised FAST to synthesise W-Cr-Y alloys with sintering temperatures around 1800 K, carefully controlling the heating rate and isothermal holding time (i.e., the length of time that the alloy is sintered at the maximum sintering temperature) [166]. These parameters were especially important, as they impose an apparent effect upon the oxidation resistance of the resultant alloy, as shown in Figure 2.22. They found that the samples of W-Cr-Y sintered via FAST, using the fastest heating rate (200 K min⁻¹) and zero isothermal holding time exhibited the greatest oxidation resistance (curve 4 in Figure 2.20).

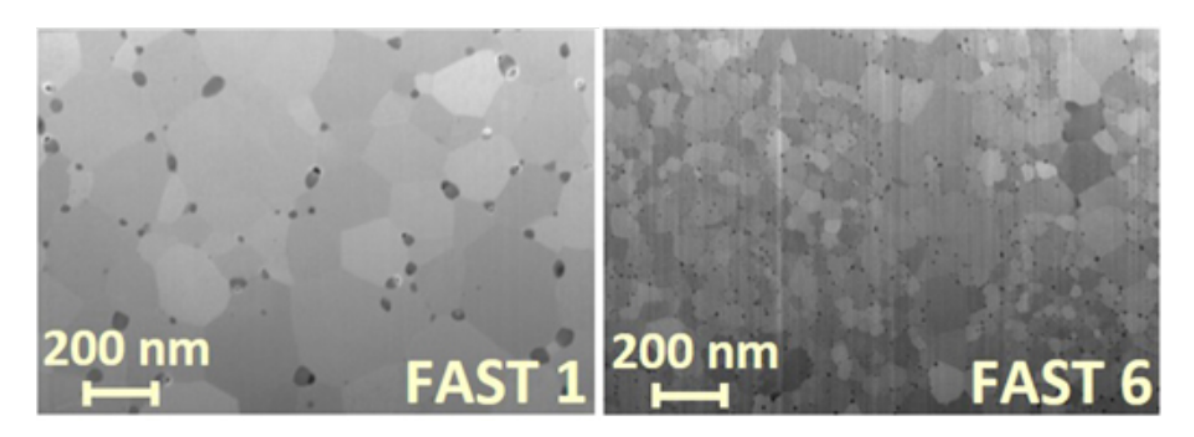


Figure 2.21: Grain structures of W-Cr-Y synthesised under (left) 'FAST 1' and (right) 'FAST 6' conditions [166].

Furthermore, SEM analysis revealed that by reducing the isothermal holding to zero, the suppression of grain growth in the alloy could be achieved. The SEM images obtained by Litnovsky et~al. are shown in Figure 2.21, where 'FAST 1' was obtained after holding the sample at 1823 K for 1 min and 'FAST 6' was obtained with no isothermal holding, only rapid heating to 1733 K. Later research by Klein et~al. investigated the effect of grain size on oxidation and found that the passivation of the alloy was correlated with grain size [176]. For instance, W-Cr-Y synthesised using the 'FAST 1' parameters exhibited W-Cr grain sizes of around 0.33 μ m, whereas the sample synthesised using the 'FAST 6' parameters exhibited grain sizes around 0.26 μ m, and notably lower mass loss via sublimation of WO₃.

2.5.4 Spinodal Decomposition

The tungsten-chromium solid solution is not thermodynamically stable at relatively low temperatures, as visualised in the phase diagram shown in Figure 2.22 [177]. The alloy is known to undergo spinodal decomposition, forming regions within the bulk structure with large differences in composition [178]. It is important to note that this phenomenon is distinct from nucleation, which involves large compositional changes within the system, typically at structural features such as grain boundaries

or surfaces. The temperature below which segregation occurs is known as the orderdisorder transition temperature (ODTT), which is dependent on composition. Not only is the ODTT dependent on the concentration of the main alloying elements, but it is also influenced by the presence of dopants. For example. Sobieraj *et al.* found that the presence of just 1-2% Y in W₇₀Cr₃₀ reduced the ODTT from 1700 K to 1300 K [179]. This is extremely noteworthy as it implies that an alloy with the composition W₇₀Cr₂₉Y₁ may transition from an ordered (spinodally decomposed) structure to a disordered solid solution when a loss of coolant accident occurs (see Section 2.4.4). Likewise, other studies suggest that it is possible to suppress the rate of decomposition at 1273 K by doping with tantalum [180]. Therefore, it is important to understand the spinodal decomposition of W-Cr-Y alloys and the effect that this phenomenon has on their mechanical and passivating properties.

A detailed study by Chen et al. investigated spinodal decomposition at 1273 K, showing that the $(\alpha W, Cr)$ phase gradually segregates to form a Cr-rich $(\alpha Cr, W)$ grains and a Cr-poor $(\alpha W, Cr)$ grains [181]. The Cr-rich phase was found to form at the grain boundaries, along with yttrium oxide nanoparticles, and its chromium content gradually decreased over time. On the other hand, the Cr-poor phase slowly increased in chromium content over several days. Likewise, they observed grain growth over the course of 100 hours. Although they found that the hardness of the alloy decreased over time, the coarsening of the $(\alpha Cr, W)$ grains led to increased grain boundary strengthening. The oxidation behaviour of the alloy also changes after spinodal decomposition. In particular, the Cr-poor phase, depleted of the passivating element, was more susceptible to oxidation [182].

2.5.5 Oxidation of Tungsten-Based SMART Alloys

As discussed above, multiple factors affect the passivating behaviour of tungstenbased SMART alloys, e.g., the chemical composition of the alloy, its grain sizes,

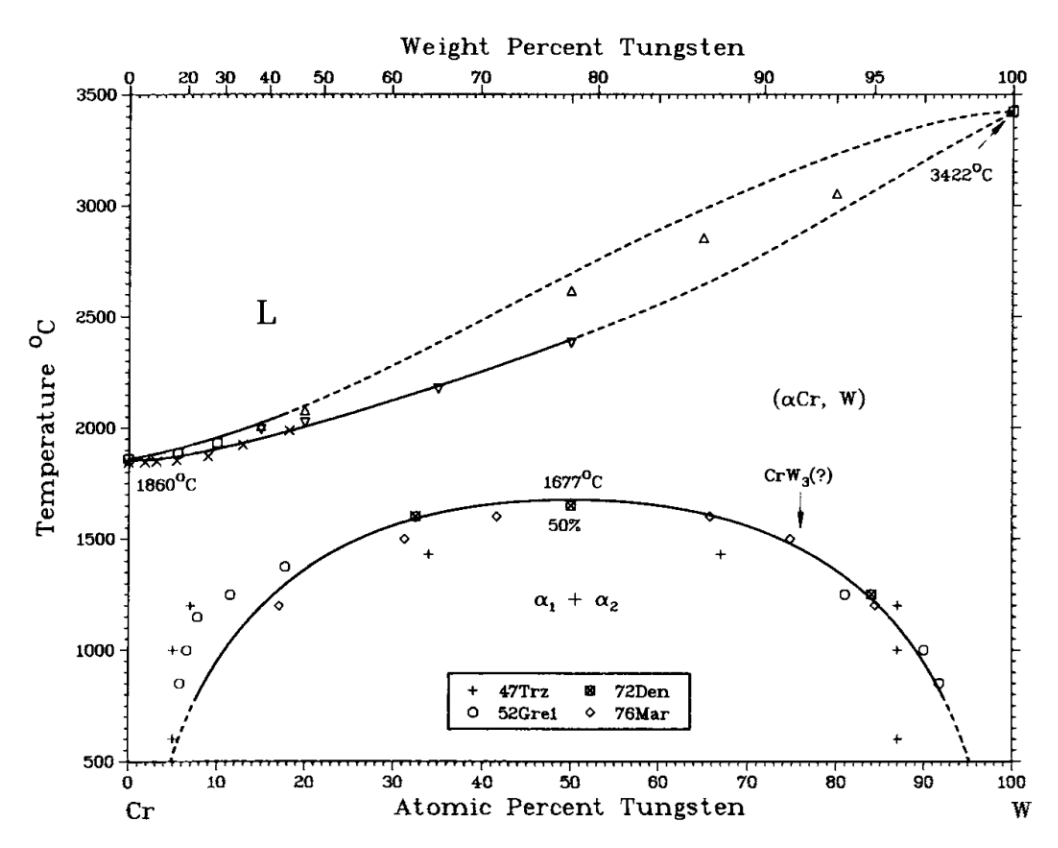


Figure 2.22: Phase diagram of the tungsten-chromium system from experimental data. The region of spinodal decomposition is shown in the lower portion of the phase diagram (the $\alpha_1 + \alpha_2$ region), whereas the (α Cr, W) denotes the homogeneous solid solution at high temperature [177].

and the effect of spinodal decomposition. Some of these properties interrelate, such as the presence of yttrium affecting the spinodal decomposition rate or the alloy's decomposition affecting the grain sizes. On an atomistic level, the behaviour of tungsten-based SMART alloys is complex. However, by reviewing the research conducted over the last five to ten years, a so-far incomplete picture of the oxidation mechanism in these alloys can be assembled.

Some key differences between the oxidation of W-Cr and W-Cr-Y can be seen in Figure 2.23. In the absence of the active element, the passivating layer of Cr_2O_3 , which forms at the surface of the alloy, is less dense, enabling the diffusion of oxygen into the bulk alloy. Figure 2.23a shows the various microstructural changes that form under these conditions, ranging from the internal oxidation of chromium to

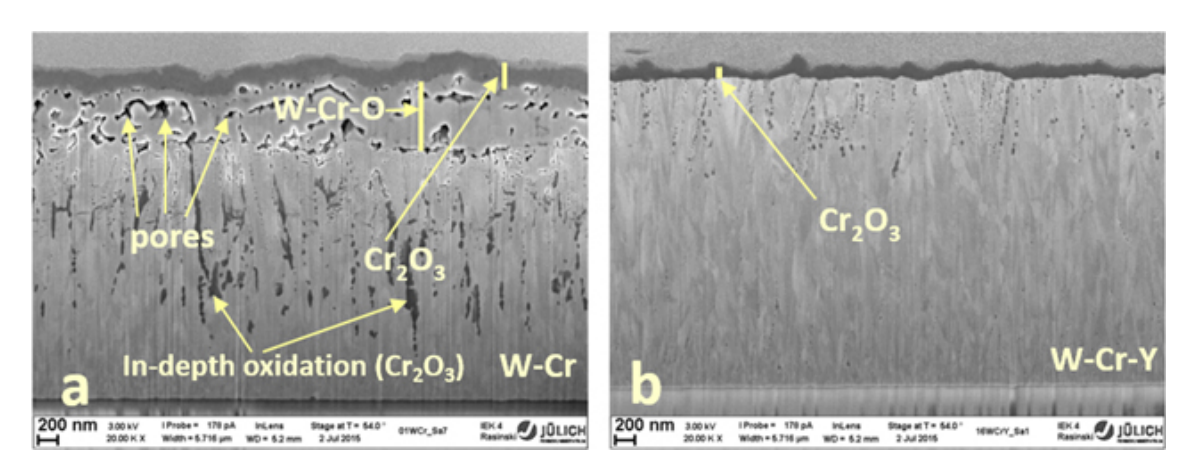


Figure 2.23: Cross-section of W-Cr and W-11.4Cr-0.6Y alloys after 10 minutes of oxidation in 80% Ar, 20% O₂ atmosphere at 1273 K [166].

the formation of mixed tungsten-chromium oxides close to the surface and the subsequent formation of pores. These microstructural defects are detrimental to the alloy, as they can lead to catastrophic failure of the protective oxide scale and embrittlement of the alloy itself. On the other hand, the inclusion of a small amount of yttrium ($e.g.~0.6~\rm wt\%$) leads to a dense, protective layer of $\rm Cr_2O_3$ at the surface of the alloy, as shown in Figure 2.23b.

In 2020, Klein et al. reported the effect of yttrium content, oxygen impurities and transmutation elements on the oxidation behaviour of W-11.4W-xY - i.e., 11.4 wt% Cr and a varied concentration of Y [183]. The cross-sectional images from the paper are shown in Figure 2.24, showing the change in microstructure with increasing yttrium concentration. The greatest oxidation resistance was observed in W-11.4W-0.6Y (0.6 wt% Y), which, as can be seen in Figure 2.24b, contains the largest number of fine, dispersed Y-containing nanoparticles. Further investigation then compared the oxidation of this composition at different oxygen impurity levels, revealing that the lower the oxygen impurity concentration before oxidation, the greater the oxidation resistance of W-11.4W-0.6Y. The results of oxidation experiments by Klein et al. are shown in Figure 2.25 and 2.26.

In addition, they presented the X-ray diffraction measurements of the W-

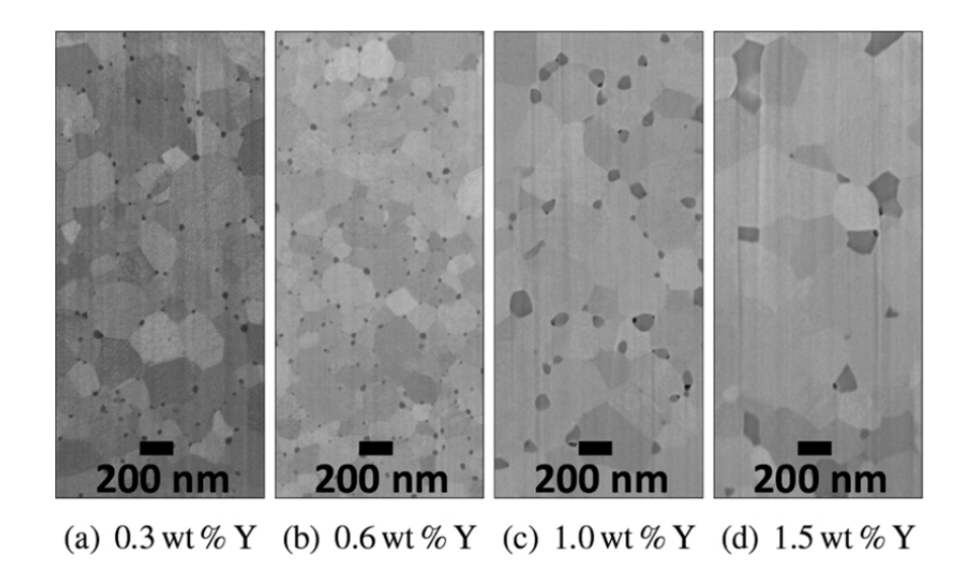


Figure 2.24: Microstructure cross-sections of W-11.4Cr-xY at various Y concentrations. The small, dark spots are identified as a Y-containing phase [183]

11.4Cr-xY alloys, as shown in Figure 2.27. For all compositions, they observed diffraction peaks corresponding to the tungsten-chromium oxide phase Cr₂WO₆, which exhibits a structure similar to that of WO₂. This is likely to be the mixed oxide phase observed in Figure 2.23a, as it is not observed in the W-Cr-Y with optimal oxidation resistance. However, for W-11.4Cr-0.6Y, the diffraction peaks were almost indistinguishable, suggesting that, at this composition, the formation of the mixed oxide phase was almost fully suppressed.

The experiments by Chen et al., discussed briefly in Section 2.5.4, showed spinodal decomposition's effect on the passivating ability of W-Cr-Y. They identified two stages over the course of 20 hours: an initial stage (3 hours) of internal oxidation during which the Cr_2O_3 layer grows at a slower rate than the internal oxides. By their analysis of the cross-sections of the alloy, they attribute this to the initial depletion of Cr-poor grains close to the surface and the subsequent oxidation of the remaining tungsten. During the second stage, the Cr-rich regions of the inner oxide layer contribute to the formation of the Cr_2O_3 scale as oxygen slowly diffuses into the bulk. This theory implies that the grains closest to the surface (within a few

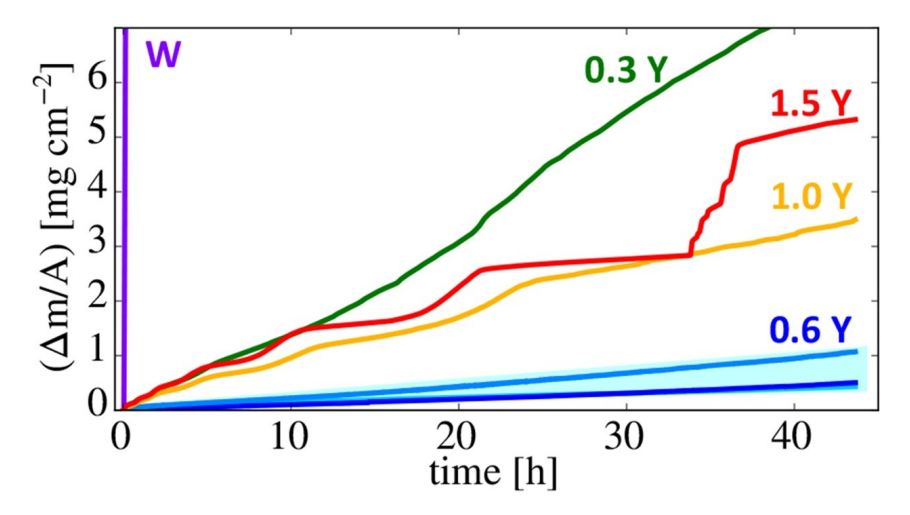


Figure 2.25: Mass change of W-11.4Cr-xY at various concentrations of Y [183].

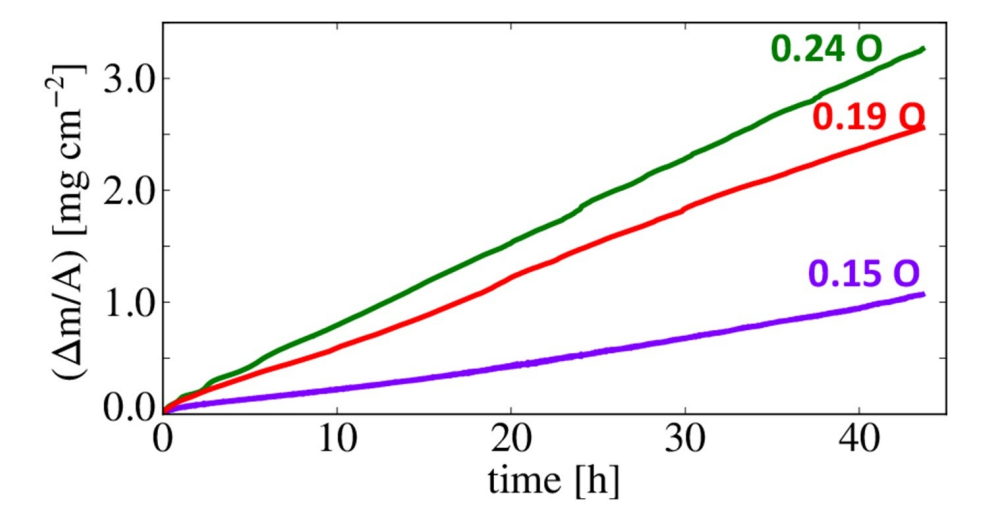


Figure 2.26: Mass change of W-11.4Cr-0.6Y at various concentrations of O [183].

 μ m) form a so-called 'sacrificial layer' where oxidation of tungsten is an inevitable but necessary part of the passivating process.

Another study by Chen et al. investigated the effect of doping tungstenchromium alloy with Y_2O_3 , rather than elemental yttrium [184]. They report that substituting Y with Y_2O_3 reduces the linear oxidation rate of the alloy by approximately half, though the oxidised samples of W-Cr-Y and W-Cr-Y₂O₃ had noticeably different microstructures. In W-Cr-Y₂O₃, yttrium-containing nanoparticles were more uniformly dispersed across the Cr_2O_3 scale. Their EDX

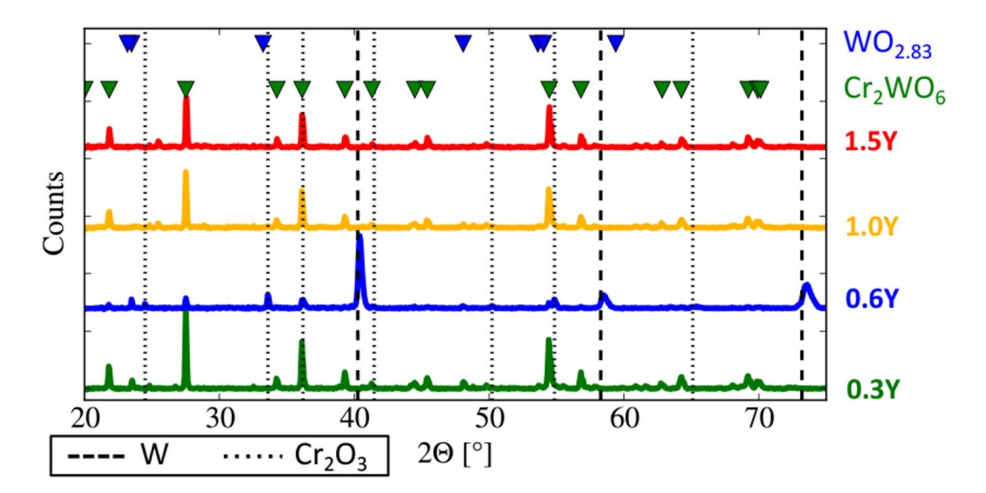


Figure 2.27: X-ray diffraction patterns of W-11.4Cr-xY at various concentrations of Y [183].

analysis identified these particles as YCrO₃, and they suggested that chromium began to act as the active element, scavenging impurity oxygen from the bulk alloy in the absence of pure yttrium.

Even from Figure 2.26, it is clear that oxygen is an impurity which must be avoided if optimal oxidation resistance is to be obtained. However, whilst this is possible in laboratory conditions, it is likely unavoidable when scaling up to the industrial production of tungsten-based SMART alloys [185, 186, 166]. Even with the most stringent vacuum controls, 'pure' metal powders of tungsten, chromium, and especially yttrium are bound to contain impurities, including oxygen. Klein et al. proposed that oxygen impurities not bound to yttrium are likely to be found at grain boundaries and vacancies, where they are likely to encounter chromium. Therefore, the higher the oxygen content in the alloy, the higher the activation energy of diffusion of chromium and the lower the flux of chromium ions to the surface.

2.6 Research Aims

Owing to their significant benefits over pure tungsten, tungsten-based SMART alloys - in particular, those containing chromium as the alloying element and yttrium as the active element - are seen as an attractive, next-generation material for fusion first walls. In recent years, the development of tungsten-based SMART alloys has shifted from the laboratory scale to the industrial scale [187]. However, its technology readiness level is still too low for widescale implementation in most upcoming fusion devices, such as STEP. Many unknowns must be addressed before they can be confidently utilised in these projects.

Utilising the atomistic simulation techniques discussed in Section 3, this thesis aims to address the underlying mechanisms behind the oxidation behaviour observed in both tungsten and tungsten-based SMART alloys. In Chapter 5, the relationship between the various tungsten oxide phases will be explored at the density functional theory level of theory, followed by an investigation of oxygen diffusion through the various experimentally confirmed oxide phases. Then, in Chapters 6 and 7, the roles of yttrium and chromium in tungsten-based SMART alloys will be investigated from first principles. In this way, this research aims to provide a foundation for understanding the phenomenon observed in oxidation experiments on self-passivating tungsten alloys.

Chapter 3

Theory

In recent years, atomistic simulations have become progressively more complex due to the constant improvements in computer hardware and software. What was previously thought impossible or impractical ten years ago is becoming more achievable in today's world. Similarly, the need for simulations has become increasingly apparent, especially where nuclear fusion is concerned. As has been described in the previous chapter, the environments to which plasma-facing materials are subjected in a nuclear fusion reactor are among the most extreme conditions possible. Computational experiments allow us to bridge the gap between what we do and do not know without needing a complete, working reactor or a specially-designed facility that emulates one.

Atomistic simulations are distinguished from other types of simulations due to the fact that they consider the motion of individual atoms, as the name suggests. This differentiates them from higher-level models, e.g., coarse-grained modelling, meso- and nanoscale simulations, and simulations on the continuum level, such as finite element analysis. Atomistic simulations are broadly divided into two categories depending on the way in which the interatomic forces are calculated.

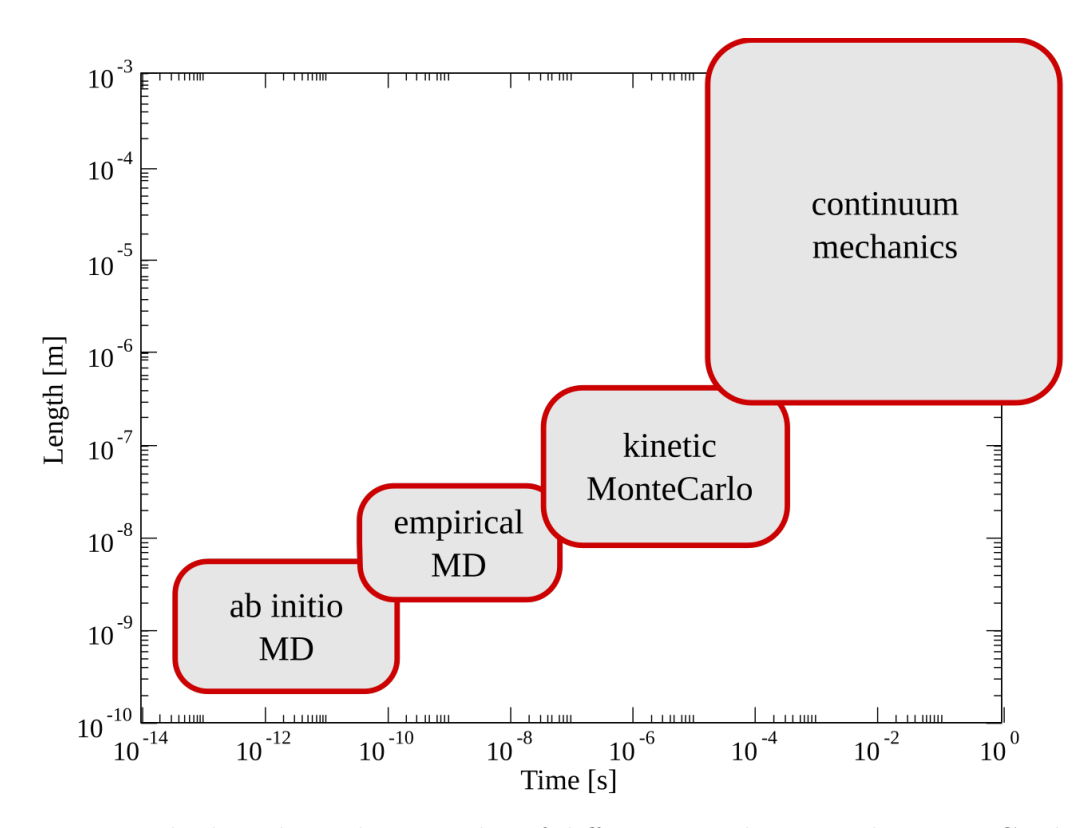


Figure 3.1: The length- and timescales of different simulation techniques. Credit to David Holec, under CC BY-SA 4.0.

The first category is that of quantum mechanical simulations, which attempt to solve the many-bodied Schrödinger equation to obtain information on the electronic structure of the system. There is a substantial computational expense associated with quantum mechanical simulations, and, therefore, approximations are typically required to make them more tractable. The second involves the use of Newtonian (or 'classical') mechanics to calculate the forces between atoms based on an empirically derived interatomic potential. Although these simulations do not yield information about the system's electronic structure, they are useful for predicting large systems' properties. Their much lower computational cost per atom (compared to quantum mechanical calculations) makes it possible to perform simulations on systems of the order of hundreds of billions of atoms.

In this thesis, both quantum mechanical and classical simulations have been employed. Density functional theory (Section 3.2.2) simulations have been conducted

using the Vienna Ab-initio Simulation Package (VASP) [188, 189, 190, 191]. On the other hand, classical molecular dynamics (Section 3.1.2) has been conducted using the Large-scale Atomic/Molecular Massively Parallel Simulator (LAMMPS) [192]. This chapter will discuss the principles and technicalities of the techniques used.

3.1 Procedures in Atomistic Simulations

3.1.1 Energy Minimisation

In both classical and quantum mechanical simulations, the input geometry of the system may not necessarily be the lowest energy configuration. In some cases, this may arise due to the nature of the source data; for solids, the input geometry may be derived from X-ray or neutron diffraction sources or generated computationally if the symmetry of the crystal is known. The use of empirical pair potentials or density functional theory does not necessarily yield the true input geometry, and both methods come with their own assumptions and approximations, discussed below, which introduce systematic error. Providing the parametrisation of a calculation is sufficiently accurate, the lowest energy configuration can be found via the energy minimisation process. This involves the relaxation of the system's atomic coordinates to find the local minimum in the potential energy surface.

During any energy minimisation procedure, the ions are moved in a direction which attempts to minimise the system's total energy according to the forces acting upon them. At each step, the interaction between ions is recalculated. The recalculation of these forces in classical molecular dynamics is much more trivial than in density functional theory; in the latter, the electronic ground state of the new ionic configuration must be calculated. Broadly speaking, the energy minimisation procedure may also be carried out in one of two ways. The first is

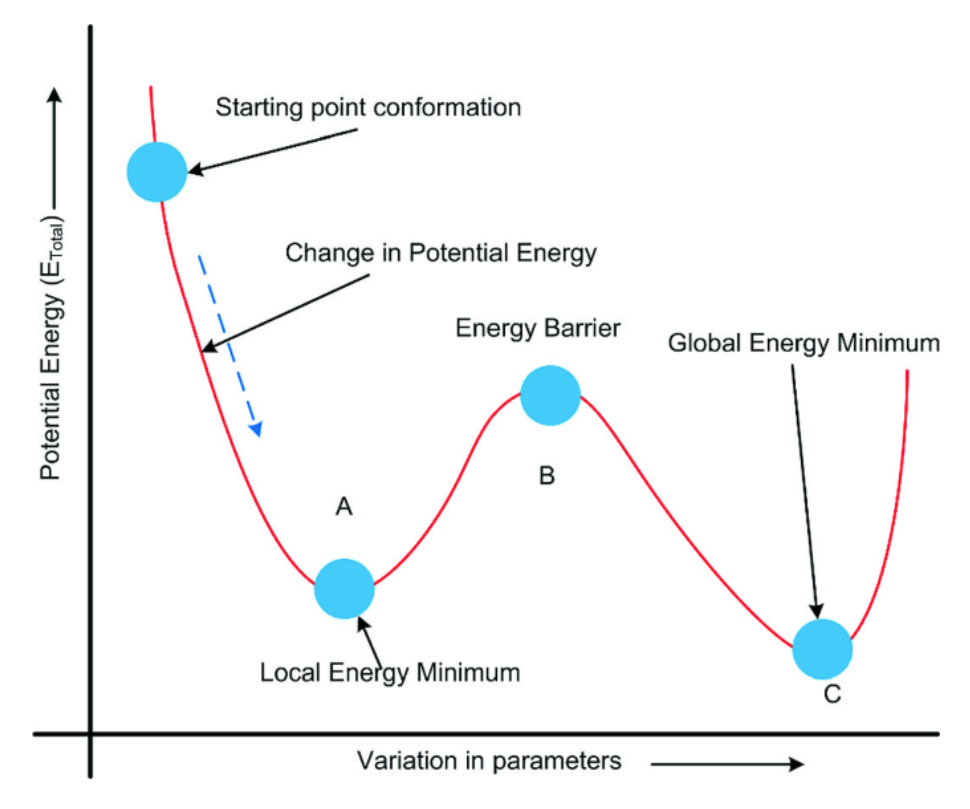


Figure 3.2: Simplified example of a potential energy surface and a representation of the energy minimisation process [193].

to maintain a constant cell volume, which only considers the strain on individual ions, whilst the second is to maintain a constant cell pressure, wherein the lattice parameters of the cell are allowed to relax to minimise the strain. These are sometimes referred to as the NVT and NPT ensembles, respectively. Whilst the latter is more computationally expensive, it is standard practice to perform energy minimisations at constant pressure, and any energy minimisations carried out in this thesis have been performed thusly unless specified otherwise. Several algorithms exist for performing energy minimisations [194]. In this thesis, the main algorithm used is the conjugate gradient (CG) algorithm, described below.

The exact implementation of the conjugate gradient algorithm depends on the software being used. The algorithm generally begins by determining the system's potential energy in its initial configuration and, therefore, the forces acting upon each ion. Therefore, the search direction, p_0 , is set to the negative of the potential

energy gradient, *i.e.*, $p_0 = -\nabla V$. A step size, α_k , is determined *via* a line search algorithm (or similar), and the atomic positions are updated accordingly using the equation,

$$\mathbf{x}_{k+1} = \mathbf{x}_k + \alpha_k p_k \tag{3.1}$$

where \mathbf{x} is the three-dimensional coordinates of a given ion, and k is the current step. After the ions have been moved, the new potential energy is calculated, ∇E_{k+1} , followed by a new search direction, p_{k+1} .

As implemented in LAMMPS, the new search direction is found using the Polak-Ribière method. In this variation of the conjugate gradient algorithm, the value β_k measures the difference between the gradients of the potential energy in consecutive steps, and is given by,

$$\beta_k = \frac{(\nabla E_k - \nabla E_{k+1})^{\mathrm{T}} \nabla E_k}{\nabla E_{k+1}^{\mathrm{T}} \nabla E_k}$$
(3.2)

This value is then applied to calculate the new direction,

$$p_{k+1} = -\nabla E_{k+1} + \beta_k p_k. \tag{3.3}$$

In VASP, the predictor-corrector variant of the conjugate gradient algorithm is employed. This variant efficiently explores the configuration space by alternating between trial (or predictor) steps and corrector steps. In the trial steps, the search direction, p_k , is updated based on information from the previous iteration, *i.e.*, the trial step size is determined in the manner described above and applied using Equation 3.1. In the corrector steps, the corrector search direction, q_k , is further

refined based on the actual gradient of the potential energy, i.e., $q_k = -\nabla E_{k+1}$. A corrector step size, $\hat{\alpha}$, is calculated *via* a line search algorithm and used to correct the ionic positions,

$$\mathbf{x}_{k+1} = \mathbf{x}_k + \hat{\alpha}_k q_k. \tag{3.4}$$

Both of these variants achieve the same goals. By considering either the residual of the gradient in successive steps (as in the Polak-Ribière variant) or by correcting the search direction (as in the predictor-corrector variant), the minimisation is protected from rapid variations in the potential energy along the search path, which might otherwise lead the minimisation into unphysical configurations.

3.1.2 Molecular Dynamics

Molecular dynamics (MD) involves the stepwise solution of Newton's equations of motion, which is not particularly challenging in isolation. However, solving them efficiently for systems containing thousands, millions, or even billions of atoms remains an active area of research. The most widely used class of algorithms for this purpose is based on the Verlet algorithm, which will be discussed below.

At the beginning of a molecular dynamics simulation, each atom is given an atomic position, \mathbf{r}_i and a velocity, \mathbf{v}_i . The magnitude of this velocity is, on average, related to the system's temperature. Each atom will also experience a total force, \mathbf{f}_i , due to its interactions with surrounding ions. This force can be calculated from quantum mechanics (Section 3.2) or from an empirical pair potential (Section 3.3), which gives rise to the distinction between *ab initio* molecular dynamics (AIMD) and classical molecular dynamics. Irrespective of the technique used to obtain the force, the acceleration of each atom can be determined, and the velocity of the atoms

after an appropriate timestep, τ , can be calculated,

$$v = v_0 + \int_0^\tau \frac{F}{m} dt \tag{3.5}$$

The velocity of each atom can also be described in terms of the rate of change of its position over time,

$$v = \frac{d}{dt}x\tag{3.6}$$

Therefore, the position of the atom after one timestep of length τ can be calculated by combining Equations 3.5 and 3.6:

$$x = x_0 + \int_0^{\tau} \frac{dx}{dt} dt = x_0 + \int_0^{\tau} \left(v_0 + \frac{F}{m} \tau \right) = x_0 + u\tau + \frac{1}{2} \frac{F}{m} \tau^2$$
 (3.7)

However, the force acting upon each atom is related to its position relative to its neighbours by Equation 3.49. This is overcome in two ways. Firstly, timesteps in molecular dynamics are typically so small that the change in the potential between t = 0 and $t = \tau$ is as small as possible whilst allowing simulations to be performed on relevant timescales. As such, timesteps are typically on the order of femtoseconds to picoseconds (10^{-15} to 10^{-12} s). Secondly, further terms can be introduced to Equation 3.7 to incorporate the change in force as a function of time, *i.e.*,

$$x = x_0 + u\tau + \frac{1}{2}\frac{F}{m}\tau^2 + \frac{\ddot{x}}{m}\tau^3 + \mathcal{O}^{4,5,6..}$$
(3.8)

where \ddot{x} is the third derivative of the position ('jerk') and $\mathcal{O}^{4,5,6...}$ are terms including the fourth, fifth, sixth (etc.) derivatives. These higher-order terms provide greater

accuracy, but at higher computational cost. Therefore, they are not typically included.

These simple expressions for calculating v and x after a single timestep have the property of being reversible. The position of any atom at time $t + \tau$ can be found even if the timestep is negative. These can be written as,

$$x(t+\tau) = x(t) + u(t)\tau + \frac{1}{2}\frac{F(t)}{m}\tau^2 + \frac{x'''(t)}{m}\tau^3 + \dots$$
 (3.9)

$$x(t-\tau) = x(t) - u(t)\tau + \frac{1}{2}\frac{F(t)}{m}\tau^2 - \frac{x'''(t)}{m}\tau^3 + \dots$$
 (3.10)

which may be combined and rearranged to give the velocity-Verlet algorithm:

$$x(t+\tau) = 2x(t) - x(t-\tau) + \frac{F(t)}{m}\tau^{2}$$
(3.11)

In Equation 3.11, both the first- and third-order terms cancel each other out, removing the need to calculate them at each timestep. As a result, Verlet algorithms are referred to as being 'low order', which is desirable for two reasons: (1) calculating higher-order derivatives is more computationally expensive, and (2) it allows timesteps to be increased as much as possible without introducing the aforementioned error which arises from the change of potential over time.

3.1.3 Temperature Accelerated Dynamics

Owing to the short timesteps mentioned above, modern molecular dynamics codes have great difficulty in reaching simulation lengths greater than a few microseconds. Even then, billions of timesteps are required to reach the microsecond timescale. This can be overcome by considering the system as a sequence of infrequent events. In an infrequent event system, the stepwise evolution of the system can be described as a vibrational motion within a single minima on the potential energy surface and, occassionally, by transition of the system across a dividing surface to another local minima. These transitions are the so-called infrequent events, occurring on the order of many multiples of the vibrational period of the system in the energy minima. Several methods exist that can exploit this infrequent event system, including temperature accelerated dynamics [195], kinetic Monte Carlo [196], hyperdynamics [197] and parallel replica dynamics [198]. These methods are able to reach timescales many orders of magnitude greater than ordinary molecular dynamics, without sacrificing the atomistic detail in the process.

In temperature accelerated dynamics (TAD) [195], the overall objective is to accelerate the stepwise evolution of the system by exploring the available infrequent events at a high temperature to construct an accurate lower-temperature description of the transitions being made. Two key assumptions are made: firstly, that the system obeys harmonic transition state theory (hTST), which was discussed in Section 2.3.6. The second assumption is that an Arrhenius law defines the rate law for transitions out of an energy minimum, *i.e.*,

$$k_j = \nu_{0,j} \exp\left[-E_j/k_B T\right]$$
 (3.12)

where k_j is the transition rate along path j, E_j is the barrier height along the path, and $\nu_{0,j}$ is the temperature-independent pre-exponential factor.

The second assumption leads to a method by which observed transitions at a high temperature, T_{high} , can be projected onto a timeline at low temperature, T_{low} . In other words, a transition time, t_{low} , along path j at temperature T_{low} , can be

found if the high-temperature transition time, t_{high} , has be obtained:

$$t_{low,j} = t_{high,j} \frac{k_{high,j}}{k_{low,j}} = t_{high,j} \exp\left[E_j \left(\frac{1}{k_B T_{low}} - \frac{1}{k_B T_{high}}\right)\right]$$
(3.13)

Therefore, the low-temperature transition time can be found if the height of the barrier can be calculated. This relation reveals an important caveat of the technique: since transition rates increase with temperature, transitions with higher energy barriers, E_j , will increase faster. Therefore, events which occur fastest at T_{high} are not necessarily the most probable events at T_{low} .

3.1.3.1 The TAD Algorithm

Central to the TAD method is a special kind of molecular dynamics called basinconstrained molecular dynamics (BCMD). In BCMD, the system is placed in an initial state (i.e., minima on the potential energy surface) and allowed to evolve until it naturally escapes into a neighbouring state. The new state is typically detected by stopping the BCMD simulation after a given number of steps and performing an energy minimisation, then comparing the positions of the atoms to determine whether the system has either changed or relaxed back into its original state. If the system has transitioned into a new arrangement, the height of the energy barrier between the two states is calculated via the nudged elastic band method described in Section 3.1.5. Information regarding the new state is recorded, and the system is then reflected back into its initial state to begin the process again until the confidence criterion is met - that is, the point at which the probability that all possible pathways have been explored exceeds a given percentage. Once this is met, the transition rate at T_{high} is obtained using the Arrhenius relation shown in Equation 3.13. This is then extrapolated back to T_{low} as shown in Figure 3.3. When t_{low} has been calculated for all transitions, the transition with the lowest value of t_{low} is accepted. The system is

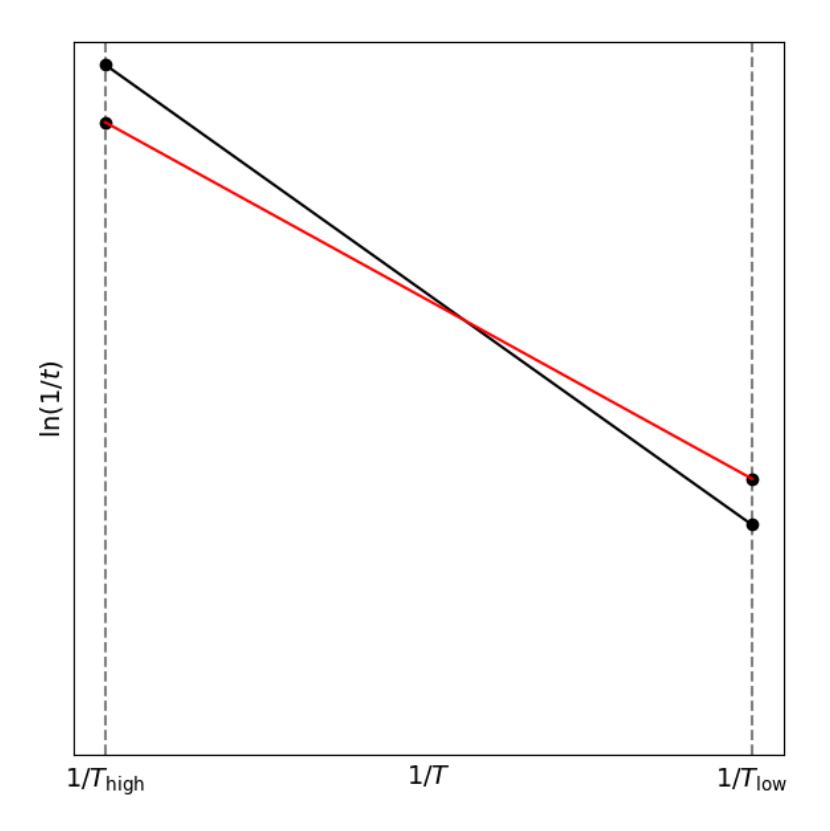


Figure 3.3: Example of the extrapolation of the transition time (t) from T_{high} back to T_{low} in a generic TAD procedure. Two possible transitions are shown with different transition times at T_{low} , with the fastest transition at the target temperature shown in red.

then set to the corresponding end state, and the BCMD loop described previously begins again.

Practically, the TAD algorithm introduces some limitations in terms of the system to which it can be applied. It cannot be used on systems with low migration barriers, such as those encountered in the study of soft matter or grain boundaries, as the algorithm will preferentially select these transitions. As a result, the acceleration of the system in real time, which is simply the sum of all selected values of t_{low} , is significantly reduced for these systems. However, TAD is particularly useful for studying systems with larger migration barriers (*i.e.*, systems of infrequent events), such as binary W-Cr alloys, as will be discussed in Chapter 8.

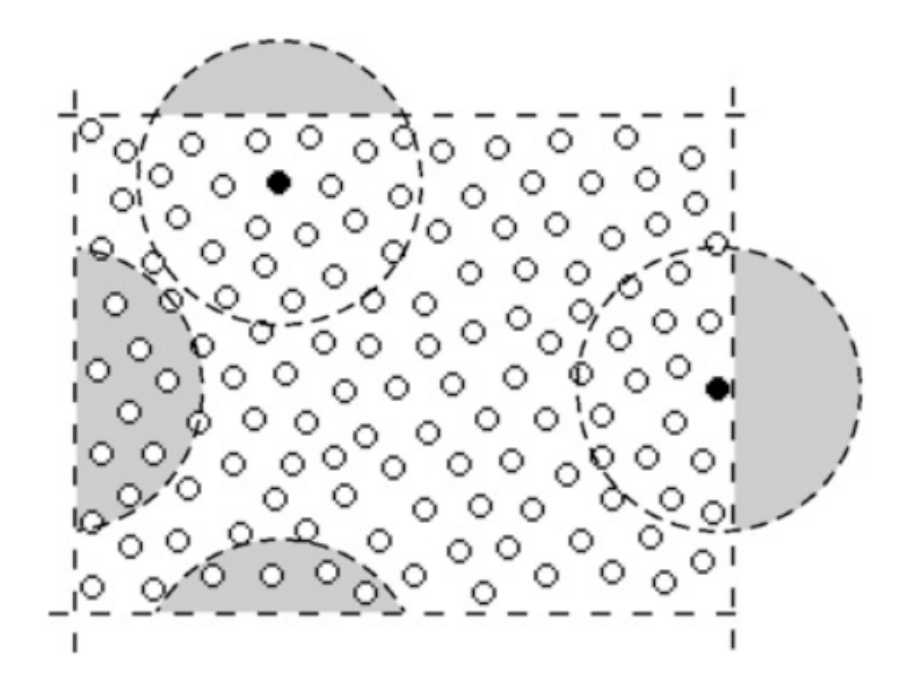


Figure 3.4: A simplified, two-dimensional representation of periodic boundary conditions. The dashed circles encompass the atoms interacting with the highlighted atoms (black), whereas the dashed lines represent the periodic boundary. [199].

3.1.4 Periodic Boundary Conditions

Crystalline solids typically exhibit grain sizes on the micrometre scale, many orders of magnitude greater than the distance between neighbouring atoms. It is computationally infeasible to perform simulations on this many atoms at the DFT and MD levels of theory due to the large number of degrees of freedom scaling with system size. However, it is not necessary to consider such large systems when calculating bulk properties, owing to the periodic nature of the crystal. As discussed in Section 2.3.1, the crystal structure on a mesoscopic scale can be reduced to just a small number of atoms that form a distinct, repeatable unit representing the system as a whole: the unit cell.

The results of simulations on a system's unit cell are transferable to the bulk system by utilising periodic boundary conditions. As shown in Figure 3.4, the implementation of this involves forcing particles near one boundary (*i.e.*, a face of

the unit cell) to interact with particles near the opposite boundary. Essentially, the unit is virtually (rather than physically) replicated in all three spatial dimensions. In classical molecular dynamics, the maximum distance at which a neighbouring atom is considered to be interacting with a given atom (the cut-off radius) is usually defined. This is typically done for computational expedience rather than accuracy; as long as a sufficient number of nearest-neighbour interactions has been included, the interaction of distant atoms can be neglected.

However, whilst this applies to perfect crystalline systems, periodic boundary conditions may introduce a self-interaction error in defect systems when a defect's periodic image interacts with itself. Therefore, the supercell approach is employed to reduce this self-interaction error. The number of unit cells along each axis defines a supercell. For example, a $2\times2\times2$ supercell is two unit cells in height, breadth and depth, for a total of 2^3 unit cells in the simulation. The supercell approach is also employed when performing simulations on grain boundaries and surfaces; it allows the interfaces between grains or between the bulk crystal and the vacuum to be isolated from their periodic images. Rigorous testing must be conducted for each system to ensure that the bulk properties of the solid are well converged with respect to supercell size.

3.1.5 Nudged Elastic Band Method

The nudged elastic band method (NEB) is a technique employed in modern atomistic simulation codes to find the minimum energy path between two states [200]. Both LAMMPS and VASP, used throughout this work, have their own implementations of the NEB method. This allows the computation of migration barriers for use in the study of diffusion. A typical NEB simulation begins with the energy minimisation of both the starting and ending points. A series of intermediate images generate an initial guess of the minimum energy path the system must traverse. These

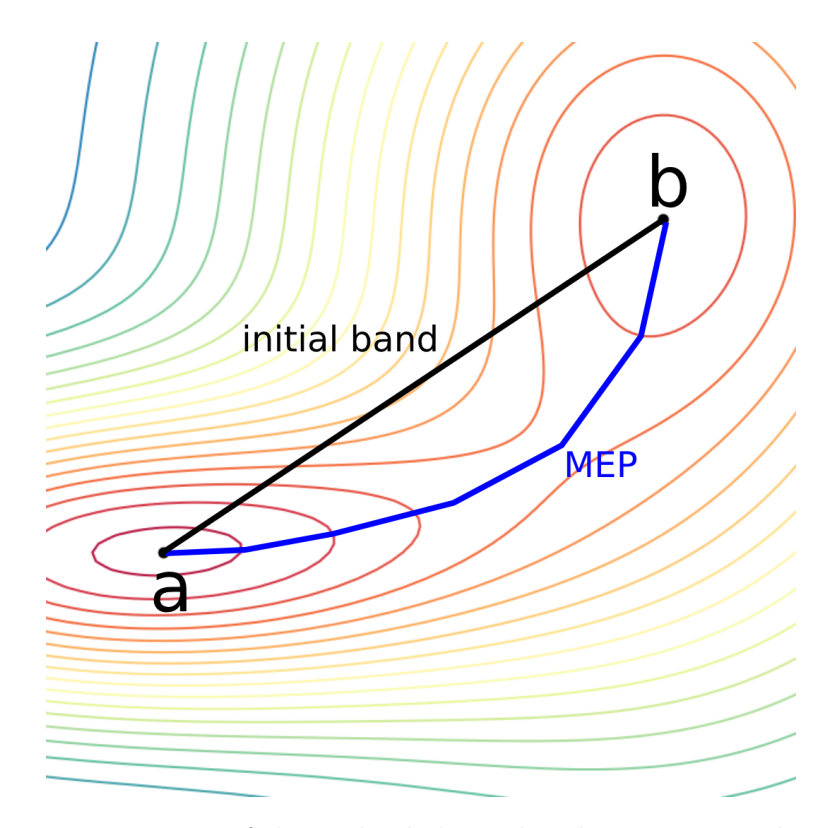


Figure 3.5: Representation of the nudged elastic band on a potential energy surface and the elucidation of the minimum energy path (MEP) from an initial band.

images are connected by virtual springs to form the eponymous 'elastic band'. All images, except for the fixed initial and final states, are then relaxed under forces decomposed into components perpendicular and parallel to the reaction path. The atomic forces drive the relaxation perpendicular to the path to find the minimum energy configuration, while virtual spring forces act only along the path to prevent the images from collapsing to the local minimum, thereby maintaining a reasonable distribution along the path. Importantly, the elastic band is constrained only to relax perpendicular to the minimum energy path, preventing the images from relaxing into the nearest local minima.

In the climbing image NEB variant (CI-NEB), the image with the highest energy - typically the transition state - is pushed towards the saddle point. Whilst this means that the images along the elastic band are no longer equidistant, the CI-NEB variant has been shown to provide better convergence over the non-climbing image

variant [201]. The determination of migration barriers in Chapters 5, 8 and 9 utilises the CI-NEB variant of this technique.

3.1.6 Special Quasirandom Structure (SQS) Approach

The special quasirandom structure (SQS) approach aims to construct a supercell which best reproduces the correlation functions (i.e., nearest-neighbour interactions) in a true random system, such as a mixed binary alloy. In practice, this involves generating a large number of randomised structures and calculating the error between their correlation functions and the ideal correlation functions (or 'objective function') of a random system, which can be predicted analytically. From combinatorics, the total number of configurations for a general system $A_aB_b...Z_z$ is,

no.configs =
$$\frac{N!}{\prod n_i!}$$
, (3.14)

where N is the total number of atoms, and $\prod n_i = a! \cdot b!...z!$. Therefore, the total number of configurations can be vast for even small values of N. Once symmetry is considered, the number of configurations may be greatly reduced, and, ultimately, checking each configuration's correlation function against the objective function is not computationally expensive in and of itself. As such, the SQS approach is utilised in Chapter 7 to generate representative structures for the mixed W-Cr system at different Cr concentrations using sqsgenerator [202]. In this case, 16 atom supercells were used, allowing for an exhaustive comparison of all configurations to find the SQS. The correlation functions were calculated up to the third coordination shell and were weighted by the reciprocal of the shell number, i.e., N^{-1} .

3.1.7 Calculation of ΔG_{mix} in Binary Alloys

The Gibbs energy of mixing, ΔG_{mix} , for a solid system determines the propensity of its components to spontaneously segregate (for $\Delta G_{mix} > 0$) or mix (for $\Delta G_{mix} < 0$), and is given by the Gibbs equation,

$$\Delta G_{mix} = \Delta H_{mix} - T\Delta S_{mix} \tag{3.15}$$

where ΔH_{mix} and ΔS_{mix} are the enthalpy of mixing and entropy of mixing, respectively.

The enthalpy of mixing for a solid binary system of N atoms consisting of element a and b, i.e., $a_{n_a}b_{n_b}$, is given by,

$$\Delta H_{mix} = E_{tot} - (n_a \mu_a + n_b \mu_b) \tag{3.16}$$

where n_i and μ_i are the number of atoms of type i and their corresponding chemical potential, and E_{tot} is the total energy of the system in its mixed state. The total energy and the chemical potentials of the constituent atoms can be obtained from simple MD and DFT simulations. However, for systems where there are multiple atoms of type b, assuming the host lattice is of type a, special care must be taken in finding an appropriate configuration of the system. In this thesis, the Gibbs energy of mixing of the W-Cr binary alloy at different concentrations of Cr has been predicted using the Special Quasirandom Structure (SQS) approach to identify a representative configuration of the system at each concentration, which was described in Section 3.1.6.

The entropy of mixing has been estimated to be equal to the configurational

entropy, which is given by,

$$S_{con} = -k_b N \left(X_a \ln(X_a) + X_b \ln(X_b) \right) \qquad ; \qquad X_i = \frac{n_i}{N}$$
 (3.17)

where k_b is the Boltzmann constant and X_i is the molar fraction of element i.

Importantly, the temperature at which a binary system moves from segregation to mixing, or vice versa, can be found by solving Equation 3.15 for temperature,

$$T^* = \frac{\Delta H_{mix}}{\Delta S_{mix}}. (3.18)$$

3.2 Quantum Mechanics

3.2.1 Principles of Quantum Mechanics

The exact ground state energy of a system of ions and electrons can be computed by finding the solution to the time-independent Schrödinger equation, which takes the form,

$$\hat{H}\Psi(\mathbf{r}_1, \mathbf{r}_2...\mathbf{r}_N) = E\Psi(\mathbf{r}_1, \mathbf{r}_2...\mathbf{r}_N), \tag{3.19}$$

where \hat{H} is the Hamiltonian operator, $\Psi(\mathbf{r}_1, \mathbf{r}_2...\mathbf{r}_N)$ is the many-body wavefunction which describes the system, and E is the corresponding eigenvalue which represents the energy of the system. The Born-Oppenheimer approximation assumes that the ions are static, being orders of magnitude heavier than the electrons, and that,

therefore, the electrons move instantaneously in response to any movement of the ions. As a result, it is possible to separate the wavefunction of the system into a nuclear component and an electronic component, and to calculate the ground state energy of the system by considering only the electronic part of the Hamiltonian operator.

Taking this approximation into account, the Hamiltonian operator, \hat{H} , can be written explicitly as,

$$\hat{H} = T_e + V_{ne} + V_{ee} = -\frac{1}{2} \sum_{i=1}^{N} \nabla_i^2 - \sum_{a=1}^{N} \frac{Z_a}{|\mathbf{r}_i - \mathbf{R}_a|} + \sum_{i < j}^{N} \frac{1}{|\mathbf{r}_i - \mathbf{r}_j|}$$
(3.20)

where T_e is the kinetic energy operator of the electron; V_{ne} and V_{ee} are the nucleuselectron and electron-electron potential operators, respectively; Z_a is the Coulombic charge on atom a; and ∇_i^2 is the Laplace operator of electron i. Equation 3.20 is given in atomic units. Furthermore, relativistic effects are not considered, and the spin coordinates have been omitted.

To find the ground state energy of the system, E_0 , Equation 3.19 is solved under the constraint that the wavefunction is anti-symmetric, *i.e.*, Ψ changes sign if the coordinates of any two electrons are swapped. In this way, the electrons are treated as fermions and obey the Pauli exclusion principle. For a given wavefunction, the energy of the system is the expectation value of \hat{H} :

$$E[\Psi] = \int \Psi^* \hat{H} \Psi d\mathbf{r} \equiv \left\langle \Psi | \hat{H} | \Psi \right\rangle \tag{3.21}$$

where $E[\Psi]$ denotes that the energy is a functional of the wavefunction. Therefore, the ground state energy, E_0 , can be found by finding the corresponding wavefunction, Ψ_0 . As per the variational theorem, the energy of the system will be greater than the ground state energy unless $\Psi = \Psi_0$.

One of the simplest ways of finding the many-body wavefunction of a system is *via* the Hartree-Fock approximation, also known as the self-consistent field method. In this method, the wavefunction is represented by a Slater determinant, which guarantees the anti-symmetric property of the wavefunction and the system's compliance with the Pauli exclusion principle. The Slater determinant takes the form,

$$\Psi_{HF} = \frac{1}{\sqrt{N!}} \begin{vmatrix} \phi_1(\mathbf{r}_1) & \phi_1(\mathbf{r}_2) & \cdots & \phi_1(\mathbf{r}_N) \\ \phi_2(\mathbf{r}_1) & \phi_2(\mathbf{r}_2) & \cdots & \phi_2(\mathbf{r}_N) \\ \vdots & \vdots & & \vdots \\ \phi_N(\mathbf{r}_1) & \phi_N(\mathbf{r}_2) & \cdots & \phi_N(\mathbf{r}_N) \end{vmatrix}$$
(3.22)

By substituting Ψ_{HF} into Equation 3.20, the expression for the Hartree-Fock energy becomes,

$$E_{HF} = \int \phi_i^*(\mathbf{r}) \left(\hat{T} + \hat{V}_{ne} \right) \phi_i(\mathbf{r}) d\mathbf{r}$$

$$+ \frac{1}{2} \sum_{i < j}^{N} \int \frac{\phi_i^*(\mathbf{r}_1) \phi_i(\mathbf{r}_1) \phi_j^*(\mathbf{r}_2) \phi_j(\mathbf{r}_2)}{|\mathbf{r}_i - \mathbf{r}_j|} d\mathbf{r}_1 d\mathbf{r}_2$$

$$- \frac{1}{2} \sum_{i < j}^{N} \int \frac{\phi_i^*(\mathbf{r}_1) \phi_j(\mathbf{r}_1) \phi_i^*(\mathbf{r}_2) \phi_j(\mathbf{r}_2)}{|\mathbf{r}_i - \mathbf{r}_j|} d\mathbf{r}_1 d\mathbf{r}_2$$
(3.23)

in which the electron-electron potential operator, \hat{V}_{ee} , can be written explicitly as an expression with two terms. The first of these terms (second in Equation 3.23) describes the electrostatic potential, which includes an unphysical self-interaction when i = j. This self-interaction is corrected by the final term of Equation 3.23,

which is known as the exchange term. Finally, be applying the constraint that the orbitals, ϕ_i , of the Slater determinant are orthonormal to each other - *i.e.*, there is no interaction between electrons of one orbital and another - the Hartree-Fock equations arise, which take the form,

$$\left[-\frac{1}{2}\nabla^2 + \nu_{ext} + \int \frac{\rho(\mathbf{r})'}{\mathbf{r} - \mathbf{r}'} d\mathbf{r}' \right] \phi_i(\mathbf{r}) + \int \nu_X(\mathbf{r}, \mathbf{r}') \phi_i(\mathbf{r}') d\mathbf{r}' = \epsilon_i \phi_i(\mathbf{r})$$
(3.24)

in which the non-local exchange potential, ν_X , is explicitly,

$$\int \nu_X(\mathbf{r}, \mathbf{r}')\phi_i(\mathbf{r}')d\mathbf{r}' = -\sum_j^N \int \frac{\phi_j(\mathbf{r})\phi_j^*(\mathbf{r}')}{|\mathbf{r} - \mathbf{r}'|}\phi_i(\mathbf{r}')d\mathbf{r}'$$
(3.25)

The major limitation of the Hartree-Fock approach is that correlation is not considered; the electrons are considered to interact with a mean field potential which includes their Coulombic interactions and the non-local exchange potential. In reality, the interactions between electrons depends upon their positions relative to one another.

3.2.2 Density Functional Theory

Density functional theory is an alternative method which aims to address the effect of electron correlation in Hartree-Fock theory. It is based on two theorems proven by Hohenberg and Kohn in 1964 [203]:

1. The external potential, $\nu(\mathbf{r})$, is (to within a constant) a unique functional of the electron density, $\rho(\mathbf{r})$.

2. The electron density that minimises the energy of the overall functional is the true electron density corresponding to the full solutions of the Schrödinger equation.

In essence, density functional theory redefines the problem in terms of the total electron density, $\rho(\mathbf{r})$, rather than the many-body wavefunction of the system, Ψ . From the first theorem, it follows that electron density determines the Hamiltonian operator and, consequently, the wavefunction of the system may be determined from the Hamiltonian operator. The second theorem follows naturally as an adaptation of the variational principle (Equation 3.21). That is, for a trial electron density, ρ_t , the energy of the system is,

$$E[\rho_t] = \left\langle \Psi_t | \hat{H} | \Psi_t \right\rangle \ge E_0 \tag{3.26}$$

and, therefore,

$$\delta \left[E[\rho] - \mu \left(\int \rho(\mathbf{r}) d\mathbf{r} - N \right) \right] = 0$$
 (3.27)

where μ is the electronic chemical potential and N is the number of electrons. Equation 3.27 implies that there is some universal functional, $E[\rho]$, independent of the actual system of interest, which can be applied to obtain the exact ground state density and energy of any system.

Following on from Equation 3.20, the energy functional can be written in terms of the kinetic energy, $\hat{T}[\rho]$, the potential operators, $\hat{V}_{ne}[\rho]$ and the electron density, \hat{V}_{ee} , i.e.,

$$E[\rho] = \hat{T}[\rho] + \hat{V}_{ne}[\rho] + \hat{V}_{ee}[\rho]$$
 (3.28)

in which the interaction with the external potential, \hat{V}_{ne} , is,

$$\hat{V}_{ne}[\rho] = \int \hat{V}_{ne}\rho(\mathbf{r})d\mathbf{r}$$
(3.29)

However, the kinetic energy and electron-electron terms are unknown. Kohn and Sham proposed that the system can be considered as one consisting of N non-interacting electrons, described by a determinant wavefunction of N so-called Kohn-Sham orbitals, ϕ_i . In this system, the kinetic energy of the Kohn-Sham orbitals is known:

$$\hat{T}_s = -\frac{1}{2} \sum_{i}^{N} \left\langle \phi_i | \nabla^2 | \phi_i \right\rangle \tag{3.30}$$

Furthermore, the electron density of the system is given by the equation,

$$\rho(\mathbf{r}) = \sum_{i}^{N} |\phi_i|^2 \tag{3.31}$$

Using this, the Coulombic interactions between electrons can be expressed in terms of the electron density. This takes a form similar to the second term in 3.24, *i.e.* the Hartree term,

$$V_H[\rho] = +\frac{1}{2} \int \frac{\rho(\mathbf{r}_1)\rho(\mathbf{r}_2)}{|\mathbf{r}_1 - \mathbf{r}_2|} d\mathbf{r}_1 d\mathbf{r}_2$$
(3.32)

Therefore, the functional described in Equation 3.28 can be re-written as,

$$E[\rho] = \hat{T}_s[\rho] + \hat{V}_{ne}[\rho] + \hat{V}_H[\rho] + E_{XC}[\rho]$$
(3.33)

where $E_{XC}[\rho]$ is the so-called exchange-correlation functional:

$$E_{XC}[\rho] = (\hat{T}[\rho] - \hat{T}_s[\rho]) + (\hat{V}_{ee}[\rho] - \hat{V}_H[\rho])$$
(3.34)

As shown in Equation 3.34, the exchange-correlation functional is simply the total error obtained by treating the system as a set of non-interacting particles and by treating the electron-electron interaction classically. Combining the equations above with Equation 3.23, the Kohn-Sham orbitals therefore satisfy the equation,

$$\left[-\frac{1}{2} \nabla^2 + \nu_{ne}(\mathbf{r}) + \int \frac{\rho(\mathbf{r}')}{|\mathbf{r} - \mathbf{r}'|} d\mathbf{r}' + \nu_{XC}(\mathbf{r}) \right] \phi_i(\mathbf{r}) = \epsilon_i \phi_i(\mathbf{r})$$
(3.35)

where ν_{XC} is a potential based on the the functional derivative of the exchangecorrelation energy with respect to the density itself:

$$\nu_{XC}(\mathbf{r}) = \frac{\delta E_{XC}[\rho]}{\delta \rho} \tag{3.36}$$

The Kohn-Sham equations (Equation 3.35) can only be solved exactly if the exact form of the exchange-correlation potential is known, however, there is currently no way of knowing this exact form. Only accurate approximations of the exchange-correlation can be obtained empirically. On the other hand, these approximations are independent of the system of interest. A good approximation that yields accurate ground state properties for several systems can therefore be used in wider studies in

an unbiased and predictive way. The search for increasingly accurate forms of the exchange-correlation potential is central to the development of density functional theory [204].

3.2.3 Exchange-Correlation Potentials

3.2.3.1 Local Density Approximation

Kohn and Sham proposed the earliest and simplest form of the exchange-correlation potential, though its roots can be traced back to the Thomas-Fermi model of a homogeneous electron gas. In the Local Density Approximation (LDA), the electron density is assumed to be uniform in all directions for an infinitesimally small volume, $n(\mathbf{r})d(\mathbf{r})$. The exchange-correlation potential takes the form,

$$E_{XC}^{LDA} \approx \int \rho(\mathbf{r}) \epsilon_{XC}(\rho(\mathbf{r})) d\mathbf{r}$$
 (3.37)

where ϵ_{XC} is the exchange-correlation energy of each particle, *i.e.* the local density. By expressing the exchange-correlation potential in terms of the local density, it can be separated into two terms:

$$\epsilon_{XC} = \epsilon_X + \epsilon_C \tag{3.38}$$

where ϵ_X and ϵ_C are the exchange and correlation energies, respectively. The latter has been obtained empirically from quantum Monte-Carlo simulations, whilst the former can be written explicitly in the Dirac form,

$$\epsilon_X(\rho) = -\frac{3}{4} \left(\frac{3}{\pi}\right)^{1/3} \int \rho(\mathbf{r})^{4/3} d\mathbf{r}$$
 (3.39)

Despite the assumption that the electron density is homogeneous, the local density approximation yields reliably accurate properties for many materials, such as structure, elastic moduli, vibrational properties and phase stability. However, it is a poor approximation for the purpose of studying binding energies, reaction energies and migration barriers in most materials. Studies found that the accuracy of the local density approximation arises out of its ability to describe the exchange-correlation hole, as well as the fact that errors in the exchange energy and errors in the correlation energy cancel one another out. As such, the local density approximation is typically only used as a guideline in the atomistic study of materials.

3.2.3.2 Generalised Gradient Approximation

In order to calculate accurate properties and energies, the inhomogeneity of the electron density cannot be ignored. The generalised gradient approximation (GGA) extends the local density approximation by factoring in the density gradient, *i.e.*,

$$E_{XC}^{GGA} \approx \int \rho(\mathbf{r}) \epsilon_{XC}(\rho, \nabla \rho) d\mathbf{r}$$
 (3.40)

This form ensures that the exchange-correlation hole is properly described, as well as the inhomogeneities in the electron density. The result is much more accurate ground state energies and electronic structures compared to the local density approximation, and it is due to the generalised gradient approximation that density functional theory became a widely-utilised computational technique in the 1990's.

As density functional theory developed further, more and more exchange-

correlations based on the GGA approach were developed, each with different parametrisations. Perhaps the best-known GGA functional is that which was proposed by Perdew, Burke and Ernzerhof in 1996 - the so-called 'PBE' functional [205]. A revision of the PBE functional for use in the study of solids is also widely-utilised, and is known as the PBEsol functional [206]. Both of these functionals are used extensively throughout this thesis.

3.2.3.3 Hybrid Functionals

The generalised gradient approximation is not without its limitations. Despite its accuracy in calculating ground state properties, GGA functionals often underestimate the band gap in solids and have difficulties predicting the lattice constants of heavy metals [207, 208]. This underestimation is primarily due to the tendency of GGA functionals to over-delocalise electrons, reducing the energy cost of adding an electron and thus underestimating the true band gap. Among the post-GGA methods which have been developed, the so-called 'hybrid' functionals are widely utilised. This class of exchange-correlation functional gets its name from the fact that some degree of exact Hartree-Fock exchange is reintroduced:

$$E_{XC}^{hybrid} \approx \alpha E_{XC}^{HF} + \beta E_{XC}^{GGA} \tag{3.41}$$

where $\alpha + \beta = 1$ and $\alpha, \beta > 0$. By reintroducing exact Hartree-Fock exchange, which treats exchange interactions non-locally, hybrid functionals partially correct the over-delocalisation of electrons seen in GGA and recover more accurate electron localisation. This has the effect that the underestimation of the band gap which arises from the GGA approach is counterbalanced by the overestimation of the band gap which arises from the Hartree-Fock approach. However, the complexity of this approach can make the use of hybrid functionals computationally expensive,

particularly in the plane-wave approach described below. In this work, the HSE06 and B3LYP hybrid functionals have been employed to calculate band gaps.

3.2.4 Plane-Wave DFT

The choice of basis set (the set of functions used to represent the wavefunction) is of great importance in the practical application of density functional theory. Several types of basis sets exist, however, the work presented in this thesis utilises one specific type: the plane-wave basis set. The plane-wave approach arises from Bloch's theorem:

The exact eigenfunctions of an electron in a periodic system are $\psi_k(\mathbf{r}) = \exp(i\mathbf{k}\cdot\mathbf{r})u_k(\mathbf{r})$ where $u_k(\mathbf{r}+a) = u_k(\mathbf{r})$ has the same periodicity as the crystal.

In this theorem, the functions $\exp(i\mathbf{k}\cdot\mathbf{r})$ are periodic, giving this basis set its name. The use of a plane-wave basis set also enables the use of Fast Fourier Transform (FFT) algorithms to perform calculations in either real space (\mathbf{r} -space) or reciprocal space (\mathbf{G} -space) as necessary. Modern DFT codes use a dual-space approach, performing calculations partly in real space and partly in reciprocal space, choosing whichever space allows each step (e.g., potential evaluation, kinetic energy) to be computed most efficiently, leading to significant performance improvements.

The Fourier series expansion of the wavefunction in Bloch's theorem may be written as,

$$\psi_{i\mathbf{k}}(\mathbf{r}) = \sum_{\mathbf{G}}^{|\mathbf{G}| < G_{max}} c_{i\mathbf{k},\mathbf{G}} e^{i(\mathbf{k}+\mathbf{G})\cdot\mathbf{r}}, \qquad (3.42)$$

where the Fourier coefficients $c_{i\mathbf{k},\mathbf{G}}$ are stored on the reciprocal lattice, \mathbf{G}_{hkl} . Equation 3.42 demonstrates that the total wavefunction is a sum of individual planewaves, each of which has a wavelength, λ . The shortest wavevector in reciprocal space, \mathbf{G}_{max} therefore has the highest energy, which is referred to as the cut-off energy, E_{cut} . These are related by the equation,

$$E_{cut} = \frac{\hbar^2 \mathbf{G}_{max}^2}{2m_e},\tag{3.43}$$

where m_e is the rest mass of the electron and \hbar is the reduced Planck constant $(\hbar = \frac{h}{2\pi})$. The result is that increasing the cut-off energy allows for more plane-wave basis functions to be used in the description of the wavefunction, increasing the accuracy of the calculation at the expense of computational expedience.

3.2.4.1 k-point Sampling

In periodic systems, the Brillouin zone is a primitive cell containing exactly one lattice point (a 'Wigner-Seitz' primitive cell) which is entirely enclosed by planes which are perpendicular bisectors of the reciprocal lattice vectors [209]. Rather than calculating the electronic density at every point within the Brillouin zone of each ion, the electron density is calculated by sampling a set of k-points within the Brillouin zone and integrating over these k-points:

$$\rho(\mathbf{r}) = \frac{1}{V_{BZ}} \int_{BZ} \rho_{\mathbf{k}}(\mathbf{r}) d^3 \mathbf{k}.$$
 (3.44)

The distribution of k-points within the Brillouin zone is an important consideration in electronic structure calculations. The objective is to accurately calculate the electronic structure with the fewest k-points possible, as the total number of k-points

sampled scales as a multiple of the number of ions in the system (not accounting for symmetry). The k-points are typically distributed in a grid, or mesh, wherein denser meshes generally give more accurate results. A common method of defining this k-point mesh, which is employed in this thesis, is the Monkhorst-Pack k-point mesh [210, 211]. The Monkhorst-Pack mesh is defined by the number of k-points in each reciprocal lattice direction, in the form $a \times b \times c$. The optimal number of k-points in each direction is obtained via convergence testing, i.e., gradually increasing a, b and c until the total energy of the system per ion increases by a very small amount ($\sim 0.01 \text{ eV at}^{-1}$). Throughout this thesis, a k-point spacing of 0.02 Å^{-1} in reciprocal space provided sufficient k-point density to achieve this level of accuracy.

3.2.5 Pseudopotentials

The number of plane-wave basis functions required to accurately describe sharp variations in the external potential can be computationally expensive. This is particularly the case close to the ion, where the steep ionic potential causes strong oscillations in the wavefunction. In the pseudopotential approach, the core states are replaced by an effective potential - *i.e.*, the core electrons are effectively frozen and their wavefunctions are not computed. At the same time, the effective potential - or 'pseudopotential' - allows the valence electrons to be computed using significantly fewer basis functions and electrons. Pseudopotentials have a defined cut-off radius (r_{cut}) , beyond which the energies of electrons in the pseudopotential and all-electron approaches are identical. The 'softness' of the pseudopotential is defined by this parameter, where pseudopotentials with larger r_{cut} being described as soft.

Three main forms of the pseudopotential are typically employed in the simulation of materials: norm-conserving pseudopotentials (NCPs), ultrasoft pseudopotentials (USPs), and the projector augmented wave method (PAW).

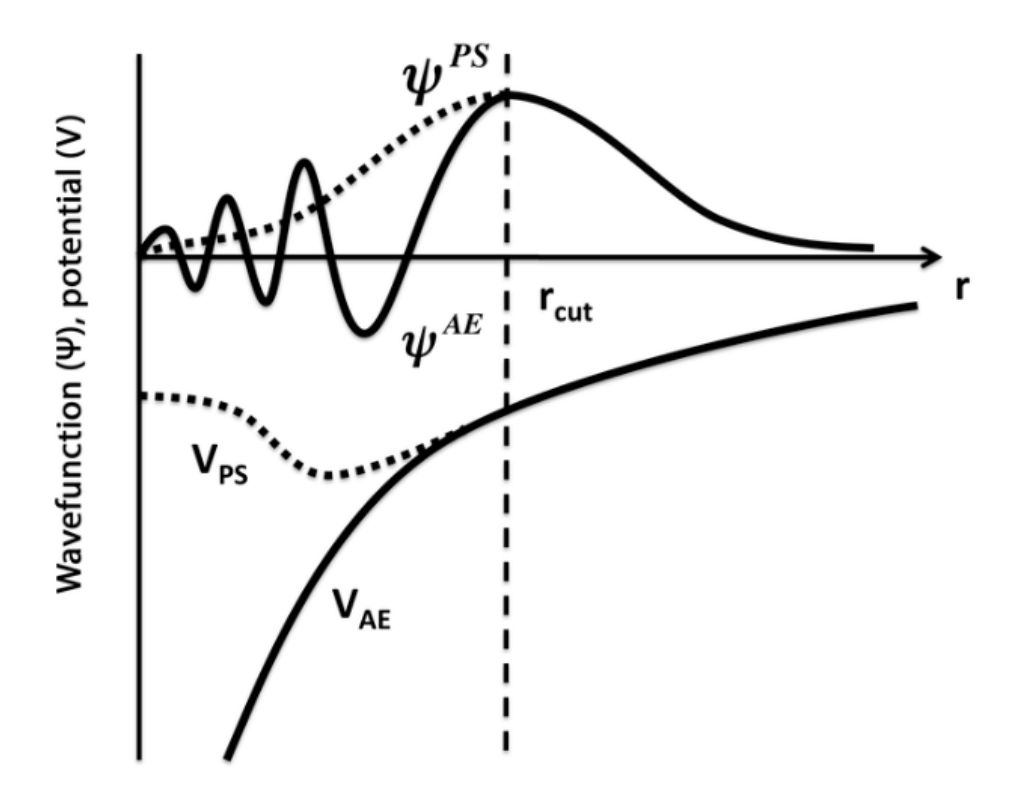


Figure 3.6: The external potential and the wavefunction of the all-electron solution (AE) and under the psuedopotential approach (PS) [212].

In the norm-conserving approach, the pseudo-wavefunction matches the all-electron wavefunction outside the cut-off radius, whilst the norm (the integral of the squared magnitude of the wavefunction over all space) of the psuedo-wavefunction matches that of the all-electron wavefunction within the core radius. The conservation of the norm within the core radius allows for accurate physical properties at close range, *i.e.*, in scattering simulations. Ultrasoft pseudopotentials, on the other hand, use a generalised charge density to compensate for the non-conservation of the norm of the wavefunction. As a result, the pseudo-wavefunctions can be made much smoother, greatly reducing computational cost at the expense of transferability.

Combining the positive aspects of NCPs and USPs, the projector augmented

Table 3.1: Valence orbitals included in the pseudopotentials employed throughout this thesis.

Species	Configuration	Total electrons
$\overline{\mathbf{W}}$	$ \begin{vmatrix} 5s^2, 5p^6, 5d^5, 6s^1 \\ 3s^2, 3p^6, 3d^5, 4s^1 \\ 4s^2, 4p^6, 4d^2, 5s^1 \end{vmatrix} $	14
\mathbf{Cr}	$3s^2, 3p^6, 3d^5, 4s^1$	14
\mathbf{Y}	$4s^2, 4p^6, 4d^2, 5s^1$	11
O	$2s^2, 2p^4$	6

wave method offers significant benefits compared to both of these approaches. The PAW method splits the system's electrons into core electrons, described by a pseudopotential, and valence electrons, which are treated explicitly. The pseudo-wavefunction of the core states and the all-electron wavefunction of the valence states are connected by a linear transformation,

$$\Psi = \Lambda \tilde{\Psi},\tag{3.45}$$

where Ψ and $\tilde{\Psi}$ are the all-electron wavefunction and the pseudo-wavefunction respectively, and Λ is the transformation operator [213]. This allows for the all-electron solution to be reconstructed if necessary, providing accuracy close to that of all-electron methods, lower cut-off radii (and hence requiring fewer basic functions), and excellent transferability between lighter and heavier elements. The PAW method is utilised in this thesis, as it is the main pseudopotential method employed by the VASP code. Importantly, the pseudopotentials used for each metal (W, Cr and Y) treated some semi-core electrons as valence electrons. Whilst, in theory, this leads to additional computational cost, the additional cost was not enough to make these pseudopotentials computationally intractable. The electronic configuration and total number of valence electrons for each element is shown in Table 3.1.

3.2.6 The DFT+U Formalism

Both the local density approximation and the generalised gradient approximation are known to underestimate band gaps in strongly correlated materials such as transition metal oxides and Mott insulators - typically those with localised d and f orbitals. This can be traced back to the so-called 'delocalisation error', which, as the name implies, is the DFT energy error arising from the over-delocalisation of electrons. The delocalisation error often manifests in an underestimation of the band gap in insulators and semiconductors; in some cases, LDA and GGA functionals can predict these materials to be metallic in nature.

The DFT+U formalism aims to address this by treating the strong on-site Coulombic interaction between localised interactions with an additional Hubbard-like term. This term contains both the Coulombic interaction, U, and the exchange interaction, U, and the exchange interaction, U, and the DFT+U formalism is given the form,

$$E_{tot} = E_{DFT} + E_{Hub} - E_{dc} \tag{3.46}$$

where E_{hub} is the contribution to the total energy from the Hubbard-like term, and E_{dc} subtraction which accounts for double-counting. The exact form of E_{hub} depends on the treatment of U and J, and falls into two categories. The first, proposed by Liechtenstein $et\ al.$, treats U and J as independent variables [214]. The second is a simplified approach which was proposed by Anasimov and Dudarev ($et\ al.$) and considers only an effective Coulombic interaction, $U_{eff} = U - J$ [215].

In this work, the simplified rotationally-invariant approach by Dudarev *et al.* has been employed in order to accurately predict the band gaps of tungsten oxides. Therefore, calculation of the U_{eff} is important. The linear response *ansatz* proposed by Cococionni *et al* has been used to calculate U_{eff} *ab initio*, rather than fitting it

to the empirical band gap [216]. For a singular W atom, a small change is made in the U parameter, V, ranging from V = -0.25 eV to 0.25 eV in steps of 0.05 eV. At each step, the occupancy of the W 5d orbitals of the atom is computed in both the self-consistent (SCF) and non-self-consistent fields (NSCF). The W 5d occupancies are then plotted against V, and the U parameter is calculated as:

$$U = \chi^{-1} - \chi_0^{-1} \approx \left(\frac{\partial N_I^{SCF}}{\partial V_I}\right)^{-1} - \left(\frac{\partial N_I^{NSCF}}{\partial V_I}\right)^{-1}$$
 (3.47)

where, N_I^{SCF} and N_I^{NSCF} is the number of electrons occupying the d orbital of the W atom to which V is applied in the SCF and NSCF, respectively. As such, the U parameters used in this thesis are presented in the relevant methodology in Chapter 5.

3.3 Interatomic Potentials

An interatomic potential is a mathematical function that describes the energy and resulting forces between atoms as a function of their positions in a system. Generally speaking, the forces between interacting atoms can be obtained from the potential that each atom is exposed to, *i.e.*,

$$m_i a_i = \mathbf{f}_i \qquad ; \qquad \mathbf{f}_i = \frac{\partial}{\partial \mathbf{r}_i} U$$
 (3.48)

where m_i , a_i and \mathbf{f}_i are the mass, acceleration and force acting upon particle i, respectively, and U is the potential energy of the system. The non-bonding potential energy of a system of atoms may be written as,

$$V(\mathbf{r}_{1}...\mathbf{r}_{N}) = \sum_{i,j}^{N} V_{2}(\mathbf{r}_{ij}) + \sum_{i,j,k}^{N} V_{3}(\mathbf{r}_{ijk}) + \sum_{i,j,k,l}^{N} V_{4}(\mathbf{r}_{ijkl}) + ...$$
(3.49)

where $V_2(\mathbf{r}_{ij})$ is the energy of the interaction between atoms i and j at a separation of \mathbf{r}_{ij} , *i.e.*, their pairwise interaction. The higher-order terms of the equation V_3 , V_4 , etc., are generally ignored due to the dominance of the pairwise interaction. The pairwise interaction, V_2 , can be broken down into two parts: the Coulombic potential, $V_{ij}^{Coulomb}$, and the short-range potential, V_{ij}^{sr} .

3.3.0.1 Coulombic Potential

In classical mechanics, the interaction experienced by two charged bodies in space is given by,

$$V_{ij}^{Coulomb} = \frac{q_i q_j}{4\pi \epsilon_0 r_{ij}} \tag{3.50}$$

where q_i and q_j are the charges of bodies i and j, ϵ_0 is the permittivity of free space, and r_{ij} is the separation between the bodies. Due to the inverse relation between the potential and the separation of the i and j, the Coulombic interaction is a long-ranged interaction. Fully capturing the Coulombic potential of a single particle requires the summation of many pairwise interactions and, therefore, a large number of neighbouring ions at greater computational expense. Furthermore, by considering Equation 3.50 as r_{ij} approaches zero, it becomes apparent that considering the Coulombic interaction alone is insufficient:

$$\lim_{r_{ij} \to 0} \frac{q_i q_j}{4\pi\epsilon_0 r_{ij}} = -\infty \tag{3.51}$$

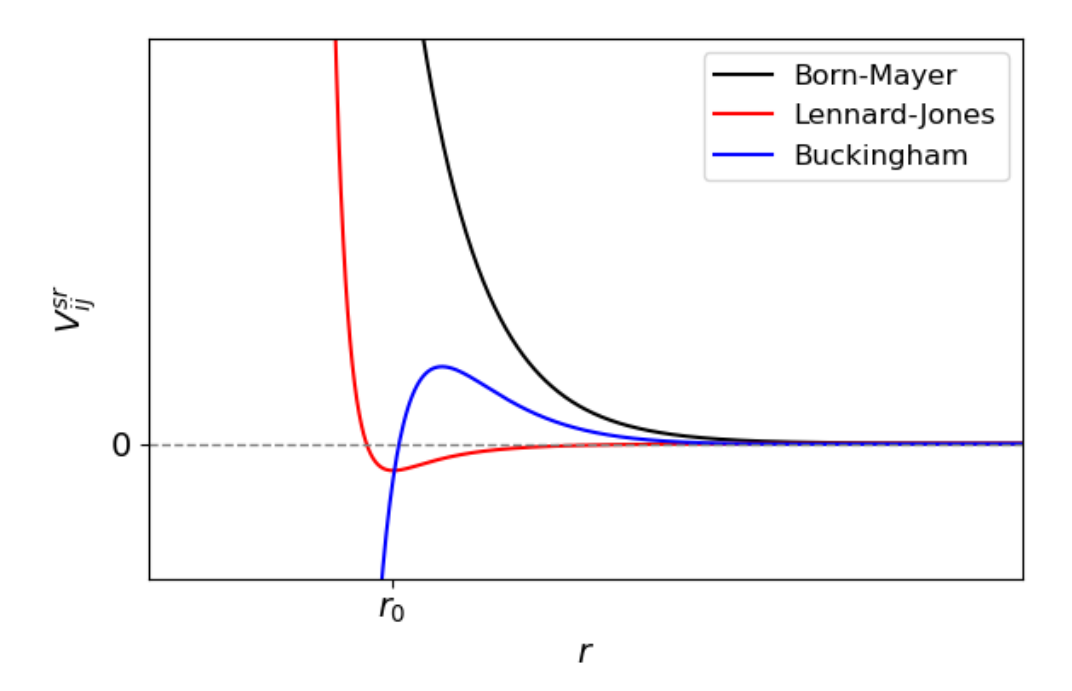


Figure 3.7: Examples of the Born-Mayer, Lennard-Jones and Buckingham potentials for arbitrary values of V_{ij}^{sr} and r. r_0 denotes the equilibrium distance between two particles in the Lennard-Jones potential. The mathematical forms of the potentials are given in Equations 3.52, 3.53, 3.54.

In other words, if the long-range Coulombic interaction is considered alone, the lowest energy configuration is supposedly found by placing two atoms on top of one another.

3.3.0.2 Short Range Potential

In order to overcome the unphysical behaviour when two atoms are brought together, a short-ranged interaction must be added to stop the atoms in the system from collapsing onto one another. This repulsive interaction arises out of the Pauli exclusion principle, which states that no two interacting fermions (*i.e.*, electrons) may occupy the same quantum state. Multiple mathematical descriptions of the short range potential have been proposed, but, in general, all exhibit exponential or exponential-like decay as a function of r_{ij} . For instance,

$$V_{ij}^{sr} = A_{ij} \exp\left(\frac{-r_{ij}}{B_{ij}}\right) \tag{3.52}$$

$$V_{ij}^{sr} = \frac{A_{ij}}{r_{ij}^{12}} - \frac{C_{ij}}{r_{ij}^{6}}$$
(3.53)

$$V_{ij}^{sr} = A_{ij} \exp\left(\frac{-r_{ij}}{B_{ij}}\right) - \frac{C_{ij}}{r_{ij}^6}$$
 (3.54)

which are the Born-Mayer, Lennard-Jones and Buckingham potentials respectively. These are visualised in Figure 3.7. In the above equations, V_{ij}^{sr} is the short-range potential between species i and j, r_{ij} is their separation, and A_{ij} , B_{ij} and C_{ij} are empirically-confirmed coefficients.

3.3.1 Embedded Atom Potentials

The interatomic potentials described above are known as pair potentials for the simple fact that consider the pairwise interaction of atoms/ions. As shown in Equation 3.49, and as mentioned in section 3.3, N-body contributions to the potential energy may also be included, though these are generally more computationally expensive. However, in 1983 and 1984, Daw and Baskes proposed the embedded atom method (EAM) [217], which describes the total energy of a system of n atoms as,

$$E_{tot} = \sum_{i}^{n} \left[\frac{1}{2} \sum_{i} \phi(r_{ij}) + F(\bar{\rho}_i) \right] \qquad ; \qquad \bar{\rho}_i = \sum_{j} \rho(r_{ij})$$
 (3.55)

where r_{ij} is the distance between ions i and j, ϕ is their pairwise interaction, ρ is

another pairwise interaction which contributes to the density term $\bar{\rho}$. $F(\bar{\rho})$ is the so-called 'embedding function'.

The theory behind the embedded-atom potential is derived from density functional theory, which is discussed in Section 3.2. In short, the energy associated with embedding an atom in a system is a functional of the electron density of the system prior to the atom being embedded. The term $\rho(r)$ gives the local electron density as a function of distance from the atom, and the density term $\bar{\rho}(r)$ is the electron density of the host system with atom i removed. Therefore, in Equation 3.55, $\phi(r_{ij})$ is the classical electrostatic pairwise interaction, and $F(\bar{\rho})$ is the quantum-mechanical energy of embedding atom i into a homogeneous electron gas with a density of $\bar{\rho}_i$. The latter term can be obtained from quantum-mechanical calculations and fitted semi-empirically.

EAM potentials are widely employed in metallic systems and alloys due to their accuracy, where many-body interactions are especially important. Their semi-empirical nature, which arises from the density functional theory roots of the method, means that the potentials are also transferable within systems containing the same elements. In this thesis, the Fe-W-Cr EAM potential by Bonny *et al.* has been used in all MD simulations [218].

Chapter 4

Model Validation

As this thesis concerns the calculation of thermodynamic quantities from first principles, special attention must be given to the parameters with which these values are obtained. As discussed in Section 3.3.1, density functional theory has several important parameters. Among these are the plane-wave cut-off energy, E_{cut} , and the choice of exchange-correlation functional. This chapter discusses the justification for the selection of E_{cut} used throughout the remainder of this thesis, and compares the accuracy of the PBE and PBEsol exchange-correlation functionals for the constituent elements: tungsten, chromium, yttrium and oxygen. In addition, the molecular dynamics simulations carried out in this thesis have been performed using the embedded atom potential by Bonny $et\ al.$, available on the NIST Interatomic Potential Repository [218, 219, 220]. This potential was designed for use in Fe-Cr-W systems, i.e., Fe-Cr alloys doped with W, and, at the time of the work carried out in this thesis, was the only interatomic potential containing both W and Cr.

The accuracy of the exchange-correlation functionals and the Fe-Cr-W EAM potential will be assessed by comparing bulk lattice parameters, electronic structure,

single- and polycrystalline elastic properties, and the phonon dispersions of the metallic species. For oxygen, the O-O bond length and the HOMO-LUMO gap will be compared against hybrid functionals (HSE06 and PBE0). The phonon dispersion spectra presented in this chapter 4 were obtained using the pre-processing and post-processing scripts implemented in *phonopy* [221, 222]. Likewise, the elastic constants calculated herein were obtained using the pre-processing and post-processing scripts implemented in *VASPKIT* [223].

4.1 Plane-wave Cut-off Energy

As discussed in Section 3.2.4, a higher plane-wave cut-off energy, E_{cut} , increases the accuracy of density functional theory calculations. However, increasing E_{cut} increases the computational cost of the calculation as more plane-wave basis functions are included in the description of the wavefunction. Therefore, a balance between the number of basis functions and the cost of individual calculations must be found. To find the optimal value of E_{cut} , a body-centred cubic system containing tungsten and at least one atom of chromium, yttrium and oxygen was made. The difference in the system's total energy per atom with respect to the energy at the highest cut-off energy, dE, was plotted against E_{cut} , as shown in Figure 4.1. The difference in total energy per atom rapidly decreases to 0.005 eV at around E_{cut} = 520 eV, and 0.001 eV above E_{cut} = 700 eV. Based on this, the value of E_{cut} throughout this thesis is 520 eV, as the error of 0.005 eV per atom was found acceptable in exchange for computational expedience.

Table 4.1: Computational parameters used for DFT and MD calculations, unless specified otherwise.

Method	Parameter		
	Plane-wave cutoff energy: 520 eV Pseudopotentials: Semi-core electrons treated as valence Energy convergence tolerance: $\delta E < 1 \times 10^{-6}$ eV		
\mathbf{DFT}	Ionic convergence tolerance: $\delta F < 0.01 \text{ eV Å}^{-1}$		
	Smearing method:		
	1st order Methfessel-Paxton (metals)		
	Gaussian (insulators)		
	Tetrahedral method ^a (single-point energy)		
	Smearing width: 0.02 eV		
	k-point spacing:		
	$0.02 \text{ Å}^{-1} \text{ (insulators)}$		
	$0.01 \text{ Å}^{-1} \text{ (metals)}$		
	DFT+ U and spin polarisation as required.		
	Interatomic potential: Fe-Cr-W EAM [218]		
MD	Timestep: 0.01 ps		
	Energy convergence tolerance: $1 \times 10^{-25} \text{ eV}$		
	Force convergence tolerance: $1 \times 10^{-25} \text{ eV Å}^{-1}$		

^a with Blöchl corrections [224].

4.2 Summary of Parameters

Based on Chapter 3.3.1 and the convergence testing presented in Section 4.1, the computational parameters used in DFT and MD simulations throughout this thesis are presented in 4.1. Whilst some parameters depend upon the system of interest and the nature of the study - such as DFT+U parameters, spin polarisation and k-point mesh - these parameters apply to all simulations carried out herein, unless specified otherwise.

For density functional theory calculations, the treatment of the valence orbitals in the PAW pseudopotentials are given in Table 3.1 in Chapter 3.3.1. The energy convergence tolerance in Table 4.1 refers to the maximum allowed change in total energy between successive electronic steps required to achieve convergence when determining the energy-minimised wavefunction for a given structure. Likewise,

the ionic convergence tolerance is the maximum force acting on any atom during geometry minimisation. The electronic smearing method refers to the handling of the occupation of electronic states near the Fermi level, and aids in the convergence of electronic calculations. The Methfessel-Paxton smearing method improves the accuracy of calculations on metallic systems, whereas Gaussian smearing is applicable for insulators. Where highly-accurate energies are required, the tetrahedron method with Blöchl corrections has been employed [224].

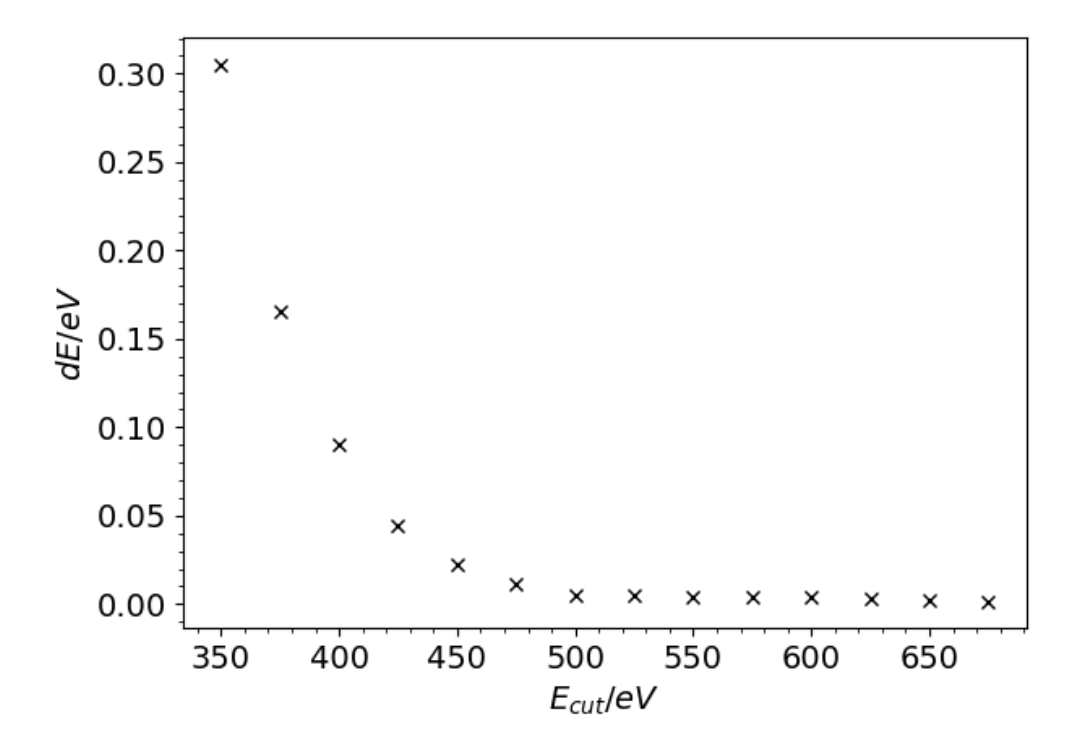


Figure 4.1: Convergence testing on the plane-wave cut-off energy, E_{cut} .

4.3 Tungsten

4.3.1 Physical Structure and Chemical Potential

The lattice parameters of bcc-W calculated in this work are presented in Table 4.2. Tungsten is paramagnetic; therefore, only the non-magnetic configuration has been investigated as a close approximation. PBE predicts the optimised lattice parameter in non-magnetic bcc-W to be 3.185 Å, whilst PBEsol and the Fe-Cr-W potential predicts it to be 3.157 Å and 3.161 Å, respectively. Experimentally, the lattice parameter of bcc-W is known to be 3.165 Å [225, 226]. The PBEsol functional is known to provide lattice parameters closer to those observed experimentally by alleviating the underbinding seen in PBE, and the EAM potential was fitted in order to reproduce the experimental lattice parameter. Therefore, it is no surprise that PBEsol and the EAM potential yield accurate lattice parameters.

For PBE, a similar overestimation of the lattice parameter is seen in other theoretical studies at the DFT level of theory. Table 4.2 shows an overestimation of the lattice parameter by about 0.01 Å in the works of Jiang et~al. and Liu et~al., which agree more closely with the experimental lattice parameter than that calculated in this thesis. The lattice parameter appears sensitive to the choice of pseudopotential: Jiang et~al. utilised a PAW pseudopotential which did not treat semi-core electrons as valence, resulting in a lattice parameter closer to the experimental value [227]. On the other hand, USPs and NCPPs yield slightly larger lattice parameters [228, 229, 230]. Nevertheless, these lattice parameters are ~ 0.03 Å ($\sim 1\%$) larger than the experimental value. Likewise, Liu et~al. reports a lattice parameter of 3.17 Å using PAW pseudopotentials, though the states treated as valence were not reported [225]. Furthermore, in their study, a cut-off energy of 350 eV was used, which Figure 4.1 shows introduces a significant error in the total energy of the system. It is possible that a similar error is also present in the lattice

Table 4.2: Optimised lattice parameter (a) of bcc-W calculated using PBE and PBEsol GGA functionals and the EAM potential for the Fe-Cr-W system by Bonny et al., compared to existing theoretical and experimental work.

\mathbf{Study}	${ m a/\AA}$
This work	
PBE	3.185
PBEsol	3.157
EAM	3.165
Materials Project ^a [231]	3.17
Jiang et al. ^a [227]	3.1755
Liu et al. ^a [225]	3.17
Samolyuk et al. ^b [228]	3.1903
Qian et al. c [229]	3.1835
Romaner et al. ^c [230]	3.187
Liu et al. ^d [232]	3.165
Featherston et al. ^d [226]	3.165

^a DFT study (VASP-PAW).

parameter, however, this has not been tested rigorously in this thesis, nor in the works referenced in Table 4.2.

The enthalpy of atomisation, ΔH_{atom} for W was calculated by considering the reaction,

$$W_{(s)} \longrightarrow W_{(g)}$$
 (4.1)

where $W_{(s)}$ refers to a W atom in the bcc lattice and $W_{(g)}$ refers to an isolated W atom in the gas phase. Therefore, the enthalpy of atomisation for a 2-atom bcc-W unit cell is,

^b DFT study (QE-USP).

^c DFT study (QE-NCPP).

^d Experimental data.

$$\Delta H_{at} = E_{unit} - 2E_{gas} \tag{4.2}$$

where E_{unit} is the total energy of the unit cell and E_{gas} is the energy of the gas-phase atom. The latter was calculated by placing a single W atom in a fixed simulation cell measuring $10.00 \times 10.01 \times 10.02$, with the anisotropy in the lattice parameters introduced to break the symmetry of the cell.

The enthalpy of atomisation for W as predicted using the PBE exchange-correlation functional is 8.85 eV, and 9.75 eV for the PBEsol functional. The experimental value of ΔH_{atom} for W is 8.79 eV [233], and the EAM potential predicted a value of 8.90 eV. As such, the PBEsol functional overestimates the enthalpy of atomisation by a margin of 11.03%, whereas the error in ΔH_{atom} under the PBE functional is just 0.68%. This indicates that, although the PBEsol functional may predict lattice parameters which are closer to the experimental values, the total energy of the system is not nearly as accurate. Accurate energies are required to investigate defect behaviour and migration energies; therefore, the PBE functional is the more suitable choice of exchange-correlation functional. The chemical potential of W, calculated by dividing the total energy of the solid system by the number of atoms in the unit cell, is -12.955 eV for the PBE functional and -13.805 eV for the PBEsol functional.

4.3.2 Electronic Structure

The overall electronic structure of bcc-W is consistent between density functional theory calculations using the PBE and PBEsol exchange-correlation functionals, as shown in Figure 4.2. The only major difference between the calculated band structures is the Fermi level, which lies at -6.28 eV according to the PBE functional

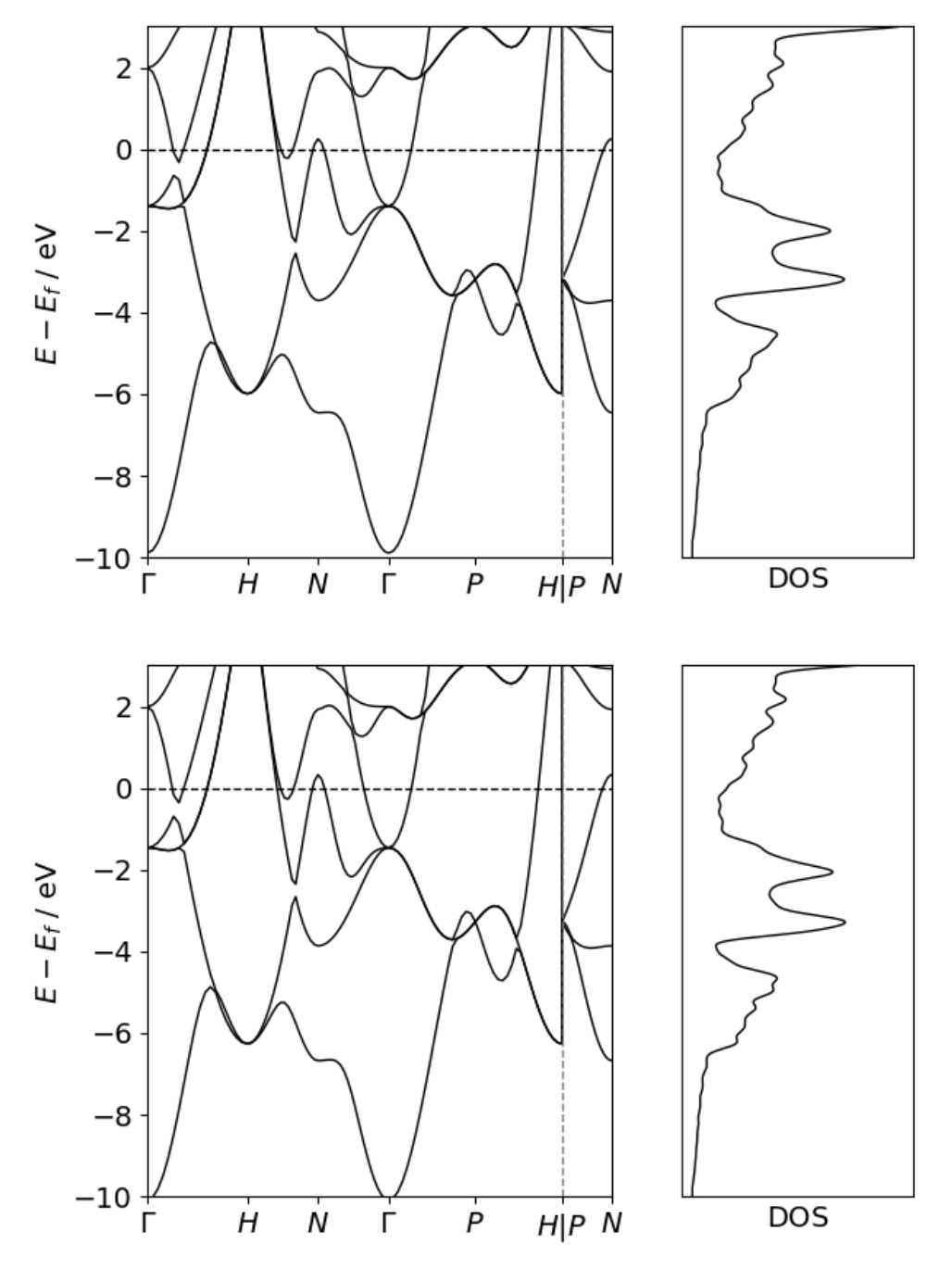


Figure 4.2: Band structure and electronic density of states of bcc-W obtained using the (top) PBE and (bottom) PBEsol exchange-correlation functionals, relative to the Fermi level.

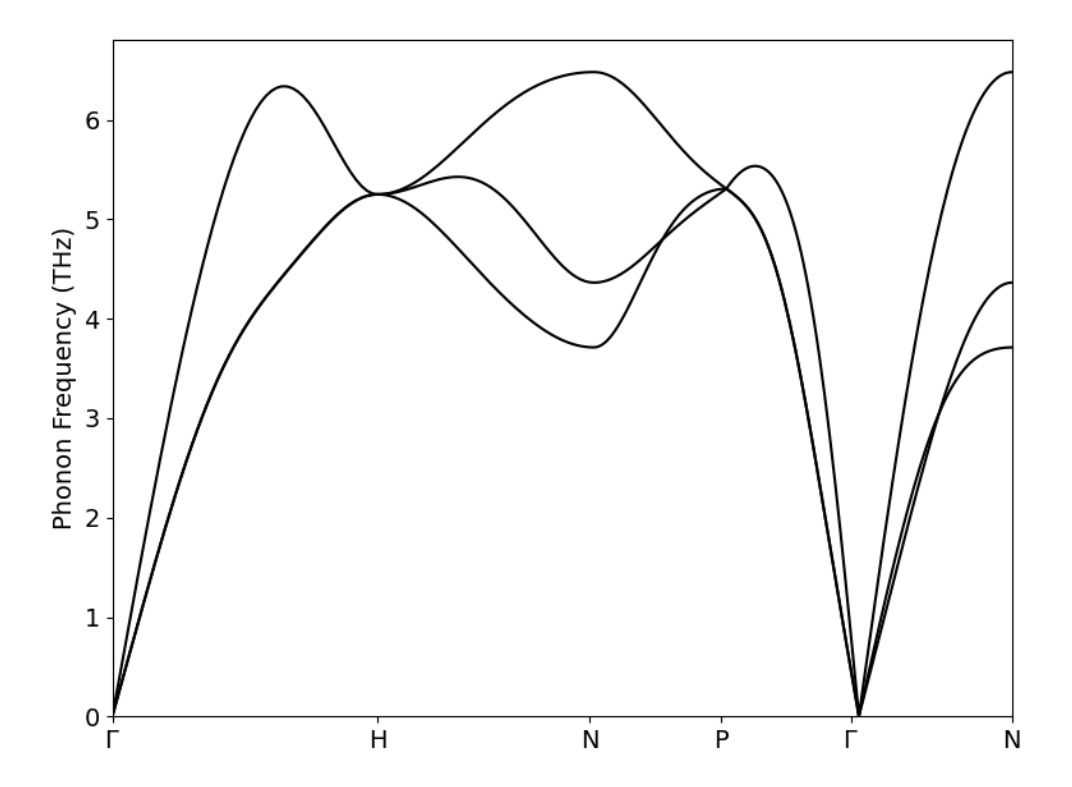


Figure 4.3: Phonon dispersion of bcc-W obtained using the PBE exchange-correlation functional.

and -6.54 eV according to the PBEsol functional. Furthermore, the calculated spectra are consistent with experimental hard X-ray photoelectron spectroscopy measurements, showing the characteristic three peaks below the Fermi level [234].

4.3.3 Lattice Dynamics

The phonon dispersion of bcc-W, as calculated using the PBE exchange-correlation functional, is shown in Figure 4.3. Three acoustic modes are observed, with that of the higher frequency being the longitudinal branch, and the two of lower frequency being the transverse branches [235]. The transverse branches show non-degeneracy between the H and P lattice points, with a crossing of the modes between the N and P points, consistent with existing theoretical data obtained using very

similar density functional theory parameters [236, 237, 238]. The phonon frequencies predicted herein also agree with experimental data, with the highest frequency being found at the N point on the longitudinal acoustic mode at just over 6 THz [239, 240]. However, the works of Larose et al. and Maksimenko et al. suggest that the frequency of the two transverse modes is around 4 THz at the N point. The calculations presented herein show a much wider margin of about 0.7 THz between the two transverse modes at the N point, suggesting an overestimation of the stiffness of one vibration, and an underestimation of the stiffness of the other. Nevertheless, the discrepancy when compared to experimental values is sufficiently small, and agrees well with previous DFT results.

4.3.4 Elastic Properties

Table 4.3: The single crystal elastic constants and averaged bulk modulus (B_0) , Young's modulus (E_0) and shear modulus (G_0) of bcc W polycrystal calculated using the PBE exchange-correlation functional. All values in GPa.

Study	C11	C12	C44	${f B}_0$	${f E}_0$	\mathbf{G}_0
This work	513.7	201.3	143.2	305.4	385.9	148.8
Qi et al. ^a [241]	528.5	193.4	148.7	306.8	-	156.8
Luo et al. a [242]	511.1	201.2	134.7	302.9	-	-
Guo et al. ^a [243]	512.4	194.6	141.9	301.0	-	-
Koci et al. ^a [244]	513.0	199.0	140.0	329.0	-	-
Materials Project ^a [231]	521.0	193.0	138.0	302.0	-	148.0
Cereceda et al. ^b [245]	524.0	204.9	161.2	311.3	408.7	160.1
Tersoff et al. ^b [246]	541.8	205.2	163.2	307.9	442.2	170.9
Finnis et al. ^b [247]	532.6	205.0	163.2	314.2	418.7	151.5
Hertzberg et al. ^c [248]	501.0	198.0	151.0	299.0	388.8	151.5

^a Density functional theory (GGA) study.

The single-crystal elastic constants and averaged polycrystalline elastic properties for bcc-W are shown in Table 4.3. There are three independent elastic

^b Molecular dynamics (EAM potential) study.

^c Experimental data.

constants in the body-centred cubic lattice: C_{11} , which describes elastic strain along the principal crystallographic axis; C_{12} , which describes the elastic coupling between perpendicular axes; and C_{44} , which is related to the crystal's resistance to shear deformation. The values of C_{11} , C_{12} and C_{44} determined in this work agree with existing work at the DFT level of theory, particularly the values reported by Luo et al. and Guo et al. [243, 242]. In general, the values calculated via DFT systematically overestimate C_{11} and C_{12} , whilst slightly underestimating C_{44} . On the other hand, molecular dynamics studies utilising EAM-based approaches consistently overestimate the single-crystal elastic constants [245, 246, 247]. Despite this, the values calculated in this work are generally in good agreement with experiment, exhibiting errors of only 0.5%, 1.5% and 5.5% in C_{11} , C_{12} and C_{44} , respectively.

Similar trends are observed in the averaged bulk polycrystalline properties due to their relations with the single crystal stiffness tensor elements. The properties of interest are the bulk modulus, B_0 , Young's modulus, E_0 , and the shear modulus, G_0 . As shown in Table 4.3, the simulations performed herein accurately predict the bulk and Young's moduli of bcc-W, *i.e.*, the compressive and tensile behaviour of W. On the other hand, the shear modulus is slightly underestimated compared to the experiment, moreso than under the USP approach by Qi *et al* [241]. As before, the values calculated using EAM-based approaches generally overestimate the polycrystalline elastic properties. However, the values calculated in this work are in very good agreement with experiment, with absolute errors of 2.0%, 0.8% and 2.0% in B_0 , E_0 and G_0 , respectively.

Table 4.4: Minimum energy per unit cell (E_0) , optimized lattice parameter (a), and energy difference (ΔE_0) between AFM and NM configurations of bcc Cr, calculated using PBE and PBEsol GGA functionals.

Study	${ m E}_0/{ m eV}$	${ m a}/{ m \AA}$	$\Delta { m E}_0/{ m meV}$
This work			
PBE (AFM)	-19.258	2.850	53.0
PBE (NM)	-19.205	2.830	-
PBEsol (AFM)	-20.712	2.804	50.0
PBEsol (NM)	-20.662	2.802	-
EAM	-	2.866	-
Kübler et al. ^a [249]	-	2.85	60.0
Guo et al. (AFM) ^a [250]	-	2.87	-
Guo et al. (NM) ^a [250]	-	2.85	-
Xu et al. (AFM) ^a [251]	-	2.86	-
Xu et al. (NM) ^a [251]	_	2.85	-
Prithwish et al. ^a [252]	-	2.88	-
Materials Project ^a [231]	_	2.97	-
Yang et al. ^b [253]	-	2.88	-
Lee et al. ^b [254]	-	2.88	-
Lin et al. ^b [255]	_	2.88	-
Olsson et al. ^b [256]	-	2.88	-
_			
Bodeker et al. ^c [257]	_	2.88	-
$\mathbf{Kittel^c}$ [258]	-	2.89	-

^a Density functional theory (GGA) study.

4.4 Chromium

4.4.1 Physical Structure and Chemical Potential

The lattice parameters of bcc-Cr as predicted in this work are presented in Table 4.4. The paramagnetic configuration of bcc-Cr, which occurs above T=311 K, has been approximated via the non-magnetic (NM) configuration in this work. The antiferromagnetic (AFM) configuration is the most stable configuration for both functionals at 0 K, in agreement with experimental observation up to 311 K.

^b Molecular dynamics (EAM potential) study.

^c Experimental data.

Kübler et al. report that the energy difference between the antiferromagnetic and paramagnetic configurations is approximately 0.06 eV (60 meV)[249]. In agreement with existing work, the energy difference has been calculated to be 50 meV under the PBEsol functional and 53 meV using the PBE functional in this work, with the antiferromagnetic ground state favoured in both cases.

Both the PBE and PBEsol functionals employed in this work slightly underestimate the lattice parameter in both AFM and NM bcc-Cr, which is commensurate with existing DFT studies. Surprisingly, the PBEsol functional significantly underestimates the lattice parameter, with an absolute error of about 3%. On the other hand, the error in the lattice parameter is approximately 1% for AFM Cr, as predicted by the PBE functional, and is therefore considered to be in reasonable agreement with experimental data. The EAM potential predicted a value of a = 2.866 Å, which is much closer to the experimental value of a = 2.88 Å. As in the case of W, this accuracy is not surprising, as the potential was fitted to reproduce the lattice parameter, and similar agreement is seen in existing EAM-based studies in the literature.

The enthalpy of atomisation, ΔH_{atom} for Cr was calculated by considering the reaction,

$$Cr_{(s)} \longrightarrow Cr_{(g)}$$
 (4.3)

The values of ΔH_{atom} as predicted by the PBE and PBEsol exchange-correlation functionals, respectively, are 4.07 eV and 4.63 eV. These were calculated using the method described in Section 4.3. The experimental value of ΔH_{atom} for antiferromagnetic Cr is 4.09 eV [233], and the EAM potential predicted a value of 4.10 eV. As seen in Section 4.3.1, the PBEsol functional once again overestimates the enthalpy of atomisation, this time by 13.2%, compared to an absolute error of

only 0.49% for the PBE functional. The chemical potential of antiferromagnetic chromium, which is half the value of E_0 shown in Table 4.4, is -9.629 eV for the PBE functional and -10.356 eV for the PBEsol functional.

4.4.2 Electronic Structure

The electronic band structure and electronic density of states for antiferromagnetic bcc-Cr, obtained using the PBE and PBEsol exchange-correlation functionals, respectively, are shown in Figure 4.4. It is noted that the electronic density of states is truncated due to the maximum number of bands available to the simulation. Both calculations reveal the electron hole at the H point in the Brillouin zone and the electron pocket near the Γ point, which are characteristic features of chromium below the Néel temperature [249]. The pseudogap, *i.e.*, the reduction of electronic states at the Fermi level, E_F , is a consequence of the aforementioned features in the band structure, which gives rise to the spin density wave observed by Overhauser [259]. This feature has been confirmed by Bisti *et al.* using photoemission spectroscopy [260].

According to Skriver $et\ al.$, the peak in the density of states just below the Fermi level is characteristic of the antiferromagnetic ordering in Cr [261]. It arises due to the interaction between the spin density wave and the electronic bands, and its magnitude is dependent upon the density of the k-point mesh used in the calculation. However, since the k-point density is consistent between the band structure calculations in this work, the choice of exchange-correlation functional evidently affects this feature. Given that the peak is less pronounced in the band structure calculated using the PBEsol functional, it can be ascertained that this exchange-correlation functional does not capture the strength of the electronic interactions at the Fermi level as accurately as the PBE functional.

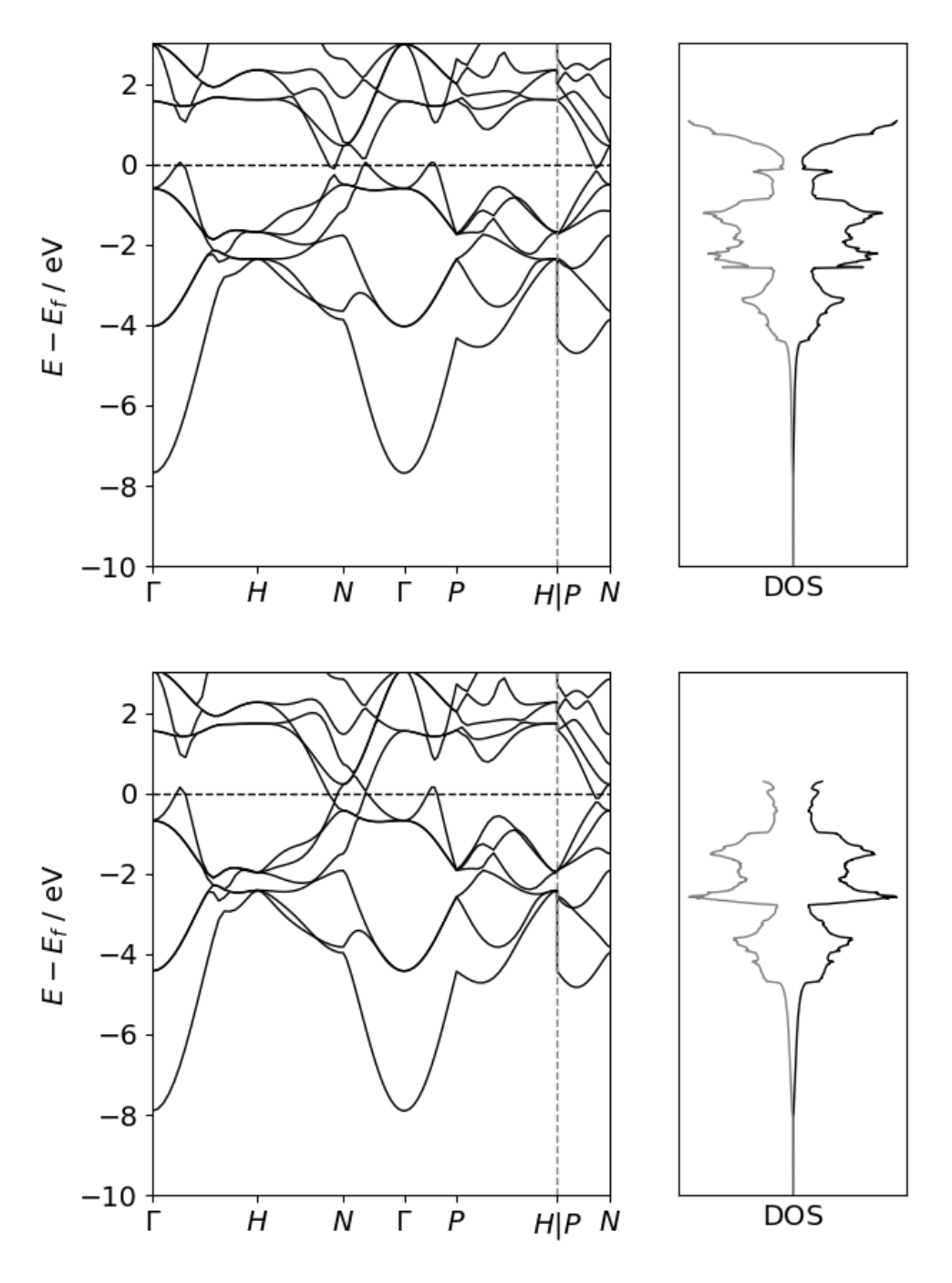


Figure 4.4: Band structure and electronic density of states of bcc-Cr obtained using the (top) PBE and (bottom) PBEsol exchange-correlation functionals, relative to the Fermi level. For the electronic density of states, the up-spin component is shown black, and the down-spin component is shown in grey.

4.4.3 Lattice Dynamics

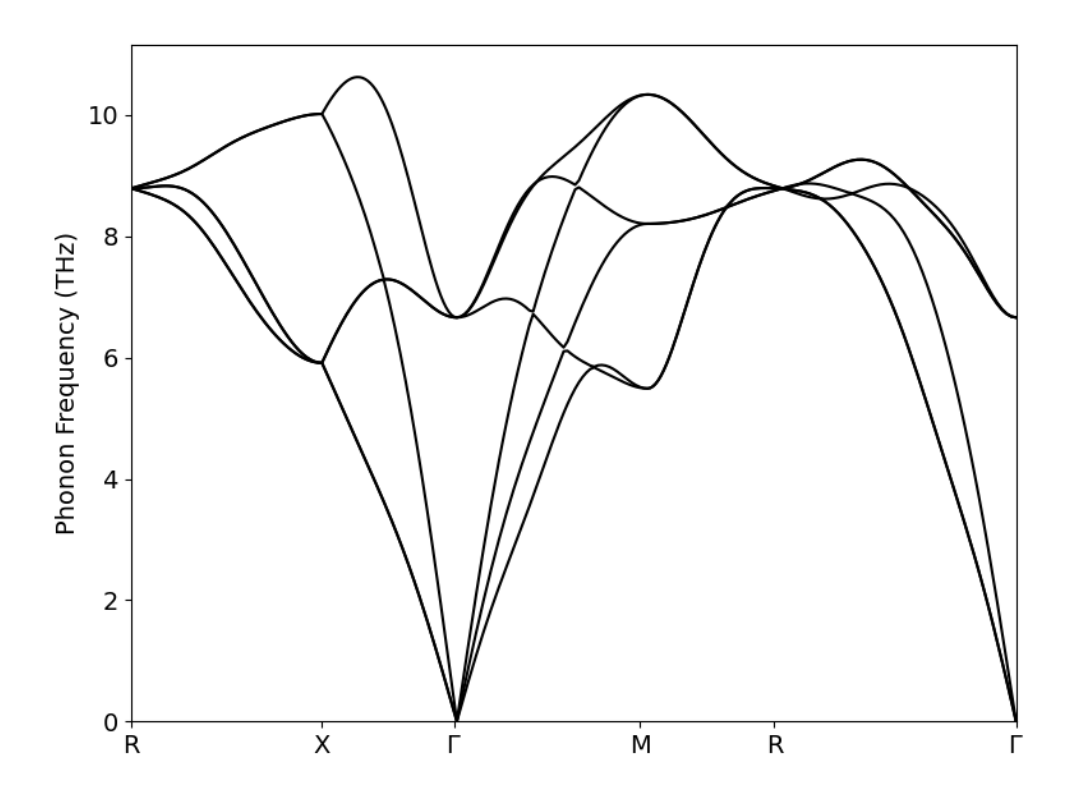


Figure 4.5: Phonon dispersion of antiferromagnetic bcc-Cr obtained using the PBE exchange-correlation functional.

The phonon dispersion of antiferromagnetic Cr, shown in Figure 4.5, consists of both acoustic and optical modes. The optical modes arise from the necessity of having two atoms in the simulation cell to capture the antiferromagnetic ordering of the system. Due to the lack of availability of phonon dispersion data on antiferromagnetic Cr, the frequencies of the acoustic modes can be carefully compared against experimental data for non-magnetic Cr [262]. This is possible on the basis that the acoustic modes arise from vibrations where all atoms in the unit cell move in a concerted manner and are primarily governed by the elastic properties of the material (see 4.4.4). In agreement with experimental data, three acoustic branches are observed at the Γ point: one longitudinal branch, with a maximum frequency at the M point of just over 10 THz, and two transverse branches with phonon frequencies of 8 and 6 THz, respectively. The similarity in phonon

frequencies compared to the experimental non-magnetic phonon dispersion indicates that the strength of the interatomic bonding in Cr (irrespective of magnetic ordering) is accurate for the PBE exchange-correlation functional.

4.4.4 Elastic Properties

Table 4.5: The single crystal elastic constants and averaged bulk modulus (B_0) , Young's modulus (E_0) and shear modulus (G_0) of AFM bcc-Cr polycrystal calculated using the PBE exchange-correlation functional. All values in GPa.

Study	C11	C12	C44	${f B}_0$	${f E}_0$	\mathbf{G}_0
This work	462.0	71.0	106.0	202.3	332.1	135.4
Guo et al. ^a [243]	421.0	73.0	119.0	191.0	-	-
Xu et al. ^a [251]	429.7	59.9	95.0	-	-	-
Prithwish et al. ^a [252]	_	-	-	177.2	-	-
Materials Project ^a [231]	395.0	154.0	64.0	234.0	-	77.0
Yang et al. b [253]	391.0	89.6	103.2	190.1	-	-
Lee et al. ^b [254]	390.9	89.7	103.4	190.1	-	-
Lin et al. ^b [255]	398.4	93.1	103.0	194.8	-	-
Olsson et al. [256]	410.8	105.9	104.9	208.0	-	_
Palmer et al. ^c [263]	394.0	94.0	101.0	194.0	334.0	141.0
Blöchl et al. ^c [213]	391.0	91.0	103.0	189.0	-	_

^a Density functional theory (GGA) study.

The single-crystal elastic constants and averaged polycrystalline elastic properties for antiferromagnetic bcc-Cr are shown in Table 4.5. Compared to experimental data [263, 213], C_{11} is significantly overestimated by the PBE exchange-correlation functional, which is consistent with the tighter binding of Cr atoms predicted by the underestimated lattice parameter. This is also seen in the elastic constants reported by Guo et al. and Xu et al., who report values of 421.0 GPa and 429.7 GPa, respectively [250, 251]. At the same time, the anisotropy arising from the magnetic ordering may weaken the off-diagonal coupling, C_{12} , hence the

^b Molecular dynamics (EAM potential) study.

^c Experimental data.

underestimation in this elastic constant. The absence of spin-orbit coupling may impact the calculation of these parameters, especially as the real magnetic ordering of Cr below the Néel temperature is that of a spin density wave rather than being truly antiferromagnetic. Nevertheless, the averaged polycrystalline elastic properties of Cr are in agreement with experimental data; despite the overestimation in C_{11} and C_{12} , the properties which derive from these values (the bulk and Young's moduli) are accurate. Similarly, the shear stiffness, C_{44} , and the shear modulus agree with experimental data.

Table 4.6: Optimised lattice parameter (a) and axial ratio (c/a) of hcp-Y calculated using PBE and PBEsol GGA functionals, compared to theoretical and experimental data.

Study	$\mathrm{a/\AA}$	c/a
This work		
PBE	3.652	1.59
PBEsol	3.595	1.55
Mehl et al. ^a [264]	3.59	1.49
Sigalas et al. ^a [265]	3.52	1.59
Materials Project ^a [231]	3.64	1.61
Lide et al. ^b [233]	3.64	1.57

^a DFT study.

4.5 Yttrium

4.5.1 Physical Structure and Chemical Potential

The lattice parameters of hcp-Y predicted in this work are shown in Table 4.6. PBE predicts a lattice parameter of a=3.652 Å and the axial ratio c/a=1.59. On the other hand, PBEsol predicts the lattice parameter a=3.595 Å the ratio c/a=1.55. By comparison, the experimental lattice parameters are a=3.64 Å and c/a=1.57. As such, the PBE functional is more accurate at predicting the value of a but slightly overestimates the axial ratio, whilst the PBEsol functional both underestimate a and c/a. Compared to existing DFT data, the lattice parameters determined in this work using the PBE functional are in much better agreement with the experimental values.

The enthalpy of atomisation, ΔH_{atom} for Y was calculated by considering the reaction,

^b Experimental data.

$$Y_{(s)} \longrightarrow Y_{(q)}$$
 (4.4)

As such, the enthalpy of atomisation for the PBE functional was calculated to be 4.15 eV, and 4.57 eV for the PBEsol functional. These were calculated using the method described in Section 4.3. The experimental value of ΔH_{atom} for Y is 4.36 eV. Interestingly, both the absolute error in ΔH_{atom} in both cases is around 4.8%; neither the PBE nor the PBEsol functional predicts the enthalpy of atomisation of yttrium as accurately as the PBE functional does for tungsten and chromium (see Section 4.3.1 and Section 4.4.1). The chemical potential of yttrium, as calculated using the PBE and PBEsol functional, respectively, is -12.866 eV and -13.638 eV.

4.5.2 Electronic Structure

Yttrium is metallic with a complex electronic band structure, as shown in Figure 4.7. The differences are minimal when comparing the band structure and electronic density of states as calculated using the PBE exchange-correlation functional versus the PBEsol functional. The former exhibits slightly broader bands, especially above the Fermi level, whereas the latter exhibits sharp features indicative of greater localisation of electrons. The greater localisation of electrons predicted by the PBEsol functional results in the stronger overlap of the Y 4d orbitals and is the cause of the underestimation of the lattice parameters discussed above. Conversely, the good agreement between the experimental lattice parameters and their corresponding values, as calculated using the PBE exchange-correlation functional, suggests that the PBE functional accurately predicts the electronic structure of Y [266].

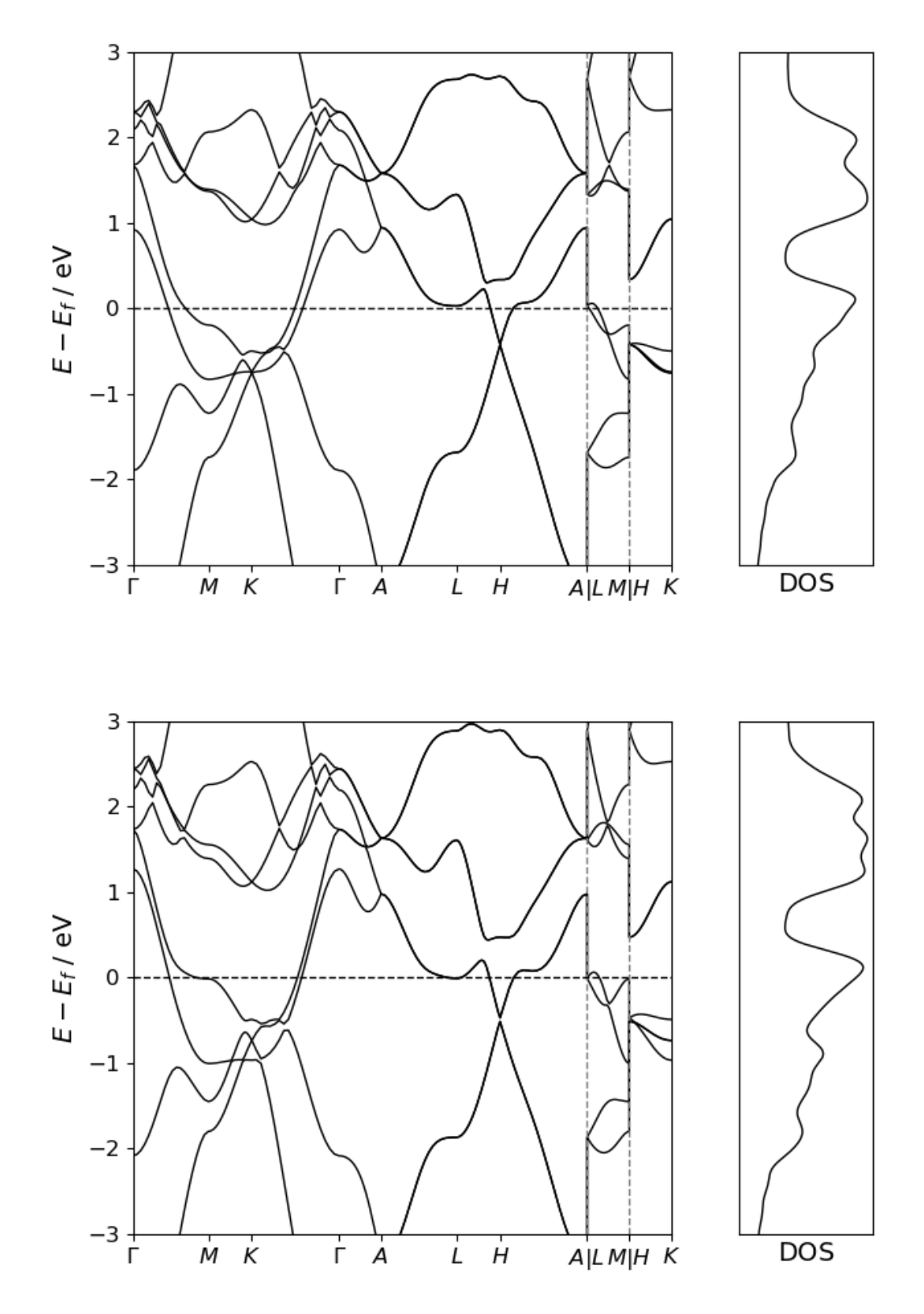


Figure 4.6: Band structure and electronic density of states of hcp-Y obtained using the (top) PBE and (bottom) PBEsol exchange-correlation functionals, relative to the Fermi level.

4.5.3 Lattice Dynamics

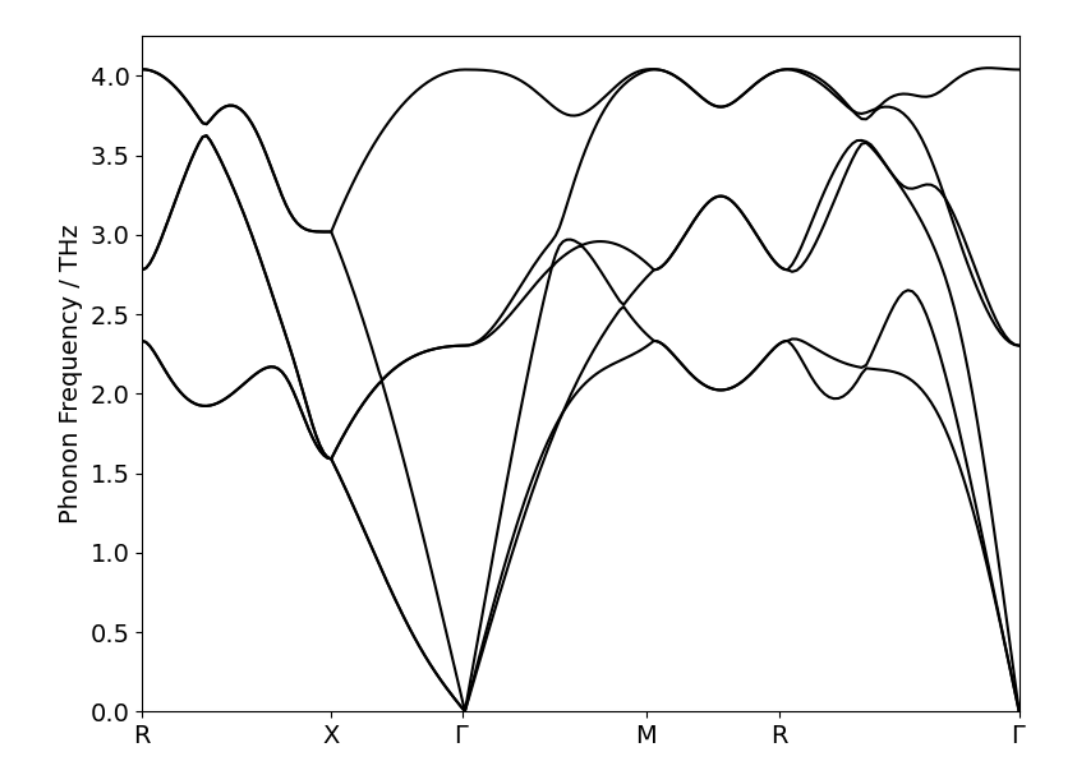


Figure 4.7: Phonon dispersion of hcp-Y obtained using the PBE exchange-correlation functional.

The phonon dispersion of hcp-Y as obtained using the PBE exchange-correlation functional is shown in Figure 4.7. As expected, the absence of imaginary modes in the phonon dispersion signals that this Y configuration is dynamically stable. A notable feature of the phonon dispersion is the relatively flat optical modes at around \sim 4.0 THz, indicating strongly localised vibrations. This may be partly responsible for yttrium's relatively low thermal conductivity, \sim 17 W m⁻¹ K⁻¹, compared to other metals such as copper, as these optical modes do not effectively transfer energy across the lattice.

Table 4.7: The single crystal elastic constants and averaged bulk modulus (B_0) , Young's modulus (E_0) , and shear modulus (G_0) of polycrystalline hcp-Y calculated using the PBE exchange-correlation functional. All values in GPa.

Study	\mathbf{C}_{11}	\mathbf{C}_{12}	\mathbf{C}_{13}	\mathbf{C}_{33}	\mathbf{C}_{44}	\mathbf{C}_{66}	${f B}_0$	\mathbf{E}_0	\mathbf{G}_0
This work	75.9	23.6	21.2	78.9	25.1	26.2	40.3	64.6	26.2
Smith <i>et al.</i> ^a [267]	83.4	29.1	19.0	80.1	26.9	24.7	-	-	-
Savage <i>et al.</i> ^a [268]	79.0	29.1	32.6	78.7	24.9	25.0	-	-	-
Lide <i>et al.</i> ^a [233]	-	-	-	-	-	-	41.2	63.5	25.6

^a Experimental data.

4.5.4 Elastic Properties

The single crystal elastic constants and averaged bulk polycrystalline elastic properties of hcp-Y are shown in Table 4.7, demonstrating the reliability of the PBE functional in predicting the elastic properties of this material. The single crystal elastic constants agree well with the experimental data provided by Smith *et al.* and Savage *et al.*. Likewise, the averaged bulk polycrystalline properties calculated in this work match closely with published experimental data [233].

4.6 Oxygen

The accuracy of the chemical potential of oxygen, μ_O , is crucial to calculating the enthalpy of formation for the oxides of interest. In this thesis, μ_O is considered in both the oxygen-rich and oxygen-poor limit, the former of which is half the DFT energy of the O_2 dimer, *i.e.* $\mu_O^{rich} = 4.94$ eV according to the PBE functional, and $\mu_O^{rich} = 5.14$ eV according to the PBEsol functional. However, previous studies have shown that the overbinding effect of the PBE functional in O_2 often leans to binding energies much larger than the experimental value [269, 270].

To investigate this effect, the bond length, binding energy and HOMO-LUMO gap of the O₂ dimer have been determined using the PBE and PBEsol GGA functionals, as well as the PBE0 and B3LYP hybrid functionals. The description of the HOMO-LUMO gap is essential when considering the binding of gaseous O_2 to metal surfaces, during the first stages of oxidation, since the filling of the π_{2p}^* orbitals by the metal substrate induces the cleavage of the O-O bond. In the O_2 molecule, the 12 valence electrons occupy the σ_s , σ_s^* , π_{2p} , σ_{2p} and π_{2p}^* molecular orbitals. In the ${}^{3}\Sigma_{g}$ (triplet) state, the antibonding π_{2p}^{*} orbitals are partially occupied by two unpaired electrons of the same spin. The partially-filled up-spin π_{2p}^* molecular orbitals are considered to be the HOMO in the O_2 dimer, whilst the down-spin π_{2p}^* orbitals are considered to be the LUMO. In Figure 4.8, the HOMO is set at 0 eV. The σ orbitals are those whose peaks in this figure are half the height of the π orbitals. Interestingly, the GGA exchange-correlation functionals predict the energy of the up-spin σ_{2p} state to be lower than the up-spin π_{2p} state. The opposite is true for the hybrid exchange-correlation functionals. In both cases, there is significant exchange splitting between the up- and down-spin orbitals, with the up-spin channel being shifted to lower energy by the two unpaired electrons in the π_{2p}^* orbitals.

As shown in Table 4.8, using the PBE exchange-correlation functional introduces

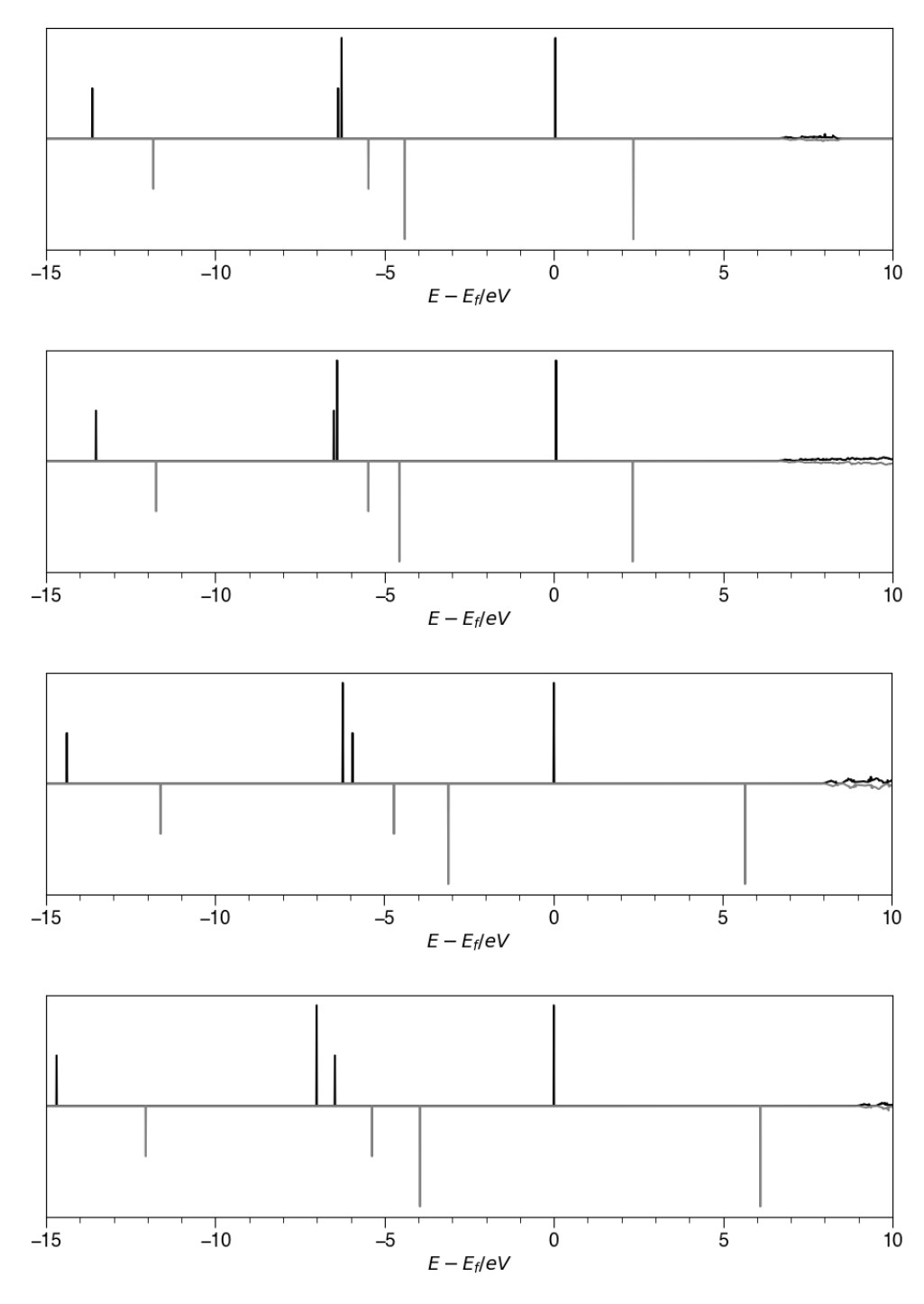


Figure 4.8: The molecular orbitals of the O_2 dimer in the triplet state and their energies as calculated in this work using the (a) PBE, (b) PBEsol, (c) PBE0 and (d) B3LYP exchange-correlation functionals. The up-spin states are shown in black, whilst the down-spin states are shown in grey.

Table 4.8: Bond lengths (L), binding energies (E_{bind}) , and HOMO-LUMO gaps (ΔE_{gap}) predicted using the PBE and PBEsol GGA exchange-correlation functionals and the B3LYP and PBE0 hybrid functionals in this work, compared to previous theoretical and experimental data.

Study	$L/{ m \AA}$	E_{bind}/\mathbf{eV}	$\Delta E_{gap}/\mathbf{eV}$
This work			
PBE	1.236	6.81	2.30
PBEsol	1.227	7.17	2.26
B3LYP	1.225	5.16	6.10
PBE0	1.209	4.42	5.65
Pan et al. (PBE) ^a [271] Pan et al. (HSE06) ^a [271]	1.23 1.21	6.75 5.20	2.30 '> 5'
Lide et al. b [233]	1.21	5.20	-

a DFT study. Exact ΔE_{gap} not reported.

an error of almost 2% in the bond length of the O₂ dimer. Both PBE and PBEsol overestimate the binding energy of the dimer by a considerable amount and, likewise, provide relatively small HOMO-LUMO gaps. The B3LYP hybrid functional exhibits an similar overbinding effect to the GGA functionals, with a bond length of 1.225 Å. However, the binding energy of the O₂ dimer as calculated using B3LYP shows the strongest agreement with the experimental value of 5.23 eV. On the other hand, the PBE0 functional provides a bond length with the closest agreement to the experimental value at 1.209 Å, whilst somewhat underestimating the magnitude of the binding energy at 4.42 eV. Compared to the GGA functionals, the hybrid DFT approach predicts a much larger HOMO-LUMO gap of around 6 eV compared to 2.3 eV, which is commensurate with experimental data. These observations are also in agreement with existing theoretical data on the O-O bond length and binding energy. The work of Pan et al. also predicts a bond length of around 1.23 Å using the PBE functional, and a bond length of 1.21 Å with the hybrid HSE06 functional. Likewise, the binding energies that they report are in line with the values presented herein.

^b Experimental data.

For the purposes of this study on the thermodynamics of oxides, it is computationally prohibitive to study the systems of interest using a hybrid DFT approach. Therefore, the PBE and PBEsol functionals are utilised throughout the rest of this study, and the comparisons to the hybrid DFT data here serves to highlight a source of systematic error introduced by their usage.

Chapter 5

Oxygen Vacancy Formation in the Tungsten Oxides

The contents of this chapter have been published in Computation Materials Science 252 (2025), p. 113781 [1].

Under the Wagner theory of oxidation, discussed in 2.4.3, the growth of the oxide layer is controlled by the rate of ion transport, which is dependent on the concentration gradients through the oxide scale[272]. In this chapter, we examine the thermodynamics and kinetics for oxygen transport, mediated via vacancies, through the tungsten oxide phases WO₂, WO₃, and the so-called 'Magnéli' phases W₁₈O₄₉ and W₂₅O₇₃, shown in Figure 5.1, to better understand the oxidation process. To support this discussion, a detailed review of the physical structure of each phase and investigation into the evolution of their electronic structures with increasing oxygen content is provided.

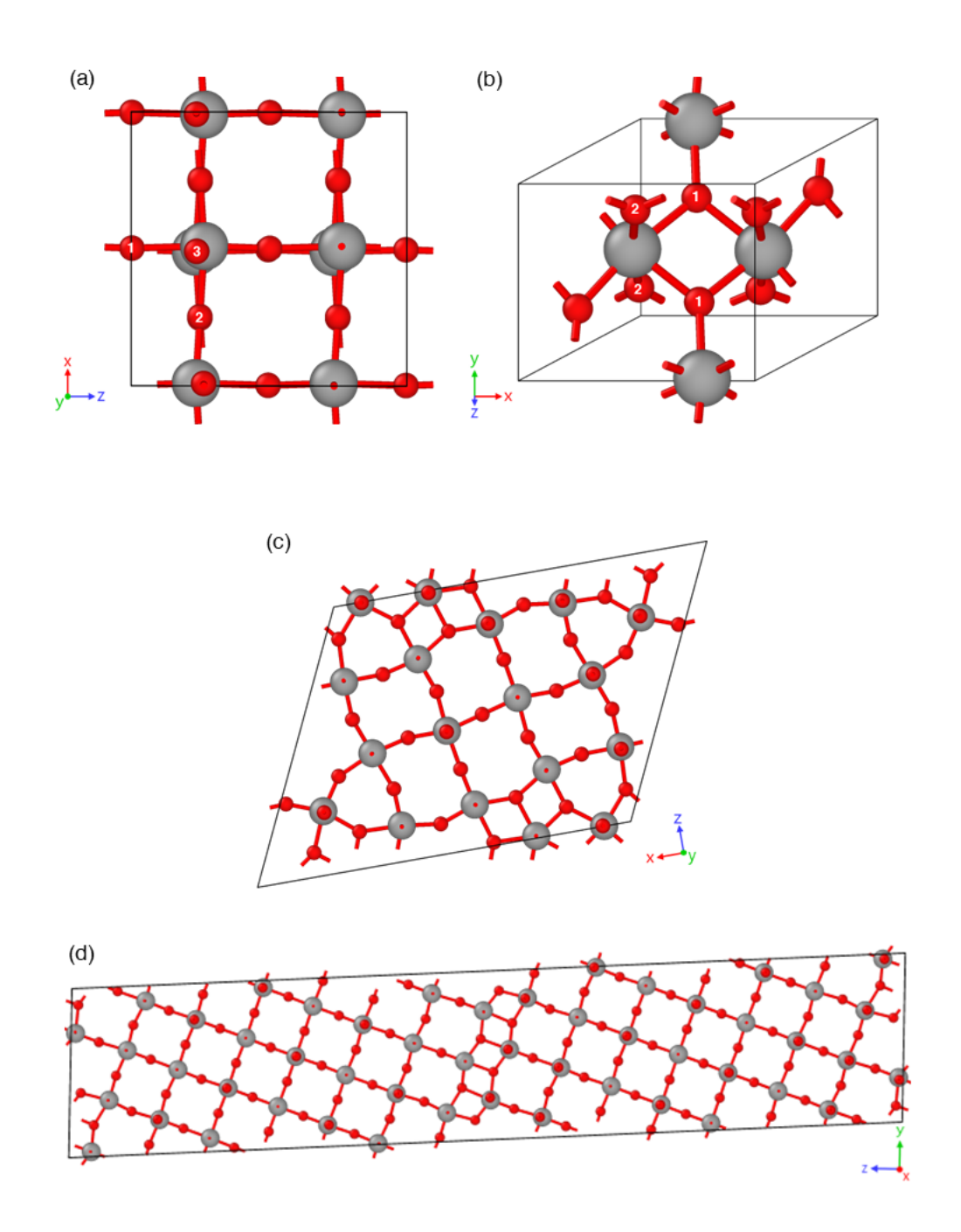


Figure 5.1: Unit cells of (a) WO_3 , (b) WO_2 , (c) $W_{18}O_{49}$ ($WO_{2.72}$) and (d) $W_{25}O_{73}$ ($WO_{2.92}$). Grey atoms denote tungsten. Red atoms denote oxygen. Unique Oxygen sites in WO_2 and WO_3 are denoted by the numbers 1-2 and 1-3, respectively.

Table 5.1: The values of U for each species investigated in this chapter, calculated according to the method detail by Cococionni *et al.* and discussed in Section 3.2.6 [216].

Species	U / eV
\mathbf{WO}_2	4.13
$\mathbf{W}_{18}\mathbf{O}_{49}$	4.23
$\mathbf{W}_{25}\mathbf{O}_{73}$	3.75
\mathbf{WO}_3	5.13

5.1 Methodology

All calculations herein were performed at the DFT level of theory as discussed in Chapter 4. All calculations were performed in spin-polarised mode; the magnetic moments were relaxed during the energy minimisation process and were initially set to $\pm 5.0~\mu\mathrm{B}$ as necessary to test both ferromagnetic, antiferromagnetic and non-magnetic configurations. To account for on-site Coulombic interactions between localised W 5d electrons, all calculations were performed under the rotationally invariant DFT+U formalism as described in Section 3.2.6. As such, the U parameters used in this work are summarised in Table 5.1.

The formation energy of the oxygen vacancies in the tungsten oxide phases was calculated according to Equation 2.16 in Section 2.3.3. Since WO₃ is non-metallic and may exhibit multiple charge states, it was necessary to calculate the dielectric tensor for WO₃ ab initio, using density functional perturbation theory (DFPT) as implemented in VASP. The dielectric tensors for all other phases were not required, as the charge correction factor (see Equation 2.17) inherently reduces to zero for uncharged systems. For WO₃, the calculated dielectric tensor was predicted to be roughly isotropic:

$$\epsilon = \begin{bmatrix} 57.02 & 0.01 & -0.07 \\ -1.02 & 58.06 & -1.02 \\ -0.07 & 0.01 & 54.77 \end{bmatrix}$$

$$(5.1)$$

This dielectric tensor differs quite significantly from the dielectric tensors used in some of the studies which this work has been compared against. For instance, Linderälv calculated an anisotropic dielectric tensor [273]:

$$\epsilon = \begin{bmatrix} 72.00 & 0.00 & -1.93 \\ 0.00 & 38.73 & 0.00 \\ -1.93 & 0.01 & 8.32 \end{bmatrix}$$
 (5.2)

On the other hand, the experimental work of Deb predicts an isotropic dielectric tensor with diagonal elements of 30 [274]. The Materials Project database reports the dielectric tensor of WO_3 as [231]:

$$\epsilon = \begin{bmatrix} 38.79 & 0.00 & 0.49 \\ 0.00 & 170.8 & 0.00 \\ 0.55 & 0.00 & 196.5 \end{bmatrix}$$
 (5.3)

Therefore, it is expected that some discrepancy between the oxygen vacancy formation enthalpy of WO_3 in the +1 and +2 charged states may arise from the difference in the charge correction term.

The chemical potential of oxygen was defined at two limits. Under the oxygenrich condition, μ_O^{O-rich} was determined as described in Section 4.6. In the oxygenpoor limit, the chemical potential was determined according to:

$$\mu_O^{\text{O-poor}} = \frac{\mu_{W_y O_x} - y \mu_{W_{(s)}}}{x} \tag{5.4}$$

where $\mu_{W_yO_x}$ and $\mu_{W_{(s)}}$ are the chemical potentials of the tungsten oxide and tungsten metal, respectively.

The migration barriers of oxygen diffusion were calculated using the climbing image nudged elastic band method as implemented in the VASP Transition State Tools package [201]. This procedure is discussed in Section 3.1.5. In the case of WO_3 , the migration energies for the +2, +1 and 0 charge states were calculated individually.

5.2 Results and Discussion

5.2.1 Stability at 0 K

An initial search of the tungsten-oxygen system was carried out to obtain the enthalpy of formation of the tungsten oxides across a range of oxygen concentrations. As such, the resulting convex hull is shown in Figure 5.2, with a more detailed section between 60 and 80 at% O shown in Figure 5.3. The initial structures were obtained from a range of experimental and theoretical sources listed on the Inorganic Crystal Structure Database (ICSD) and the Materials Project database [275, 231]. Two of the tungsten oxide phases - W₃O and NaCl-like WO had positive values of ΔH_f , at +0.74 eV at⁻¹ and +0.23 eV at⁻¹, respectively. The stable phases of the tungsten-

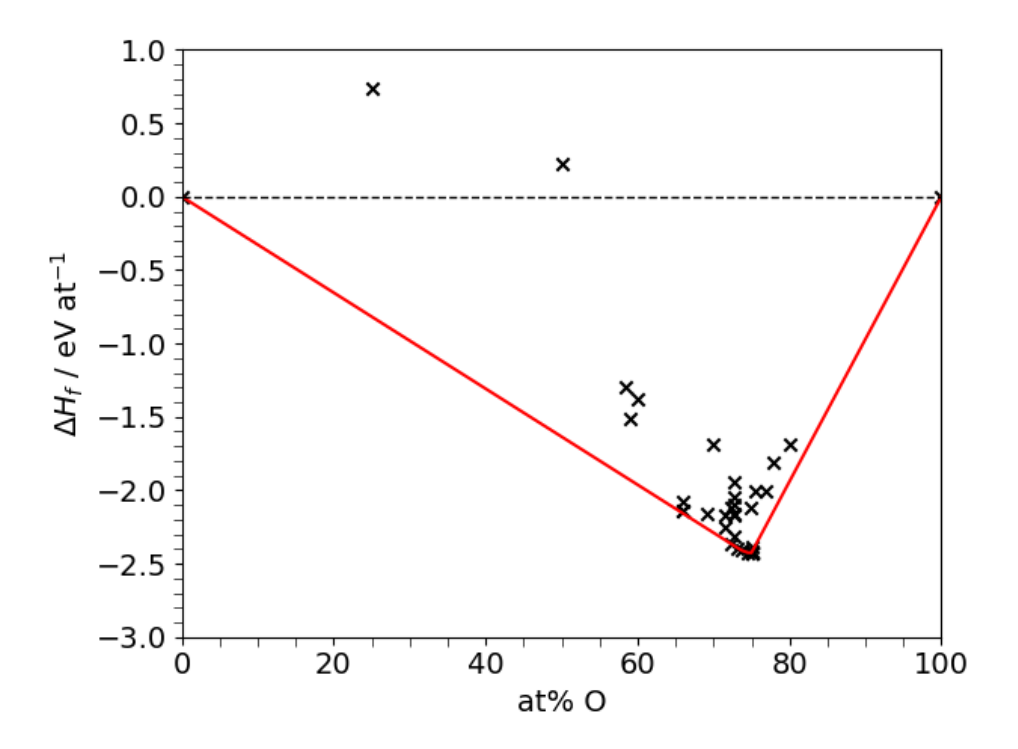


Figure 5.2: The convex hull showing the enthalpies of formation for a wide range of W_xO_y systems as a function of the atomic percentage of oxygen. The red line denotes the convex hull itself, consisting of the thermodynamically stable tungsten oxide phases.

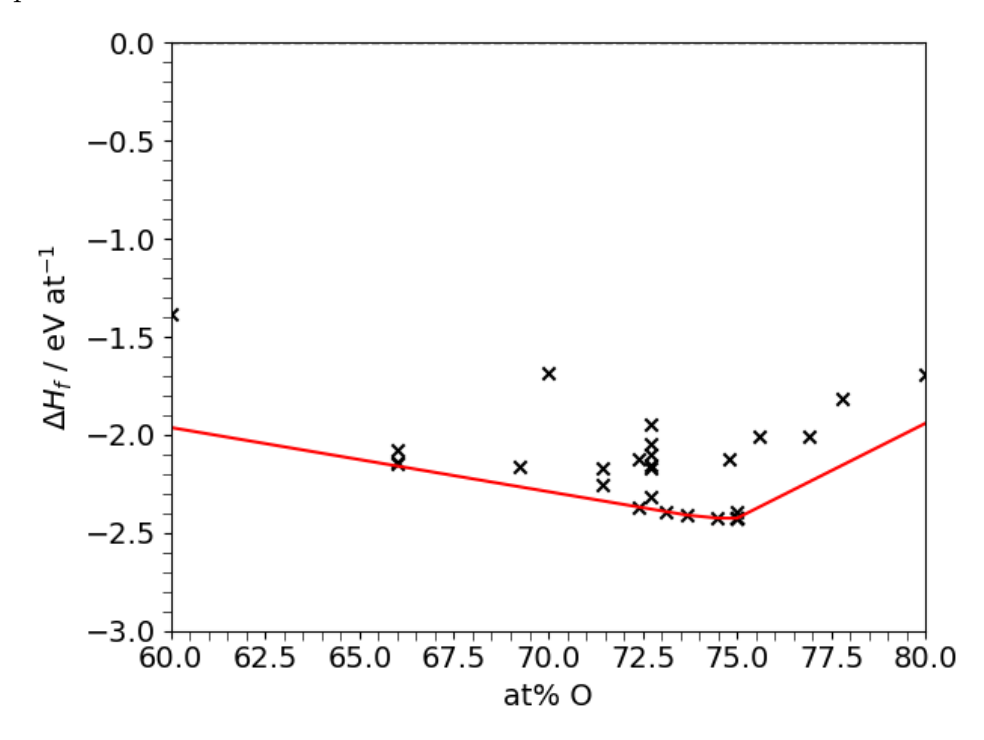


Figure 5.3: The section of the W_xO_y convex hull (shown above) from 60 to 80 at% O, showing the stable tungsten oxide phases.

oxygen system predicted by this convex hull were WO₂, WO_{2.625}, WO_{2.72}, WO_{2.8}, WO_{2.92} and WO₃, and are shown more clearly in Figure 5.3, represented as the points which lie on the convex hull itself (denoted as a red line). Of these, WO₂, WO_{2.72}, WO_{2.92} and WO₃ were selected for further study. Their crystal structures are presented in Figure 5.1 and was discussed in more detail in Section 2.4.2.

5.2.2 Crystal Structure

For each phase of interest, the lattice parameters, cell angles and band gaps calculated using different exchange-correlation functionals are presented in Table 5.2. Local and semi-local exchange-correlation functionals, such as the LDA and GGA functionals, are known to underestimate the band gap, E_g . In contrast, hybrid functionals such as HSE06 are expected to give much more accurate values [281]. However, using hybrid functionals is prohibitively costly for studying the large number of defect formation energies required in this work. Further, there are known issues with using hybrid functionals in calculations concerning metallic materials [282]. Therefore, the HSE06 functional was only used to examine bulk WO₃ in this work.

For room-temperature monoclinic WO₃, the results presented in Table 5.2 show that the DFT simulations performed here overestimate the lattice parameters, irrespective of the functional used and are particularly marked for the semi-local functionals. As highlighted in Table 5.2, this overestimation has been observed in several studies using different functionals, DFT codes and parametrisations. While it is true that the PBE typically overestimates lattice parameters and the LDA underestimates them, both overestimate the volume of WO₃. The employment of the hybrid functional, which offers a better description of the correlated WO₃, somewhat ameliorates the problem. However, there is still evidence of some overestimation of the lattice parameter, and the *U*-parameter appears to have little impact on this

parameter of '-', while DFT studies without a U correction are listed as U=0. Band gaps not evaluated are marked with a '-'. Table 5.2: Lattice parameters and band gaps (E_g) , where applicable, for WO₃, WO₂, W₁₈O₄₉, and W₂₅O₇₃. Asterisks (*) denote parameters, cell volumes, and band gaps calculated in this work. Experimental values are indicated with a U

Sundberg et al.	PBE	PBE *		Salje et al.	PBE	PBE *		Bolzan $et al.$	PBE	PBE	PBE *	LDA *		Loopstra et al.	Saenz et al.	Tanisaki et al.	PBE	HSE06	HSE06 *	PBE *	LDA *		XC Functional U / eV a / Å) b / Å c Å
ı	5.20	3.75		1	5.20	4.13		ı	5.20	0.00	4.84	4.84		1	ı	ı	5.20	0.00	0.00	5.13	5.13		U / eV
11.93	12.26	12.12		18.33	18.29	18.32			5.62	5.82	5.61	5.52		7.31	7.30	7.30	7.72	7.39	7.53	7.71	7.61		a / Å)
3.82	3.86	3.86 59.	W_{25}	3.79 14.0	3.86	3.78	W_{18}	4.90	4.95	4.96	4.95	4.89	WO_2	7.54	7.54	7.53	7.68	7.64	7.62	7.68	7.61	W	b / Å
59.72	60.57	59.83	O_{73}	14.04	14.20	14.03	O_{49}	5.66	5.72	5.75	5.72	5.64	<i>O</i> ₂	7.69	7.69	7.68	7.75	7.75	7.69	7.74	7.63	ွှ	c Å
98.30	97.91	93.51		115.20	109.71	115.21		120.68	120.93	120.48	120.93	120.42		90.90	90.91	90.54	91.50	90.30	90.77	90.09	90.01		β /°
2721.60	2866.39	2799.03		995.41	1008.87	971.57		154.48	159.12	156.44	165.99	152.24		423.85	423.27	422.16	459.49	440.43	445.76	458.30	441.87		$\beta / \sim V / \mathring{\mathbf{A}}^3$
ı	1	1		1	ı	1		ı	ı	ı	ı	ı		$2.6 \sim 3.2$	ı	1	ı	2.80	2.53	1.34	0.79		E_g (eV) Ref
[136]	[231]	ı		[280]	[231]	1		[279]	[231]	[134]	1	1		[278]	[277]	[140]	[231]	[276]	ı	ı	ı		Ref

Table 5.3: Optimised bond lengths in WO_3 and WO_2 . The number of the oxygen atom in the W-O bond is given in Figure 5.4.

	7	W - O_x	Bond	Leng	h / A	Å
XC Functional	1	2	3	4	5	6
			W	\mathbf{O}_3		
LDA	1.93	1.88	1.90	1.91	1.95	1.86
PBE	1.87	2.00	1.96	1.90	1.85	2.03
HSE06	1.81	2.00	2.01	1.82	1.76	2.16
			\mathbf{W}	\mathbf{O}_2		
LDA	2.06	2.06	2.00	2.00	2.00	1.95
PBE	2.07	2.05	2.09	2.11	2.03	2.01

fact.

Upon examination of individual W-O bond lengths within one WO₆ octahedra, it can be seen that the average bond length in WO₃ is around 1.94 Å when optimised using the PBE exchange-correlation functional. As shown in Table 5.3, there is a considerable distortion in the a-axis when optimised using the PBE functional. The deviation in our calculated structural parameters may be due to the initial structure employed in these calculations, which were available on the Inorganic Crystal Structural Database [283, 136, 284]. Namely, there is a degree of uncertainty in the positions of oxygen ions introduced by the Rietveld refinement of neutron powder refraction and X-ray diffraction experiments [285, 286, 287]. Combined with the close similarities in structure between the various WO_3 phases, there is an increased likelihood of the structure relaxing into a local DFT minimum, which is not the global minimum on the potential energy surface. As a precaution against this, the symmetry of the system was not constrained during ionic relaxation, and the choice of electronic convergence criterion in the determination of the wavefunction at each step was tightened to ensure that highly accurate forces acting on each atom were predicted.

A similar discrepancy compared to experimental data was observed for mono-

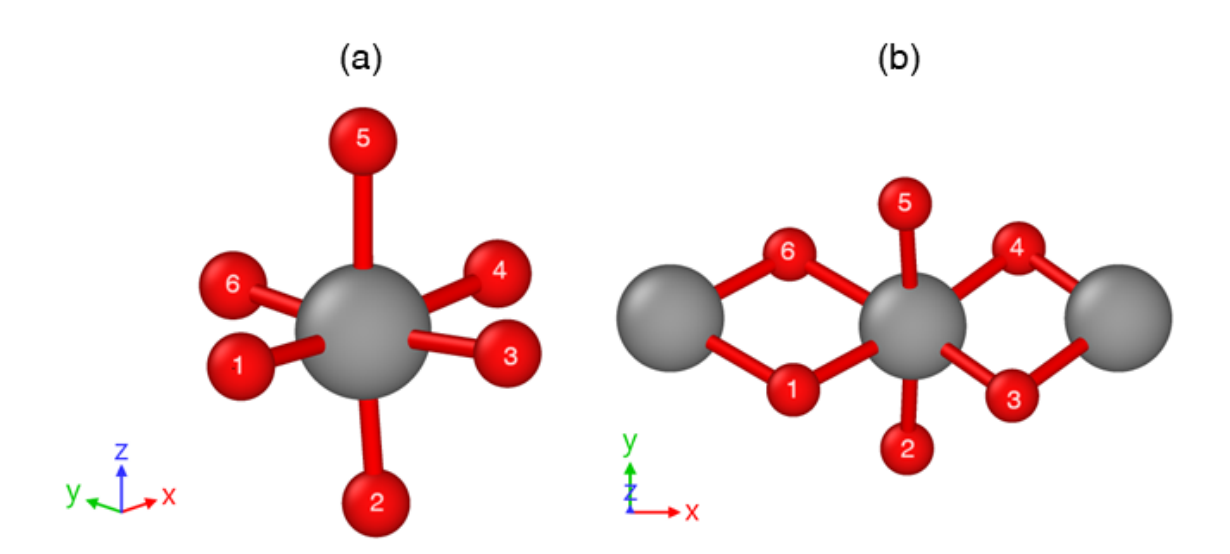


Figure 5.4: The numerical labels assigned to oxygen atoms in (a) WO_3 and (b) WO_2 for discussion of W-O_x bond lengths. Grey atoms represent tungsten and red atoms represent oxygen. The labels 1-2 for WO_2 and 1-3 for WO_3 also correspond to the unique oxygen sites highlighted in Figure 5.1.

clinic WO₂ using the PBE functional, particularly in the a- and c-axes. However, the results align with previous DFT studies on the same phase [231, 134]. In addition, the average bond length in WO₂ optimised using the PBE exchange-correlation functional is 2.08 Å. This is considerably higher than the average bond length in WO₃. However, there is much more distortion in the bond lengths in WO₂ when optimised using the PBE functional compared to the LDA functional.

 $W_{25}O_{73}$ and $W_{18}O_{49}$ were optimised using only the PBE exchange-correlation functional. The lattice parameters obtained for these phases are much closer to the experimentally observed values. However, the computed values in the a- and c-axes for $W_{25}O_{73}$ are slightly larger. Upon examination of the structure of $W_{25}O_{73}$, the overestimation of the lattice parameters in the a- and c-axes may be attributed to the similarity in geometry between this phase and WO_3 , as the former contains large regions of corner-sharing WO_6 octahedra whilst the latter consists solely of the same octahedral motifs.

5.2.3 Electronic Structure

The projected density of states (PDOS) for each phase was obtained using the PBE functional with the DFT+U formalism. Figure 5.5 shows the gradual evolution of the total density of states with increasing oxygen content, from WO₂ through to WO₃. The PDOS of the W 5d and O 2p states are shown in blue and red, respectively, and each plot is shifted such that the Fermi level is at zero. WO_2 , $W_{18}O_{49}$ and $W_{25}O_{73}$ are all predicted to be metallic, with their Fermi levels lying within bands exhibiting primarily W 5d character. It is noted that the density of states in WO_2 just above the Fermi level is non-zero, hence, despite it is not an insulator as the scale of Figure 5.5 might otherwise suggest. Experimentally, $W_{18}O_{49}$ is shown to possess semiconductor properties due to its surface being covered with oxygen atoms; however, bulk W₁₈O₄₉ is metallic [288]. In WO₂, there is a band of W 5d states just below the Fermi level; as the oxygen content of the system increases, this band increases in energy and eventually forms the conduction band seen in the DOS of WO₃. The Magnéli phases exhibit features from the DOS of both WO₂ and WO_3 , and the band gap exhibited in WO_3 can first be seen in the DOS of $W_{18}O_{49}$, although the Fermi level still lies within the band.

The magnetic moments of each atom in each phase were allowed to relax to their lowest-energy configurations. WO₂ was predicted to be ferromagnetic with magnetic moments of $+0.5~\mu_B$. This magnetic ordering is also predicted by the high-throughput calculations recorded on the Materials Project database. On the other hand, Kuklin *et al.* report that antiferromagnetic ordering is favourable, with magnetic moments of $\pm 0.4~\mu_B$. The experimental work of Dissanayake *et al.* reports that WO₂ is weakly paramagnetic at all temperatures [289]. In W₁₈O₄₉, ferrimagnetic ordering was predicted with magnetic moments ranging from +0.146 to $+0.494~\mu_B$ on each W atom. The distribution of magnetic moments is shown in Figure 5.6. In W₂₅O₇₃, a total magnetic moment of $+0.005~\mu_B$ was

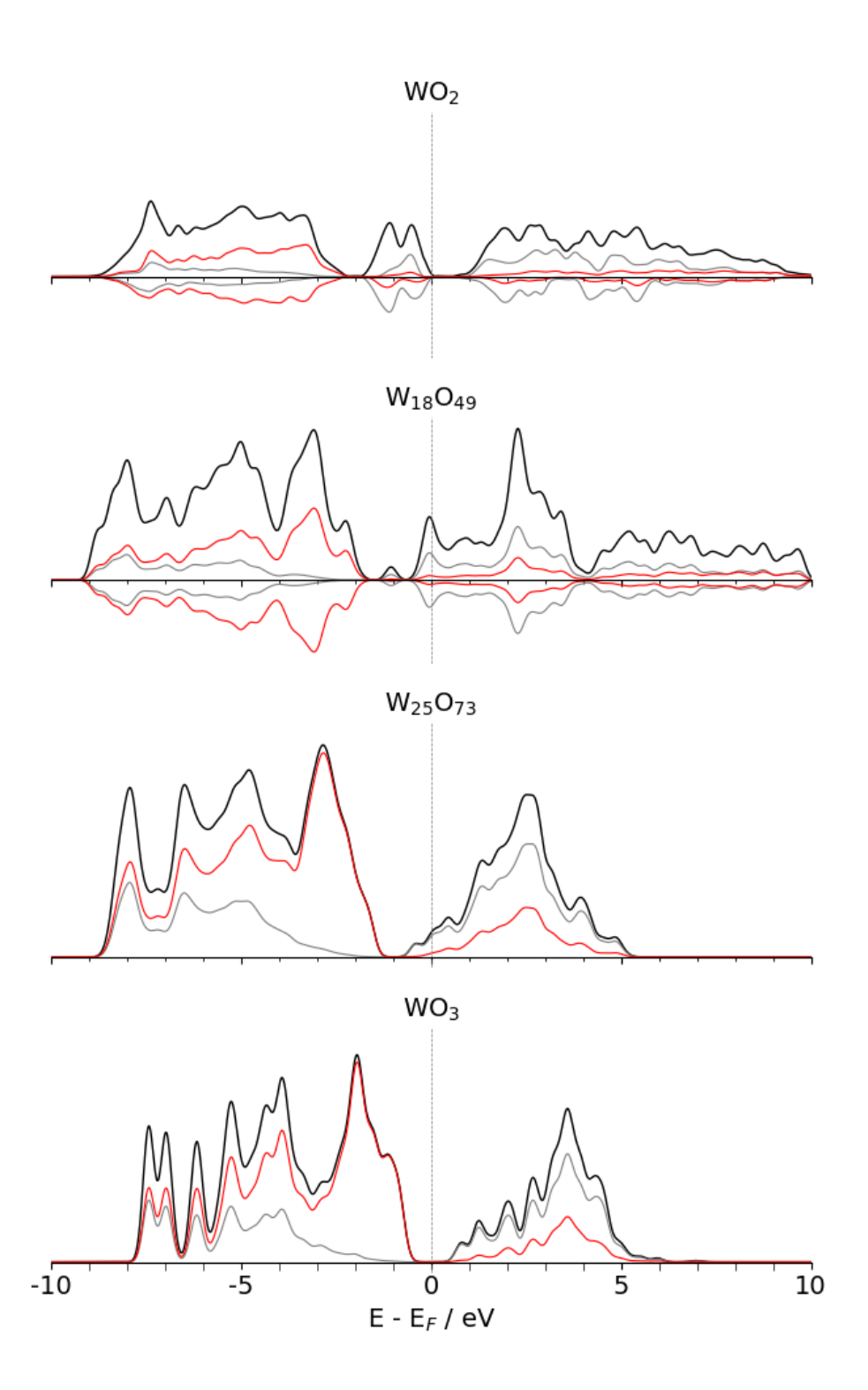


Figure 5.5: Projected and total density of states of the tungsten oxide phases investigated in this study. The Fermi level was set to zero. The black line represents the total density of states and the red and grey lines represent the projected density of states for the O 2p and W 5d orbitals respectively. The grey vertical line denotes $E - E_f = 0$.

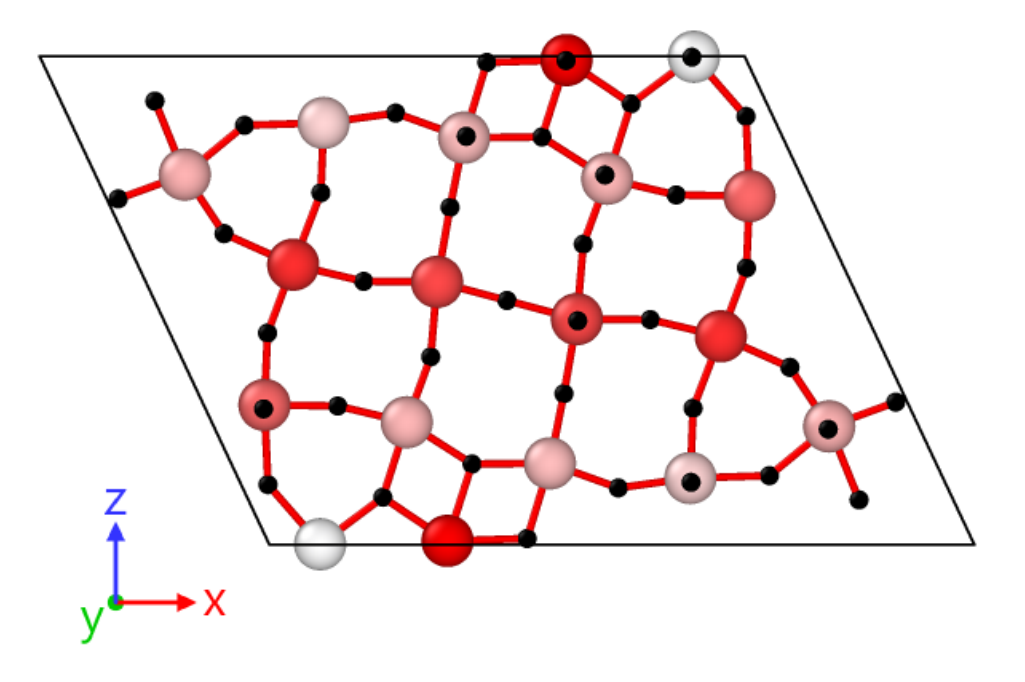


Figure 5.6: Distribution of magnetic moments in $W_{18}O_{49}$, ranging from 0.000 μ_B (white) to +0.494 μ_B (red). The larger atoms denote tungsten, whilst the smaller atoms denote oxygen.

predicted, indicating negligible magnetic ordering. Finally, in WO₃, the ground state configuration in these calculations was non-magnetic. It is known experimentally that WO₃ is paramagnetic, however, due to the limitations of the DFT method, the paramagnetic ordering in WO₃ cannot be accurately represented, and therefore the non-magnetic configuration is taken as the best available approximation [141]. Nevertheless, the decreasing magnetic moments between WO₂ and WO₃ are commensurate with magnetic susceptibility experiments performed on these phases [290]. Henceforth, any discussion regarding the perfect crystals of these phases refers to those in their magnetic ground states described here.

As discussed above, semi-local functionals typically underestimate the band gaps in insulating materials. This is evident in Figure 5.5 where, for WO₃, the band gap is shown to be about 1.34 eV. This is almost half of the experimentally observed values, which lie in the range 2.6 to 2.8 eV. Varying the U parameter between U=0 eV and U=6 eV has a marginal effect on the size of the band gap in WO₃, as shown in Figure 5.7; an increase in the U parameter from 0 to 5.13 eV raised the band gap by approximately 0.2 eV. This is likely due to the effective +6 charge on W in WO₃, resulting in a de-occupation of the 5d orbitals, meaning that the effect of applying a correction to these orbitals is minimal. However, using the hybrid HSE06 functional, the band gap is predicted to be $E_g=2.53$ eV, which closely matches previous hybrid DFT studies on WO₃ (2.56 eV)[276] as well as experimental values [278].

5.2.4 Oxygen Vacancy Formation Energies

The oxygen vacancy formation energies for WO₃ as a function of the Fermi level are presented in Figure 5.8 (note the plot is presented up to the band gap predicted using the HSE06 functional). In each plot, the black line denotes the vacancy formation energy of the V_{O1} defect, the blue line the V_{O2} and the red line the V_{O3} defect. The positions of these defects are shown in Figure 5.1. The overall trend is as would

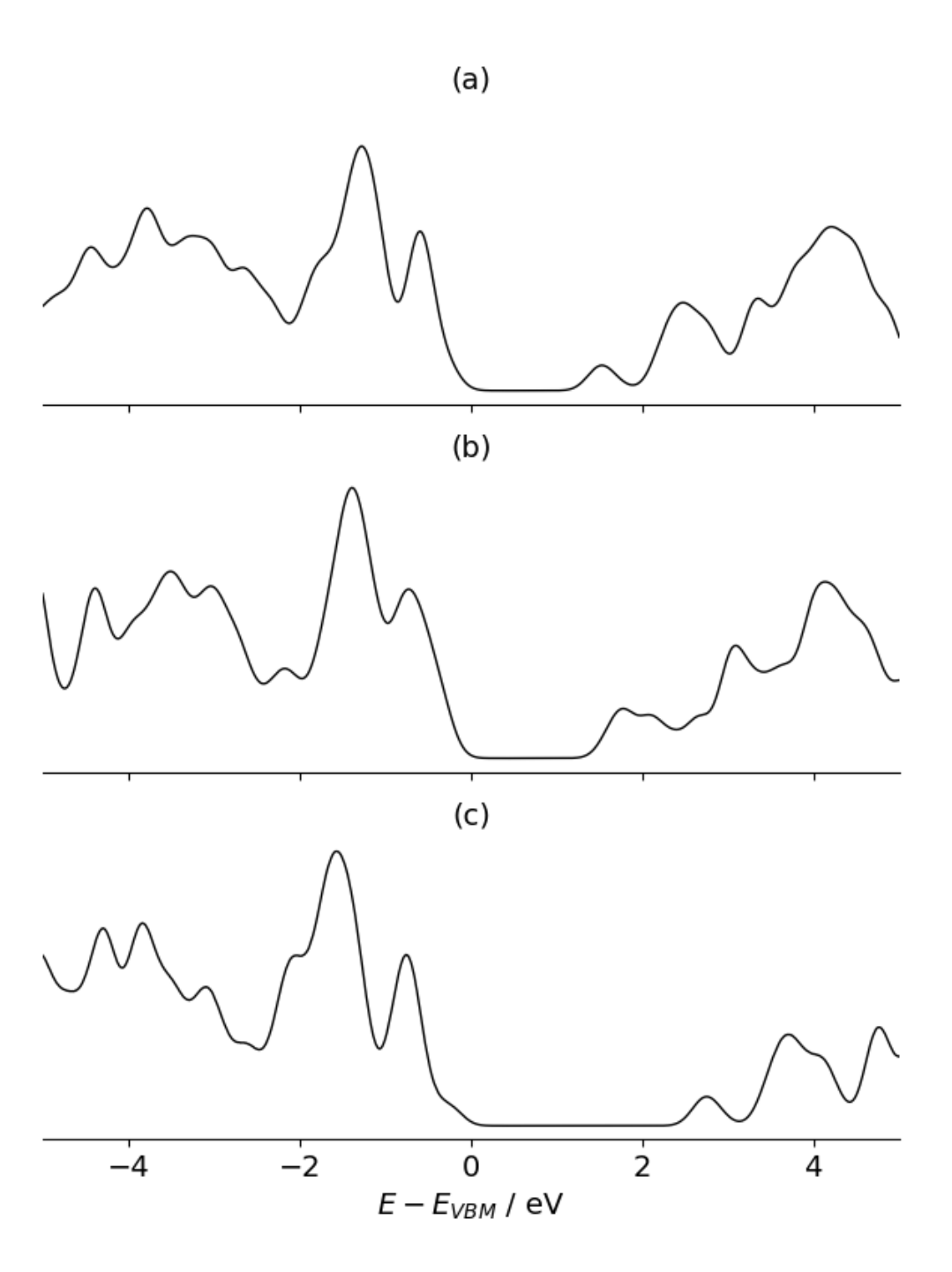


Figure 5.7: Total electronic density of states for monoclinic WO_3 , calculated with a U parameter of (a) 0 eV and (b) 5.13 eV. The total electronic density of states, as calculated using the HSE06 hybrid functional, is shown in (c). The plots have been centered on the valence band maximum for ease of comparison.

report values only under O-rich conditions. the valence band maximum. In the O-rich case, the oxygen chemical potential is taken as half the energy of the O_2 molecule; in the O-poor case, it is determined from the oxide and the metal. Chatten et al. [291] and Lambert-Mauriat et al. [292] Table 5.4: Defect formation energies for oxygen vacancy defects in WO_2 and WO_3 . For WO_3 , all defect energies are quoted at

Oxide	Defect	Charge	This	Work	Linder	älv [273]	Chatten [291]	Lambert-Mauriat [292]
			O-rich	O-poor	_	O-poor	O-rich	O-rich
WO_3	V_{O1}	0	3.22	0.75		0.77	4.53	3.52
WO_3	$V_{\rm O2}$	0	3.11	0.65		0.67	4.41	3.06
WO_3	V_{O3}	0	3.28	0.81		0.77	3.46	2.87
WO_3	V_{O1}	土	1.18	-1.29		-0.99	ı	ı
WO_3	$V_{\rm O2}$	+	1.03	-1.44		-1.19	ı	ı
WO_3	V_{O3}	+	1.14	-1.33		-0.99	ı	ı
WO_3	V_{O1}	+2	-0.76	-3.23		-2.65	ı	ı
WO_3	$V_{\rm O2}$	+2	-0.95	-3.42		-2.85	ı	1
WO_3	$V_{\rm O3}$	+2	-0.84	-3.30		-2.65	ı	ı
WO_2	V_{O1}	0	5.48	4.56		2.48	ı	ı
WO_2	$V_{\rm O2}$	0	4.38	3.46		3.04	ı	ı

be expected for a typical oxygen vacancy, with the $V_{\rm O}^{2+}$ defect dominant at the valence band maximum and a transition to the $V_{\rm O}^0$ defect just past the midgap. On first inspection this may appear to contrast with the results of Linderälv, where the transition appears much closer to the conduction band, however, this is due to the choice of bandgap. In this work the x-axis extends to the HSE06 bandgap of 2.53 eV, while Linderälv only considers up to 1.7 eV, which is the bandgap from the PBE functional, when plotted on the same axis, the results look similar. A more detailed comparison of the formation energies is presented in Table 5.4.

This work and that of Linderälv [273] employ different approaches to account for finite size effects, making the comparison of charged defects in WO₃ complex. Therefore, the charge-neutral defects are considered first. Under oxygen-rich conditions, the formation energies calculated in this study are between 3.11 and 3.22 eV compared to Linderälv's values of 3.34 to 3.44 eV with a discrepancy on the order of 0.2 eV. This small discrepancy may arise due to the chemical potentials or the choice of the exchange-correlation functional (here the PBE was used, whereas Linderälv employed the vdW-DF-CX functional). It should be noted that the difference in the formation energies for the defects under oxygen-rich and poor conditions are also very similar with 2.47 eV determined here compared to 2.67 eV from Linderälv. In the Linderälv study the V_{O2} defect was predicted to have the lowest formation energy and a similar trend is observed here. This study suggests that there is a small energy difference between the oxygen vacancy on the O1 and O3 sites, while Linderälv predicts them to have the same energy. As the charge state of the defect increases the discrepancy between the tresults determined here and Linderälv increases, with differences of ~ 0.5 eV and ~ 0.75 eV for the +1and +2 charge states respectively. This may be a result of the different correction methods used to address the finite-size effects. Both techniques employ a point charge correction that considers the dielectric properties of the host material. There are significant differences between the dielectric tensors determined for WO₃ here

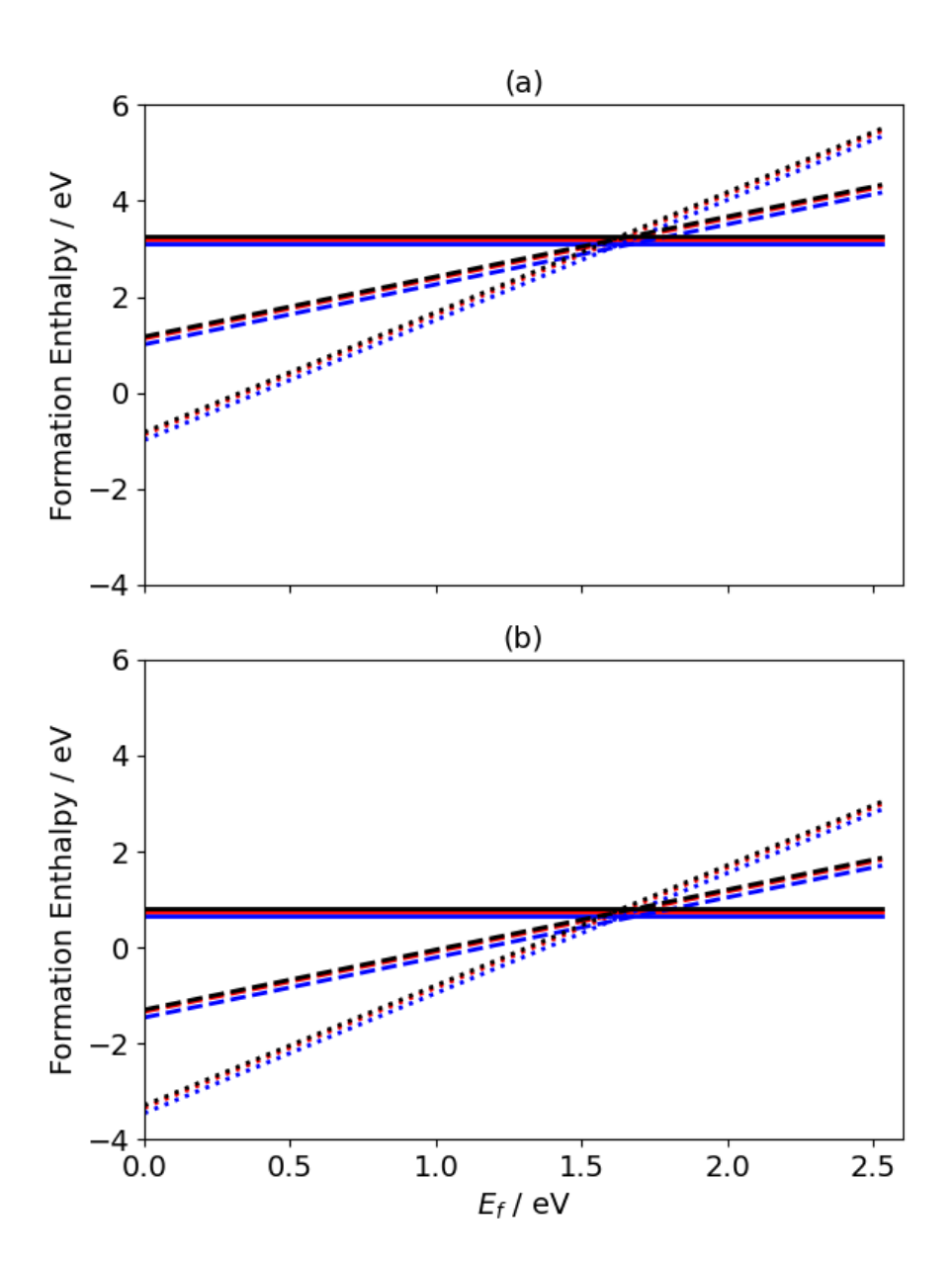


Figure 5.8: Oxygen vacancy formation energy in tungsten trioxide as a function of the Fermi level in the (a) O-rich and (b) O-poor limits. The solid line denotes the +0 charge state, the dashed line denotes the +1 charge state, and the dotted line denotes the +2 charge state. The valence band maximum lies at 0 eV, whilst the conduction band maximum begins at 2.53 eV. The blue line the $V_{\rm O2}$ and the red line the $V_{\rm O3}$ defect.

and that predicted by Linderälv, which may explain the discrepancy. Ultimately, however, the overall agreement with the work of Linderälv is good for the defects in WO₃. Several other studies have also calculated formation energies for the charge-neutral oxygen vacancy. Both Chatten et al. [291] and Lambert-Mauriat et al. [292] predict an ordering of $V_{O3} < V_{O2} < V_{O1}$ for the thermodynamic stability of the oxygen vacancy defects, which disagrees with both the ordering predicted here and that of Linderälv [273]. It should be noted these works used relatively small supercells, however, the values are in the same range. Further, values of 3.72 and 5.3 eV have been presented by Trioni et al. [293] and Wang et al. [294], however, they do not quote which site they had simulated. This final value from Wang et al. is an outlier, however, it should be noted that it is the only simulation to employ a hybrid functional.

WO₂ is metallic, therefore, only the neutral charge state is considered for the two unique oxygen vacancy sites, labelled 1 and 2 in Figure 5.1. The values calculated for the oxygen vacancy formation energies in WO₂ are summarised in Table 5.4, clearly showing the wide range of formation energies and the effect of the chemical potential of oxygen. In the oxygen-poor limit, the values presented here agree with those proposed by Huang et al. (2.49 eV), who calculated the chemical potential of oxygen in the manner described here with a U parameter of 6.2 eV [295]. By contrast, the values presented in this work are considerably higher in the oxygen-rich limit than those proposed by Linderälv (3.54 eV and 2.98 eV respectively). This is not likely due to the choice of chemical potential as these appear to be relatively similar based on the WO₃ results. The difference between the oxygen-rich and poor regimes have been reduced to \sim 1.05 eV here and 0.5 ev for Linderälv. In addition to the energies being distinctly different, the ordering of the sites is also different. This may be a labelling issue as it is difficult to identify sites from the images presented in this previous study.

The Magnéli phases $W_{18}O_{49}$ and $W_{25}O_{73}$ are vastly more complicated than

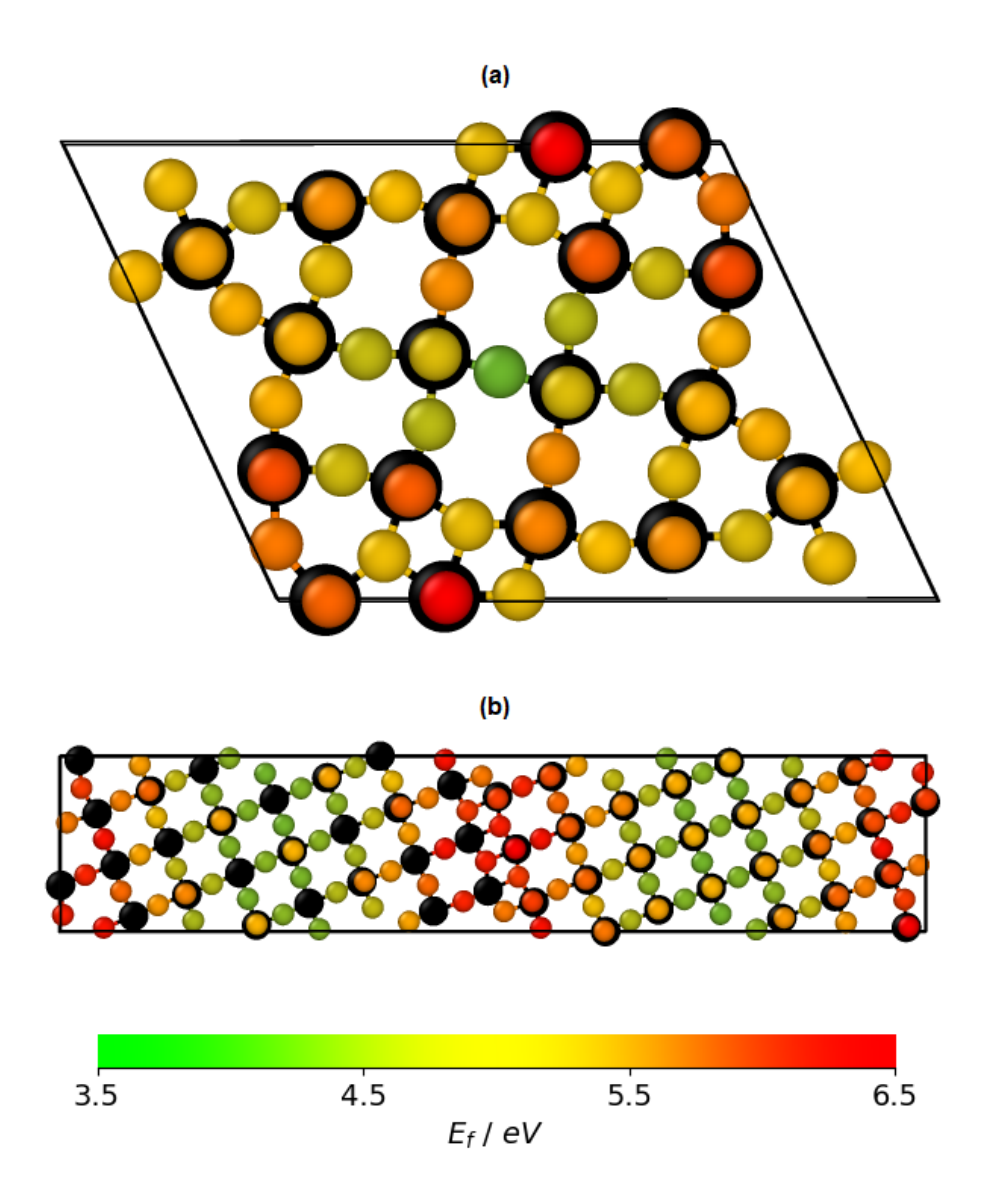


Figure 5.9: Oxygen vacancy formation energies in the Magnéli phases (a) $W_{18}O_{49}$ and (b) $W_{25}O_{73}$. The black atoms represent tungsten, whilst the oxygen atoms are coloured according to their oxygen vacancy formation enthalpy. The formation enthalpies are calculated in the O-rich limit.

those of WO_2 and WO_3 . These phases have 25 and 147 unique oxygen vacancy sites, respectively. Therefore, the oxygen vacancy formation energies in the oxygen-rich limit are shown in Figure 5.9. The highest values of the vacancy formation energies occur in regions of the unit cell which are comprised of WO_2 -like motifs, whereby each oxygen atom is coordinated to three tungsten atoms. Oxygen vacancy formation energies in these regions are as high as 6.57 eV in $W_{18}O_{49}$. On the other hand, the lowest oxygen vacancy formation energy is found in the center of the unit cell, bridging two WO_6 octahedra, with a value of 3.55 eV.

The bond W-O bond lengths in both W₁₈O₄₉ and W₂₅O₇₃ are shown in Figure 5.10. In regions where the oxygen vacancy formation energy is higher, oxygen is coordinated to three tungsten atoms with bond lengths ranging from 1.98 to 2.09 Å. This is comparable to the W-O bond lengths predicted in WO₂, which are around 2.08 Å. Lower oxygen vacancy formation energies are found in regions where oxygen is coordinated to only two tungsten atoms (as in WO₃), where shorter bond lengths of between 1.84 and 1.97 Å are observed. Again, this is comparable to the W-O bond lengths predicted in WO₃, which are around 1.94 Å. From these observations, the Magnéli phases appear to be composed of WO₃-like and WO₂-like regions, both in terms of physical and electronic structure.

5.2.5 Oxygen Vacancy Migration Barriers

Finally, we present the migration barriers between oxygen vacancy sites in WO₃ and WO₂. The values calculated for the neutral (q = 0) system closely correspond to existing data reported by Le *et al.*, who reported migration barriers of ≈ 0.14 eV for the V_{O1} \longleftrightarrow V_{O2} pathway and values between $0.87 \approx 1.07$ eV for the V_{O1} \longleftrightarrow V_{O3} pathway [296]. Therefore, the accuracy of NEB calculations employed in this chapter are considered sufficient.

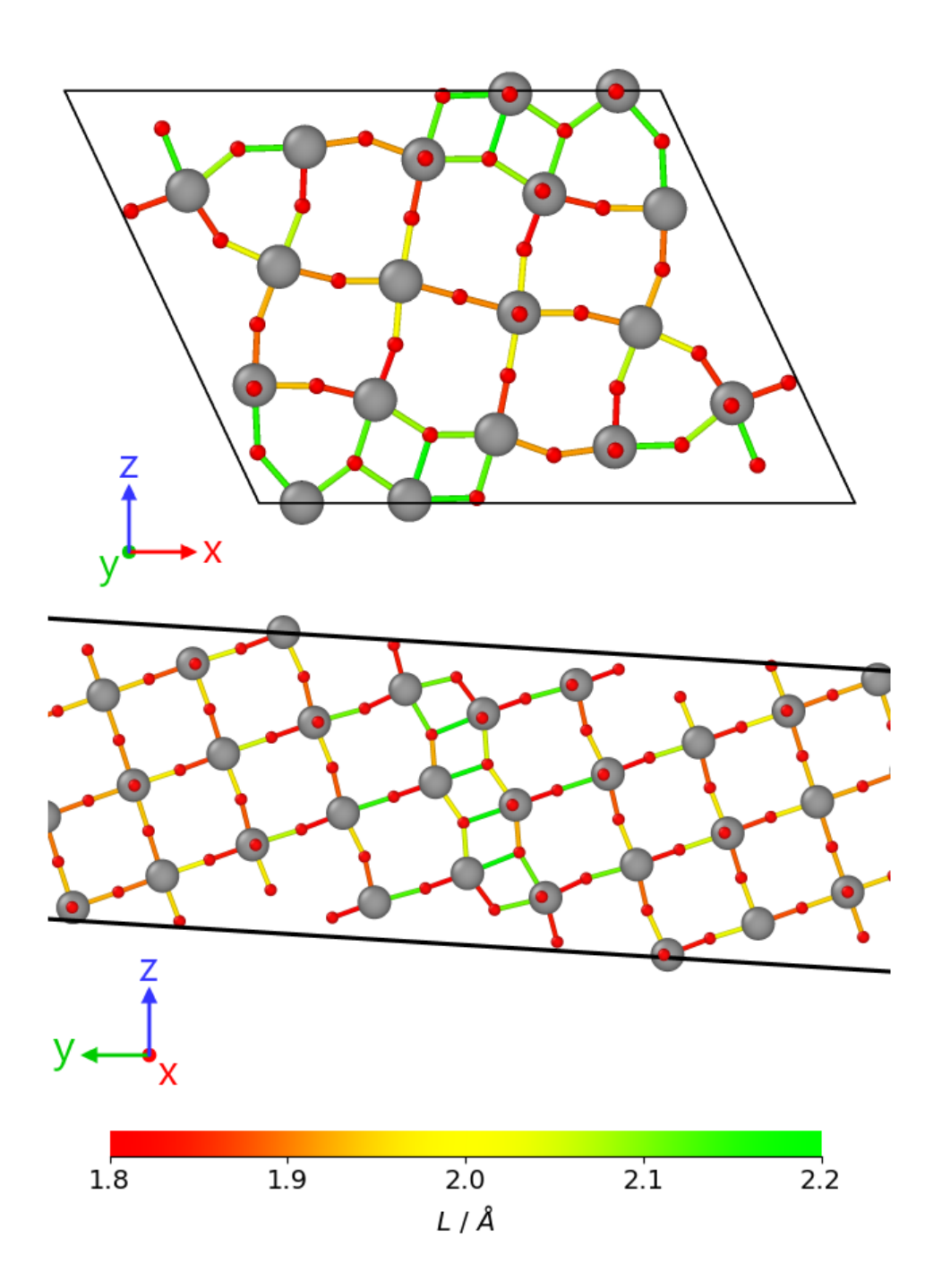


Figure 5.10: Bond lengths in $W_{18}O_{49}$ and $W_{25}O_{73}$. The view of $W_{25}O_{73}$ has been truncated along the y-axis for clarity.

Table 5.5: Oxygen vacancy migration barriers through tungsten trioxide in the +0, +1, and +2 charge states between two unique oxygen vacancy sites, i.e., A to B. Values for the reverse migration (B to A) are included in brackets.

	$\Delta H_{V_A \leftrightarrow V_B} \ / \ { m eV}$					
${f q}$	$1 {\leftrightarrow} 2$	$1{\leftrightarrow}3$	$2 {\leftrightarrow} 3$			
0	0.153 (0.733)	0.765 (0.781)	0.799 (0.234)			
+1	$0.222 \ (0.750)$	$0.665 \ (0.664)$	$0.791 \ (0.262)$			
+2	0.126 (0.741)	0.726(0.741)	$0.780 \ (0.161)$			

Table 5.6: Oxygen vacancy migration barriers through tungsten dioxide. As there are only two unique oxygen vacancy sites, the migration barrier between two identical, adjacent vacancy sites has also been included.

$$\begin{array}{c|c} & \Delta H_{V_A \leftrightarrow V_B} / \mathbf{eV} \\ \mathbf{q} & 1 \leftrightarrow 2 & 1 \leftrightarrow 1 \\ \hline \mathbf{0} & 1.81 \ (2.90) & 3.12 \ (3.12) \end{array}$$

As shown in Table 5.5, the migration barrier required to migrate the V_{O1} vacancy to V_{O2} vacancy, and from V_{O3} to V_{O2} , are considerably smaller than the energy required to move between vacancies V_{O1} and V_{O3} . This corresponds to a preference for oxygen moving along the a-axis. Furthermore, the q=+1 system exhibits noticeably different migration energies to the q=0 and q=+2 systems, likely due to the unpaired electron present in this system. The anisotropy in the migration energies suggests that the orientation of WO_3 may impact the rate at which the oxide interface grows into tungsten, aligning with the orientation dependency observed by Schlueter $et\ al.\ [297]$.

In WO₂, the barrier for oxygen diffusion is strongly directional. The migration barrier required to migrate the V_{O1} vacancy to the V_{O2} vacancy is 1.81 eV, whilst migration in the reverse direction has a barrier of 2.90 eV. Similar values were obtained by Huang et al., in which the migration barriers were 1.86 eV and 2.19 eV respectively [295]. Linderälv predicted barriers of \sim 2.5 and 3 eV to move between the O1 and O2 sites and back again [273]. These barriers are on the same scale as those predicted here even if there are significant discrepancies in the formation energies.

The significantly larger migration barriers mean that WO₂ is far less permeable to oxygen compared to WO₃, indicating that WO₂ and WO₂-like regions in the Magnéli phases protect the pure tungsten metal from further oxidation. This protective behaviour has been observed experimentally and attributed broadly, but not unanimously, to WO₂ or the Magnéli phases [298, 148, 299]. The overall rate of diffusion of oxygen through the oxide will depend on the isotropies in the activation energies determined here, the orientation of the oxide on the surface and the magnitude of the driving force across the oxide layer.

5.3 Summary

In this work, we have reviewed the physical structure of the key tungsten oxide phases observed during the oxidation of tungsten. As the tungsten-oxygen ratio evolves, from WO_2 through to WO_3 , we see a corresponding evolution of the electronic density of states for each phase. The W 5d states that lie just below the Fermi level in WO_2 shift to higher energies as the oxygen content increases, until they rise above the Fermi level in WO_3 , which becomes an insulator.

By investigating the evolution of the electronic structure, the bond lengths in the WO₂ and WO₃ phases, and the oxygen vacancy formation energies of the four tungsten-oxygen systems of interest, we show that the substoichiometric phases, $W_{18}O_{49}$ and $W_{25}O_{73}$, can be considered to be made of regions displaying WO₂-like and WO₃-like properties (namely, bond lengths and oxygen vacancy formation energies). It is suggested that the oxygen diffusion migration barriers may exhibit similar trends. This would account for the orientation dependence of the oxidation of tungsten, as well as the observation that the Magnéli phases only form thin, transient layers between WO₂ and WO₃. It has been shown that the migration barriers for oxygen diffusion in WO₂ are much larger than those observed in WO₃ (1.81 \sim 2.90

eV vs. $0.15 \sim 0.80$ eV respectively). Furthermore, it is shown that oxygen migration in the $\langle 100 \rangle$ direction is strongly preferred in WO₃, with migration barriers as little as 0.13 eV in the +2 charge state. Therefore, if the Magnéli phases are orientated such that their a-axis lies perpendicular to the oxide-air interface, rapid diffusion of oxygen would be expected through the WO₃-like regions. However, should they be orientated such that their WO₂-like regions occlude the WO₃-like regions from the oxide-air interface, then diffusion of oxygen through the b- or c-axes would be much slower. In this way, the orientation dependence of the system and the effect of the formation of columnar W₂₅O₇₃ on the oxidation of tungsten arises out of the oxygen vacancy formation energies and diffusion barriers.

Chapter 6

Stability of Oxide Phases in W-Cr-Y SMART Alloys

The contents of this chapter have been published in Nuclear Materials and Energy 45 (2025), p. 101987 [2].

It has been proposed that the self-passivating properties of W-Cr-Y alloys are closely related to the availability of Cr at the surface during oxidation [183]. The introduction of Y has been shown to enhance the oxidation protection of the alloy by enabling the formation of a denser Cr_2O_3 layer at the surface. Yttrium's high affinity for oxidation may enable the rapid diffusion of Cr to the surface; however, the mechanism responsible for this is presently uncertain. As a result, the protective Cr_2O_3 layer may form before any appreciable oxidation of W or internal Cr takes place.

In this chapter, the thermodynamics for the formation of possible oxide phases in the W-Cr-Y-O system is investigated to provide a functional understanding of yttrium's impact on the alloy's oxidation. In addition to Cr₂O₃, X-ray diffraction

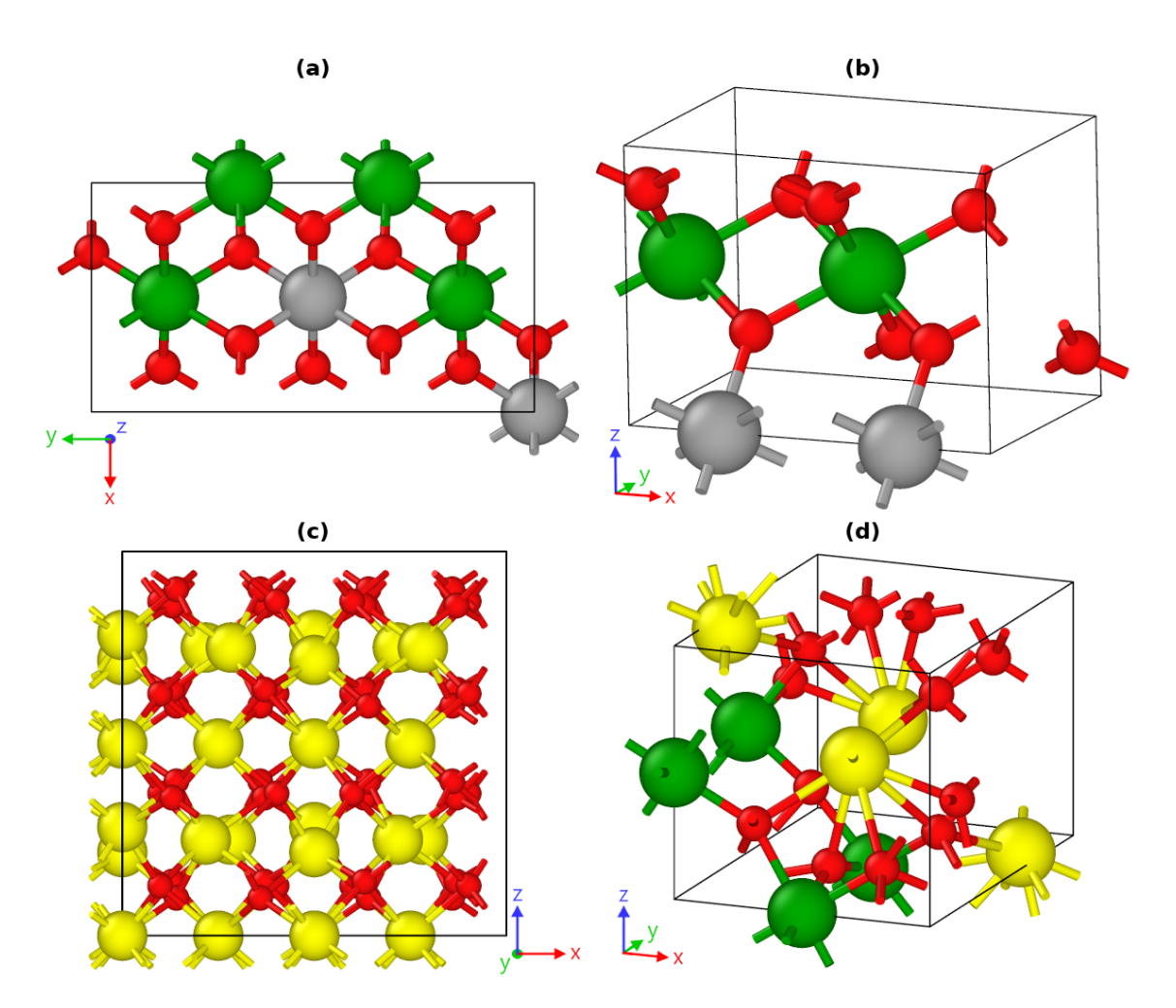


Figure 6.1: Unit cells of (a) Cr_2WO_6 , (b) $CrWO_4$, (c) Y_2O_3 and (d) $YCrO_3$. Grey atoms denote tungsten. Red atoms denote oxygen. Green atoms denote chromium. Yellow atoms denote yttrium.

studies have shown that mixed ternary oxides may also form during the oxidation of W-Cr-Y allows, including Cr₂WO₆, CrWO₄, Y₂O₃ and YCrO₃. As these have been reported in the literature, these phases - in addition to WO₂ and WO₃ - are the phases of interest in this chapter, and their structures are shown in Figure 6.1. It is noted that WO₂, but not WO₃, has been selected as the binary tungsten oxide phase due to its semi-protective properties, as highlighted in Chapter 5.

6.1 Methodology

All calculations in this chapter were performed using DFT as described in Chapter 4. Lattice parameters, ground state energies and enthalpy of atomisation for the constituent metallic species are presented in Chapter 4. Defect calculations were performed based on a 250-atom supercell ($5\times5\times5$ unit cells) of bcc-W at constant pressure, which was constructed from the optimised unit cell described in Table 6.1. The defect formation enthalpies were calculated using Equation 2.16, as described in Section 2.3.3.

6.2 Lattice Parameters and Atomisation Energies of Bulk Phases

Table 6.1 displays the lattice parameters and atomisation energies of the bulk phases in their standard state calculated using the PBE and PBEsol exchange correlation functionals. The lattice parameters and atomisation energies of the constituent elements were discussed in Chapter 4. In the oxide phases, the PBEsol functional also gave better agreement with the experimentally-obtained lattice parameters in most systems; notable outliers include Cr_2O_3 and $YCrO_3$, where the lattice parameter along the c axis showed worse agreement for the PBEsol functional than the PBE functional, and $CrWO_4$, where PBE predicts a closer agreement with experiment on the whole.

However, as discussed in Chapter 4, the PBEsol functional fails to accurately predict the atomisation energies of the investigated species. For the oxide phases, the difference in atomisation energies was more pronounced due to the cumulative errors in the atomisation energies of the constituent elements, particularly in the binding

Table 6.1: Summary of lattice parameters and energy of atomisation of the oxide phases considered in this chapter, using the PBE and PBEsol exchange-correlation functionals. Experimental data obtained from [233, 300].

Species	Lattice	E_{atom} / ${f eV}$				
Species	PBE	PBEsol	Exp.	PBE	PBEsol	Exp.
	a = 5.605	a = 5.548	a = 5.57			
$\mathbf{WO}_{2(s)}$	b = 4.951	b = 4.909	b = 4.90	21.42	22.99	20.78
	c = 5.719	c = 5.667	c = 5.66			
C _n O	a = 5.023	a = 4.966	a = 4.951	20.25	30.32	20.74
$\mathbf{Cr}_2\mathbf{O}_{3(s)}$	c = 13.33	c = 13.09	c = 13.57	28.35	30.32	20.14
$\mathbf{Y}_2\mathbf{O}_{3(s)}$	10.66	10.54	10.60	36.59	36.61	37.24
	a = 5.557	a = 5.497	a = 5.520			
$\mathbf{YCrO}_{3(s)}$	b = 7.575	b = 7.471	b = 7.536	32.69	34.71	31.09
	c = 5.257	c = 5.185	c = 5.255			
Cr. WO	a = 4.603	a = 4.555	a = 4.579	52.80	59.87	55 91
$\mathbf{Cr}_2\mathbf{WO}_{6(s)}$	b = 8.901	c = 8.755	c = 8.663	92.00	99.67	55.31
	a = 9.433	a = 9.348	a = 9.44			
$\mathbf{CrWO}_{4(s)}$	b = 5.523	b = 5.460	b = 5.94	36.06	41.49	37.72
	c = 4.721	c = 4.682	c = 4.74			

Table 6.2: Formation enthalpies of point defects in bcc-W, calculated using the PBE and PBEsol exchange-correlation functionals. The EAM potential by Bonny *et al.* has also been used to calculate the formation enthalpy of Cr defects and the tungsten vacancy [218].

	ΔH_f / ${ m eV}$				
Defect	PBE	PBEsol	\mathbf{EAM}		
$\overline{\mathbf{V}_W}$	3.18	3.04	3.62		
Cr_W	0.38	0.40	1.30		
Cr_{TIS}	8.31	8.59	9.10		
Cr_{OIS}	10.56	9.13	9.02		
O_W	3.27	3.10	_		
O_{TIS}	0.91	0.57	_		
O_{OIS}	1.15	0.83	_		
Y_W	2.38	1.86	_		

energy of the O_2 molecule. Again, the PBE functional yields closer agreement with the experimental values, with absolute errors between 2-3% for the binary oxides and around 5% for the ternary oxides. On the other hand, the PBEsol functional exhibits errors of 5-10% for the oxide phases.

Therefore, for accurate defect and oxide formation energies, the PBE exchange-correlation functional will be employed in the remainder of this chapter. Even so, the PBE functional still underestimates the magnitude of the enthalpy of formation of oxide phases, as will be shown below. This may be a result of two factors: (1) the experimental data incorporates the entropy of formation, whereas this chapter considers only the enthalpy of formation (at 0 K); (2) systemic error in the *ab initio* calculation of the chemical potentials of constituent elements, especially oxygen, propagate throughout the calculation of the enthalpy of formation for the oxide phases.

6.3 Defect Formation Energies in bcc-W

Table 6.2 shows the formation enthalpies of point defects accommodating Cr, O and Y in bulk bcc-W as well as the tungsten vacancy, V_W . Interstitial defects of Y have not been included due to their extremely high formation enthalpies. There are a wide range of experimental and theoretical values for the formation enthalpy of a tungsten vacancy presented in the literature. Li et al. report that the experimentally-obtained value of V_W is 3.7 \pm 0.2 eV, whilst Mason et al. reports a similar theoretical range of 3.61-3.77 eV [301, 302]. Previous density functional theory studies have reported vacancy formation energies of between 3.11 and 3.56 eV [273, 303, 231]. Therefore, the formation energies calculated in this chapter are in the same range as previous DFT studies on the tungsten vacancy, though these are still somewhat lower than the experimental value of $3.7 \pm 0.2 \text{ eV}$ [301]. The EAM potential by Bonny et al., which is employed more extensively in later chapters, predicts a vacancy formation enthalpy which is closer in agreement to the value reported by Li et al.. However, it the formation enthalpy of the substitutional Cr_W defect, as calculated using the EAM potential, is much higher than the corresponding DFT values, suggesting that the strength of the interaction between W and Cr is overestimated. The ramifications of this will be further discussed in Chapter 7.

The results in Table 6.2 show that oxygen at the tetrahedral interstitial site is the most favourable interstitial configuration, followed by the octahedral interstitial site. Oxygen substitution onto a tungsten site has a much higher enthalpy of formation. These values can be directly compared to similar values from Zhao *et al.* of 1.01 eV and 0.7 eV for the octahedral interstitial site (OIS) and tetrahedral interstitial site (TIS) respectively, which indicates good agreement [304]. Further, Alkhamees *et al.*, reported ΔH_f values of -1.75 eV -1.43 eV for the TIS and OIS and 0.67 eV for substitution onto the tungsten site. The shift in values is a result of the difference in the chemical potential of oxygen, μ_O , which has been used. In this

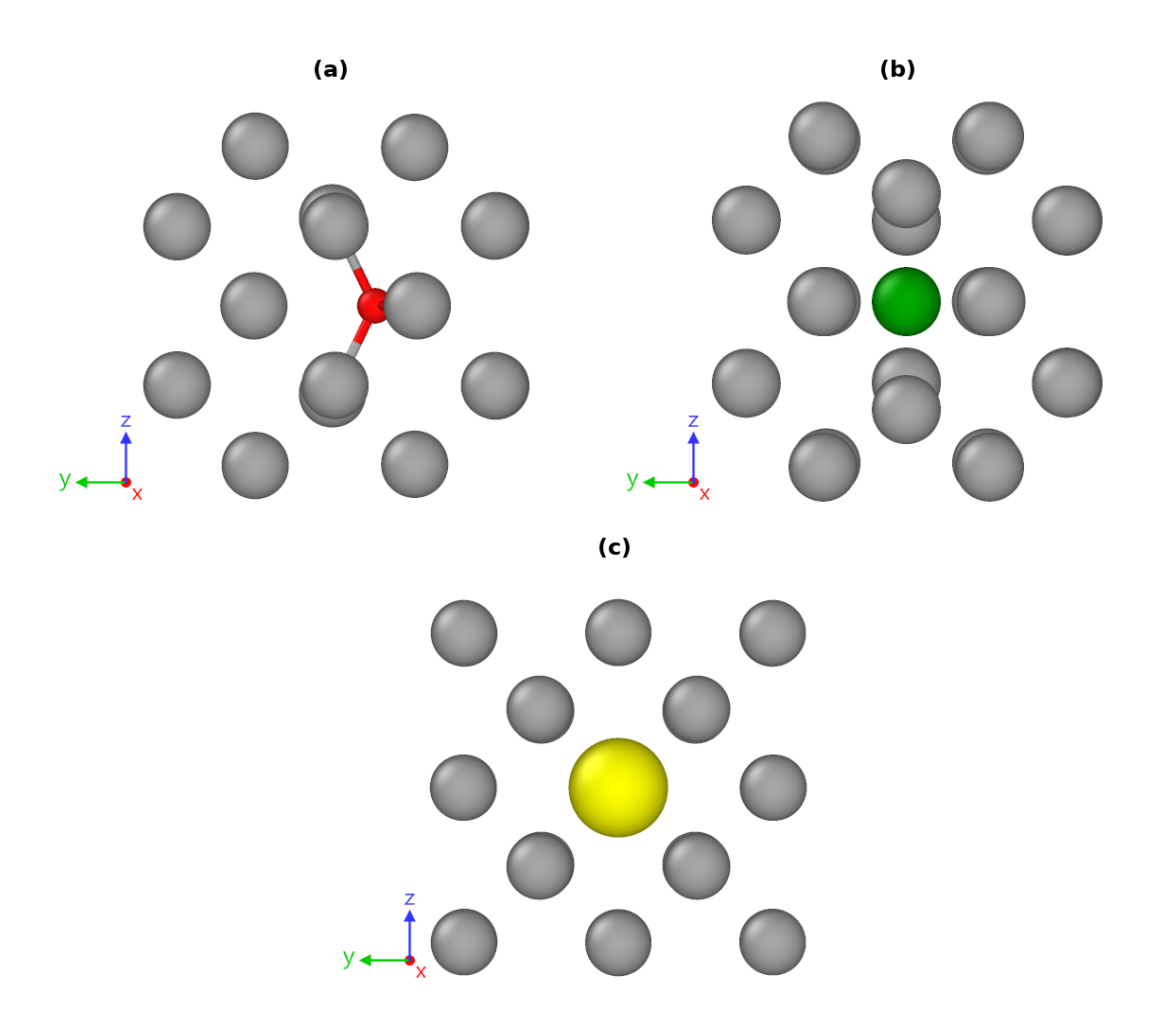


Figure 6.2: Some of the defects studied in this chapter: (a) O_{TIS} , (b) Cr_{OIS} and (c) Y_W .

chapter, $\mu_O = -4.94$ eV, whilst Alkhamees et al. employed a value of $\mu_O = -2.60$ eV [305], although it is noted that no justification is provided for this choice. For comparison, by using the chemical potential of oxygen as reported by Alkhamees et al., we obtain ΔH_f values of -1.43, -1.19, and 0.93 eV respectively, indicating reasonable agreement with this previous work. Ghosh and Ghosh predict values of -5.6 eV for the TIS and -4.4 eV for the OIS. In calculation of these values they used an isolated oxygen atom for the calculation of μ_O and the minimisation was performed under constant pressure conditions, therefore, they cannot be directly compared with the values presented here, however, this again suggests that the tetrahedral site is the favourable interstitial site [306].

Akbas et al. calculated a formation energy for a Y_W defect of 0.031 eV at⁻¹ in their 16 atom supercells [307], in which the cell parameters were allowed to relax. In this work, the enthalpy of formation was 0.010 eV at⁻¹. This significant difference is likely due to the vastly different supercell sizes (16 atoms vs. 250 atoms herein). No previous values for Cr incorporation in W could be found. However, the EAM potential by Bonny et al. predicts that the formation enthalpy for the Cr_W defect is three times greater than that predicted by both the PBE and PBEsol functionals, despite being in reasonably good agreement for the octahedral and tetrahedral interstitial defects. This deficiency in the interatomic potential will be further investigated in Chapter 7. Overall, the formation enthalpies for the tungsten vacancy and accommodation of all extrinsic species considered here are positive.

Table 6.3: Formation enthalpy of oxide phases observed during the oxidation of W-Cr-Y smart alloys, from both constituent metallic phases and molecular oxygen, and from point defects in bulk bcc-W. The formation enthalpy per oxygen atom present in the oxide and the experimental formation enthalpy (where available) have also been given.

Reaction	ΔH_f / eV	Exp.	ΔH_f per O / eV
$W + O_2 \rightarrow WO_2$	-5.75	-6.08	-2.87
$W + 2 O_W \rightarrow WO_2$	-22.18		-11.09
$W + 2 O_{OIS} \rightarrow WO_2$	-17.93		-8.97
$W + 2 O_{TIS} \rightarrow WO_2$	-17.45		-8.73
$2 \operatorname{Cr} + 1.5 \operatorname{O}_2 \to \operatorname{Cr}_2\operatorname{O}_3$	-9.86	-11.69	-3.29
$2 \operatorname{Cr} + 3 O_W \to \operatorname{Cr}_2 \operatorname{O}_3$	-34.50		-11.50
$2 \operatorname{Cr} + 3 O_{OIS} \to \operatorname{Cr}_2 \operatorname{O}_3$	-28.14		-9.38
$2 \operatorname{Cr} + 3 O_{TIS} \to \operatorname{Cr}_2 \operatorname{O}_3$	-27.41		-9.14
$2 Cr_W + 3 O_W \to Cr_2O_3$	-28.64		-9.55
$2 Cr_W + 3 O_{OIS} \rightarrow Cr_2O_3$	-22.28		-7.43
$2 Cr_W + 3 O_{TIS} \to Cr_2O_3$	-13.33		-4.44
$2 \text{ Y} + 1.5 \text{ O}_2 \rightarrow \text{Y}_2\text{O}_3$	-18.08	-19.66	-6.03
$2 Y + 3 O_W \rightarrow Y_2O_3$	-42.72		-14.24
$2 \text{ Y} + 3 O_{OIS} \rightarrow \text{Y}_2\text{O}_3$	-36.36		-12.12
$2 \text{ Y} + 3 O_{TIS} \rightarrow \text{Y}_2\text{O}_3$	-35.62		-11.87
$2 Y_W + 3 O_W \rightarrow Y_2 O_3$	-73.21		-24.40
$2 Y_W + 3 O_{OIS} \rightarrow Y_2O_3$	-66.85		-22.28
$2 Y_W + 3 O_{TIS} \rightarrow Y_2O_3$	-66.11		-22.04
$Y + Cr + 1.5 O_2 \rightarrow YCrO_3$	-14.19	-13.78	-4.73
$Y + Cr + 3 O_W \rightarrow YCrO_3$	-43.51		-14.50
$Y + Cr + 3 O_{OIS} \rightarrow YCrO_3$	-37.14		-12.38

$Y + Cr + 3 O_{TIS} \rightarrow YCrO_3$	-36.41	-12.14
$Y_W + Cr_W + 3 O_{OIS} \rightarrow YCrO_3$	-57.70	-19.24
$Y_W + Cr_W + 3 O_{TIS} \rightarrow YCrO_3$	-56.97	-18.99
$Y_W + Cr_W + 3 O_W \rightarrow YCrO_3$	-64.06	-21.36
$2 \operatorname{Cr} + W + 3 \operatorname{O}_2 \to \operatorname{Cr}_2 WO_6$	-18.59	-3.10
$2 \text{ Cr} + W + 6 O_{OIS} \rightarrow \text{Cr}_2WO_6$	-55.15	-9.19
$2 \operatorname{Cr} + W + 6 O_{TIS} \to \operatorname{Cr}_2 WO_6$	-53.68	-8.95
$2 \operatorname{Cr} + \operatorname{W} + 6 O_W \to \operatorname{Cr}_2 \operatorname{WO}_6$	-67.87	-11.31
$2 Cr_W + W + 6 O_{OIS} \rightarrow Cr_2WO_6$	-71.29	-11.88
$2 Cr_W + W + 6 O_{TIS} \rightarrow Cr_2WO_6$	-69.82	-11.64
$2 Cr_W + W + 6 O_W \rightarrow Cr_2WO_6$	-84.01	-14.00
$Cr + W + 2 O_2 \rightarrow CrWO_4$	-12.39	-3.10
$Cr + W + 4 O_{OIS} \rightarrow CrWO_4$	-36.76	-9.19
$Cr + W + 4 O_{TIS} \rightarrow CrWO_4$	-35.79	-8.95
$Cr + W + 4 O_W \rightarrow CrWO_4$	-45.25	-11.31
$Cr_W + W + 4 O_{OIS} \rightarrow CrWO_4$	-46.75	-11.69
$Cr_W + W + 4 O_{TIS} \rightarrow CrWO_4$	-45.77	-11.44
$Cr_W + W + 4 O_W \rightarrow CrWO_4$	-55.23	-13.81

6.4 Formation Enthalpy of Oxide Phases in W-Cr-Y SMART alloys

The formation enthalpies of all oxide phases are presented in Table 6.3, from both pure metal and molecular oxygen, and from the point defects discussed above. The formation enthalpies normalised on a per oxygen atom present in the oxide basis have also been provided, as it is useful to consider the formation enthalpy of an oxide in the context of how many oxygen atoms are required to form it. Due to the positive formation enthalpies of the substitutional and interestitial point defects, the formation enthalpy of the oxide phases decreases significantly when the chemical potentials of the point defects are used. Assuming that each element is solvated in the bcc-W lattice in its most-preferred form, *i.e.*, W, O_{TIS} , Cr_W , Y_W), the following equations become relevant:

$$W + O_2 \rightarrow WO_2$$
 $\Delta H_f = -2.87 \text{ eV per O}$ (6.1)

$$2Cr_W + 3O_{TIS} \rightarrow Cr_2O_3$$
 $\Delta H_f = -4.44 \text{ eV per O}$ (6.2)

$$Cr_W + W + 4O_{TIS} \rightarrow CrWO_4$$
 $\Delta H_f = -11.44 \text{ eV per O}$ (6.3)

$$2Cr_W + W + 6O_{TIS} \to Cr_2WO_6$$
 $\Delta H_f = -11.64 \text{ eV per O}$ (6.4)

$$Y_W + Cr_W + 3O_{TIS} \rightarrow YCrO_3$$
 $\Delta H_f = -18.99 \text{ eV per O}$ (6.5)

$$2Y_W + 3O_{TIS} \rightarrow Y_2O_3$$
 $\Delta H_f = -22.04 \text{ eV per O}$ (6.6)

Despite the higher total enthalpy of formation for Cr₂WO₆, it becomes apparent as to why there is such a narrow region in which the W-Cr-O ternary phases form [300]. When comparing the enthalpies of formation and factoring in the number of oxygen atoms required to form one mole of either of the W-Cr-O ternary phases, a

clear preference for the formation of W-Y-O or Y-O phases emerges.

6.5 Binding Capacity of Y

The data presented above suggests that there is a strong driving force for the formation of separate Y_2O_3 and $YCrO_3$ phases from yttrium and oxygen accommodated bulk tungsten as Y_W and O_{TIS} . The implication of this is that the introduction of yttrium into the SMART alloy has the effect of removing oxygen from the bulk to form yttrium containing oxides.

This observation is supported by experiments that investigate the oxidation resistance of SMART alloys as a function of the wt% of oxygen relative to yttrium. The binding capacity of Y can be defined by considering the impurity oxygen content (in % of the total weight of the system) required to form a given yttrium-containing oxide in stoichiometric quantities based on the amount of Y present. Klein *et al.* report that the binding capacity of Y for the reaction

$$2Y + 2Cr + 3O_2 \rightarrow 2YCrO_3$$
 (6.7)

in an alloy with a Y content of 0.6 wt% is 0.32 wt% [183]. However, the optimal oxidation resistance observed was found in samples containing 0.6 wt% Y and 0.15 wt% O. Considering the reaction

$$2Y + 1.5O_2 \rightarrow Y_2O_3$$
 (6.8)

in an alloy with 0.6 wt% Y, the binding capacity of Y is calculated to be 0.16 wt%. Therefore, in conjunction with empirical data, the oxidation resistance of W-Cr-Y smart alloys is optimised when the residual oxygen content in the alloy is no greater than the stoichiometric amount required to form Y_2O_3 . This observation, coupled

with the thermodynamic driving force for the formation of Y_2O_3 , suggests that incorporation of Y removes all oxygen from the W-Cr grains, and that removing this impurity enables the more rapid diffusion of Cr to the surface to form an oxide layer. The interaction between oxygen and chromium in bulk W-Cr is subject to ongoing chapter.

6.6 Summary

In this chapter, the enthalpy of formation for the stable oxide phases observed during the oxidation of the W-Cr-Y alloy is discussed. The highly exothermic process of forming Y_2O_3 from the Y_W and O_{TIS} point defects, primarily resulting from the high formation enthalpy of the Y_W defect itself, indicates that it is extremely thermodynamic unfavourable for bcc-W to accommodate both Y and O simultaneously. Instead, the formation of Y_2O_3 as a separate phase is highly preferred. Furthermore, the formation of Y-Cr-O ternary phases is preferential to the formation of Cr-W-O ternary phases, indicating that the formation of the latter should only be expected in cases where there is insufficient Y to bind all available oxygen. In the context of W-Cr-Y smart alloys, the affinity of O to Y is such that Y may sequester any residual oxygen content in the alloy during synthesis to form Y-containing nanoparticles in the intergranular spaces. In addition, the formation of Y-containing oxide particles at the grain boundaries will likely have a strengthening effect on the alloy, typical of oxide-dispersion strengthened alloys. Based on the high formation enthalpy of Y_W and the preferential formation of Y_2O_3 , future chapters will treat the bulk W-Cr-Y as grains consisting of W, Cr and residual O, aiming to explore the diffusion of Cr within those and the effect of O on the diffusion process.

Chapter 7

Segregation of Chromium in W-Cr Alloys

In the previous chapter, the formation enthalpies of the oxide phases expected to form during the oxidation of W-Cr-Y SMART alloys were calculated, demonstrating yttrium's high affinity for residual oxygen. By comparing the residual oxygen levels in the SMART alloy to the quantity of Y which offered the greatest oxidation resistance, we identified the role of Y as an 'oxygen getter' in the system. Since both Y and O are likely not to be present within the bulk material, the self-passivating behaviour of W-based SMART alloys may be related to the migration of Cr in the (W,Cr) grains. As discussed in Section 2.5.4, the W-Cr system is known to be thermodynamically unstable at relatively low temperatures, and segregates into $(\alpha Cr, W)$ and $(\alpha W, Cr)$ regions at the order-disorder transition temperature. This, itself, is dependent upon the Cr concentration of the system, as well as any impurities that are present. This chapter concerns the segregation of W-Cr, both as a bulk phase and to the grain boundary.

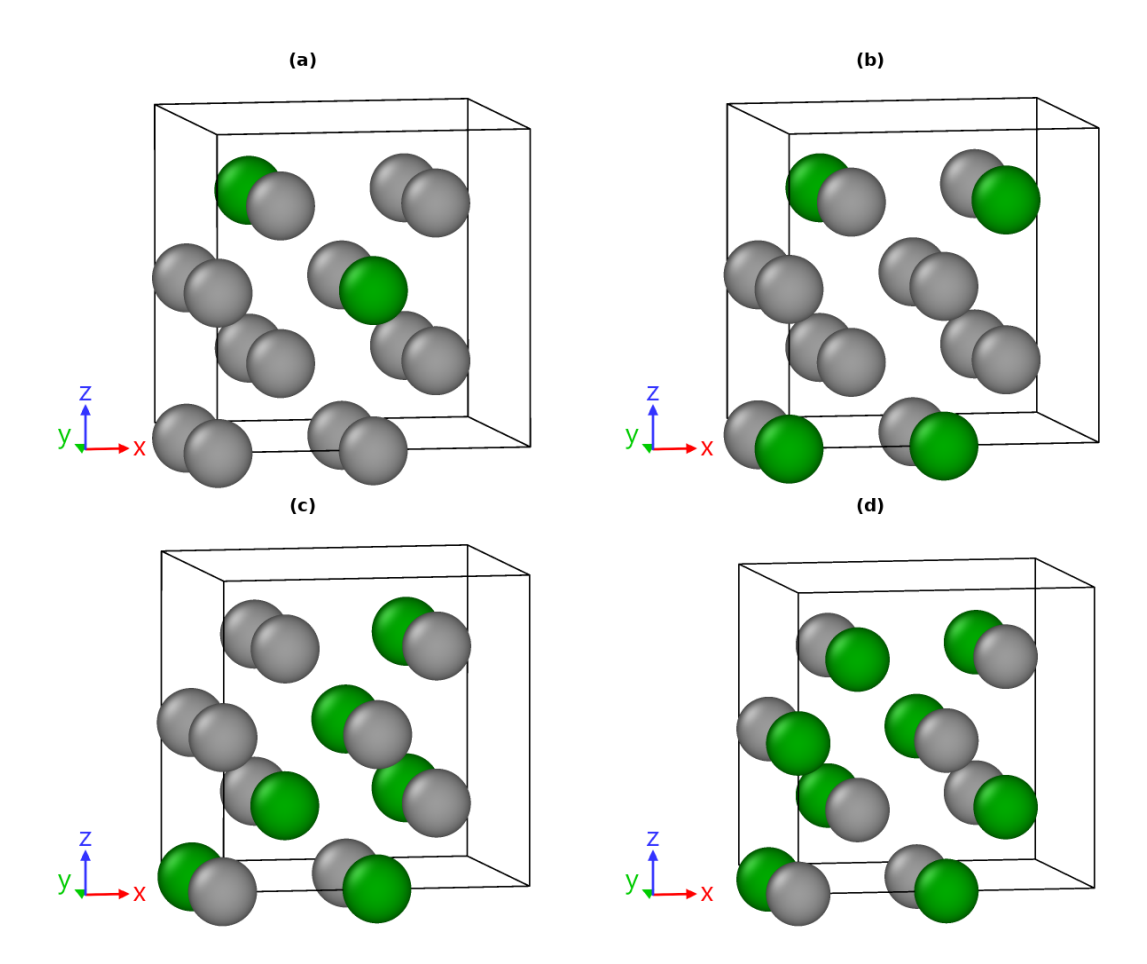


Figure 7.1: Configurations of W-Cr predicted by the special quasirandom structure approach for (a) 12.5%, (b) 25%, (c) 37.5% and (d) 50% Cr. The grey atoms denote W, and the green atoms denote Cr. These are identical to the configurations above 50 at% Cr.

7.1 Methodology

All DFT calculations in this chapter were performed as per the methodology described previously. As such, the enthalpy of formation for W-Cr at different Cr concentrations was calculated at the DFT level of theory on structures that were obtained *via* the special quasirandom structure approach, described in 3.1.6. Each SQS supercell consisted of 16 atoms. Chromium vacancy formation enthalpies were subsequently obtained by exhaustively searching all Cr sites within the resultant structures. These calculations were performed at constant pressure on 250-atom

supercells ($5\times5\times5$ unit cells) constructed from the SQS structures. All defect formation enthalpies were calculated using Equation 2.16, as described in Section 2.3.3.

To study the role of grain boundaries in W-Cr, the stability of the $\langle 210 \rangle [100]$, $\langle 310 \rangle [100]$, and $\langle 210 \rangle [110]$ grain boundaries were calculated by finding the grain boundary energy, γ_{GB} , which is,

$$\gamma_{GB} = \frac{E_{perf} - E_{GB}}{A},\tag{7.1}$$

where E_{perf} is the DFT energy of a perfect supercell of N atoms, E_{GB} is the DFT energy of a supercell with the same number of atoms containing the grain boundary, and A is the cross-sectional area of the grain boundary. These grain boundaries were identified as some of the most stable [100]- and [110]-symmetric grain boundaries by Frolov et al. [308]. The grain boundary supercells were constructed by rotating the optimised bcc-W unit cell by the misorientation angle, θ_{GB} . For each of the grain boundaries mentioned previously, the misorientation angle was 26.57°, 18.43° and 35.26°, respectively. This supercell was then mirrored along the $\langle 010 \rangle$ to produce the supercell centred on the grain boundary, which lay on the xz-plane. Importantly, the distance between the grain boundary and its periodic image must be sufficiently large to prevent self-interaction. Therefore, the constituent half-supercells were no smaller than 10 Å in width along the $\langle 010 \rangle$ direction.

Both the molecular statics and molecular dynamics simulations in this chapter were performed using the LAMMPS software package using the Fe-W-Cr interatomic potential by Bonny *et al.* [192, 218]. The molecular statics simulations carried out in Section 7.2 were done so in the NPT ensemble, *i.e.*, the cell volume was allowed to relax. In Section 7.3.1, the MD simulation was run for a total of 4,000,000 steps at 0.001 ps per timestep (*i.e.*, 4 ns) at a temperature of 1800 K in the NVT

ensemble. In total, The simulation supercell consisted of 270,000 atoms, which were divided evenly between two grains, joined at a $\langle 210 \rangle [100]$ grain boundary on the xz plane. The concentration of each grain was 10% and 30% respectively, constructed by randomly replacing W atoms with Cr.

7.2 Thermodynamics of W-Cr Segregation

The enthalpy of mixing, ΔH_{mix} , of the W-Cr system across a range of Cr concentrations was calculated using both density functional theory and the embedded atom potential by Bonny et al. Due to the complexity of the system, energy minimisation on all configurations of the W-Cr system at the DFT level of theory was not possible, hence, the SQS approach was used to obtain the representative configurations of the system at each concentration shown in Figure 7.1. The quasirandom nature of these configurations means that they are inherently representative of the disordered phase which is observed at higher temperatures, as seen in Figure 2.22. The values of ΔH_{mix} as calculated using DFT agree well with the previous work of Sobieraj et al., who reported values of up to 0.117 eV at⁻¹ [179]. On the other hand, energy minimisations using the EAM potential were not prohibitively costly and, therefore, all possible configurations of the W-Cr system in the 16-atom supercell could be explored. As a result, Figure 7.2 shows ΔH_{mix} as a function of the atomic concentration of Cr in the system. Notably, as shown in Figure 7.3, the highest value of ΔH_{mix} predicted by the EAM potential corresponds to the same disordered structure as the SQS approach. However, the EAM potential vastly overestimates the enthalpy of mixing, which was expected due to the overestimation of the formation enthalpy of the Cr_W defect, as discussed in Chapter 6.

A similar discrepancy is also seen in the lattice parameter of the system. On the whole, the lattice parameters predicted by the EAM potential are larger than those

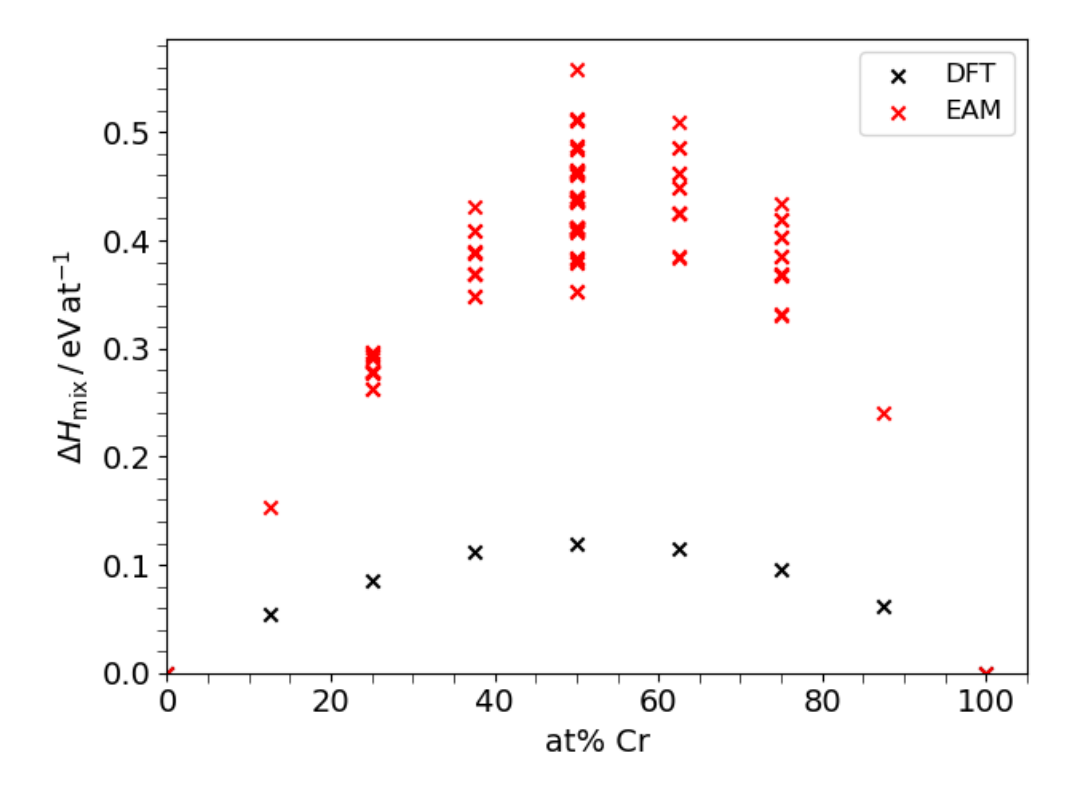


Figure 7.2: The enthalpy of mixing for the W-Cr system across the Cr concentration range, calculated using density functional theory (black) and molecular statics (red) using the Fe-Cr-W potential by Bonny $et\ al.$

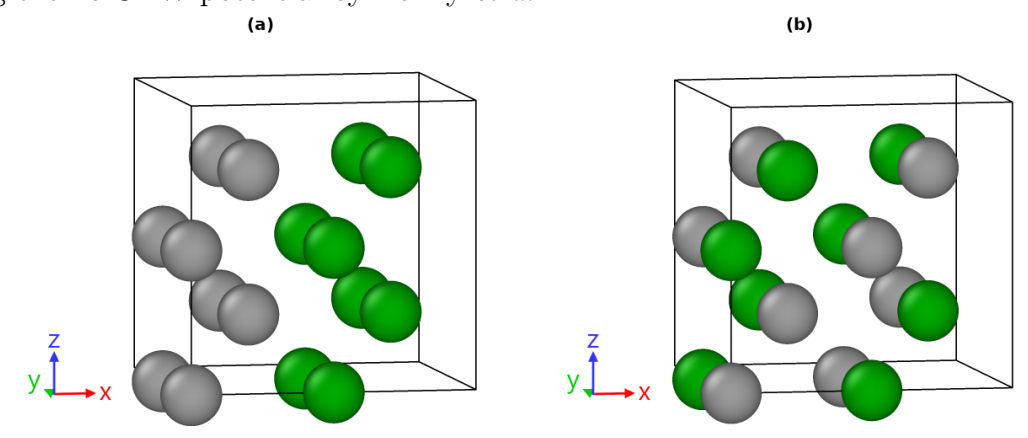


Figure 7.3: The configurations with the (a) lowest and (b) highest ΔH_{mix} at 50 at% Cr. Note that (b) also matches the SQS structure at 50 at% Cr shown in Figure 7.1.

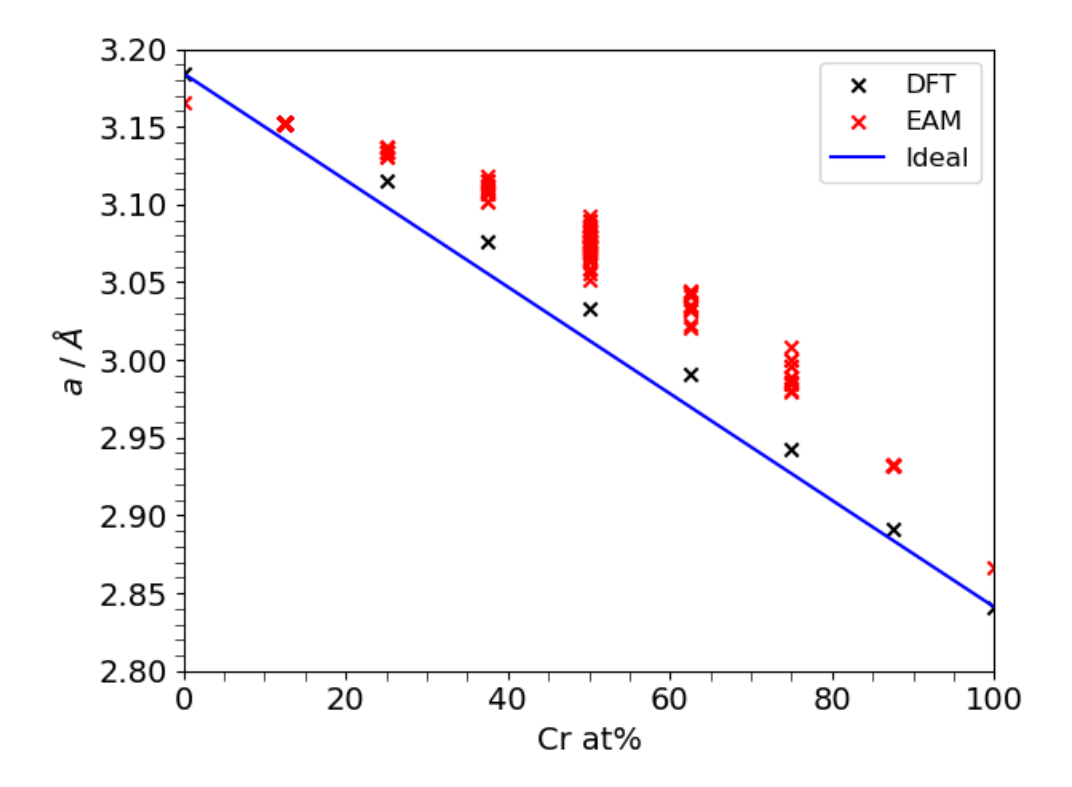


Figure 7.4: The lattice parameter of the W-Cr system across the Cr concentration range, calculated using density functional theory (black) and molecular statics using the Fe-Cr-W potential by Bonny *et al*, compared to the expected value as per Vegard's Law (blue).

predicted via DFT. An exceptions to this is the lattice parameter of pure W, where the EAM potential more closely reflects the experimental value, as was discussed in Chapter 4. The values determined by both DFT and the EAM potential show a positive deviation from the ideal value predicted Vegard's law, which is,

$$a_{A_{1-x}B_{x}} = (1-x)a_{A} + xa_{B}, (7.2)$$

where a_j is the lattice parameter of crystal structure j, which consists of elements A and B. This positive deviation can be interpreted as a repulsion of Cr and W in the lattice, leading to an expansion of the crystal structure. Accordingly, the enthalpy of formation is highest when the repulsive interactions between Cr and W are at

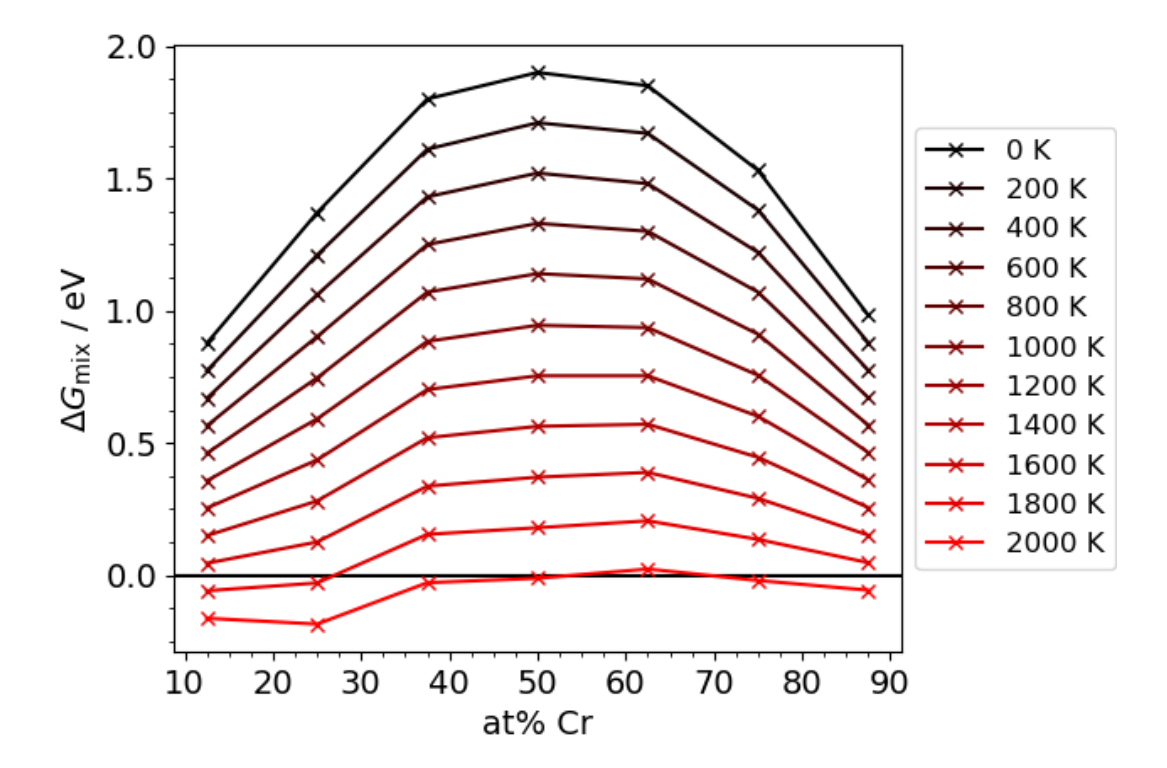


Figure 7.5: The Gibbs energy of mixing, ΔG_{mix} for the W-Cr system in configurations obtained *via* the SQS approach, calculated for a range of temperatures from 0 to 2000 K.

their greatest. As shown in Figure 7.4, the deviation from Vegard's Law is especially strong for the structures calculated using the EAM potential, which further suggests that the interaction between W and Cr is misrepresented in this potential.

By considering the configurational entropy, S_{conf} , the Gibbs free energy of mixing, ΔG_{mix} , can be estimated for a range of temperatures according to Equation 3.15. Figure 7.5 shows ΔG_{mix} as a function both of Cr concentration and temperature, showing that, above ~1700 K, the W-Cr system undergoes mixing. In other words, below this temperature, the system segregates into separate W and Cr phases. This temperature, the ODTT, is depend on Cr concentration; above 1700 K, both W-rich and Cr-rich phases begin to mix, whilst phases that have equivalent concentrations of both do not mix until around 2000 K.

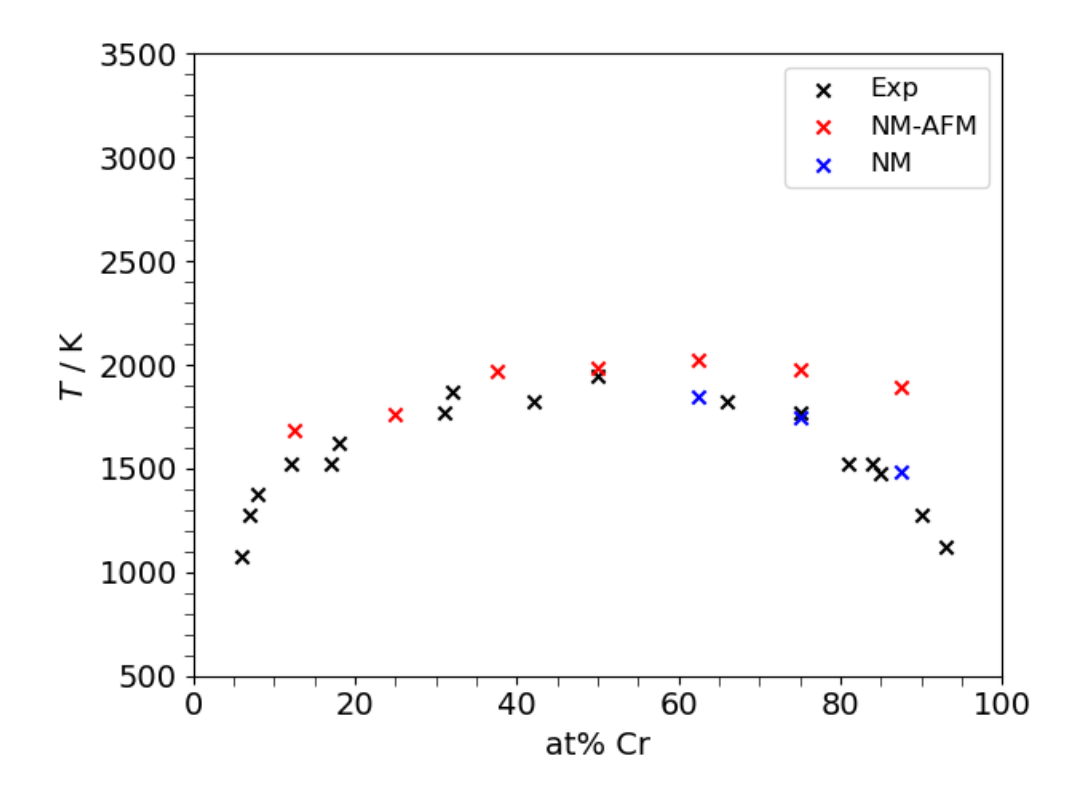


Figure 7.6: Predicted spinodal phase diagram of the W-Cr system based on density functional theory calculations on the structures obtained via the SQS approach. Simulations in which the magnetic moments were allowed to relax are show in red (NM-AFM), whilst those in which the magnetic moments were fixed at 0 μB are shown in blue (NM). The experimental values of the order-disorder transition temperature are shown in black [177].

By dividing ΔH_{mix} by ΔS_{conf} , the temperature at which $\Delta G_{mix} = 0$ can be obtained. This is the order-disorder transition temperature, or the temperature at which W-Cr segregates or mixes. In Figure 2.22, the ODTT is denoted as a dome in the lower portion of the phase diagram, which is based on the works of Naidu *et al* [177]. Therefore, Figure 7.6 shows the same region of the W-Cr phase diagram as predicted by the density functional theory calculations reported herein. There is good agreement between the calculated and experimental phase diagrams in the W-rich regime, until around 60 at% Cr. This is because the calculations were carried out spin-polarised, initial with antiferromagnetic ordering. Whilst the magnetic ordering of the W-rich regime converged to a non-magnetic solution, the Cr-rich regime retained this magnetic ordering, resulting in a higher ODTT than what was

observed experimentally. However, at these temperatures, pure Cr is far above the Néel temperature. Therefore, by constraining the magnetic moments in the Cr-rich configurations to zero, ODTT values which were commensurate with experimental values were observed.

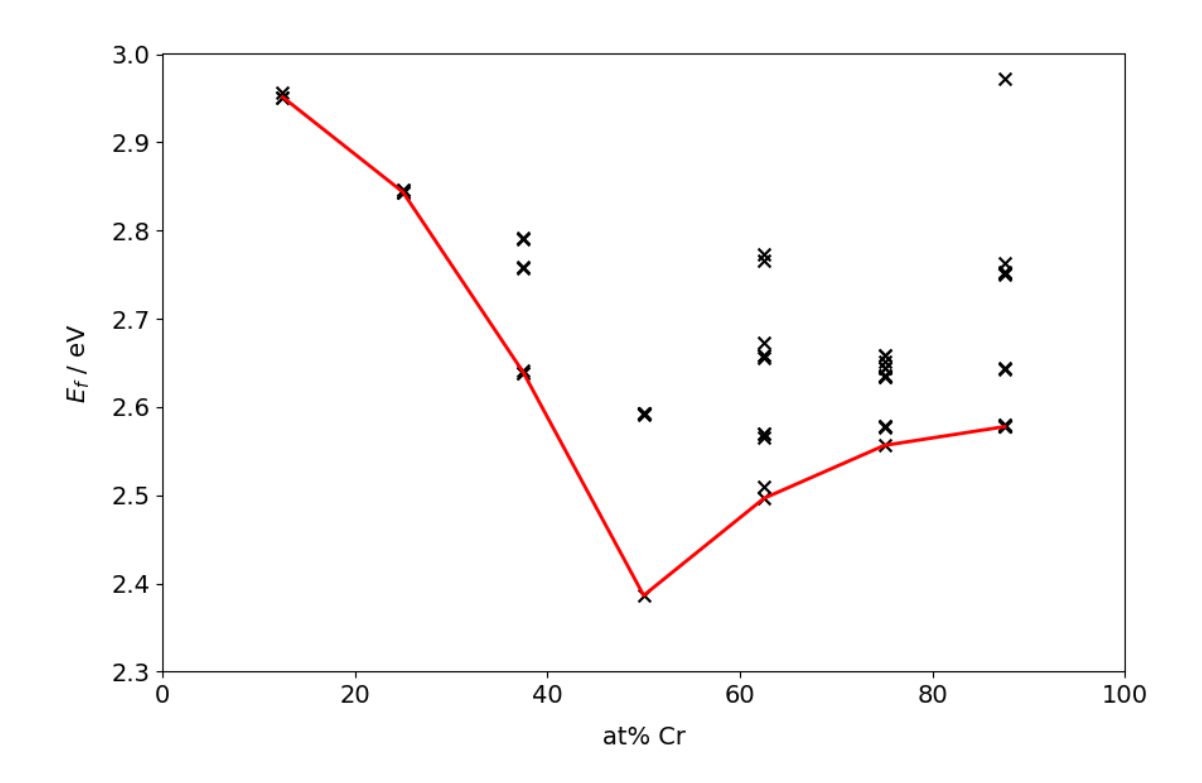


Figure 7.7: The Cr vacancy formation enthalpy in W-Cr as a function of Cr concentration.

Finally, the defect formation enthalpy of V_{Cr} was calculated for all Cr sites in the derived SQS configurations, and are presented in Figure 7.7. The minimum vacancy formation enthalpy lies at 50 at% Cr, as the removal of one Cr atom from this configuration relieves the most relative strain in the system. At higher Cr concentrations, the vacancy formation enthalpy was spread across a range of values due to the unique chemical environments surrounding the Cr atom which was being removed. In addition, the minimum formation enthalpies at each concentration step tends towards the vacancy formation enthalpy of the majority constituent metal. Considering the concentration of Cr in W-Cr-Y alloys, this shows that grains of

Table 7.1: Grain boundary energies, γ_{GB} , of three low-symmetry grain boundaries in pure W. The grain boundary cross-section is given by $b \times c$, and the total energy difference is $\Delta E = E_{grain} - E_{bulk}$. Reference values from [308, 309].

G.B.	${ m b/\AA}$	$\mathrm{c}/\mathrm{\AA}$	$\Delta E/{ m eV}$	$\gamma_{GB}/{ m J} { m m}^{-2}$	$ m Lit./J~m^{-2}$
$\overline{\langle 210 angle [100]}$	1		20.87	2.62	~ 2.5
$\langle 310 angle [100]$			19.41	2.35	~ 2.3
$\langle 112 angle [110]$	21.09	4.47	4.07	0.69	$0.6 \sim 0.73$

the W-Cr alloy which have a higher local Cr concentration - *i.e.*, grains of ~ 30 at% Cr - are much more susceptible to vacancy formation. This may influence the vacancy-mediated diffusion of Cr through the W-Cr system by increasing the vacancy concentration in those grains.

7.3 Grain Boundary Segregation in W-Cr-Y

7.3.1 Solubility of Cr and Y at W Grain Boundaries

Having confirmed that the W-Cr system undergoes spinodal decomposition, in corroboration with existing experimental work [177, 178], the segregation of Cr from the bulk to the grain boundary was investigated. Up to now, it was predicted that the self-passivating properties of the W-Cr and W-Cr-Y systems were linked to the diffusion of Cr along the grain boundaries in the alloy. To begin investigating this behaviour, the relative stabilities of some grain boundaries in pure W were explored. Figure 7.8 shows the geometry-optimised supercells containing the $\langle 210 \rangle [100]$, $\langle 310 \rangle [100]$, and $\langle 112 \rangle [110]$ grain boundaries in pure W. The grain boundary energies, γ_{GB} , of these boundaries are shown in Table 7.1, and closely match the values reported in both experimental and theoretical studies found in the literature [308, 309].

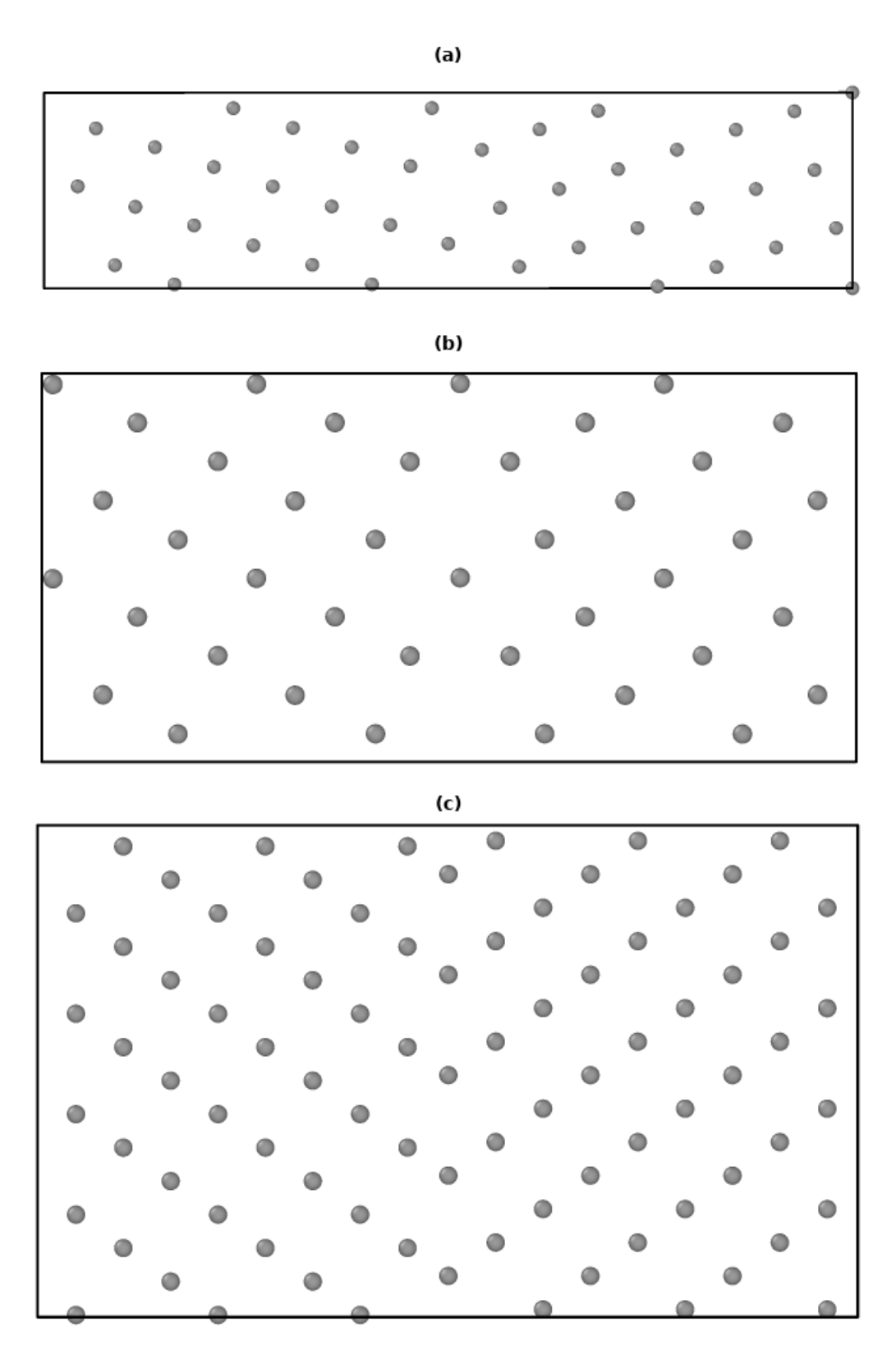


Figure 7.8: The (a) $\langle 210 \rangle [100]$, (b) $\langle 310 \rangle [100]$, and (c) $\langle 112 \rangle [110]$ grain boundaries in pure W.

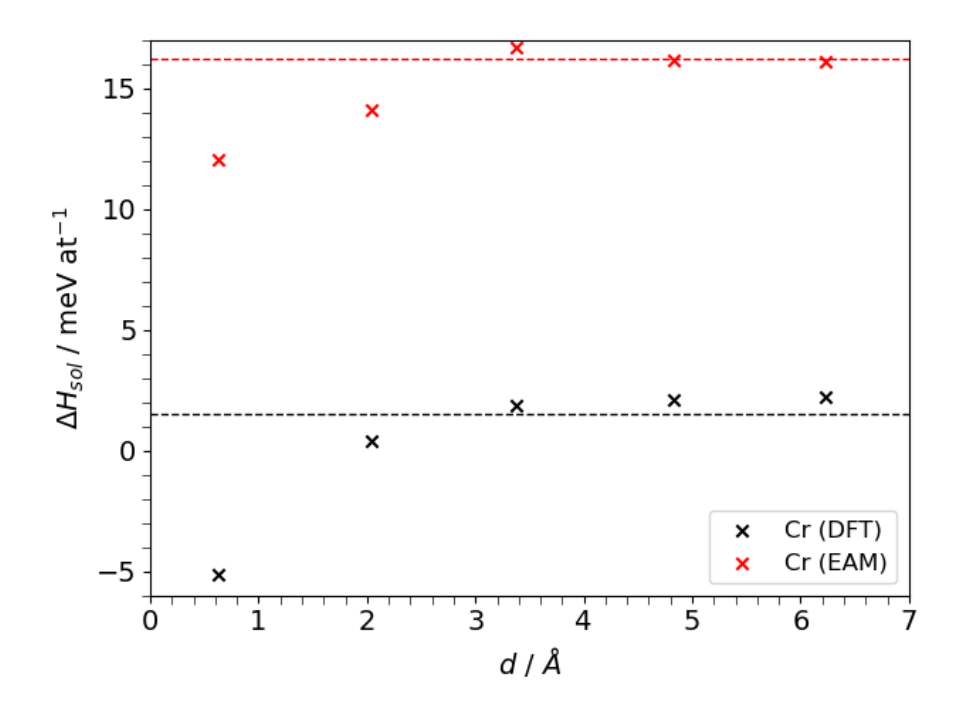


Figure 7.9: The enthalpy of solution of Cr as a function of distance from the $\langle 210 \rangle [100]$ grain boundary in W, as calculated using the PBE functional and the EAM potential by Bonny *et al.*. The enthalpy of formation of the Cr_W defect in the bulk is given as a dashed line for each data set.

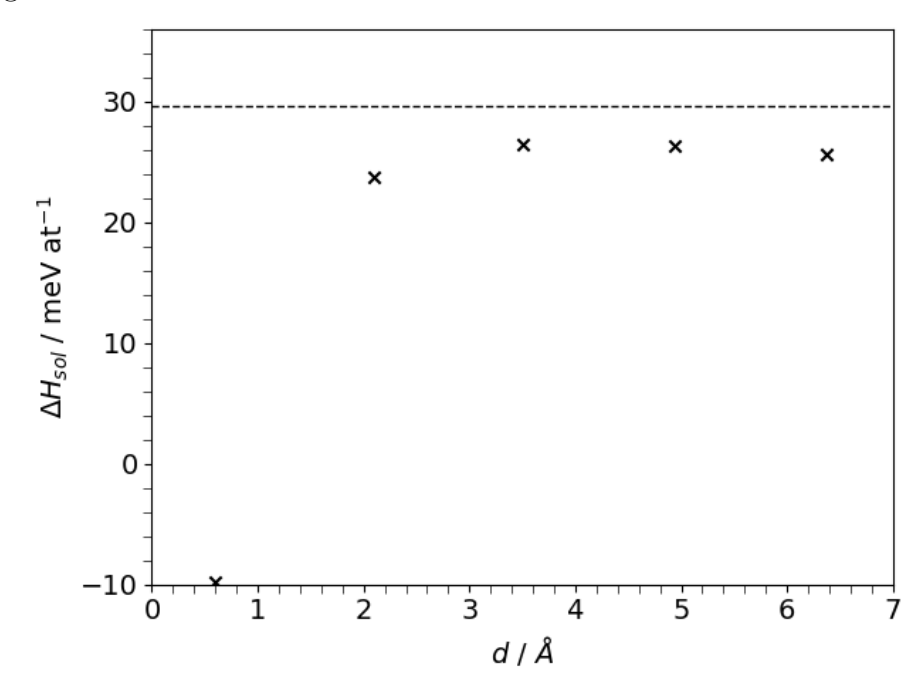


Figure 7.10: The enthalpy of solution of Y as a function of distance from the $\langle 210 \rangle [100]$ grain boundary in W. The enthalpy of formation of the Cr_W defect in the bulk is given as a dashed line.

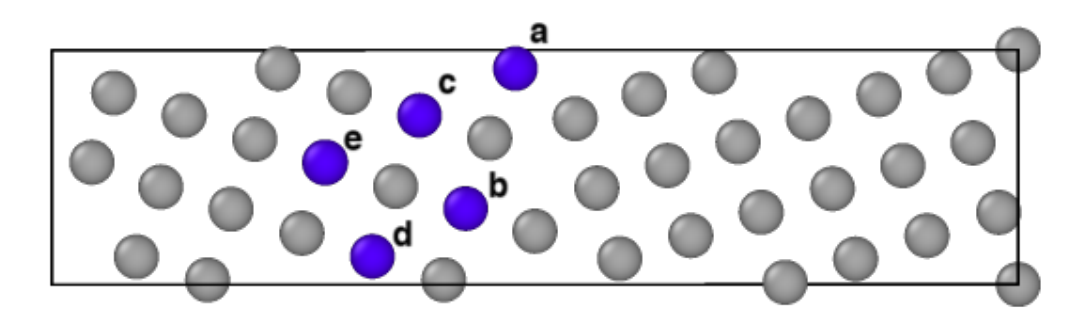


Figure 7.11: The substitution sites a through e in the $\langle 210 \rangle [100]$ grain boundary.

To begin examining the segregation of the alloying elements to the grain boundaries, the enthalpy of solution, ΔH_{sol} was calculated for Cr and Y in pure W. The enthalpy of solution, ΔH_{sol} , measures the solubility of a solute atom at or near the grain boundary. In this context, it is essentially the enthalpy change as a result of the substitution of metal ion M with solute N, where M is in the vicinity of a grain boundary. It also measures the change in γ_{GB} as a result of placing solute N at the grain boundary. In this work, the solubility of Cr and Y at the $\langle 210 \rangle [100]$ grain boundary was of interest, in part due it being well-reported in the literature, and owing to its stability relative to other grain boundaries in pure W.

Consequently, the solubility of Cr at this grain boundary is presented in Figure 7.9, as calculated using both DFT and the EAM potential. The position of the grain boundary, d=0, is defined as the plane which bisects the simulation cell on the xz-plane. Close to the grain boundary, at position 'a' in Figure 7.11, the value of ΔH_{sol} as determined by the PBE functional is -5.10 meV at⁻¹. The negative value indicates a net reduction in the γ_{GB} as a result of the presence of Cr at the grain boundary. However, as the substitution site was moved towards the bulk W environment, i.e., sites 'd' and 'e', ΔH_{sol} tended towards the formation enthalpy of the Cr_W defect reported in Chapter 6, which was 1.50 meV at⁻¹. The actual value of ΔH_{sol} predicted by the PBE exchange-correlation functional reached a maximum value of 2.20 meV at⁻¹. Using the EAM potential, however, ΔH_{sol} was positive both at the grain boundary and in the bulk. The value tended towards the enthalpy

of formation of the Cr_W defect, which was calculated in Chapter 6. Similarly, a reduction in ΔH_{sol} was observed close to the grain boundary, indicating a preference for solution here.

Similarly, the solubility of Y at the $\langle 210 \rangle [100]$ grain boundary is shown in Figure 7.10. A similar pattern is seen here, where the value of ΔH_{sol} is negative when the solute atom substitutes a W atom close to the grain boundary, this time with a value of -9.80 meV at⁻¹. In the bulk, ΔH_{sol} reaches a maximum value of 26.47 meV at⁻¹, which is substantially lower than the defect formation enthalpy of the Y_W defect, which was reported as 35.25 meV at⁻¹. The discrepancy between ΔH_{sol} and ΔH_f is likely due to the difference in k-point sampling between the two sets of calculations. The bulk region of the supercell is sufficiently distant from the grain boundary that its properties are not affected by proximity to the interface. In both the Cr and Y cases, the value of ΔH_{sol} does not change significantly beyond 3 Å from the grain boundary, suggesting that it has reached its bulk value. Therefore, expanding the distance between the grain boundaries is not likely to affect this result. Nevertheless, these results highlight the stabilising effect of both Cr and Y solutes at this grain boundary in pure W. When coupled with the thermodynamic drive for the segregation of W and Cr, especially at W:Cr concentration ratios close to parity, the solubility of both Cr at the grain boundaries is likely to increase with Cr concentration.

7.3.2 Effect of Cr Concentration on Grain Boundary Segregation

To examine the behaviour of Cr at grain boundaries in a W-Cr alloy, molecular dynamics simulations were performed at 1800 K using a simulation supercell consisting of 270,000 atoms, as described in Section 7.1. The start and end

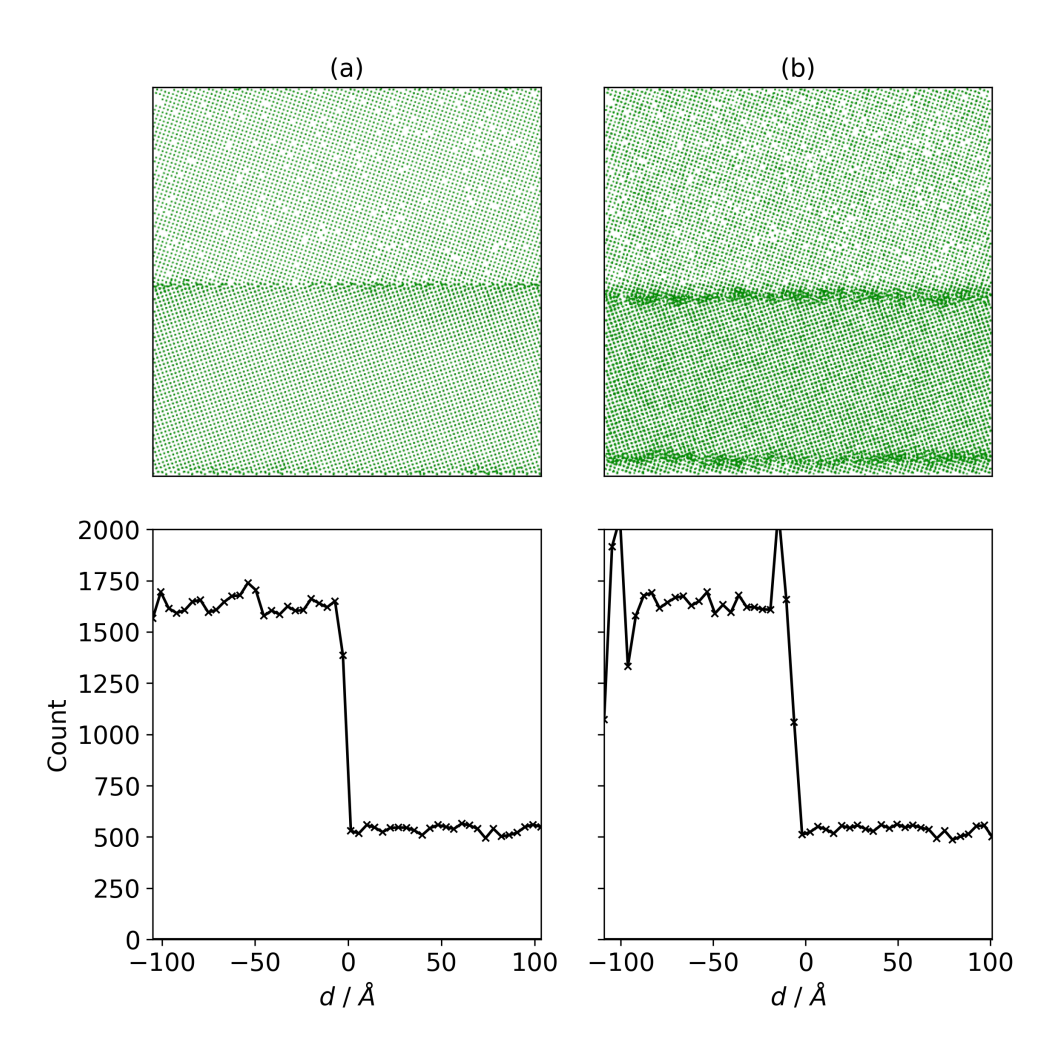


Figure 7.12: Segregation of Cr to the $\langle 210 \rangle [100]$ grain boundary in W-Cr, with grain concentrations of 10 at% and 30 at% Cr. The number of Cr atoms as a function of distance from the grain boundary (d=0) is shown beneath the view of the simulation cell along the [010] axis. The initial and final configurations of the simulation cell are shown in (a) and (b), respectively.

configurations of these grains are shown in Figure 7.12, which displays only the positions of the Cr atoms for clarity. The disparity in the concentrations of the grains establishes a concentration gradient across the grain boundary, and represents the inhomogeneous Cr concentrations in the grain of a real alloy. After 4,000,000 timesteps, a clearly denser band of Cr developed at the grain boundary; however, the top-down view is sometimes misleading, as Cr atoms displaced from their lattice sites may give the illusion that there has been a migration of Cr to the grain boundary.

Therefore, to ascertain if this was the case, the total number of Cr atoms was plotted against the distance from the grain at the start and end of the simulation. Shown in the lower half of Figure 7.12, a sharp rise in the number of Cr atoms at the grain boundary (~ 0 Å) can be seen, suggesting that Cr had segregated to the boundary. It is noted that a similarly sharp rise in Cr concentration is observed at \sim -100 Å, as this is another grain boundary which arises due to the periodic boundary conditions of the simulation. Another detail of this simulation is that the 30 at% grain actually reduced in width over the course of the simulation. This is likely due to the thermodynamic observations noted in Figures 7.2 and 7.4, that the higher concentration grain exhibits a greater strain field. Not only does Cr migrate towards the grain boundary, due to the gradient established by the negative enthalpy of solution at the boundary, but it moves towards the lower concentration grain to relieve the strain in the higher concentration grain. Importantly, it is noted that the Cr concentration of the 10 at grain does not change over the course of the simulation. On the other hand, there is a notable decrease in the Cr concentration in the center of the 30 at% grain. This raises the question as to why there is a net movement of Cr towards the grain boundary within the 30 at grain, but not in the 10 at% grain. The root cause of this phenomenon is investigated in the following chapter.

7.4 Summary

The W-Cr system is known to undergo spinodal decomposition below the ODTT, which is dependent upon the Cr concentration of the system. Despite this, spinodal decomposition is kinetically controlled and does not occur at room temperature. In this chapter, the ODTT was predicted to a sufficient level of accuracy by calculating the enthalpy of formation of the W-Cr system at the DFT level of theory across a range of Cr concentrations. The enthalpy of formation as predicted using the Fe-W-Cr EAM potential of Bonny et al. was not sufficiently accurate to predict the ODTT. The segregation of W-Cr was also confirmed by examining the lattice parameters as a function of Cr, which demonstrated a positive deviation from Vegard's Law, indicative of repulsion between W and Cr.

Subsequently, the segregation of Cr and Y to the grain boundaries in pure W was confirmed via DFT calculations on the $\langle 210 \rangle [100]$ boundary. The negative enthalpy of solution of each solute atom at the grain boundary corresponds to a decrease in the grain boundary energy, γ_{GB} and may promote the grain boundary diffusion of these solute atoms. In the W-Cr system, large-scale segregation of Cr to the grain boundary was observed on the molecular dynamics timescale at 1800 K, where a concentration gradient between the grains promoted the migration of Cr atoms to the grain boundary. However, this migration was only observed in the higher concentration grain. The reason for this will be the focus of Chapter 8, which will closely examine the diffusion of Cr in bulk W-Cr grains at various concentrations relevant to W-Cr-Y SMART alloys.

Chapter 8

Migration of Chromium in W-Cr Alloys

In Chapter 6, the formation enthalpies of the oxide phases expected to form during the oxidation of W-Cr-Y SMART alloys were calculated, demonstrating yttrium's high affinity for residual oxygen. By comparing the residual oxygen levels in the SMART alloy to the quantity of Y which offered the greatest oxidation resistance, we identified the role of Y as an 'oxygen getter' in the system. The segregation of the W-Cr solid solution was then confirmed in Chapter 7, as well as the segregation of Cr and Y solutes to the $\langle 210 \rangle$ grain boundary in pure W. Molecular dynamics simulations identified that the segregation of Cr to the same grain boundary in W-Cr was especially pronounced when there was a concentration gradient.

Therefore, to understand how impurity oxygen affects Cr migration to the alloy's surface, it is imperative to understand the mechanism by which Cr diffuses through bulk W-Cr. In this chapter, a simple vacancy-hopping mechanism is assumed due to the very high formation enthalpies of the Cr_{OIS} and Cr_{TIS} defects discussed in Chapter 6, which rules out the interstitial and interstitalcy mechanisms mentioned in

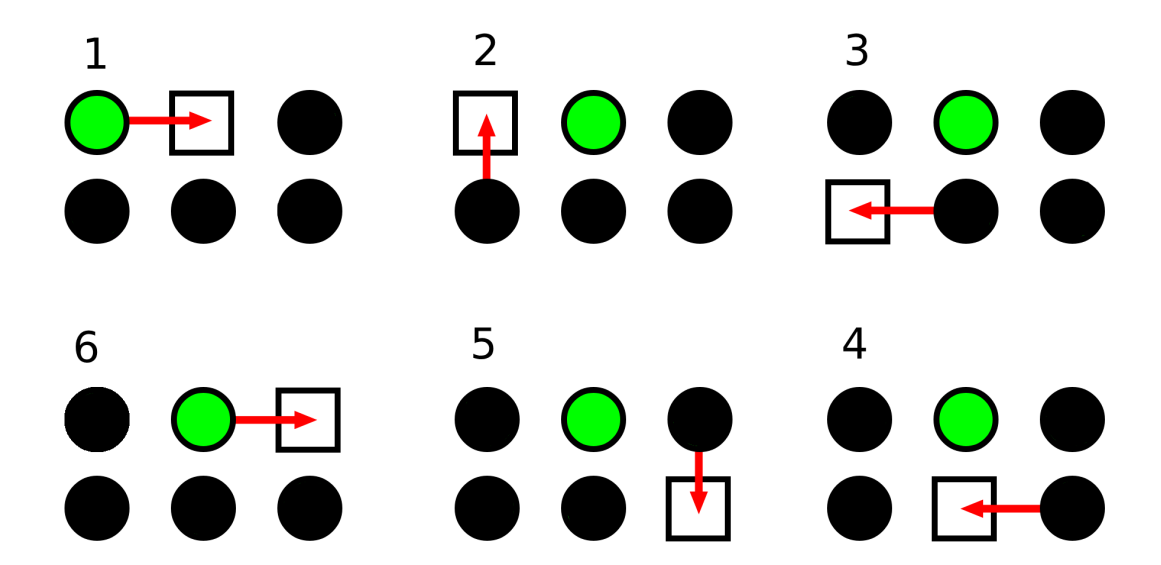


Figure 8.1: Simplified illustration of the sequence of atom-vacancy exchanges required for the atom of interest (green) to migrate through a lattice (black) via a vacancy-hopping mechanism.

Section 2.3.5. Therefore, for Cr to migrate through a crystal lattice, it must exchange places with a neighbouring vacancy in the direction of travel. The initial step and associated migration barrier are relatively simple to simulate in either *ab initio* or molecular dynamics codes. However, continuous migration over longer distances requires that the atom of interest exchanges places with a vacant lattice site such that it does not simply return to its initial position. For this to occur, the vacancy must move 'ahead' of the atom of interest, as illustrated in Figure 8.1. This makes the simulation of long-ranged diffusion in a real alloy computationally intractable at the DFT level of theory. To simulate a single atom moving two lattice sites away from its original position, multiple simulations must be performed in series, and a prohibitive number of possible combinations must be considered. Although this may be feasible in the case of a single defect atom in a perfect body-centred cubic lattice, where multiple vacancy migration pathways may be symmetrically equivalent, this lattice symmetry will not be present where a real, asymmetric alloy is concerned.

Therefore, in this chapter, we employ temperature accelerated dynamics (described in Section 3.1.3) to rapidly explore the phase space of W-Cr alloys with varying Cr concentrations. TAD has multiple advantages over techniques such as Kinetic Monte Carlo (KMC) or Object Monte Carlo (OMC). TAD does not require prior knowledge of transition rates or possible transitions, which would ordinarily be obtained *via* density functional theory. Also, it accelerates the sampling of 'rare' events which would otherwise need to be rigorously described in KMC or OMC. Therefore, by utilising TAD, it is possible to assess the migration of Cr through bulk W-Cr in an efficient and unbiased manner by considering the most likely vacancy hops at the temperature of interest.

8.1 Methodology

Temperature accelerated dynamics simulations were performed at $T_{high} = 1800$ K to obtain migration trajectories at $T_{low} = 1300$ K. In this case, T_{low} was selected due to its relevance in the context of fusion reactor first walls, *i.e.*, the temperature of the first wall during a loss of coolant accident. Simulations were performed on randomly generated bcc W-Cr configurations in LAMMPS using the Fe-W-Cr interatomic potential by Bonny *et al.* [192, 218] in the NVT ensemble. The Cr concentration of the simulation cell was varied from 5 to 35 at% in steps of 5 at%. Simulation supercells containing 127, 431, and 1457 atoms were studied, each with a single W vacancy. All simulations were run for a maximum of 24 hours.

To validate the migration barriers obtained from TAD, CI-NEB calculations at the DFT level of theory were performed as described previously. Nine intermediate images were used in the CI-NEB calculations, with a spring constant of -5.0 eV/ \mathring{A}^2 acting between images. The initial and final positions used in each CI-NEB simulation were obtained by randomly selecting two adjacent configurations from

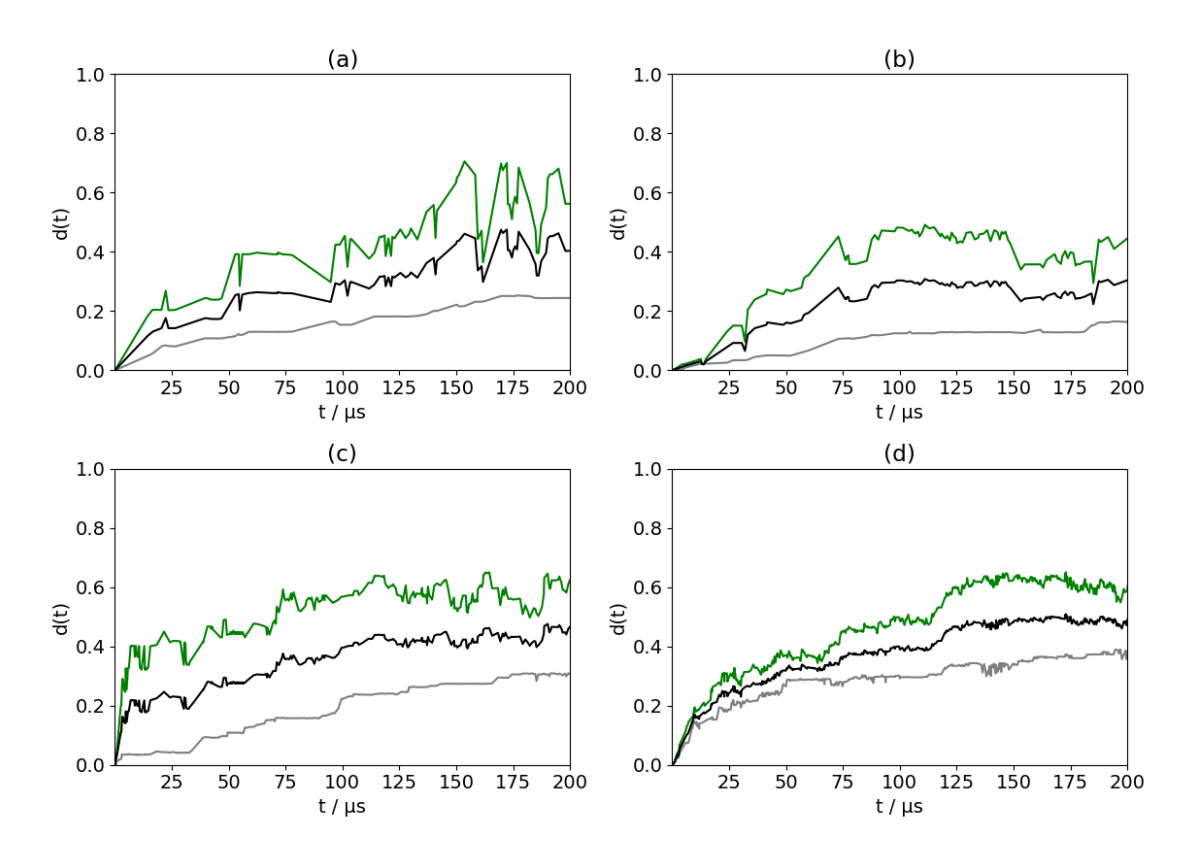


Figure 8.2: Average displacements, d(t), of Cr (green) and W (grey) atoms in 128-atom W-Cr supercells at different Cr concentrations, (a) 5 at%, (b) 10 at%, (c) 20 at%, and (d) 35 at%. The total average displacement is shown in black.

the TAD output in which a Cr atom and a vacancy had exchanged positions.

8.2 Effect of Cr concentration

The mean square displacement (MSD) over time, $d(t)_i$, of W and Cr atoms during vacancy-mediated TAD simulations on 127-atom supercells was calculated according to the equation,

$$d(t)_{i} = \frac{\sqrt{\delta x(t)^{2} + \delta y(t)^{2} + \delta z(t)^{2}}}{N_{i}}$$
(8.1)

Table 8.1: Cumulative elapsed time over the course of the simulation at each Cr concentration.

Cr at%
 5
 10
 20
 35

 t /
$$\mu$$
s
 641
 589
 401
 253

where $d(t)_i$ is the MSD of species i at time t; x(t), y(t) and z(t) are the total displacements in each crystallographic axis; and N_i is the number of atoms of species i present in the simulation. The MSD up to $t = 200 \ \mu s$ is presented in Figure 8.2, displaying the initial period of rapid Cr and W transport. The gradient of the MSD is related to the diffusivity of the species; therefore, it is shown that the diffusivity of Cr is greater than that of W, for reasons that are discussed later. As shown in Table 8.1, the cumulative elapsed time for each simulation extended beyond the limits shown in 8.2. However, the gradient of the MSD becomes greatly reduced after around $200 \ \mu s$. In cells with lower Cr concentration, i.e., $5 \ at\%$ and $10 \ at\%$, there appears to be no net diffusion on the timescale of the simulation, suggesting that Cr does not move from its lattice site after an initial period of migration. On the other hand, at higher Cr concentration, i.e., $35 \ at\%$, the MSD continues to increase slowly, indicating that Cr can migrate even after the initial period of displacement. This is indicative of the segregation of Cr and W, followed by the continuous migration of Cr atoms facilitated by higher Cr concentrations.

Visual determination of segregation in complex systems such as W-Cr is challenging. Therefore, to ascertain whether W and Cr segregated from one another, the Cr-Cr radial distribution function (RDF) was obtained. The timestep at which the RDF was extracted, t_{seg} , was determined by finding the timestep at which the primary cluster of Cr atoms was packed the closest. This was determined by finding the cluster of Cr atoms with the highest atom count and the lowest radius of gyration, r_g , across all timesteps.

Figure 8.3 shows the radius of gyration and the Cr cluster sizes at each timestep.

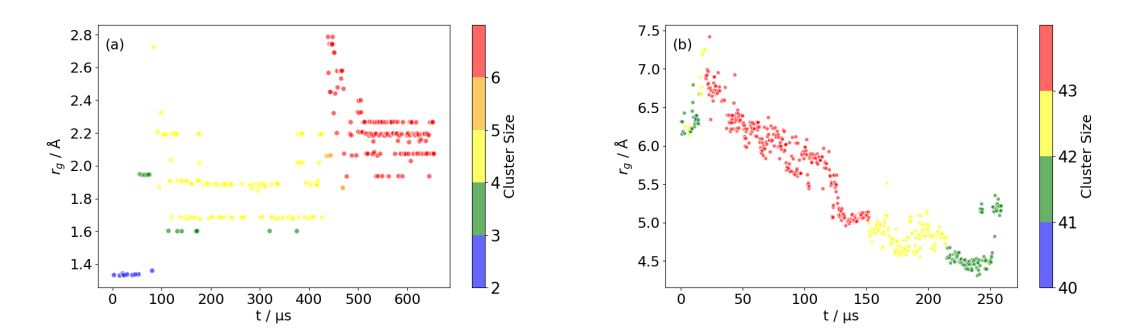


Figure 8.3: Radius of gyration of Cr clusters in W-Cr as a function of time, coloured according to the number of Cr atoms in the cluster, for (left) 5 at% and (right) 35 at% Cr concentrations.

The radius of gyration of a cluster of element i is defined via:

$$r_{g,i} = \sqrt{\frac{r_1^2 + r_2^2 + \dots + r_{n_i}^2}{N_i}},$$
(8.2)

where r_{n_i} is the position of atom n of species i relative to the cluster's center of mass, and N_i is the total number of atoms of i in the cluster. For the examples shown in Figures 8.3 and 8.3, the most closely-packed Cr cluster at 5 at% Cr concentration, consisting of all 6 Cr atoms, was reached at 438 µs. By comparison, the most closely-packed Cr cluster at 35 at% Cr concentration, consisting of 43 Cr atoms, was obtained at 136 µs. Another pattern that is also noticeable, particularly when comparing Figures 8.2d and 8.3, is the rapid drop in r_g at around 120 µs in the 35 at% Cr simulation, correlating with a rise in Cr displacement. This pattern indicates a rearrangement of Cr atoms to form a more tightly packed cluster. Also noticeable is the jump in r_g at around 250 μ s in Figure 8.3, without a change in the number of Cr atoms in the cluster, indicating a rearrangement of the clustered atoms into a more elongated form. However, whilst this suggests the segregation of the W-Cr system, the analysis of the radius of gyration is not necessarily proof of more rapid diffusion in higher Cr concentration systems. As demonstrated in Figure 8.2, the average displacement in the 35 at% concentration was lower than in the 5

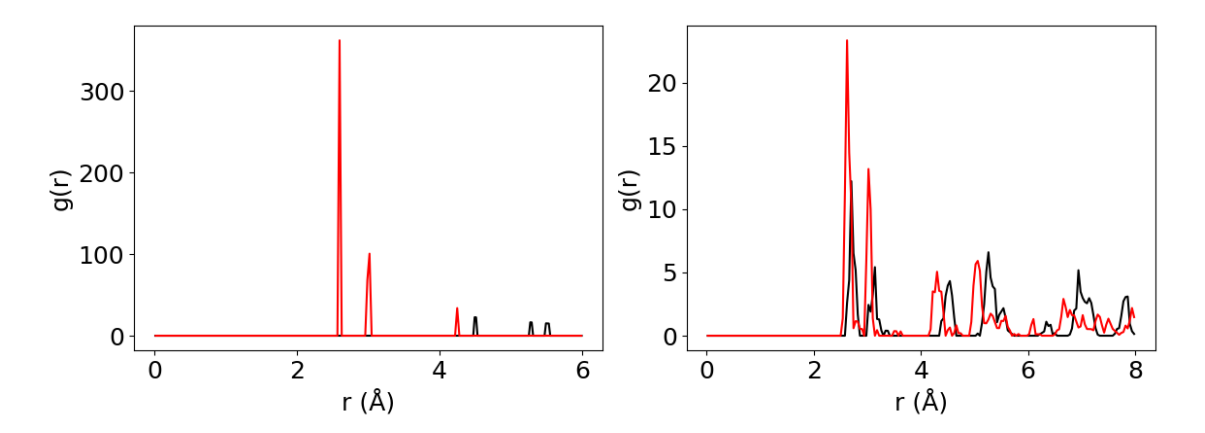


Figure 8.4: Radial distribution functions at t = 0 and $t = t_{seg}$ for the (left) 5 at% Cr and (right) 35 at% Cr systems. The RDF at t = 0 is shown in black, and at $t = t_{seg}$ in red.

at% concentration. The difference between the initial position of any given Cr atom and the Cr cluster itself is intrinsically lower in the higher Cr concentration systems. Therefore, it should be expected that the Cr cluster reaches its minimum radius of gyration faster.

Consequently, the RDFs of the 5 at% and 35 at% systems at t_{seg} are presented in Figure 8.4. As shown in Figure 8.4, the RDF of the 5 at% Cr system shifted to the left, representing the complete migration of Cr atoms from the second coordination spheres of one another to the first coordination sphere. In the 35 at% system, the shift in the RDF was more subtle due to the greater proportion of Cr in the system. At low separation (e.g., below 3 Å), there was a much smaller difference in the RDF between t = 0 and $t = t_{seg}$ than at higher separation (e.g., around 5 Å). Furthermore, it is noted that the lowest separation distances observed in the RDF of the 35 at% system were identical to those observed in the 5 at% system at $t = t_{seg}$. Therefore, it is expected that the positions of these peaks do not change, but rather, their amplitudes increase as the number of Cr atoms in the first coordination sphere increases. Likewise, the more pronounced shift in the radial distribution at progressively greater separation distances illustrates the densification of the Cr cluster.

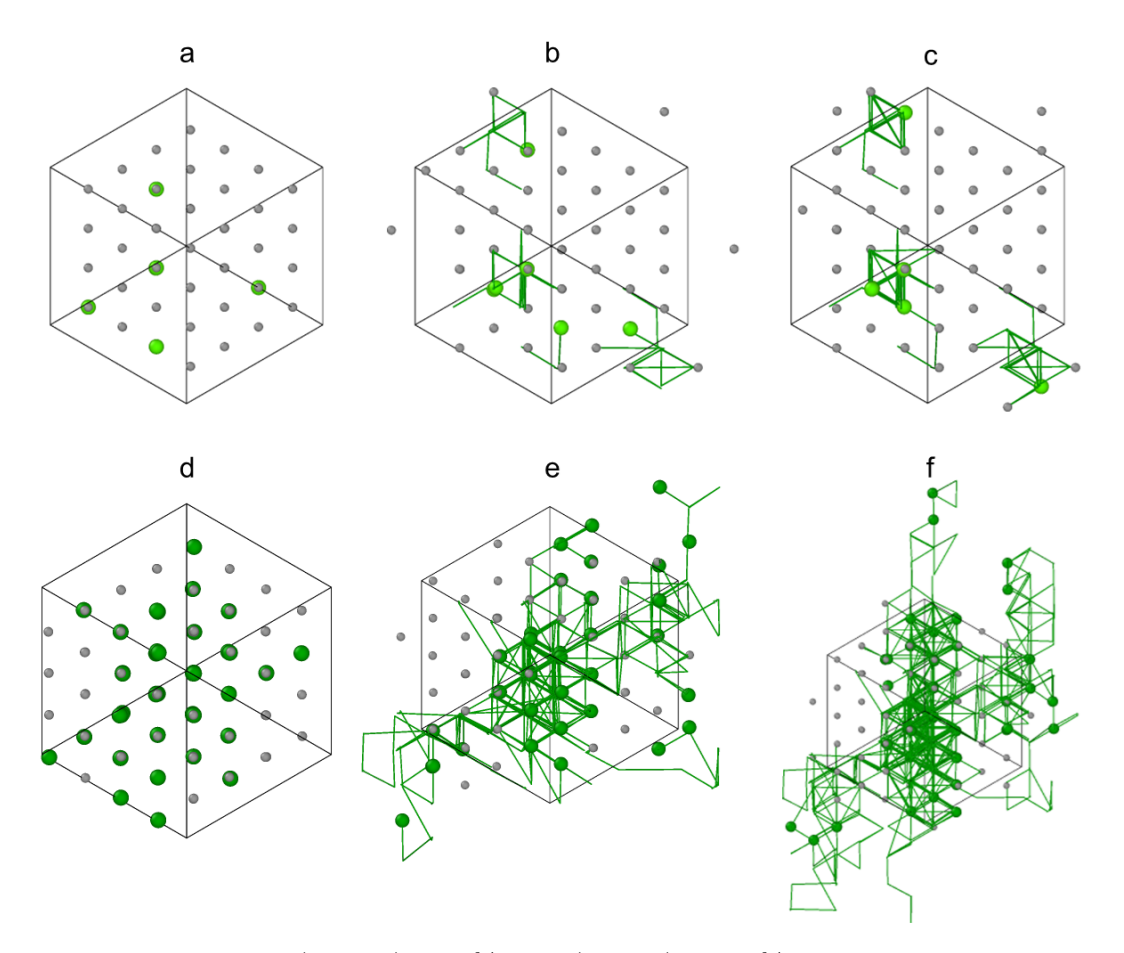


Figure 8.5: Images of (a, b, c) 5 at% and (d, e, f) 35 at% Cr concentration W-Cr, viewed along the $\langle 111 \rangle$ axis. Snapshots taken at (a, d) t=0, (b, e) $t=t_{seg}$, and (c, f) $t=t_{end}$. Grey atoms represent W. Green atoms represent Cr. Green lines show the trajectory of the Cr atoms up to and including the snapshot. Note that the trajectories have been unwrapped, *i.e.*, atoms that have moved outside the periodic boundaries of the simulation cell are shown in their actual positions.

Lastly, Figure 8.5 shows the configuration of the 5 at% and 35 at% Cr concentration cells at t=0, t_{seg} and t_{end} . Not only is the segregation of Cr apparent, but the trajectories of the Cr atoms reveal an important phenomenon observed in higher Cr concentration cells. At lower Cr concentrations, Cr atoms which have clustered did not migrate further, and any subsequent movement of Cr involved the rearrangement of atoms immediately surrounding the cluster. This is evident in Figure 8.5c, where few new unique trajectory lines can be seen relative to those present in 8.5b. Instead, new trajectory lines are drawn over existing ones, showing that Cr atoms remained bound to the cluster. On the other hand, at higher Cr concentrations, the trajectories of some Cr atoms span up to 20 Å in length from their initial positions. The migration of multiple Cr atoms between t_{seg} and t_{end} shows that Cr remains mobile even after it has segregated from W. Furthermore, the difference between t_{seg} and t_{end} in 35 at% Cr is around 123 µs, as opposed to around 216 µs in 5 at%, indicating that the higher Cr concentration system enables rapid, long-ranged diffusion of segregated Cr atoms.

In all cases, the vacancy prefers to bind to the Cr cluster. This is seen in Figure 8.5, where, at lower Cr concentrations, the movement of atoms in the cell is dominated by the localised migration of Cr atoms around the cluster. On the other hand, in higher Cr concentrations, the vacancy preferred to bind to the Cr cluster by enabling the continuous migration of Cr through the system, displacing an equal amount of W atoms in the process.

Figure 8.6 shows the migration barriers of Cr and W at each timestep. Two distinct groups of migration barriers can be seen: a band of higher migration barriers starting from around 0.8 eV in 5 at% and 0.5 eV in 35 at% Cr, and a lower band of migration barriers between 0 and 0.3 eV which is especially prominent in the latter composition. As demonstrated later, the latter consists of transitions between metastable intermediate states and true local minima, whilst the former consists of complete transitions from one local minima to the next. Notably, the migration

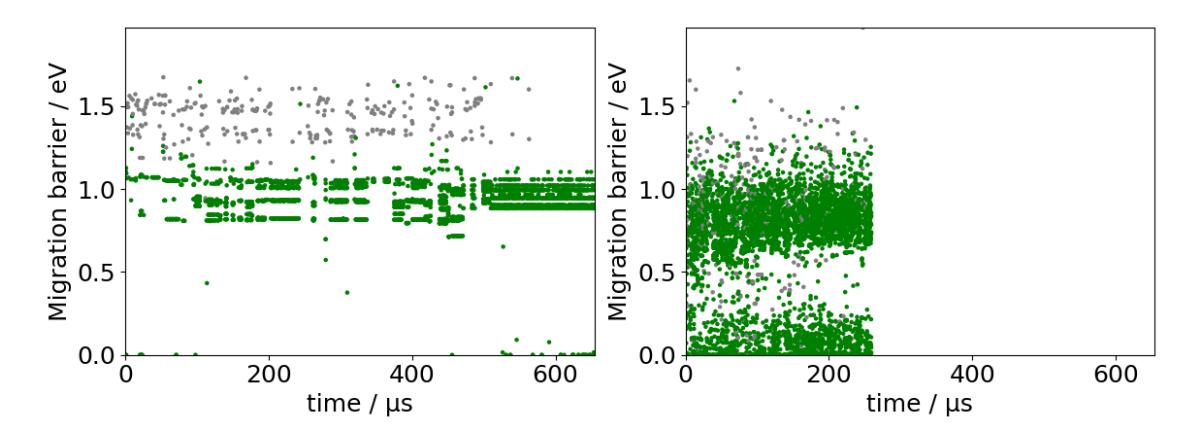


Figure 8.6: Migration barriers for all transitions observed in the simulation of (left) 5 at% and (right) 35 at% Cr systems. Green points represent barriers for the migration of Cr; grey points represent barriers for the migration of W.

barriers for Cr are lower than those of W, corroborating with existing literature on the self-diffusion of W and Cr [310]. As the migration barrier for Cr is lower, the most likely transition is the migration of Cr into a vacant lattice site. For Cr to move away from the cluster, the vacancy must also migrate away from the cluster. However, once the vacancy first exchanges positions with a Cr at the cluster's surface, the lower migration barrier of Cr means that the vacancy is far more likely to move deeper into the cluster rather than into the W-rich region of the bulk. In lower Cr concentrations, this effectively binds the clustered Cr atoms in place, and, as discussed previously, further movement of atoms in the system is mainly restricted to Cr exchanging places with the vacancy in and around the cluster. However, in higher Cr concentrations, the lower migration barriers and the binding of the vacancy to the Cr-rich region of the bulk enables the diffusion of the vacancy (and, therefore, Cr atoms) through this region.

Furthermore, as mentioned previously, increasing the concentration of Cr in the cell reduces the real elapsed time over the course of the simulation. This phenomenon is seen clearly in Figure 8.2. The lower migration barriers for complete Cr migration to a vacant site in higher concentration systems means that the time taken for the system to make the transition is lower, per Equation 3.12. In addition, the more

prominent lower band of migration barriers, representing migrations to and from intermediate states, suggests that the TAD algorithm more frequently visits these states. These effects reduce the acceleration of the simulation; however, they also indicate that a higher Cr concentration accelerates Cr migration through the system by lowering transition times.

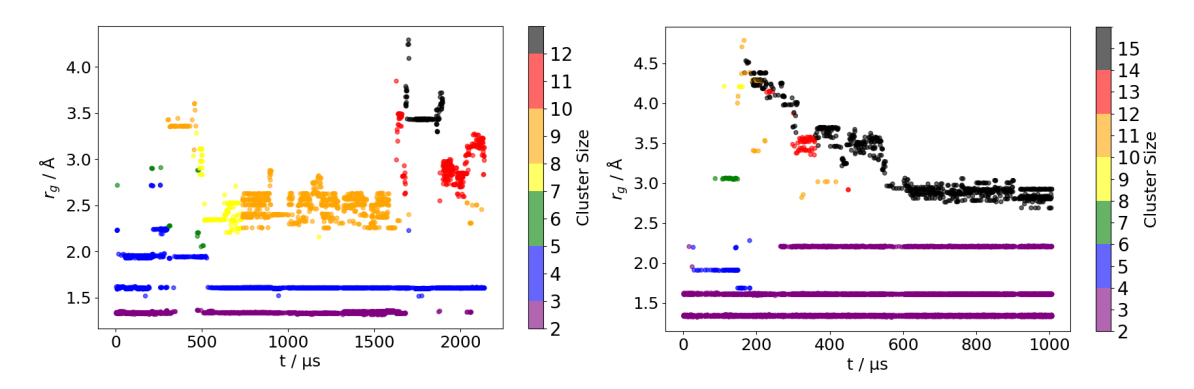


Figure 8.7: Radius of gyration of Cr clusters in W-Cr at 5 at% Cr concentration, for (a) 431-atom and (b) 1457-atom simulation cell sizes, coloured according to the number of Cr atoms in the cluster.

8.3 Effect of vacancy concentration

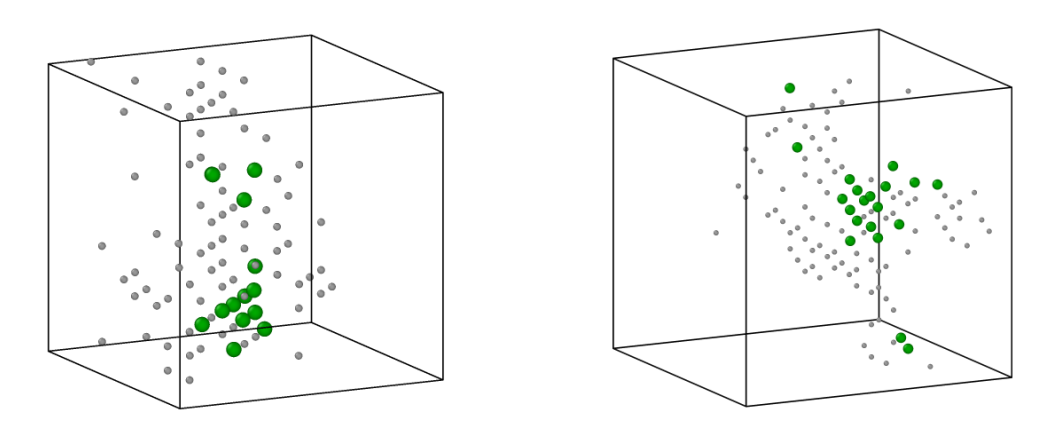


Figure 8.8: Atoms where $d(t) \geq 0.1$ at t_{seg} in W-Cr at 5 at% Cr for (a) 431-atom and (b) 1457-atom simulation cell sizes. Grey atoms represent W. Green atoms represent Cr.

The radius of gyration (see 8.2) of Cr clusters in two systems with 5 at% Cr concentration is shown in Figure 8.7, for 431-atom and 1457-atom supercells, As before, the migration of atoms was mediated by a single respectively. vacancy, and, therefore, the vacancy concentrations were 0.23\% and 0.07\%. The migration energies showed a similar trend to the migration energies at higher vacancy concentration. Compared with Figure 8.3, some key differences arise as a consequence of increasing the number of atoms in the simulation. Firstly, the maximum cluster size in these simulations is much higher, with Cr clusters of 12 atoms forming in the 431-atom simulations and 15 atoms in the 1457-atom simulations. Secondly, and perhaps more importantly, additional clusters of Cr atoms persist throughout the simulation, containing between 2 and 5 Cr atoms in the 431-atom simulation and between 2 and 6 Cr atoms in the 1457-atom simulation. The persistent size and radius of these clusters show that they are not affected by the migration of the vacancy over the course of the simulation, especially in the 1457-atom case.

The evolution of the primary Cr cluster shows that, on the timescale of this simulation, the vacancy is unable to influence the remainder of the system's Cr atoms once the cluster has formed. This implies that there is a maximum number of Cr atoms that one vacancy can sequester within a maximum radius of the cluster. To further demonstrate that this is the case, the atoms with a displacement magnitude of greater than 0.1 Å at t_{seg} were identified for the 431- and 1457-atom cells at 5 at% and are presented in Figure 8.8. It is shown that a large portion of the atoms in these simulations showed no meaningful displacement from their initial positions, indicating that they have had no interaction with the vacancy, whose effective range is limited.

At 0.23% and 0.07% vacancy concentrations and 35 at% Cr, minimal segregation was observed within the timescale afforded by the simulations conducted in this study. However, some evidence of segregation could be identified by examining the

RDF. In the early stages of segregation, the effective binding strength of the vacancy to the cluster is much weaker, owing to the presence of non-segregated Cr atoms outside the nascent cluster. The vacancy on the cluster's surface is more likely to escape by exchanging with these 'external' atoms. Conversely, as the cluster grows, the environment around the Cr cluster primarily consists of W atoms. As established previously, this leads to the vacancy preferentially exchanging with Cr atoms within the cluster. In larger simulation cells, the periodic boundary of the cell means that a vacancy must travel further away from the cluster to encounter the cluster's periodic image. The combination of these two factors means that, in the early stages of segregation in a larger simulation cell, the vacancy is both more likely to escape the nascent cluster and less likely to encounter the same cluster once it migrates away.

Due to this, lower vacancy concentrations give rise to longer times for Cr segregation despite the more rapid diffusion associated with higher Cr concentrations. Conversely, at higher vacancy concentrations, the probability of a different vacancy contributing to the growth of a nascent Cr cluster is much higher. However, the simulation of multivacancy W-Cr systems is outside the scope of this work. Temperature accelerated dynamics may not be appropriate for such simulations if the clustering of the vacancy is more energetically favourable than the migration of W or Cr, as this would result in convergence to a vacancy cluster rather than a Cr cluster.

8.4 Comparison with Density Functional Theory

To validate the results of the TAD simulations, a selection of migration barriers were calculated using density functional theory. Figure 8.9 shows an example of the simple, linear exchange between Cr and a vacant lattice site in 5 at% Cr

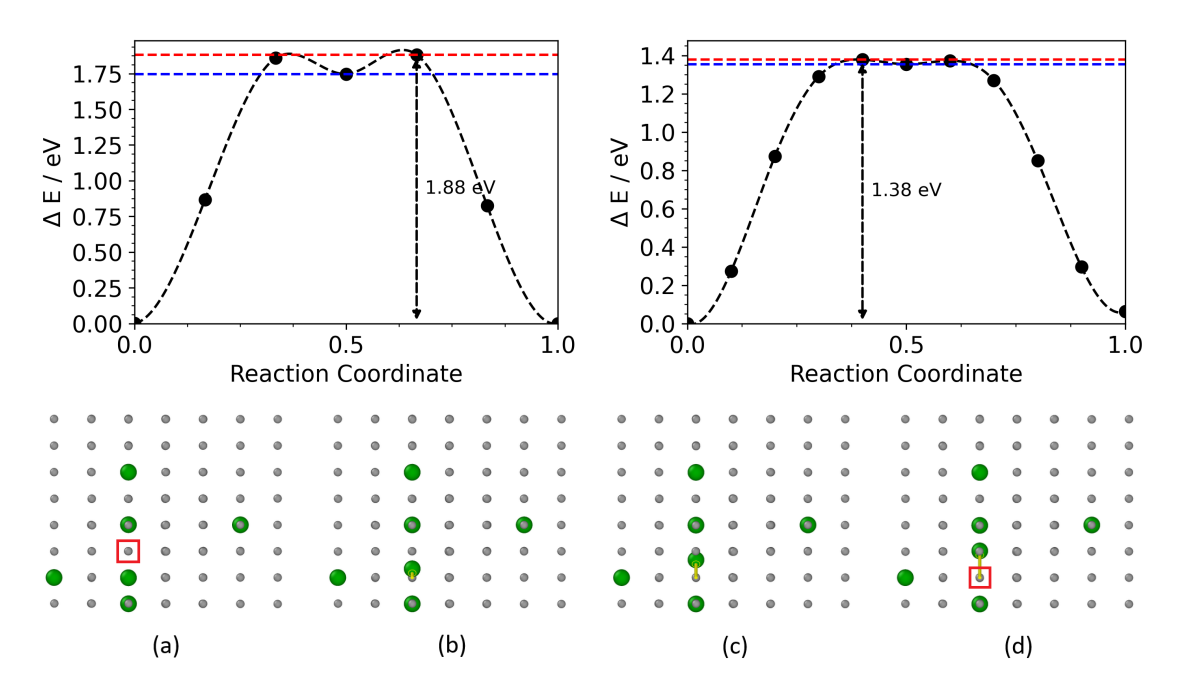


Figure 8.9: The migration barrier of a Cr atom exchanging positions with a vacancy, where the Brillouin zone has been sampled using (left) the Γ -point only, with 5 intermediate images, and (right) a $3\times3\times3$ mesh, with 9 intermediate images. The black dashed line represents a cubic spline fitted to the data for illustrative purposes. The red line represents the maximum height of the barrier to the intermediate state, whilst the blue line represents the relative energy of the intermediate state itself. Below, the 1st, 4th, 8th and 11th configurations in the latter simulation are shown in (a) through (d) respectively, with the red square denoting the vacant site, the green atoms denoting Cr, and the grey denoting W.

concentration, as well as the migration barrier associated with this process. For the purposes of analysis, the migration barrier has been calculated twice - once with the Brillouin zone sampled using only the Γ -point and again with the Brillouin zone sampled using a $3\times3\times3$ k-point mesh. Both calculations demonstrate the presence of an intermediate state; however, the barrier associated with leaving the intermediate state, as calculated using only Γ -point sampling, is an order of magnitude greater than as computed using a more dense k-point mesh. In other words, the less accurate NEB simulation stabilises the intermediate state by increasing the migration barrier that must be surmounted to escape it. This suggests that the lower migration barriers to intermediate states seen at the bottom of Figure 8.6 are a product of the interatomic potential; any inaccuracies that may have arisen in fitting the potential

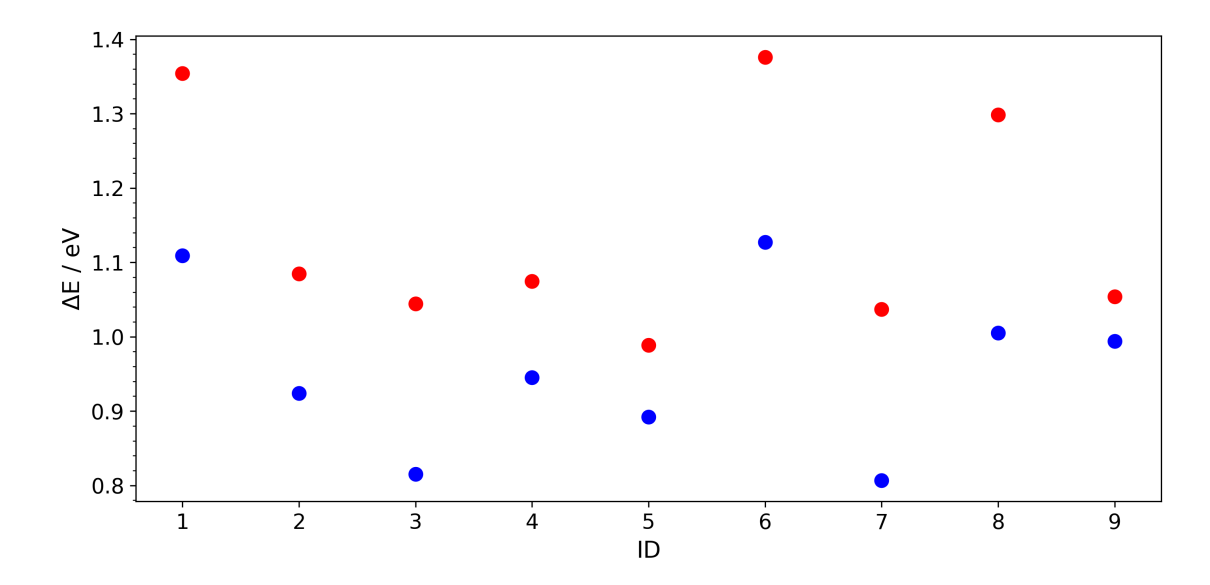


Figure 8.10: Comparison of migration barriers obtained *via* DFT (red) and TAD (blue) for 5 at% Cr concentration. Only the migration barriers obtained using nine images, as described in Section 8.1, are shown. ID is the number assigned to the randomly selected transition.

may manifest in the stability of these intermediate states.

Another notable difference between the DFT and TAD migration barriers was the magnitude of the migration barrier itself. A complete comparison between all 9 barriers sampled at the 5 at% Cr concentration is shown in Figure 8.10. On average, the barriers obtained via TAD are 0.19 ± 0.04 eV lower than those obtained via DFT. This systematic error likely arises from the interatomic potential employed in the TAD simulations. It is noted that the density functional theory data used to fit the Fe-W-Cr interatomic potential used in this work was obtained without considering the W and Cr s- and p-states as valence. In addition, the plane-wave cut-off energy was only 300 eV, as opposed to 520 eV in this work [218].

8.5 Summary

Temperature accelerated dynamics is an appropriate method for simulating monovacancy-mediated diffusion of atoms in a bcc W-Cr system up to 35 at% Cr concentration. The segregation of Cr on an atomic level and sub-millisecond timescale has been observed by analysing the radius of gyration of Cr clusters in the system and the corresponding Cr-Cr RDFs. Furthermore, temperature accelerated dynamics enables an analysis of the migration barriers of each individual vacancy hop. The migration barriers predicted by TAD show reasonable agreement with those calculated at the DFT level of theory. However, an interatomic potential tailored to the W-Cr system may yield more accurate results.

Whilst segregation occurs at all Cr concentrations sampled herein, long-range diffusion is observed at higher Cr concentrations (≥ 30 at%). This long-range diffusion is enabled by the lowering of the Cr migration barrier in higher concentration systems, leading to a greater affinity for the vacancy to exchange positions with a Cr atom. The vacancy concentration also plays an important role in the segregation of Cr, and multiple vacancies may contribute to the clustering of Cr atoms. These two observations reveal the crucial role of vacancies in the self-passivating behaviour of the W-Cr system, which is dependent upon the segregation and long-range migration of Cr atoms. Therefore, it is proposed that the presence of oxygen impurities in W-Cr may annihilate these vacancies and prevent the diffusion of Cr within the bcc lattice.

Chapter 9

Effect of Oxygen on Vacancy-Mediated Diffusion

In previous chapters, Y in W-Cr-Y has been identified as an oxygen getter for O impurities in the alloy. By assuming a vacancy exchange mechanism, the segregation and long-range diffusion of Cr in the bulk was identified using temperature accelerated dynamics, hinting at the importance of the vacancy in the movement of metal atoms in the bulk crystal. In this chapter, the effect of including O in bcc-W and 5 at% W-Cr is investigated. The migration barriers of $O_{TIS} \rightarrow O_{TIS}$ hops in bcc-W are compared against literature values, whilst, for 5 at% W-Cr, the migration barriers of Cr-V_W exchanges in the absence of O_{TIS} obtained via TAD are compared to the migration barriers in the presence of O.

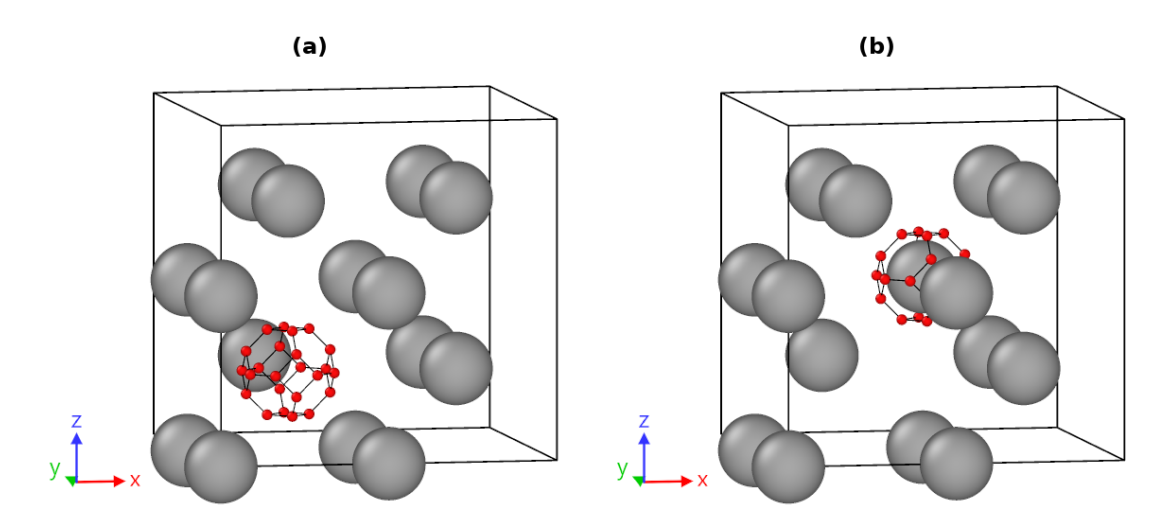


Figure 9.1: All O_{TIS} starting positions used throughout this chapter. The O_{TIS} sites were placed relative to (a) the vacancy site and (b) the first nearest neighbour. Each O_{TIS} is connected to each of its three nearest neighbours by a black line.

9.1 Methodology

The migration barriers of O in W and W-Cr were obtained via density functional theory as described in previous chapters. For W, a 128-atom supercell was constructed from the geometry-optimised unit cells, and a V_W defect was generated at the centre of the supercell. On the other hand, for W-Cr the starting configuration was taken from one of the TAD simulations discussed in 8. In particular, it corresponds to the starting configuration of the migration barrier labelled '1' in Figure 8.10, and shown in Figure 8.9. In both cases, the O defects were placed in the tetrahedral interstitial sites relative to the vacancy and its first nearest neighbour (1NN), as shown in Figure 9.1, and their positions were subsequently relaxed with the energy minimisation criteria described previously. Since the objective of this work was to establish the effect of O on the movement of metallic species, the 'forward reaction' refers to the process of metal M moving to the site initially occupied by defect V_W , i.e., $M \to V_W$.

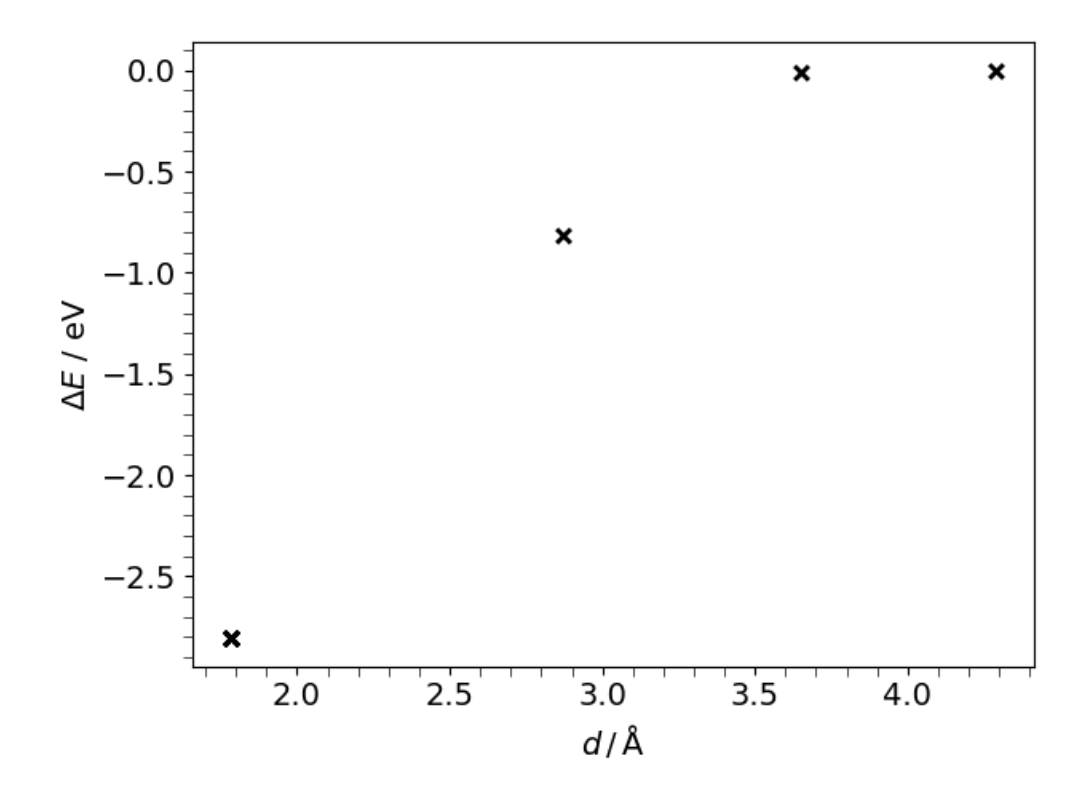


Figure 9.2: The difference in total energy of the system as a function of the distance between the vacancy and the O_{TIS} defect in bcc-W, relative to the total energy of a bcc-W system where both V_W and O_{TIS} are isolated from one another.

9.2 Migration of O around W Vacancy

To begin examining the interaction between O_{TIS} and V_W defects in W-Cr alloys, their interaction in bcc-W was first examined by considering the total energy of the system as a function of the O_{TIS} defect's position relative to the V_W defect. Figure 9.2 shows this relationship clearly. Compared to the total energy of the system when O_{TIS} and V_W are at an arbitrarily large distance, the total energy drops by 2.87 eV when the O_{TIS} defect is positioned on the V_W site. The binding effect decreases considerably with distance, and is negligible above 3.5 Å from the V_W site. This effect is especially noteworthy as it implies that vacancies in bcc-W may act as oxygen traps and serves as nucleation sites for internal oxidation.

The migration barrier of O through bcc-W depends on the intermediate state

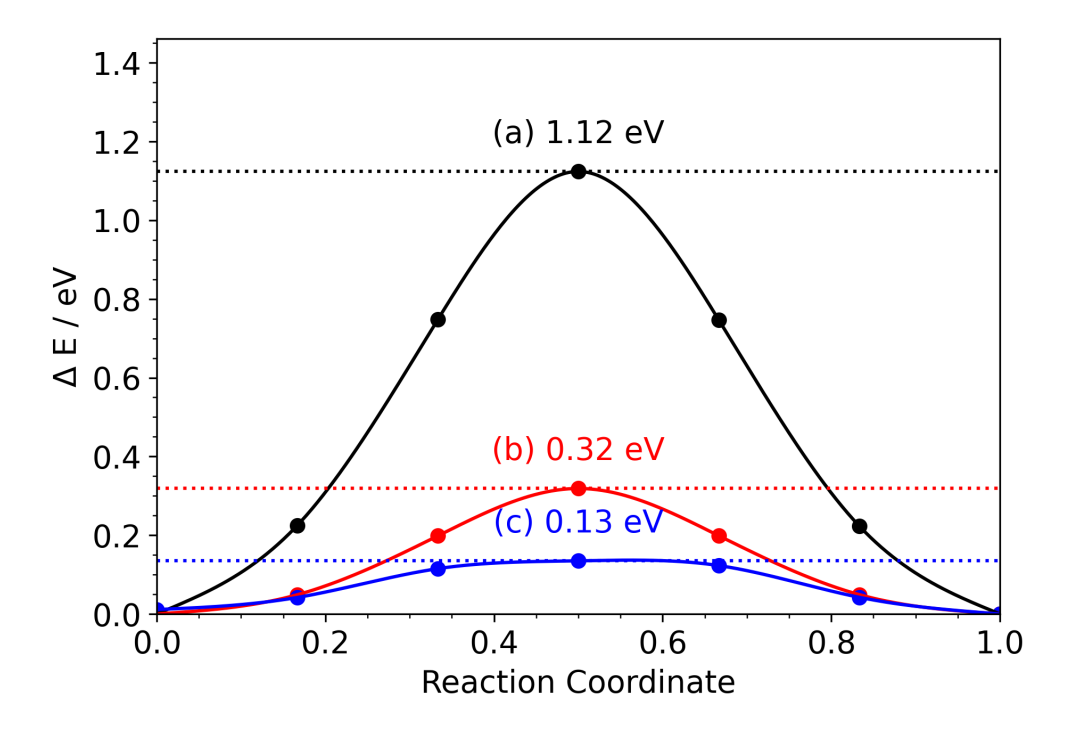


Figure 9.3: NEB profiles of O_{TIS} migration at various distances from a V_W site in bcc-W: (a) on-site, ~ 1.5 Å; (b) first nearest neighbour, ~ 2.0 Å; (c) first nearest neighbour, ~ 2.5 to 3.0 Å

which the system passes through. The work of Alkhamees et~al. described two pathways for interstitial oxygen to diffuse through a bcc-W lattice, first via moving directly to another tetrahedral interstitial site, and second via the nearby octahedral interstitial site. Their work showed that the direct transition had a migration barrier of 0.17 eV, whereas the transition via the octahedral interstitial site had a much higher migration barrier at 0.32 eV [305]. In this work, only the direct $O_{TIS} \rightarrow O_{TIS}$ transition was considered, and the migration barrier associated with it was calculated to be 0.13 eV. This discrepancy is likely a result of the plane-wave cut-off energy that Alkhamees et~al. used (350 eV). Nevertheless, the migration barrier of the transition of an oxygen defect from one tetrahedral site to another is in good agreement with existing literature, and will be referred to as the pure bulk value.

Subsequently, the V_W defect was introduced according to Figure 9.1. The

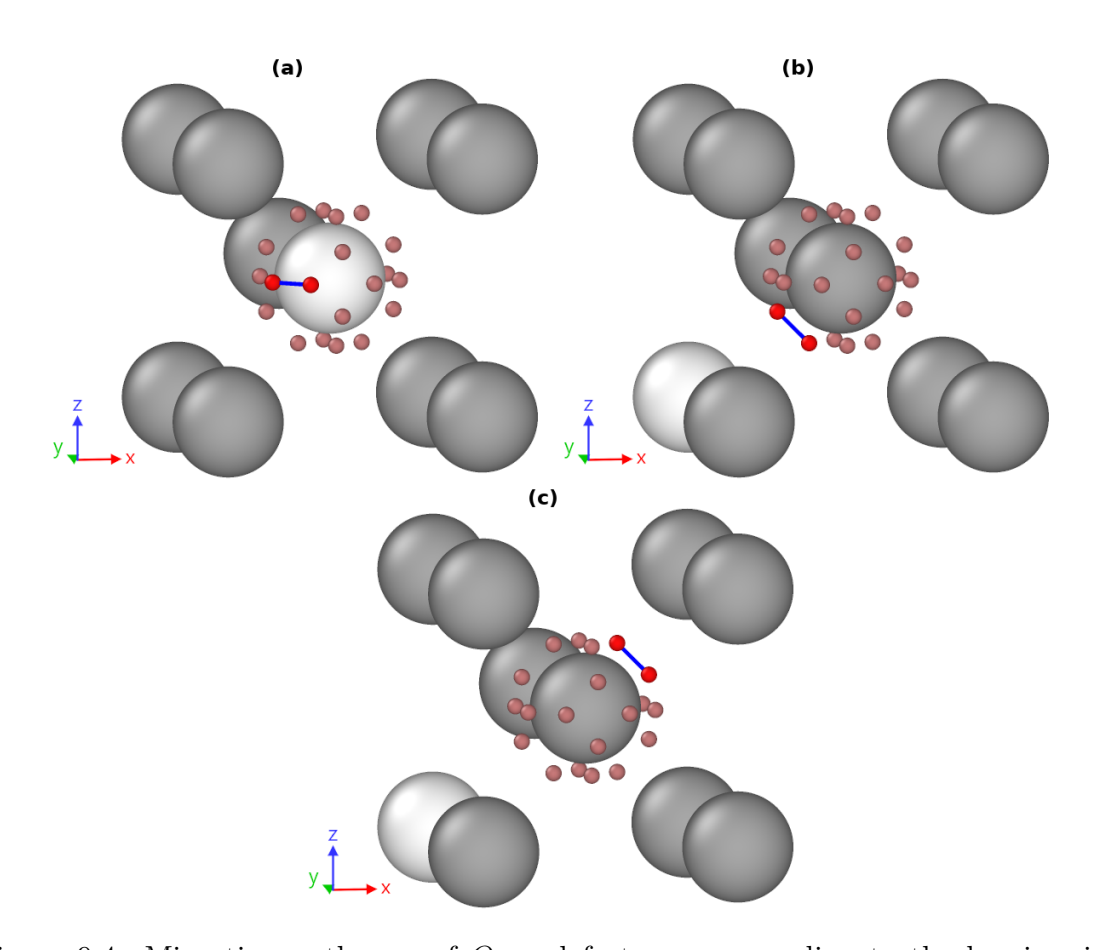


Figure 9.4: Migration pathways of O_{TIS} defects, corresponding to the barriers in Figure 9.3a, b and c. The white atom denotes the position of the vacancy, the redgrey atoms denote other O_{TIS} positions around the site, and the path between the start and end sites is shown in blue. As such, the red atoms denote the start and end positions of the single O_{TIS} defect.

migration barriers for the three closest $O_{TIS} o O_{TIS}$ transitions were calculated for each starting position, although, due to the symmetry of these positions along the $\langle 100 \rangle$ direction, most of these transitions were degenerate. As shown in Figure 9.3, the migration barriers show a dependency on the distance between the interstitial site and the vacancy. When the O_{TIS} defect was on-site, *i.e.*, it was the tetrahedral interstitial position relative to the vacancy, the migration barrier to transition to any of the adjacent TIS around the same vacancy was 1.12 eV. However, when the O_{TIS} defect was on the vacancy's first nearest neighbour, the migration barrier was significantly reduced. As shown by (b) and (c) in Figure 9.3, the migration barrier reduces to 0.32 eV on the side of the first nearest neighbour closest to the

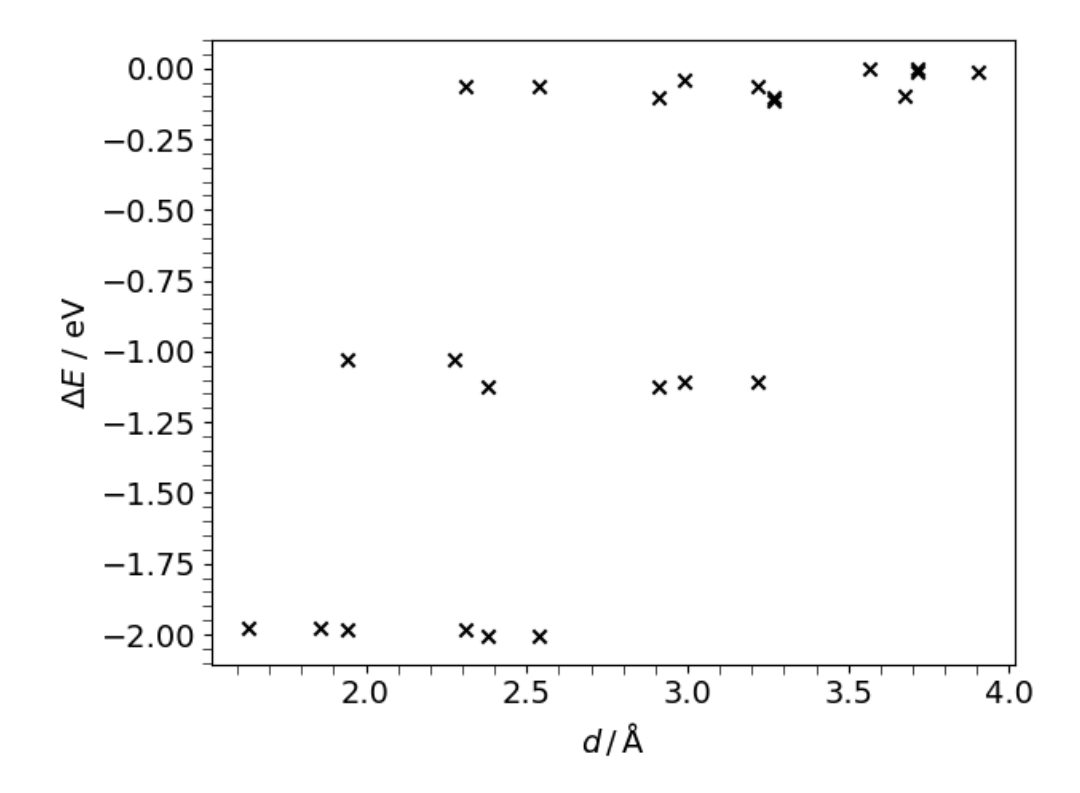


Figure 9.5: The difference in total energy of the system as a function of the distance between the vacancy and the O_{TIS} defect in 5 at% W-Cr, relative to the total energy of a bcc-W system where both V_W and O_{TIS} are isolated from one another.

vacancy, and 0.13 eV on the side furthest away from it. The migration pathways corresponding to these barriers are depicted in Figure 9.4.

This demonstrates two key effects of the vacancy in tungsten. Firstly, the W vacancy inhibits the migration of on-site oxygen by increasing the migration barrier by an order of magnitude. Secondly, the O-binding effect of the vacancy is only felt as far away as the first nearest neighbour and, even then, only on the side of the neighbouring site closest to it. At around 2.5 to 3.0 Å, the migration barrier of the O_{TIS} defect returns to its pure bulk value.

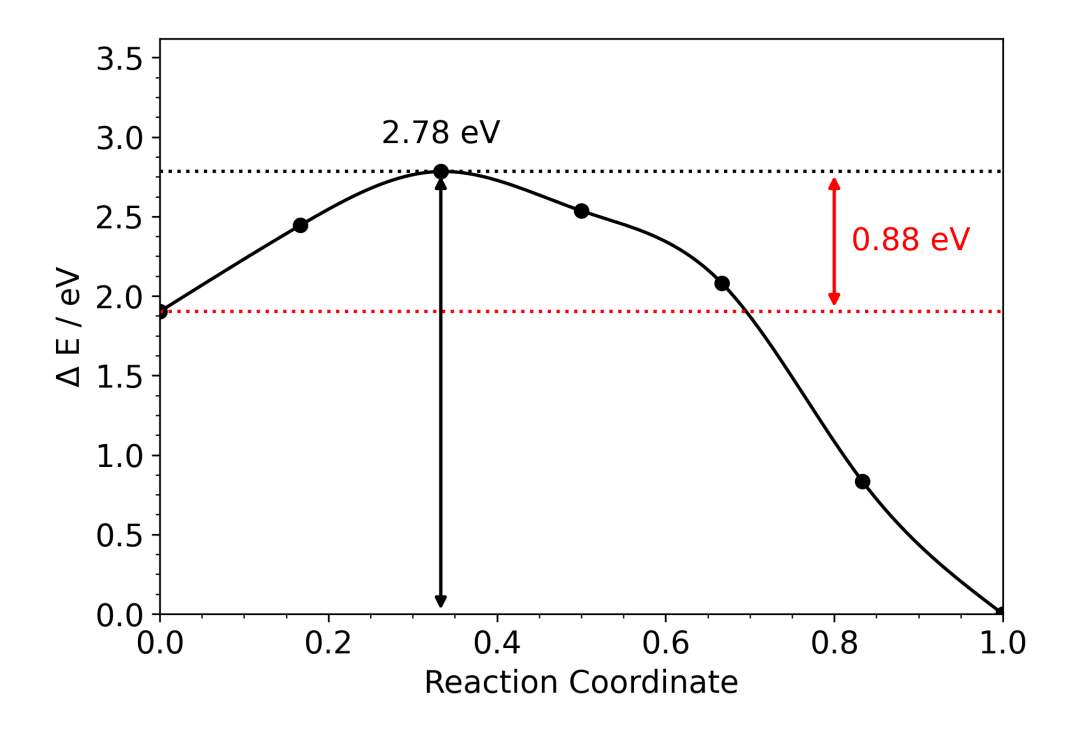


Figure 9.6: NEB profile of the vacancy-mediated migration of Cr in the presence of O_{TIS} . The heights of the forward and reverse migrations are shown in red and black respectively.

9.3 Migration of Cr in the Presence of O

For the chosen migration barrier in 5 at% Cr, the possible O_{TIS} positions around the vacancy and its first nearest neighbour were generated and subsequently relaxed. As shown in Figure 9.5, the total energy of the system as a function of the distance between O_{TIS} and V_W was considerably more complex than in bcc-W, although, this is not unexpected as the chemical environment around the site is no longer isotropic. As such, the binding energy of O_{TIS} to V_W is affected by its proximity to its neighbouring atoms, which may be either W or Cr. Nevertheless, the trend that was observed in bcc-W was also seen here: the total energy of the system was reduced by about 2 eV within approximately 2.5 Å of the vacancy, depending on the chemical environment.

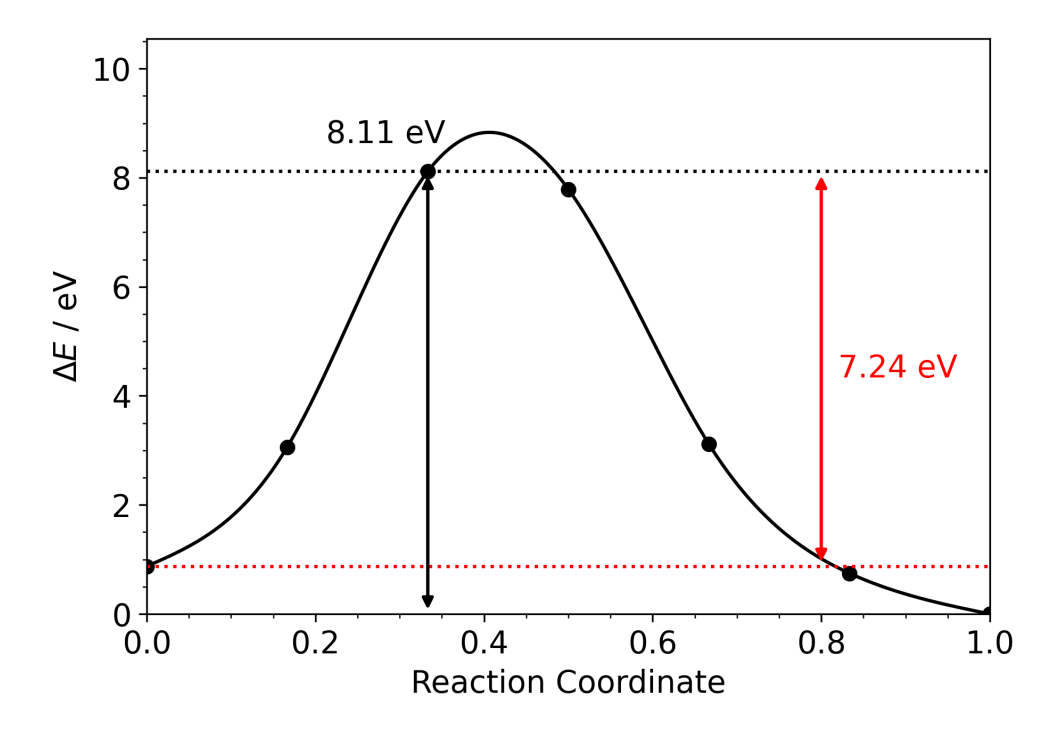


Figure 9.7: NEB profile of the vacancy-mediated migration of Cr in the presence of O_{TIS} when the defect does not lie along the $\langle 100 \rangle$ axis relative to the V_W defect and the migrating Cr ion.

Due to the large binding energy between O_{TIS} and V_W , the exchange of the vacancy with a neighbouring Cr atom incurs a much greater energetic penalty which is factored into the migration barrier. Figure 9.6 shows the NEB profile and migration barrier of Cr exchanging with the vacancy. At the start of each simulation, the O_{TIS} defect was adjacent to the Cr ion. Hence, the migration barrier of the forward reaction, $Cr \to V_W$, is shown in red, and corresponds to the movement of Cr away from the O_{TIS} defect. Alternatively, this can be seen as the movement of V_W towards the O_{TIS} defect.

Furthermore, a direct comparison between this NEB profile and the one presented in Figure 8.9 shows that the migration barrier for Cr moving directly away from the O_{TIS} defect, from 1.38 eV down to 0.88 eV. However, this is only true when Cr, O_{TIS} and V_W are aligned along the same direction; in this case, all three species align along

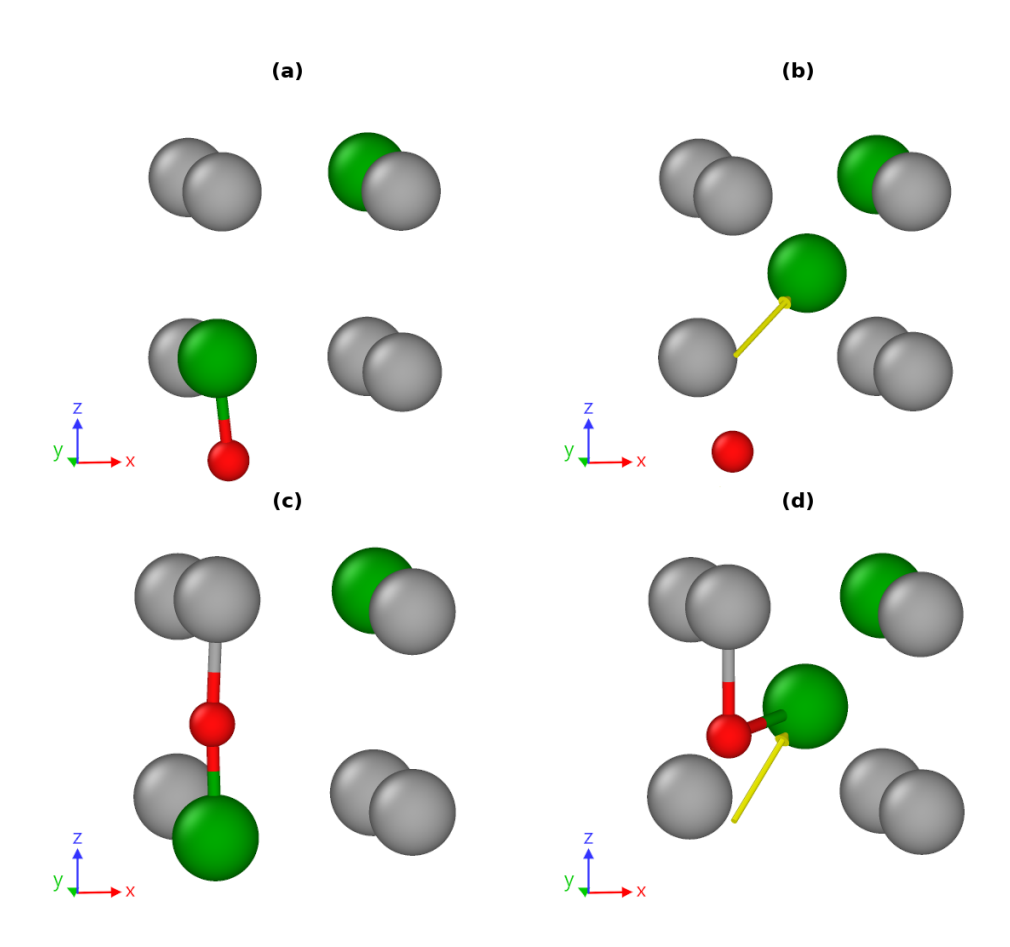


Figure 9.8: Migration pathways of Cr in the presence of O_{TIS} when the O_{TIS} -Cr-V_W angle is (a, b) 108.9°, (c, d) 53.9°. The initial configurations are (a) and (c), whilst the final configurations are (b) and (d).

the $\langle 111 \rangle$ direction such that the O_{TIS} -Cr-V_W angle was 108.9°. This configuration is illustrated in Figure 9.8a. The migration barrier of the same vacancy-mediated migration of Cr when the angle between the O_{TIS} defect and the vacancy was 53.9° is shown in Figure 9.7. This configuration is illustrated in Figure 9.8b. The migration barriers were 7.24 eV for the forward reaction and 8.11 eV for the reverse reaction due to the proximity of the Cr ion as it passed the O_{TIS} defect. These elevated migration barriers suggest that the O_{TIS} defect may even block the migration of metallic species onto neighbouring vacancy sites. To summarise, the preferred migration processes in order of migration barrier, from lowest to highest, are:

• <1 eV - Exchange of V_W and Cr when the O_{TIS} -Cr- V_W angle is $\sim 108.9^\circ$,

- $\sim 1 \text{ eV}$ Migration of O_{TIS} around V_W ,
- ~8 eV Exchange of V_W and Cr when the O_{TIS} -Cr- V_W angle is ~53.9°,

Therefore, for Cr and V_W to exchange positions, the O_{TIS} defect will most likely move to a position such that the subsequent migration barrier will be ~ 1 eV. In practice, this would involve a series of $O_{TIS} \to O_{TIS}$ migrations before the optimal configuration is achieved, followed by the $Cr-V_W$ exchange itself.

9.4 Summary

The results presented in this chapter suggest that the presence of oxygen impurities in both W and W-Cr SMART alloys causes vacancy annihilation and, therefore, the inhibition of vacancy-mediate migration of W or Cr ions. Ordinarily, oxygen moves through the bcc lattice with relative ease, with the barrier for O_{TIS} to O_{TIS} transitions being 0.17 eV according to Alkhamees et al.. However, in the presence of a V_W defect, the migration barrier rises to as high as 1.12 eV in tungsten, significantly hindering the diffusion of oxygen through the lattice. Moreover, the strong binding energy of the O_{TIS} - V_W pair not only reduces the migration barrier for Cr away from the O_{TIS} defect, but greatly hinders the movement of the vacancy thereafter. Once bound, the vacancy is unable to facilitate the migration of metallic species through the bulk crystal, inhibiting their ability to segregate to the grain boundaries. Furthermore, Figure 9.7 shows that O_{TIS} may even block the V_W -Cr exchange depending upon its relative orientation to the exchanging pair. In the context of W-Cr SMART alloys, these effects would reduce the flux of Cr atoms to the surface and may be responsible for the greater extent of oxidation seen in samples of W-Cr-Y with non-stoichiometric quantities of Y and O.

Chapter 10

Conclusions and Outlook

The work presented in this thesis concerns the processes which contribute to the oxidation and/or self-passivation of tungsten and tungsten-based SMART alloys. Both density functional theory and molecular mechanics have been employed to develop a deeper understanding of the formation of oxide phases in these systems and the migration of their constituent elements at the atomistic level.

In Chapter 4, the four constituent elements featured throughout the rest of the thesis (W, Cr, Y and O) were examined using both density functional theory and, where applicable, the Fe-Cr-W embedded atom potential by Bonny et al. Close attention was shown to the choice of exchange-correlation functional, particularly the PBE and PBEsol functionals, and their applicability for the calculation of the elements' physical and electronic properties in the bulk. For oxygen, the bond length and binding energy of the O₂ dimer were studied at both the GGA and hybrid functional levels of theory, with the latter showing greater accuracy in the prediction of the O-O bond length. However, using hybrid functionals on more complex systems is prohibitively expensive. The comparisons made between the PBE and PBEsol functionals for the metallic species - W, Cr and Y - indicated that

the PBE functional is the most suitable choice for the work in the later chapters.

Initially focusing on the oxidation of bulk tungsten, we examined the major, experimentally observed tungsten oxide phases - WO₂, W₁₈O₄₉, W₂₅O₇₃ and WO₃ - in Chapter 5. DFT+U simulations were employed to investigate the evolution of the electronic structure of the stable tungsten oxides as the tungsten-oxygen ratio increased. Namely, the electronic density of states revealed a gradual change between the metallic nature of WO₂ and the non-metallic nature of WO₃ throughout the sub-stoichiometric Magnéli phases. The vacancy formation energies in each of these structures were then calculated, further revealing the link between the WO₂ and WO₃ end members and the Magnéli phases. By combining observations on the physical structure, electronic structure, and oxygen vacancy formation energies, it was perceived that the Magnéli phases consisted of WO₂-like and WO₃-like regions. Subsequently, the migration barriers of oxygen diffusion through WO₂ and WO₃ were calculated. However, the complexity of the Magnéli phases meant that determining the migration barriers using DFT was prohibitively costly; therefore, it was proposed that the migration barriers in similar atomic environments in $W_{18}O_{49}$ and $W_{25}O_{73}$ would follow suit. Not only did the migration barriers display anisotropic behaviour, but the disparity between the migration barriers in WO₂ and WO₃ meant that oxygen diffusion throughout the Magnéli phases would display a degree of orientational dependence. In other words, should the Magnéli phases be aligned such that their WO₂-like regions occlude the WO₃ like regions from the surface, then oxygen diffusion into the bulk tungsten oxide would inherently be hindered.

Moving beyond bulk tungsten, the formation enthalpies of the binary and ternary oxide phases in W-Cr-Y SMART alloy were calculated and presented in Chapter 6. In particular, the formation enthalpies were not only calculated using the bulk metals and diatomic oxygen as reference, but also by using the chemical potentials of a range of W, Cr, Y and O defects in pure W. By comparing the formation

enthalpies in terms of the number of oxygen atoms presented in each formula unit of the oxide, a hierarchy closely matching experimental observation was established: the yttrium-containing oxides, Y_2O_3 and $YCrO_3$ form preferentially in W-Cr-Y SMART alloy, followed by the mixed W-Cr oxides, and finally the ternary oxides. Corroborating with experimental observations, the preference for the formation of Y_2O_3 was an important step in elucidating the role of Y in W-Cr-Y. Comparison of the reported optimal composition of W-Cr-Y, the oxygen impurity content in the same composition, and the stoichiometric ratio of Y and O required to form Y_2O_3 , it was proposed that the major role of yttria is likely as an oxygen scavenger in the SMART alloy - *i.e.*, it sequesters all available oxygen impurities, facilitating the rapid transport of Cr to the surface, thus providing the self-passivating behaviour of the alloy.

Based on previous chapters, and assuming the role of Y is to getter oxygen, in Chapter 7 we examined the behaviour of Cr in W with neither Y or O present in the bulk. The Gibbs energy of mixing across a range of temperatures and compositions was presented, and the enthalpy of formation for Cr vacancies were calculated across the concentration range. By calculating the order-disordered transition temperature from the Gibbs energy of mixing, the spinodal curve for the W-Cr system was calculated and showed excellent agreement with the experimental phase diagram. The Cr vacancy formation enthalpies revealed the reduction of the vacancy formation enthalpy as the composition of the system approached parity, owing to the greater reduction in the strain of the system when removing a Cr atom from W-Cr at close to 50 at% Cr. Furthermore, later work in the same chapter indicated that there was a thermodynamic driving force for Cr segregation to the $\langle 210 \rangle [100]$ grain boundary. By simulating the transport of Cr at this grain boundary, however, an important phenomenon was revealed: namely, W-Cr grains with 30 at% Cr clearly showed diffusion of Cr to the grain boundary, whereas grains with much lower Cr concentrations did not.

To further investigate this effect, temperature accelerated dynamics was employed in Chapter 8 to understand the mechanism of vacancy-mediated diffusion of Cr in binary W-Cr at different concentrations. Simulations across a range of compositions at 1300 K (the maximum temperature of the first wall during a loss of coolant accident) showed the segregation of W and Cr on an atomic level, leading to the clustering of Cr atoms and, moreover, the binding of vacancy to Cr-rich regions of the bulk. At higher Cr concentrations (≥ 30 at% Cr), the binding of the vacancy to these regions enabled the diffusion of Cr on the sub-millisecond timescale, up to displacements of around 20 Å. This highlights the importance of the vacancy in W-Cr in the local atomic rearrangements required for long-ranged diffusion and, subsequently, the self-passivating behaviour of W-Cr alloys. Based on this, the effect of the vacancy defect on the diffusion of O and Cr in W-Cr was examined at the DFT level of theory in Chapter 9. In agreement with previous literature [305], the migration barrier for oxygen diffusion between one tetrahedral interstitial site and its neighbour was around 0.17 eV. However, if the O_{TIS} defect is situated on a vacancy site, this migration barrier rises to as high as 1.12 eV. Furthermore, it was found that the binding energy of the O_{TIS} - $V_{(W,Cr)}$ pair was on the order of 2 eV. In the W-Cr system, the presence of O_{TIS} reduced the migration barrier for vacancy-mediated Cr diffusion; however, the binding energy of the resultant oxygen-vacancy pair means that the further diffusion of Cr via the same vacancy becomes virtually impossible. As such, this binding mechanism likely affects the formation of the protective Cr₂O₃ at the surface of the W-Cr-Y alloy.

The results of Chapters 6, 8, and 9 reveal the important role of yttrium, oxygen and vacancies in the self-passivating behaviour of W-Cr-Y SMART alloys. The inclusion of yttrium binds residual oxygen, which may have become ingrained within the alloy during synthesis, forming yttria-containing nanoparticles at the grain boundaries. Whilst these nanoparticles have their intrinsic effects on the properties of the alloy, the absence of impurity oxygen within the bulk W-Cr grains

permits the segregation and long-range diffusion of Cr to the grain boundaries and the surface of the alloy. On the other hand, oxygen impurities within the bulk impede the migration of vacancies, preventing them from mediating the diffusion of Cr. Therefore, it seems likely that the self-passivating performance of W-Cr-Y is linked to the ratio of yttrium and oxygen in the alloy. Synthetic procedures to create W-based SMART alloys must be mindful of the oxygen impurity levels in the alloy, and the yttrium concentration must be balanced accordingly. The management of oxygen ingress into the system may prove challenging on a practical level in the large-scale fabrication of W-Cr-Y alloys.

This thesis comprises a series of studies at the atomic level. However, the materials investigated in this work do not exist in isolation or at the length-scales to which DFT and MD simulations are limited. They will be exposed to extreme temperatures and magnetic fields throughout their lifespan, the effects of which are not yet fully understood. Likewise, their lifespan in the first wall of a tokamak fusion reactor must be orders of magnitude greater than the timescales of these simulations. Over the lifetime of a fusion reactor, W and W-based first walls will accumulate a wide range of defects due to radiation damage, transmutation products and other fusion by-products that cannot be ignored. The synthetic procedures used to manufacture the first wall panels may also introduce impurities, including not only oxygen but also elements such as nitrogen, phosphorus, and cobalt [311]. Future work must be cognisant of these defects and additional elements, going beyond the relatively simple case of just tungsten, chromium and yttrium, and aim to incorporate them into computational models accordingly.

To accurately predict the behaviour of tungsten and tungsten-based SMART alloys at higher time- and length-scales, the simulation of these materials must also go beyond the atomistic level and into the micro-, meso- and, eventually, macroscopic. At these length-scales, the behaviour of metal ions and impurities at grain boundaries and surfaces must also be understood. The work presented in this

thesis builds upon existing research to improve our understanding of the oxidation of pure tungsten and tungsten-based SMART alloys, primarily at the electronic level. Beyond the electronic level, the molecular dynamics simulations in this thesis were made possible by existing research into reduced activation steels. However, the elements covered by the Fe-Cr-W embedded atom potential and the accuracy of interactions between Cr and W limit the simulations that can be performed. To further expand in terms of scale and scope, an interatomic potential incorporating the elements of interest must be developed, enabling a much wider range of atomistic studies to be carried out. For instance, in Chapter 5, the oxygen vacancy migration barriers were calculated using DFT for WO₃ and WO₂ but not for the Magnéli phases, as the number of barriers to consider was prohibitively costly. With an interatomic potential containing both W and O, the migration barriers in W₁₈O₄₉ and W₂₅O₇₃ could be calculated with much greater efficiency using temperature accelerated dynamics. Similarly, the Cr migration barriers in W-Cr-Y alloys in the presence of impurities could be determined by the same method, expanding on the work presented in Chapters 8 and 9. In doing so, the effects of Cr, Y and O concentration may be studied across a range of compositions, providing the necessary guidance for the industrial upscaling of SMART alloy production.

At the time of writing, recent advances in computational science enable rapid progress in this field, with the widespread adoption of machine-learned interatomic potentials (MLIPs). In particular, the availability of high-throughput density functional theory databases (such as the Materials Project and the Open Materials and MatPES datasets [231, 312, 313]) has enabled the development of so-called 'universal' machine-learned interatomic potentials (uMLIPs). These uMLIPs incorporate many of the elements of the periodic table and, as such, enable the out-of-the-box simulation of material properties at the molecular dynamics level. The applicability of uMLIPs for investigating the behaviour of W-based SMART alloys remains to be seen and is the subject of ongoing work.

References

- [1] R. D. Kerr, M. R. Gilbert, and S. T. Murphy. "Relating the Formation Energies for Oxygen Vacancy Defects to the Structural Properties of Tungsten Oxides". In: Computational Materials Science 252 (2025), p. 113781.
- [2] R. D. Kerr et al. "Stability of Oxide Phases in W-Cr-Y SMART Alloys". In: Nuclear Materials and Energy 45 (2025), p. 101987.
- [3] M. Kaplan. "Million-year-old Ash Hints at Origins of Cooking". In: *Nature* (2012).
- [4] M. Qiu et al. "Earliest Systematic Coal Exploitation for Fuel Extended to 3600 B.P." In: *Science Advances* 9.30 (2023), eadh0549.
- [5] E. G. West. "Literacy and the Industrial Revolution". In: *The Economic History Review* 31.3 (1978), pp. 369–383.
- [6] J. C. Caldwell. "Transmuting the Industrial Revolution into Mortality Decline". In: Demographic Transition Theory. Dordrecht: Springer Netherlands, 2006, pp. 157–180.
- [7] United Nations Department of Economic and Social Affairs, Population Division. World Population Prospects 2022: Summary of Results. Tech. rep.
 3. UN DESA Publications, 2022.
- [8] The British Petroleum Company p.l.c. *BP Energy Outlook 2023*. Accessed: 2024-11-05. 2024.

- [9] E. Mearns. Global Energy Forecast to 2100. Accessed: 2024-11-05. 2024.
- [10] I. Hore-Lacy. *Nuclear Energy in the 21st Century*. World Nuclear University Press, 2010.
- [11] S. M. Rashad and F. H. Hammad. "Nuclear Power and the Environment: Comparative Assessment of Environmental and Health Impacts of Electricity-generating Systems". In: *Applied Energy* 65.1-4 (2000), pp. 211–229.
- [12] H. Yamagata. "Public Opinion on Nuclear Power Plants in Japan, the United Kingdom, and the United States of America: A Prescription for Peculiar Japan". In: Energy Policy 185 (2024), p. 113939.
- [13] D. Deng et al. "Radioactive Waste: A Review". In: Water Environment Research 92.10 (2020), pp. 1818–1825.
- [14] UK Department for Business, Energy and Industrial Strategy. *Energy and Emissions Projections 2022 to 2040*. Accessed: 2025-04-08. 2024. URL: https://www.gov.uk/government/publications/energy-and-emissions-projections-2023-to-2050.
- [15] Fusion Industry Association. Fusion Industry Report 2023. Accessed: 2024-11-05. 2023. URL: https://www.fusionindustryassociation.org/fusion-industry-report-archive/.
- [16] M. Richardson et al. "Technology Readiness Assessment of Materials for DEMO In-vessel Applications". In: *Journal of Nuclear Materials* 550 (2021), p. 152906.
- [17] A. B. Zylstra et al. "Burning Plasma Achieved in Inertial Fusion". In: *Nature* 601.7894 (2022), pp. 542–548.
- [18] A. J. Webster. "Fusion: Power for the Future". In: *Physics Education* 38.2 (2003), p. 135.
- [19] A. D. Sakharov and I. E. Tamm. "The Confinement of a Plasma by a Magnetic Field". In: Report to the Academy of Sciences of the USSR (1951).

- [20] M. G. Haines. "A Review of the Dense Z-Pinch". In: *Plasma Physics and Controlled Fusion* 53.9 (2009), p. 093001.
- [21] A. Pollock and S. Barraclough. "Note on a Hollow Lightning Conductor Crushed by the Discharge". In: *Journal and Proceedings of the Royal Society of New South Wales* 39 (1905), pp. 131–135.
- [22] I. V. Kurchatov. "On the Possibility of Producing Thermonuclear Reactions in a Gas Discharge". In: *Journal of Nuclear Energy* 4 (1957), pp. 193–202.
- [23] J. E. Allen and J. D. Craggs. "High Current Spark Channels". In: *British Journal of Applied Physics* 5.12 (1954), p. 446.
- [24] P. Reynolds and J. D. Craggs. "An Attempt to Produce a Thermo-nuclear Reaction in Deuterium by Means of a High Current Spark Discharge". In: *The London, Edinburgh, and Dublin Philosophical Magazine and Journal of Science* 43.337 (1952), pp. 258–260.
- [25] M. D. Kruskal and M. Schwarzschild. "Some Instabilities of a Completely Ionized Plasma". In: Proceedings of the Royal Society of London: Series A, Mathematical and Physical Sciences 223 (1954), pp. 348–360.
- [26] R. J. Tayler. "An Elementary Theory of the Transient Pinched Discharge". In: *Proceedings of the Physical Society. Section B* 70 (1957), pp. 31–38.
- [27] R. Latham et al. "Growth of Surface Instabilities in a Linear Pinched Discharge". In: *Nature* 186.4725 (1960), pp. 624–625.
- [28] L. Spitzer. "The Stellarator Concept". In: Physics of Fluids 1.4 (1958), pp. 253–264.
- [29] J. J. Thomson. Conduction of Electricity Through Gases. New York, NY, USA: Cambridge University Press, 1906, p. 106.
- [30] R. Gunn. "An Electromagnetic Effect of Importance in Solar and Terrestrial Magnetism". In: *Physical Review* 33.5 (1929), pp. 832–836.

- [31] H. Alfvén. Cosmical Electrodynamics. Oxford, United Kingdom: Clarendon Press, 1950.
- [32] A. D. Boozer, ed. Plasma Physics and Controlled Nuclear Fusion Research 1982: Proceedings of an International Conference, Baltimore, 1-8 September 1982. Vienna: International Atomic Energy Agency, 1983.
- [33] A. H. Boozer. "What is a Stellarator?" In: *Physics of Plasmas* 5.5 (1998), pp. 1647–1655.
- [34] E. Tanner. *Project Matterhorn: An Informal History*. Tech. rep. Princeton Plasma Physics Laboratory, 1977.
- [35] L. Spritzer. PM S2: Survey of Possible Plasma Oscillations in the Stellarator.Tech. rep. Princeton Plasma Physics Laboratory, 1951.
- [36] J. L. Johnson. "The Stellarator Approach to Toroidal Plasma Confinement". In: Nuclear Technology: Fusion 3.2 (1982), pp. 340–361.
- [37] J. L. Bromberg. Fusion: Science, Politics, and the Invention of a New Energy Source. Cambridge, MA: MIT Press, 1982.
- [38] N. J. Peacock et al. "Measurement of the Electron Temperature by Thomson Scattering in Tokamak T-3". In: *Nature* 224.5218 (1969), pp. 488–490.
- [39] M. Kenward. "Fusion Research the Temperature Rises". In: New Scientist 82.1156 (1979), pp. 626–630.
- [40] V. D. Shafranov et al. "On the History of the Research into Controlled Thermonuclear Fusion". In: *Physics-Uspekhi* 44 (2001), pp. 835–843.
- [41] Y Xu. "A General Comparison between Tokamak and Stellarator Plasmas". In: *Matter and Radiation at Extremes* 1.4 (2016), pp. 192–200.
- [42] L. Spritzer. PM S4: Magnetic Fields and Particle Orbits in a High-Density Stellarator. Tech. rep. Princeton Plasma Physics Laboratory, 1952.
- [43] Princeton Plasma Physics Laboratory. *Timeline*. https://www.pppl.gov/about/history/timeline. Accessed: 2024-11-05. 2021.

- [44] V. P. Smirnov. "Tokamak Foundation in USSR/Russia 1950–1990". In: Nuclear Fusion 50 (2009), pp. 1–8.
- [45] EUROFusion. *Timeline*. Accessed: 2024-11-05. Accessed: 2024-11-05. URL: https://www.euro-fusion.org/devices/jet/jet-history/.
- [46] D. Meade. "Results and Plans for the Tokamak Fusion Test Reactor". In: Journal of Fusion Energy 7.2 (1988), pp. 107–114.
- [47] Princeton Plasma Physics Laboratory. *Timeline*. Accessed: 2024-11-05. 2021. URL: https://www.pppl.gov/Tokamak%20Fusion%20Test%20Reactor.
- [48] European Commission. The JET Project: Design Proposal for the Joint European Torus. Luxembourg: EU Office of Publications, 2008.
- [49] P. H. Rebut. "The JET Preliminary Tritium Experiment". In: *Plasma Physics and Controlled Fusion* 34.13 (1992), pp. 1749–1758.
- [50] ITER Organization. *Milestones*. Accessed: 2024-11-05. 2021. URL: https://www.iter.org/sci/BeyondITER.
- [51] EFDA. The ITER Project. Accessed: 2024-11-05. 2006. URL: https://web.archive.org/web/20140914125632/http://www.efda.org/.
- [52] R. Arnoux. "INTOR: The International Fusion Reactor That Never Was". In: *ITER Newsline* (2008).
- [53] C. M. Braams and P. E. Stott. Nuclear Fusion: Half a Century of Magnetic Confinement Research. Institute of Physics Publishing, 2002.
- [54] M. Shimada. "Progress in the ITER Physics Basis". In: Nuclear Fusion 47 (S1 2007), E01.
- [55] B. Bigot. "ITER Construction and Manufacturing Progress Toward First Plasma". In: Fusion Engineering and Design 146 (2019), pp. 124–129.

- [56] M. Banks. ITER Fusion Reactor Hit by Massive Decade-long Delay and €5bn Price Hike. Accessed: 2024-11-05. 2024. URL: https://physicsworld.com/a/iter-fusion-reactor-hit-by-massive-decade-long-delay-and-e5bn-price-hike/.
- [57] G. Federici. "Overview of EU DEMO Design and R&D Activities". In: Fusion Engineering and Design 89 (2014), pp. 882–889.
- [58] G. Federici. "DEMO Design Activity in Europe: Progress and Updates". In: Fusion Engineering and Design 136 (2018), pp. 729–741.
- [59] N. J. L. Cardozo. "Economic Aspects of the Deployment of Fusion Energy: the Valley of Death and the Innovation Cycle". In: *Philosophical Transactions of the Royal Society A: Mathematical, Physical and Engineering Sciences* 377.2141 (2019), p. 20170444.
- [60] S. Entler. "Approximation of the Economy of Fusion Energy". In: *Energy* 152 (2018), pp. 489–497.
- [61] S. Banacloche. "Socioeconomic and Environmental Impacts of Bringing the Sun to Earth: A Sustainability Analysis of a Fusion Power Plant Deployment". In: Energy 209 (2020), p. 118460.
- [62] C. Waldon et al. "Concept Design Overview: A Question of Choices and Compromise". In: *Philosophical Transactions of the Royal Society A: Mathematical, Physical and Engineering Sciences* 382.2280 (2024), p. 20230414.
- [63] A. Sykes. The Development of the Spherical Tokamak. Tech. rep. International Conference on Plasma Physics, 2008.
- [64] K. Miyamoto. Plasma Physics and Controlled Nuclear Fusion. Springer, 2005,p. 62.
- [65] D. A. Gates et al. "High-performance Discharges in the Small Tight Aspect Ratio Tokamak (START)". In: *Physics of Plasmas* 5.5 (1998), pp. 1775–1783.

- [66] J. F. Rivero-Rodríguez et al. "Overview of Fast Particle Experiments in the First MAST Upgrade Experimental campaigns". In: Nuclear Fusion 64.8 (2024), p. 086025.
- [67] P. M. Valanju, M. Kotschenreuther, and S. M. Mahajan. "Super X Divertors for Solving Heat and Neutron Flux Problems of Fusion Devices". In: Fusion Engineering and Design 85.1 (2010), pp. 46–52.
- [68] A. W. Morris. "MAST: Results and Upgrade Activities". In: *IEEE Transactions on Plasma Science* 40.5 (2012), pp. 1–27.
- [69] A. W. Morris et al. "MAST Upgrade Divertor Facility: A Test Bed for Novel Divertor Solutions". In: *IEEE Transactions on Plasma Science* 46.5 (2018), pp. 1217–1226.
- [70] UKAEA. Spherical Tokamak for Energy Production. Accessed: 2021-11-05. 2020. URL: https://step.ukaea.uk/.
- [71] J. File et al. "Non-Superconducting Magnet Structures for Near-Term, Large Fusion Experimental Devices". In: Nuclear Engineering and Design 58.2 (1980), pp. 167–190.
- [72] K. Okuno, A. Shikov, and N. Koizumi. "Superconducting Magnet System in a Fusion Reactor". In: *Journal of Nuclear Materials* 329-333 (2004), pp. 141– 147.
- [73] R. Flükiger et al. "Microstructure, Composition and Critical Current Density of Superconducting Nb₃Sn Wires". In: *Cryogenics* 48.7 (2008), pp. 293–307.
- [74] M. Suenaga and K. M. Ralls. "Some Superconducting Properties of Ti–Nb–Ta Ternary Alloys". In: *Journal of Applied Physics* 40 (1969), pp. 4457–4463.
- [75] F. Buta et al. "Very High Upper Critical Fields and Enhanced Critical Current Densities in Nb₃Sn Superconductors Based on Nb–Ta–Zr Alloys and Internal Oxidation". In: *Journal of Physics: Materials* 4.2 (2021), p. 025003.

- [76] Y. Zhang and X. Xu. "Yttrium Barium Copper Oxide Superconducting Transition Temperature Modelling Through Gaussian Process Regression".
 In: Computational Materials Science 179 (2020), p. 109583.
- [77] L. Lucas. "Comprehensive Review and Critical Evaluation of the Half-Life of Tritium". In: Journal of Research of the National Institute of Standards and Technology 105 (2000), pp. 541–549.
- [78] M. Coleman and M. Kovari. *Global Supply of Tritium for Fusion R&D*. Tech. rep. International Atomic Energy Agency, 2018, p. 662.
- [79] P. Gierszewski. "Tritium Supply for Near-Term Fusion Devices". In: Fusion Engineering and Design 10 (1989), pp. 399–403.
- [80] M. Ni et al. "Tritium Supply Assessment for ITER and DEMOnstration Power Plant". In: Fusion Engineering and Design 88.9 (2013), pp. 2422–2426.
- [81] S. Lim, K. J. Chung, and Y. S. Hwang. "Tritium Breeding Ratio Optimization in Simple Multi-layer Blanket with Genetic Algorithm". In: Fusion Engineering and Design 202 (2024), p. 114365.
- [82] M. R. Gilbert. "Neutron-induced dpa, Transmutations, Gas Production, and Helium Embrittlement of Fusion Materials". In: Journal of Nuclear Materials 442.1 (2013), S755–S760.
- [83] F. B. Brown et al. "MCNP Version 5". In: Transactions of the American Nuclear Society 87.273 (2002), pp. 02–3935.
- [84] P. Goranson et al. "Design of the Plasma Facing Components for the National Spherical Tokamak Experiment (NSTX)". In: *Proceedings of the 18th IEEE/NPSS Symposium on Fusion Engineering*. 1999, pp. 67–70.
- [85] R. A. Causey, R. A. Karnesky, and C. San Marchi. "Tritium Barriers and Tritium Diffusion in Fusion Reactors". In: Comprehensive Nuclear Materials. Ed. by R. J. M. Konings. Oxford: Elsevier, 2012, pp. 511–549.

- [86] W. Eckstein et al. Sputtering Data, Report IPP 9/82. Tech. rep. Max-Planck-Institut für Plasmaphysik, 1993.
- [87] Y. Nobuta et al. "Tritium Retention Properties of Tungsten, Graphite and Co-deposited Carbon Film". In: Fusion Engineering and Design 89.7 (2014), pp. 1516–1519.
- [88] T. Ando et al. "Material Behavior of JT-60U Plasma Facing Components and Installation of B/sub 4/C-converted CFC/Graphite Tiles". In: *Proceedings of the 15th IEEE/NPSS Symposium on Fusion Engineering*. Vol. 1. 1993, pp. 541–544.
- [89] H. Atsumi, S. Tokura, and M. Miyake. "Absorption and Desorption of Deuterium on Graphite at Elevated Temperatures". In: *Journal of Nuclear Materials* 155–157 (1988), pp. 241–245.
- [90] E. Pajuste et al. "Tritium in Plasma-Facing Components of JET with the ITER-Like Wall". In: *Physica Scripta* 96 (2021).
- [91] K. J. Dietz et al. "Beryllium in JET: a Report on the Operational Experience". In: Proceedings of the IEEE Thirteenth Symposium on Fusion Engineering. Vol. 1. 1989, pp. 517–521.
- [92] K. J. Dietz and the JET Team. "Effect of Beryllium on Plasma Performance in JET". In: *Plasma Physics and Controlled Fusion* 32.11 (1990), p. 837.
- [93] B. Patel and W. Parsons. "Operational Beryllium Handling Experience at JET". In: Fusion Engineering and Design 69.1 (2003), pp. 689–694.
- [94] P. H. Chappuis et al. "Possible Divertor Solutions for a Fusion Reactor: Part
 2 Technical Aspects of a Possible Divertor". In: Fusion Engineering and
 Design 36.1 (1997), pp. 109–117.
- [95] B. Spilker et al. "Performance Estimation of Beryllium Under ITER-relevant Transient Thermal Loads". In: Nuclear Materials and Energy 18 (2019), pp. 291–296.

- [96] S. Molokov, R. Moreau, and K. Moffatt, eds. *Magnetohydrodynamics:* Historical Evolution and Trends. Springer, 2007, pp. 213–222.
- [97] M. Ono. Lithium As Plasma Facing Component for Magnetic Fusion Research. Tech. rep. United States Department of Energy, 2012.
- [98] R. Majeski et al. "CDX-U Operation with a Large Area Liquid Lithium Limiter". In: *Journal of Nuclear Materials* 313-316 (2003), pp. 625–629.
- [99] D. Stork. "Materials R&D for a timely DEMO: Key Findings and Recommendations of the EU Roadmap Materials Assessment Group". In: Fusion Engineering and Design 89.7 (2014), pp. 1586–1594.
- [100] G. A. Cottrell, R. Pampin, and N. P. Taylor. "Transmutation and Phase Stability of Tungsten Armor in Fusion Power Plants". In: Fusion Science and Technology 50.1 (2006), pp. 89–98.
- [101] M. R. Gilbert and J. C. Sublet. "Neutron-induced Transmutation Effects in W and W-alloys in a Fusion Environment". In: Nuclear Fusion 51.4 (2011), p. 043005.
- [102] J. K. Tuli. Nuclear Wallet Cards. 6th. Upton, NY: National Nuclear Data Center, Brookhaven National Laboratory, 2000.
- [103] C. Ren et al. "Methods for Improving Ductility of Tungsten A Review". In: International Journal of Refractory Metals and Hard Materials 75 (2018), pp. 170–183.
- [104] Y. H. Zhang et al. "Unveiling the Intrinsic Rrhenium Effect in Tungsten".In: Acta Materialia 264 (2024), p. 119586.
- [105] Y. Nemoto et al. "Microstructural Development of Neutron Irradiated W–Re Alloys". In: *Journal of Nuclear Materials* 283-287 (2000), pp. 1144–1147.
- [106] I. Smid et al. "Development of Tungsten Armor and Bonding to Copper for Plasma-Interactive Components". In: *Journal of Nuclear Materials* 258-263 (1998), pp. 160-172.

- [107] R. K. Williams et al. "Irradiation Induced Precipitation in Tungsten-Based W-Re Alloys". In: *Metallurgical Transactions A* 14.3 (1983), pp. 655–666.
- [108] P. Rocco and M. Zucchetti. "The Impact of Low-Activation Criteria on the Development of Novel Materials for Fusion". In: *Journal of Nuclear Materials* 212-215 (1994), pp. 649–654.
- [109] M. D. Anderton, M. J. Lloyd, and T. P. Davis. "Suppression of Rhenium and Osmium Production in Tungsten by Selective Isotopic Enrichment". In: Fusion Engineering and Design 197 (2023), p. 114073.
- [110] A. Y. Konobeyev et al. "New Evaluation of General Purpose Neutron Data for Stable W-Isotopes Up to 200 MeV". In: *European Physical Journal Conferences* 239 (2020), p. 11002.
- [111] R. Forrest et al. "Use of Integral Data to Improve the European Activation File". In: AIP Conference Proceedings 769 (2005), pp. 515–518.
- [112] H. Fan et al. "Current Mapping of Low-Energy (120 eV) Helium and Hydrogen Irradiated Tungsten by Conductive Atomic Force Microscopy". In: Journal of Nuclear Materials 486 (2017), pp. 191–196.
- [113] K. Zhu et al. "Studies of He Irradiated Tungsten Using Transmission Electron Microscope". In: *Materials Letters* 213 (2018), pp. 362–365.
- [114] G. H. Lu, H. B. Zhou, and C. S. Becquart. "A Review of Modelling and Simulation of Hydrogen Behaviour in Tungsten at Different Scales". In: Nuclear Fusion 54.8 (2014), p. 086001.
- [115] R. J. Haüy et al. Essai d'une Theorie sur la Structure des Cristaux, Appliquée à Plusieurs Genres de Substances Cristallisées. chez Gogue & Nee de La Rochelle, Libraires, Quai des Augustins, près le Pont Saint-Michel, 1784.
- [116] N. N. Greenwood. Ionic Crystals, Lattice Defects and Nonstoichiometry. Butterworths, 1968.

- [117] P. Paufler. International Tables for Crystallography, Volume A. 5th. Kluwer Academic Publishers, 2004.
- [118] E. Arnold et al. *International Tables for Crystallography, Volume B.* Kluwer Academic Publishers, 2001.
- [119] A. J. C. Wilson and V. Geist. *International Tables for Crystallography, Volume C.* Kluwer Academic Publishers, 1993.
- [120] C. Hermann. "XVI. Zur Systematischen Strukturtheorie: I. Eine Neue Raumgruppensymbolik". In: Zeitschrift für Kristallographie Crystalline Materials 68.1-6 (1928), pp. 257–287.
- [121] C. Mauguin. "Sur le Symbolisme des Groupes de Répétition et de Symétrie des Assemblages Cristallins". In: Zeitschrift für Kristallographie Crystalline Materials 76.1 (1931), pp. 542–558.
- [122] U. Guth. Kröger-Vinks Notation of Point Defects. Ed. by G. Kreysa, K. Ota, and R. F. Savinell. New York, NY: Springer New York, 2014.
- [123] Y. Kumagai and F. Oba. "Electrostatics-Based Finite-Size Corrections for First-Principles Point Defect Calculations". In: *Physical Review B* 89.19 (2014).
- [124] A. Fick. "V. On Liquid Diffusion". In: *Philosophical Magazine*, Series 1 10 (1855), pp. 30–39.
- [125] H. Mehrer. Diffusion in Solids: Fundamentals, Methods, Materials, Diffusion-Controlled Processes. Springer Berlin Heidelberg, 2007.
- [126] C. Wagner. "Beitrag zur Theorie des Anlaufvorgangs". In: Zeitschrift für Physikalische Chemie 21B.1 (1933), pp. 25–41.
- [127] G. R. Belton and R. L. McCarron. "The Volatilization of Tungsten in the Presence of Water Vapor". In: The Journal of Physical Chemistry 68.7 (1964), pp. 1852–1856.

- [128] D. K. Varghese, M. Paulose, and C. A. Grimes. "Long Vertically Aligned Titania Nanotubes on Transparent Conducting Oxide for Highly Efficient Solar Cells". In: *Nature Nanotechnology* 4.9 (2009), pp. 592–597.
- [129] K. Hara et al. "Nanocrystalline Electrodes Based on Nanoporous-Walled WO3 Nanotubes for Organic-Dye-Sensitized Solar Cells". In: Langmuir 27.20 (2011), pp. 12730–12736.
- [130] J. Yu and L. Qi. "Template-Free Fabrication of Hierarchically Flower-Like Tungsten Trioxide Assemblies with Enhanced Visible-Light-Driven Photocatalytic Activity". In: *Journal of Hazardous Materials* 169.1-3 (2009), pp. 221–227.
- [131] X. Wang, N. Miura, and N. Yamazoe. "Study of WO₃-Based Sensing Materials for NH₃ and NO Detection". In: Sensors and Actuators B: Chemical 66.1 (2000), pp. 74–76.
- [132] S. Berger et al. "High Photocurrent Conversion Efficiency in Self-Organized Porous WO₃". In: *Applied Physics Letters* 88.20 (2006), p. 203119.
- [133] C. Mardare and A. W. Hassel. "Review on the Versatility of Tungsten Oxide Coatings". In: *Physica Status Solidi A* 216 (2019), p. 1900047.
- [134] V. Shaposhnikov et al. "Ab Initio Investigation of Structural and Electronic Properties of Tungsten Dioxide". In: *Physica Status Solidi B* 248 (2011), pp. 1471–1476.
- [135] K. Viswanathan, K. Brandt, and E. Salje. "Crystal Structure and Charge Carrier Concentration of W₁₈O₄₉". In: Journal of Solid State Chemistry 36 (1981), pp. 45–51.
- [136] M. Sundberg. "The Crystal and Defect Structures of W₂₅O₇₃, a Member of the Homologous Series WO_{3-2n}". In: Acta Crystallographica Section B 32.7 (1976), pp. 2144–2149.

- [137] E. Indrea et al. "Rietveld Refinement of Powder X-ray Diffraction of Nanocrystalline Noble Metals - Tungsten Trioxide". In: Revue Roumaine de Chimie 56 (2011), pp. 589–593.
- [138] E. Salje et al. "Crystal Structure and Paramagnetic Behaviour of WO_{3-x}". In: *Journal of Physics: Condensed Matter* 9 (1999), p. 6563.
- [139] R. Diehl, G. Brandt, and E. Salje. "The Crystal Structure of Triclinic WO₃".
 In: Acta Crystallographica Section B 34.4 (1978), pp. 1105–1111.
- [140] S. Tanisaki. "Crystal Structure of Monoclinic Tungsten Trioxide at Room Temperature". In: Journal of the Physical Society of Japan 15.4 (1960), pp. 573–581.
- [141] E. Salje. "The Orthorhombic Phase of WO₃". In: Acta Crystallographica Section B 33.2 (1977), pp. 574–577.
- [142] F. Mazzola et al. "Unveiling the Electronic Structure of Pseudotetragonal WO₃ Thin Films". In: The Journal of Physical Chemistry Letters 14.32 (2023), pp. 7208–7214.
- [143] M. Weil and W. D. Schubert. "The Beautiful Colours of Tungsten Oxides".In: International Tungsten Industry Association Newsletters. 2013.
- [144] R. Tilley. Colour and the Optical Properties of Materials. Wiley, 2000.
- [145] Y. Ferro et al. "Hydrogen and Oxygen on Tungsten (110) Surface: Adsorption, Absorption, and Desorption Investigated by Density Functional Theory". In: Nuclear Fusion 63.3 (2023), p. 036017.
- [146] C. Nilsson and J. Habainy. Oxidation of Pure Tungsten in the Temperature Interval 400° to 900°C. 2013.
- [147] W. W. Webb, J. T. Norton, and C. Wagner. "Oxidation of Tungsten". In: Journal of The Electrochemical Society 103.2 (1956), p. 107.
- [148] E. A. Kellett and S. E. Rogers. "The Structure of Oxide Layers on Tungsten".In: Journal of The Electrochemical Society 110.6 (1963), p. 502.

- [149] V. K. Sikka and C. J. Rosa. "The Oxidation Kinetics of Tungsten and the Determination of Oxygen Diffusion Coefficient in Tungsten Trioxide". In: Corrosion Science 20.11 (1980), pp. 1201–1219.
- [150] S. Cifuentes, M. A. Monge, and P. Pérez. "On the Oxidation Mechanism of Pure Tungsten in the Temperature Range 600–800°C". In: Corrosion Science 57 (2012), pp. 114–121.
- [151] E. A. Gulbransen and W. S. Wysong. "Thin Oxide Films on Tungsten". In: The American Institute of Mining, Metallurgical, and Petroleum Engineers (1949), pp. 1–15.
- [152] M. R. Gilbert and R. Forrest. "Comprehensive Handbook of Activation Data Calculated Using EASY2003". In: Fusion Engineering and Design 81 (2006), pp. 1511–1516.
- [153] R. J. H. Pearce et al. "Vacuum Pumping Developments on the JET Tokamak". In: Fusion Engineering and Design 58–59 (2001), pp. 359–364.
- [154] G. A. Landis. "Degradation of the Lunar Vacuum by a Moon Base". In: *Acta Astronautica* 21.3 (1990), pp. 183–187.
- [155] G. Perez et al. "A De-coupled DEMO First Wall: Design Concept and Preliminary Analysis". In: Fusion Engineering and Design (2016), pp. 1–25.
- [156] D. Adomavicius and M. Lisak. A Conceptual Study of Commercial Fusion Power Plants, EFDA RP RE 5.0. 2005.
- [157] F. Koch and H. Bolt. "Self Passivating W-Based Alloys as Plasma Facing Material for Nuclear Fusion". In: *Physica Scripta* 2007.T128 (2007), p. 100.
- [158] F. Koch, S. Köppl, and H. Bolt. "Self Passivating W-Based Alloys as Plasma-Facing Material". In: *Journal of Nuclear Materials* 386-388 (2009), pp. 572– 574.

- [159] F. Klein et al. "SMART Alloys as Armor Material for DEMO: Overview of Properties and Joining to Structural Materials". In: Fusion Engineering and Design 166 (2021), p. 112272.
- [160] F. Koch et al. "Oxidation Behaviour of Silicon-Free Tungsten Alloys for Use as the First Wall Material". In: *Physica Scripta* 2011.T145 (2011), p. 014019.
- [161] K. Przybylski, A. J. Garratt-Reed, and G. J. Yurek. "Grain Boundary Segregation of Yttrium in Chromia Scales". In: Journal of The Electrochemical Society 135.2 (1988), p. 509.
- [162] M. F. Stroosnijder et al. "The Influence of Yttrium Ion Implantation on the Oxidation Behaviour of Powder Metallurgically Produced Chromium". In: Surface and Coatings Technology 83.1 (1996), pp. 205–211.
- [163] Neil Birks, Gerald H. Meier, and Frederick S. Pettit. *Introduction to the High-Temperature Oxidation of Metals*. Cambridge University Press, 2006.
- [164] R. Mevrel. "Cyclic Oxidation of High-Temperature Alloys". In: *Materials Science and Technology* 3.7 (1987), pp. 531–535.
- [165] E. Lang. The Role of Active Elements in the Oxidation Behaviour of High Temperature Metals and Alloys. Springer Dordrecht, 1989.
- [166] A. Litnovsky et al. "New Oxidation-Resistant Tungsten Alloys for Use in the Nuclear Fusion Reactors". In: *Physica Scripta* 2017.T170 (2017), p. 014012.
- [167] Z. Yang et al. "New Insights into the Mechanism of Yttrium Changing High-Temperature Oxide Growth of Fe-13Cr-6Al-2Mo-0.5Nb Alloy for Fuel Cladding". In: *Corrosion Science* 172 (2020), p. 108728.
- [168] S. Zhang et al. "Unveiling the Mechanism of Yttrium Significantly Improving High-Temperature Oxidation Resistance of Super-Austenitic Stainless Steel S32654". In: Journal of Materials Science and Technology 115 (2022), pp. 103–114.

- [169] C. J. Wang et al. "Effect of Yttrium on the Microstructure and Mechanical Properties of PH13-8Mo Stainless Steels Produced by Selective Laser Melting". In: *Materials* 15.15 (2022).
- [170] K. Pajor et al. "Effect of Yttrium Additions in Relation to Oxygen Content on Glass Formation in the Zr₅₀Cu₄₀Al₁₀ Alloy". In: Metallurgical and Materials Transactions A 51.9 (2020), pp. 4563–4571.
- [171] A. Inoue and A. Takeuchi. "Recent Development and Application Products of Bulk Glassy Alloys". In: *Acta Materialia* 59.6 (2011), pp. 2243–2267.
- [172] J. Brodrick, D. J. Hepburn, and G. J. Ackland. "Mechanism for Radiation Damage Resistance in Yttrium Oxide Dispersion Strengthened Steels". In: Journal of Nuclear Materials 445.1 (2014), pp. 291–297.
- [173] A. Calvo et al. "Self-Passivating W-Cr-Y Alloys: Characterization and Testing". In: Fusion Engineering and Design 124 (2017), pp. 1118–1121.
- [174] P. López-Ruiz et al. "Self-Passivating Bulk Tungsten-Based Alloys Manufactured by Powder Metallurgy". In: *Physica Scripta* 2011.T145 (2011), p. 014018.
- [175] O. Guillon et al. "Field-Assisted Sintering Technology/Spark Plasma Sintering: Mechanisms, Materials, and Technology Developments". In: Advanced Engineering Materials 16.7 (2014), pp. 830–849.
- [176] F. Klein et al. "Oxidation Resistance of Bulk Plasma-Facing Tungsten Alloys". In: *Nuclear Materials and Energy* 15 (2018), pp. 226–231.
- [177] S. V. N. Naidu, A. M. Sriramamurthy, and P. R. Rao. "The Cr-W (Chromium-Tungsten) System". In: Bulletin of Alloy Phase Diagrams 5.3 (1984), pp. 289–292.
- [178] D. E. Porter. "The Decomposition of Tungsten-Chromium Solid Solution". In: Acta Metallurgica 15.5 (1967), pp. 721–726.

- [179] D. Sobieraj et al. "Composition Stability and Cr-Rich Phase Formation in W-Cr-Y and W-Cr-Ti Smart Alloys". In: *Metals* 11.5 (2021).
- [180] J. Veverka et al. "Decreasing the W-Cr Solid Solution Decomposition Rate: Theory, Modelling and Experimental Verification". In: Journal of Nuclear Materials 576 (2023), p. 154288.
- [181] J. Chen et al. "Influence of Phase Decomposition on Mechanical Properties and Oxidation Resistance of WCrY SMART Material". In: Nuclear Materials and Energy 41 (2024), p. 101762.
- [182] Z. Xiong et al. "Strong Yet Ductile Self-Passivating W-10Cr Alloy by Laser Powder Bed Fusion". In: International Journal of Refractory Metals and Hard Materials 116 (2023), p. 106365.
- [183] F. Klein et al. "Tungsten-Chromium-Yttrium Alloys as First Wall Armor Material: Yttrium Concentration, Oxygen Content and Transmutation Elements". In: Fusion Engineering and Design 158 (2020), p. 111667.
- [184] J. Chen et al. "Effect of Yttrium and Yttria Addition in Self-Passivating WCr SMART Material for First-Wall Application in a Fusion Power Plant". In: Metals 14.9 (2024), p. 1092.
- [185] F. Klein et al. "Sublimation of Advanced Tungsten Alloys under DEMO Relevant Accidental Conditions". In: Fusion Engineering and Design 146 (2019), pp. 1198–1202.
- [186] A. Calvo et al. "Self-passivating Tungsten Alloys of the System W-Cr-Y for High Temperature Applications". In: *International Journal of Refractory Metals and Hard Materials* 73 (2018), pp. 29–37.
- [187] A. Litnovsky et al. "SMART Materials for DEMO: Towards Industrial Production". In: Fusion Engineering and Design 203 (2024), p. 114423.
- [188] G. Kresse and J. Hafner. "Ab-initio Molecular Dynamics for Liquid Metals".In: Physical Review B 47 (1 1993), pp. 558–561.

- [189] Georg Kresse and Jürgen Furthmüller. "Efficiency of Ab-initio Total Energy Calculations for Metals and Semiconductors using a Plane-wave Basis Set". In: Computational Materials Science 6.1 (1996), pp. 15–50.
- [190] G. Kresse and J. Furthmüller. "Efficient Iterative Schemes for Ab-initio Total-energy Calculations using a Plane-wave Basis Set". In: *Physical Review B* 54 (16 1996), pp. 11169–11186.
- [191] G. Kresse and D. Joubert. "From Ultrasoft Pseudopotentials to the Projector Augmented-wave Method". In: *Physical Review B* 59 (3 1999), pp. 1758–1775.
- [192] A. P. Thompson et al. "LAMMPS a Flexible Simulation Tool for Particle-based Materials Modeling at the Atomic, Meso, and Continuum Scales". In: Computer Physics Communications 271 (2022), p. 108171.
- [193] G. Kumar, R. R. Mishra, and A. Verma. Introduction to Molecular Dynamics Simulations. Ed. by A. Verma et al. Singapore: Springer Nature, 2022, pp. 1– 19.
- [194] B. Gautam. "Energy Minimization". In: ed. by R. T. Maia, R. M. de Moraes Filho, and M. Campos. Rijeka: IntechOpen, 2020. Chap. 7.
- [195] R. J. Zamora et al. "The Modern Temperature-Accelerated Dynamics Approach". In: Annual Review of Chemical and Biomolecular Engineering 7 (2016), pp. 87–110.
- [196] J. P. Tavenner, M. I. Mendelev, and J. W. Lawson. "Molecular Dynamics Based Kinetic Monte Carlo Simulation for Accelerated Diffusion". In: Computational Materials Science 218 (2023), p. 111929.
- [197] A. F. Voter. "Hyperdynamics: Accelerated Molecular Dynamics of Infrequent Events". In: *Physical Review Letters* 78 (20 1997), pp. 3908–3911.
- [198] A. F. Voter. "Parallel Replica Method for Dynamics of Infrequent Events".
 In: Physical Review B 57 (22 1998), R13985–R13988.

- [199] M. Cerrolaza et al. Numerical Methods and Advanced Simulation in Biomechanics and Biological Processes. Academic Press, 2017.
- [200] H. Jonsson, G. Mills, and K. Jacobsen. "Nudged Elastic Band Method for Finding Minimum Energy Paths of Transitions". In: Classical and Quantum Dynamics in Condensed Phase Simulations. World Scientific, 1998, pp. 385– 404.
- [201] G. Henkelman, B. P. Uberuaga, and H. Jónsson. "A Climbing Image Nudged Elastic Band Method for Finding Saddle Points and Minimum Energy Paths". In: *The Journal of Chemical Physics* 113.22 (2000), pp. 9901–9904.
- [202] D. Gehringer, M. Friak, and D. Holec. "Models of Configurationally-complex Alloys Made Simple". In: Computer Physics Communications (2023), p. 108664.
- [203] P. Hohenberg and W. Kohn. "Inhomogeneous Electron Gas". In: *Physical Review* 136 (3B 1964), B864–B871.
- [204] J. P. Perdew and K. Schmidt. "Jacob's Ladder of Density Functional Approximations for the Exchange-Correlation Energy". In: AIP Conference Proceedings 577.1 (2001), pp. 1–20.
- [205] J. P. Perdew, K. Burke, and M. Ernzerhof. "Generalized Gradient Approximation Made Simple". In: *Physical Review Letters* 77 (18 1996), pp. 3865–3868.
- [206] J. P. Perdew et al. "Restoring the Density-Gradient Expansion for Exchange in Solids and Surfaces". In: *Physical Review Letters* 100.13 (2008).
- [207] P. Borlido et al. "Exchange-correlation Functionals for Band Gaps of Solids: Benchmark, Reparametrization and Machine Learning". In: Computational Materials 6.1 (2020), p. 96.
- [208] G. X. Zhang et al. "Performance of Various Density Functional Approximations for Cohesive Properties of 64 Bulk Solids". In: New Journal of Physics 20.6 (2018), p. 063020.

- [209] L. Brillouin. "Les électrons libres dans les métaux et le rôle des réflexions de Bragg". In: *Journal de Physique et le Radium* 1.11 (1930), pp. 377–400.
- [210] H. J. Monkhorst and J. D. Pack. "Special Points for Brillouin-Zone Integrations". In: *Physical Review B* 13 (12 1976), pp. 5188–5192.
- [211] J. D. Pack and H. J. Monkhorst. ""Special Points for Brillouin-Zone Integrations" A Reply". In: *Physical Review B* 16 (4 1977), pp. 1748–1749.
- [212] A. Kenich. "Atomistic Simulation of Fission Products in Zirconia Polymorphs". PhD thesis. Imperial College London, 2020.
- [213] P. E. Blöchl. "Projector Augmented-Wave Method". In: *Physical Review B* 50 (24 1994), pp. 17953–17979.
- [214] A. I. Liechtenstein, V. I. Anisimov, and J. Zaanen. "Density Functional Theory and Strong Interactions: Orbital Ordering in Mott-Hubbard Insulators".
 In: Physical Review B 52 (8 1995), R5467–R5470.
- [215] S. L. Dudarev et al. "Electron-energy-loss Spectra and the Structural Stability of Nickel Oxide: An LSDA+U study". In: *Physical Review B* 57 (3 1998), pp. 1505–1509.
- [216] M. Cococcioni and S. Gironcoli. "Linear Response Approach to the Calculation of the Effective Interaction Parameters in the LDA + U Method". In: Physical Review B 71 (3 2005), p. 035105.
- [217] M. S. Daw, S. M. Foiles, and M. I. Baskes. "The Embedded-atom Method: a Review of Theory and Applications". In: *Materials Science Reports* 9.7 (1993), pp. 251–310.
- [218] G. Bonny et al. "On the Mobility of Vacancy Clusters in Reduced Activation Steels: an Atomistic Study in the Fe-Cr-W Model Alloy". In: *Journal of Physics: Condensed Matter* 25.31 (2013), p. 315401.

- [219] L. M. Hale, Z. T. Trautt, and C. A. Becker. "Evaluating Variability with Atomistic Simulations: the Effect of Potential and Calculation Methodology on the Modelling of Lattice and Elastic Constants". In: *Modelling and Simulation in Materials Science and Engineering* 26.5 (2018), p. 055003.
- [220] C. A. Becker et al. "Considerations for Choosing and Using Force Fields and Interatomic Potentials in Materials Science and Engineering". In: Current Opinion in Solid State and Materials Science 17.6 (2013), pp. 277–283.
- [221] A. Togo et al. "Implementation Strategies in Phonopy and Phono3py". In: Journal of Physics - Condensed Matter 35.35 (2023), p. 353001.
- [222] A. Togo. "First-Principles Phonon Calculations with Phonopy and Phono3py". In: *Journal of the Physical Society of Japan* 92.1 (2023), p. 012001.
- [223] V. Wang et al. "VASPKIT: A User-friendly Interface Facilitating Highthroughput Computing and Analysis Using VASP Code". In: *Computer Physics Communications* 267 (2021), p. 108033.
- [224] Peter E. Blöchl, O. Jepsen, and O. K. Andersen. "Improved Tetrahedron Method for Brillouin-zone Integrations". In: *Physical Review B* 49 (23 1994), pp. 16223–16233.
- [225] Y. L. Liu et al. "The Ideal Tensile Strength and Deformation Behavior of a Tungsten Single Crystal". In: Nuclear Instruments and Methods in Physics Research, Section B: Beam Interactions with Materials and Atoms 267.18 (2009), pp. 3282–3285.
- [226] F. H. Featherston and J. R. Neighbours. "Elastic Constants of Tantalum, Tungsten, and Molybdenum". In: *Physical Review* 130 (4 1963), pp. 1324– 1333.
- [227] D. Jiang et al. "First-principles Study the Phase Stability and Mechanical Properties of Binary W-Mo Alloys". In: Fusion Engineering and Design 130 (2018), pp. 56–61.

- [228] G. D. Samolyuk, Y. N. Osetsky, and R. E. Stoller. "The Influence of Transition Metal Solutes on the Dislocation Core Structure and Values of the Peierls Stress and Barrier in Tungsten". In: *Journal of Physics: Condensed Matter* 25.2 (2012), p. 025403.
- [229] Y. Qian et al. "Using First-principles Calculations to Predict the Mechanical Properties of Transmuting Tungsten under First Wall Fusion Power-plant Conditions". In: Journal of Physics: Condensed Matter 33.34 (2021), p. 345901.
- [230] L. Romaner, C. Ambrosch-Draxl, and R. Pippan. "Effect of Rhenium on the Dislocation Core Structure in Tungsten". In: *Physical Review Letters* 104 (19 2010), p. 195503.
- [231] A. Jain. "Commentary: The Materials Project: A Materials Genome Approach to Accelerating Materials Innovation". In: APL Materials 1.1 (2013), p. 011002.
- [232] X. Liu, K. Xu, and H. Zhai. "Pressure Dependence of Structural and Mechanical Properties of Single-Crystal Tungsten: A Molecular Dynamics Study". In: Metals 11.12 (2021), p. 1898.
- [233] D. R. Lide. CRC Handbook of Chemistry and Physics. 88th ed. CRC Press, 2007.
- [234] C. Kalha et al. "Lifetime Effects and Satellites in the Photoelectron Spectrum of Tungsten Metal". In: *Physical Review B* 105 (4 2022), p. 045129.
- [235] A. R. Jani and V. B. Gohel. "On the Phonon Dispersion in Tungsten". In: Journal of Physics F: Metal Physics 6.2 (1976), p. L25.
- [236] W. Szlachta, A. Bartok, and G. Csányi. "Accuracy and Transferability of Gaussian Approximation Potential Models for Tungsten". In: *Physical Review* B 90 (2014), p. 104108.

- [237] J. P. Crocombette, P. Notargiacomo, and M. C. Marinica. "Effect of the Variation of the Electronic Density of States of Zirconium and Tungsten on Their Respective Thermal Conductivity Evolution with Temperature". In: *Journal of Physics: Condensed Matter* 27 (2015), p. 165501.
- [238] C. J. Ding et al. "A Deep Learning Interatomic Potential Suitable for Simulating Radiation Damage in Bulk Tungsten". In: Tungsten 6 (2 2024), pp. 304–322.
- [239] V. N. Maksimenko et al. "The N-Body Interatomic Potential for Molecular Dynamics Simulations of Diffusion in Tungsten". In: Computational Materials Science 202 (2022), p. 110962.
- [240] J. Byggmästar et al. "Machine-Learning Interatomic Potential for Radiation Damage and Defects in Tungsten". In: *Physical Review B* 100 (2019).
- [241] X. Qi et al. "Experimental and Theoretical Studies on the Elasticity of Tungsten to 13 GPa". In: *Journal of Applied Physics* 124.7 (2018), p. 075902.
- [242] F. Luo et al. "First Principles Study of the Temperature-dependent Elastic Properties of W". In: *Philosophical Magazine Letters* 95.4 (2015), pp. 211–219.
- [243] Z. C. Guo et al. "First-principles Calculations of Elastic, Phonon and Thermodynamic Properties of W". In: Molecular Physics 114.23 (2016), pp. 3430–3436.
- [244] L. Koči et al. "Elasticity of the Superconducting Metals V, Nb, Ta, Mo, and W at High Pressure". In: *Physical Review B* 77 (21 2008), p. 214101.
- [245] D. Cereceda et al. "Assessment of Interatomic Potentials for Atomistic Analysis of Static and Dynamic Properties of Screw Dislocations in W". In: Journal of Physics: Condensed Matter 25.8 (2013), p. 085702.
- [246] J. Tersoff. "New Empirical Approach for the Structure and Energy of Covalent Systems". In: *Physical Review B* 37 (12 1988), pp. 6991–7000.

- [247] M. W. Finnis and J. E. Sinclair. "A Simple Empirical N-body Potential for Transition Metals". In: *Philosophical Magazine A* 50.1 (1984), pp. 45–55.
- [248] R. W. Hertzberg, R. P. Vinci, and J. L. Hertzberg. *Deformation and Fracture Mechanics of Engineering Materials*. John Wiley & Sons, 2020.
- [249] J. Kübler. "Spin-density Functional Calculations for Chromium". In: *Journal of Magnetism and Magnetic Materials* 20.3 (1980), pp. 277–284.
- [250] G. Y. Guo and H. H. Wang. "Calculated Elastic Constants and Electronic and Magnetic Properties of bcc, fcc, and hcp Cr Crystals and Thin Films". In: *Physical Review B* 62 (8 2000), pp. 5136–5143.
- [251] S. Xu et al. "Frank-Read Source Operation in Six Body-centered Cubic Refractory Metals". In: Journal of the Mechanics and Physics of Solids 141 (2020), p. 104017.
- [252] P. Nandi et al. "Efficacy of Surface Error Corrections to Density Functional Theory Calculations of Vacancy Formation Energy in Transition Metals". In:

 Journal of Physics: Condensed Matter 22 (2010), p. 345501.
- [253] K. Yang et al. "Modified Analytic Embedded Atom Method Potential for Chromium". In: Modelling and Simulation in Materials Science and Engineering 26.6 (2018), p. 065001.
- [254] B. J. Lee et al. "Second Nearest-neighbor Modified Embedded Atom Method Potentials for bcc Transition Metals". In: *Physical Review B* 64 (18 2001), p. 184102.
- [255] Z. Lin, R. A. Johnson, and L. V. Zhigilei. "Computational Study of the Generation of Crystal Defects in a bcc Metal Target Irradiated by Short Laser Pulses". In: *Physical Review B* 77 (21 2008), p. 214108.
- [256] Pär Olsson et al. "Two-band Modeling of α -prime Phase Formation in Fe-Cr". In: *Physical Review B* 72 (21 2005), p. 214119.

- [257] P. Bödeker et al. "Spin-density Waves and Reorientation Effects in Thin Epitaxial Cr films Covered with Ferromagnetic and Paramagnetic Layers".
 In: Physical Review B 59 (14 1999), pp. 9408–9431.
- [258] C. Kittel and P. McEuen. *Introduction to Solid State Physics*. John Wiley & Sons, 2018.
- [259] A. W. Overhauser. "Spin Density Waves in an Electron Gas". In: *Physical Review* 128 (3 1962), pp. 1437–1452.
- [260] F. Bisti et al. "Evidence of Spin and Charge Density Waves in Chromium Electronic Bands". In: *Communications Materials* 6 (1 2025), p. 70.
- [261] H. L. Skriver. "The Electronic Structure of Antiferromagnetic Chromium". In: Journal of Physics F: Metal Physics 11.1 (1981), p. 97.
- [262] G. Simonelli, R. Pasianot, and E. J. Savino. "Phonon Dispersion Curves for Transition Metals within the Embedded-atom and Embedded-defect Methods". In: *Physical Review B* 55 (9 1997), pp. 5570–5573.
- [263] S. B. Palmer and E. W. Lee. "The Elastic Constants of Chromium". In: The Philosophical Magazine: A Journal of Theoretical Experimental and Applied Physics 24.188 (1971), pp. 311–318.
- [264] M. J. Mehl and D. A. Papaconstantopoulos. "Applications of a Tight-binding Total-energy Method for Transition and Noble Metals: Elastic Constants, Vacancies, and Surfaces of Monatomic Metals". In: *Physical Review B* 54 (7 1996), pp. 4519–4530.
- [265] M. Sigalas, D. A. Papaconstantopoulos, and N. C. Bacalis. "Total Energy and Band Structure of the 3d, 4d, and 5d Metals". In: *Physical Review B* 45 (11 1992), pp. 5777–5783.
- [266] R. Eder, H. F. Pen, and G. A. Sawatzky. "Kondo-lattice-like Effects of Hydrogen in Transition Metals". In: *Physical Review B* 56 (16 1997), pp. 10115–10120.

- [267] J. F. Smith and J. A. Gjevre. "Elastic Constants of Yttrium Single Crystals in the Temperature Range 4.2–400 K". In: Journal of Applied Physics 31.4 (1960), pp. 645–647.
- [268] S. J. Savage et al. "The Elastic Constants of High-purity Yttrium". In: Journal of Physics F: Metal Physics 10.3 (1980), p. 347.
- [269] L. Wang, T. Maxisch, and G. Ceder. "Oxidation Energies of Transition Metal Oxides within the GGA+U Framework". In: Physical Review B 73 (19 2006), p. 195107.
- [270] H. R. Liu, H. Xiang, and X. G. Gong. "First Principles Study of Adsorption of O₂ on Al Surface with Hybrid Functionals". In: *The Journal of Chemical Physics* 135.21 (2011), p. 214702.
- [271] L. Pan, J. Weaver, and A. Asthagiri. "First Principles Study of Molecular O2 Adsorption on the PdO(101) Surface". In: *Topics in Catalysis* 60 (2017), pp. 401–412.
- [272] A. Atkinson. "Wagner Theory and Short Circuit Diffusion". In: *Materials Science and Technology* 4.12 (1988), pp. 104–1051.
- [273] C. Linderälv. "Structural and Thermodynamical Properties of Tungsten Oxides from First-principles Calculations". In: *Chalmers University of Technology* (2016).
- [274] S. K. Deb. "Optical and Photoelectric Properties and Colour Centres in Thin Films of Tungsten Oxide". In: The Philosophical Magazine: A Journal of Theoretical Experimental and Applied Physics 27.4 (1973), pp. 801–822.
- [275] D. Zagorac et al. "Recent Developments in the Inorganic Crystal Structure Database: Theoretical Crystal Structure Data and Related Features". In: Journal of Applied Crystallography 52.5 (2019), pp. 918–925.
- [276] W. Wang, A. Janotti, and C. G. Van de Walle. "Role of Oxygen Vacancies in Crystalline WO₃". In: *Journal of Materials Chemistry C* 4 (27 2016), pp. 6641–6648.

- [277] R. J. Sáenz-Hernández. "Correlation between Thickness and Optical Properties in Nanocrystalline γ -Monoclinic WO₃ Thin Films". In: Coatings 12.11 (2022), p. 1727.
- [278] B. O. Loopstra and H. M. Rietveld. "Further Refinement of the Structure of WO₃". In: *Acta Crystallographica, Section B* 25.7 (1969), pp. 1420–1421.
- [279] A. A. Bolzan, B. J. Kennedy, and C. J. Howard. "Neutron Powder Diffraction Study of Molybdenum and Tungsten Dioxides". In: Australian Journal of Chemistry 48 (1995), pp. 1473–1477.
- [280] K. Viswanathan, K. Brandt, and E. Salje. "Crystal Structure and Charge Carrier Concentration of W₁₈O₄₉". In: *Journal of Solid State Chemistry* 36.1 (1981), pp. 45–51.
- [281] H. Xiao, J. Tahir-Kheli, and W. A. Goddard III. "Accurate Band Gaps for Semiconductors from Density Functional Theory". In: *The Journal of Physical Chemistry Letters* 2.3 (2011), pp. 212–217.
- [282] J. Paier, M. Marsman, and G. Kresse. "Why Does the B3LYP Hybrid Functional Fail for Metals?" In: The Journal of Chemical Physics 127.2 (2007), p. 024103.
- [283] D. J. Palmer and P. G. Dickens. "Tungsten Dioxide: Structure Refinement by Powder Neutron Diffraction". In: Acta Crystallographica Section B 35.9 (1979), pp. 2199–2201.
- [284] A. Magneli. "Crystal Structure Studies on Gamma-Tungsten Oxide". In: Arkiv foer Kemi 1 (1949), pp. 223–230.
- [285] A. A. Yaremchenko, D. D. Khalyavin, and M. V. Patrakeev. "Uncertainty of Oxygen Content in Highly Nonstoichiometric Oxides from Neutron Diffraction Data: Example of Perovskite-type Ba_{0.5}Sr_{0.5}Co_{0.8}Fe_{0.2}O₃". In:

 **Journal of Materials Chemistry A 5 (7 2017), pp. 3456–3463.
- [286] J. A. Kaduk. "Chemical Reasonableness in Rietveld Analysis: Inorganics".In: Powder Diffraction 22.3 (2007), pp. 268–278.

- [287] S. Billinge and P. Tian. "Testing Different Methods for Estimating Uncertainties on Rietveld Refined Parameters Using SrRietveld". In: Zeitschrift fur Kristallographie 226 (Dec. 2011), pp. 898–904.
- [288] W. Liu et al. "A Study of the Hydrogen Adsorption Mechanism of $W_{18}O_{49}$ using First-principles Calculations". In: Computational Materials Science 154 (2018), pp. 53–59.
- [289] M. A. K. L. Dissanayake and L. L. Chase. "Optical Properties of CrO₂, MoO₂, and WO₂ in the Range 0.2-6 eV". In: *Physical Review B* 18 (12 1978), pp. 6872–6879.
- [290] M. J. Sienko and Bireswar Banerjee. "Studies in Non-stoichiometry: Magnetic Susceptibilities in the Tungsten-Oxygen System". In: Journal of the American Chemical Society 83.20 (1961), pp. 4149–4152.
- [291] R. Chatten et al. "The Oxygen Vacancy in Crystal Phases of WO₃". In: *The Journal of Physical Chemistry B* 109.8 (2005), pp. 3146–3156.
- [292] C Lambert-Mauriat and V Oison. "Density Functional Study of Oxygen Vacancies in Monoclinic Tungsten Oxide". In: *Journal of Physics: Condensed Matter* 18.31 (2006), p. 7361.
- [293] M. I. Trioni et al. "New Insight into the Electronic and Magnetic Properties of Sub-Stoichiometric WO₃: A Theoretical Perspective". In: *Crystals* 14.4 (2024), p. 372.
- [294] Fenggong Wang, Cristiana Di Valentin, and Gianfranco Pacchioni. "Electronic and Structural Properties of WO₃: A Systematic Hybrid DFT Study".
 In: Journal of Physical Chemistry C 115.16 (2011), pp. 8345–8353.
- [295] S. Huang et al. "Multilayer Interface Tracking Model of Pure Tungsten Oxidation". In: Modelling and Simulation in Materials Science and Engineering 30.8 (2022), p. 085015.

- [296] H. Le, V. Nam, and T. Phan. "Migrations of Oxygen Vacancy in Tungsten Oxide (WO₃): A Density Functional Theory Study". In: Computational Materials Science 90 (2014), pp. 171–176.
- [297] K. Schlueter and M. Balden. "Dependence of Oxidation on the Surface Orientation of Tungsten Grains". In: *International Journal of Refractory Metals and Hard Materials* 79 (2019), pp. 102–107.
- [298] S. C. Cifuentes, M. A. Monge, and P. Pérez. "On the Oxidation Mechanism of Pure Tungsten in the Temperature Range 600–800°C". In: Corrosion Science 57 (2012), pp. 114–121.
- [299] J. Habainy et al. "Formation of Oxide Layers on Tungsten at Low Oxygen Partial Pressures". In: *Journal of Nuclear Materials* 506 (2018), pp. 26–34.
- [300] K. Jacob. "Phase Relationships in the System Cr-W-O and Thermodynamic Properties of CrWO₄ and Cr₂WO₆". In: Journal of Materials Science 15 (1980), pp. 2167–2174.
- [301] X. C. Li et al. "Modified Analytical Interatomic Potential for a W-H System with Defects". In: *Journal of Nuclear Materials* 408.1 (2011), pp. 12–17.
- [302] D. R. Mason, D. Nguyen-Manh, and C. S. Becquart. "An Empirical Potential for Simulating Vacancy Clusters in Tungsten". In: Journal of Physics: Condensed Matter 29.50 (2017), p. 505501.
- [303] D. Nguyen-Manh, A. P. Horsfield, and S. L. Dudarev. "Self-interstitial Atom Defects in bcc Transition metals: Group-specific Trends". In: *Phys. Rev. B* 73 (2 2006), p. 020101.
- [304] Y. Zhao, L. Dezerald, and J. Marian. "Electronic Structure Calculations of Oxygen Atom Transport Energetics in the Presence of Screw Dislocations in Tungsten". In: Metals 9.2 (2019).
- [305] A. Alkhamees et al. "First-principles Investigation on Dissolution and Diffusion of Oxygen in Tungsten". In: *Journal of Nuclear Materials* 393.3 (2009), pp. 508–512.

- [306] S. Ghosh and C. Ghosh. "Effect of Oxygen Interstitials on Structural Stability in Refractory Metals (V, Mo, W) from DFT Calculations". In: *The European Physical Journal B* 94.5 (2021), p. 114.
- [307] S. Akbas, M. K. Ozturk, and F. Aydogan. "Effect of Yttrium Addition on Structural, Mechanical and Thermodynamic Properties of Tungsten-Yttrium Alloys". In: Nuclear Materials and Energy 42 (2025), p. 101860.
- [308] T. Frolov et al. "Structures and Transitions in bcc Tungsten Grain Boundaries and their Role in the Absorption of Point Defects". In: *Acta Materialia* 159 (2018), pp. 123–134.
- [309] W. Setyawan and R. Kurtz. "Ab-initio Study of H, He, Li and Be Impurity Effect in Tungsten σ3[112] and σ27[552] Grain Boundaries". In: Journal of Physics: Condensed Matter 26 (2014), p. 135004.
- [310] P. M. Derlet, D. Nguyen-Manh, and S. L. Dudarev. "Multiscale Modeling of Crowdion and Vacancy Defects in Body-centered-cubic Transition Metals". In: *Physical Review B* 76 (5 2007), p. 054107.
- [311] R. Liu et al. "Fabricating High Performance Tungsten Alloys Through Zirconium Micro-alloying and Nano-sized Yttria Dispersion Strengthening". In: Journal of Nuclear Materials 451.1 (2014), pp. 35–39.
- [312] L. Barroso-Luque et al. Open Materials 2024 (OMat24) Inorganic Materials Dataset and Models. Pre-print. 2024.
- [313] A. D. Kaplan et al. A Foundational Potential Energy Surface Dataset for Materials. Pre-print. 2025.